DOT-VNTSC-FA727-PM-97-27
For Official Use Only
August 1997

U.S. Department
of Transportation

WAKE VORTEX

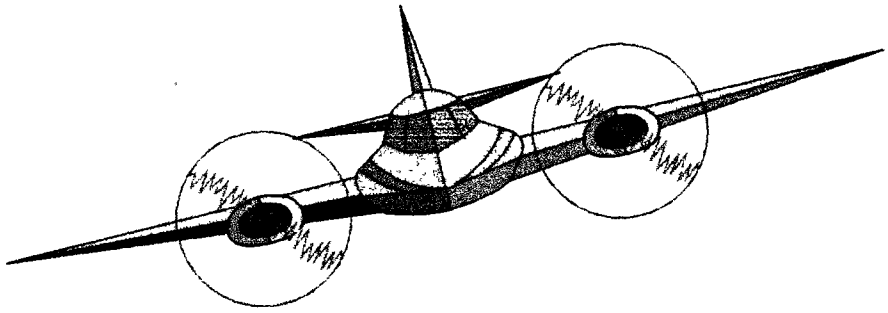

November 1996 Kennedy Airport Wake Vortex Test: Sensor Evaluation

Prepared for:

National Aeronautics and
Space Administration
Langley Research Center
Hampton, VA 23681

Prepared by:

U.S. Department of Transportation
Research and Special Programs Administration
Volpe National Transportation Systems Center
Surveillance and Sensors Division
Cambridge, MA 02142-1093

REPORT DOCUMENTATION PAGE

Form Approved
OMB No. 0704-0188

Public reporting burden for this collection of information is estimated to average 1 hour per response, including the time for reviewing instructions, searching existing data sources, gathering and maintaining the data needed, and completing and reviewing the collection of information. Send comments regarding this burden estimate or any other aspect of this collection of information, including suggestions for reducing this burden, to Washington Headquarters Services, Directorate for Information Operations and Reports, 1215 Jefferson Davis Highway, Suite 1204, Arlington, VA 22202-4302, and to the Office of Management and Budget, Paperwork Reduction Project (0704-0188), Washington, DC 20503.

1. AGENCY USE ONLY (Leave blank)	2. REPORT DATE	3. REPORT TYPE AND DATES COVERED
	August 1997	Project Memorandum November 1996 - August 1997

4. TITLE AND SUBTITLE
November 1996 Kennedy Airport Wake Vortex Test: Sensor Evaluation

5. FUNDING NUMBERS
FA727/A7072

6. AUTHOR(S)
David Burnham*

7. PERFORMING ORGANIZATION NAME(S) AND ADDRESS(ES)
U.S. Department of Transportation
Research and Special Programs Administration
Volpe National Transportation Systems Center
Cambridge, MA 02142-1093

8. PERFORMING ORGANIZATION REPORT NUMBER
DOT-VNTSC-FA727-PM-97-27

9. SPONSORING/MONITORING AGENCY NAME(S) AND ADDRESS(ES)
National Aeronautics and Space Administration
Langley Research Center
Hampton, VA 23681

10. SPONSORING/MONITORING AGENCY REPORT NUMBER

11. SUPPLEMENTARY NOTES
*Scientific & Engineering Solutions, Inc.
Orleans, MA

12a. DISTRIBUTION/AVAILABILITY STATEMENT
This document is available to the public through the National Technical Information Service, Springfield, VA 22161

12b. DISTRIBUTION CODE

13. ABSTRACT (Maximum 200 words)
In November 1996, a number of wake vortex and meteorological sensors were operated simultaneously in the middle marker region of Runway 31R at New York's Kennedy Airport. The vortex sensors included: 1)ground-based anemometer array, 2) cw 10-micron lidar, 3) fan-beam sodar, 4) RASS, 5) sonic anemometer, 6) scintillometer, and 7) vertical beam sodar. Comparisons of measurements from the different sensors are presented and used to analyze sensor capabilities and suitability for the NASA Aircraft Vortex Spacing System (AVOSS). A number of new observations were made during this test: 1) boundary thickness under wake vortex in ground effect, 2) high time resolution in situ temperature and velocity measurements inside the vortex recirculation oval, 3) directional measurements of vortex-generated sound, and 4) the influence of aircraft on meteorological conditions.

14. SUBJECT TERMS
wake vortices, wake vortex sensors, AVOSS, sodar, lidar, RASS, sonic anemometer, scintillometer

15. NUMBER OF PAGES
226

16. PRICE CODE

17. SECURITY CLASSIFICATION OF REPORT	18. SECURITY CLASSIFICATION OF THIS PAGE	19. SECURITY CLASSIFICATION OF ABSTRACT	20. LIMITATION OF ABSTRACT
Unclassified	Unclassified	Unclassified	

PREFACE

This document presents the results of a cooperative test program conducted by the National Aeronautics and Space Administration (NASA) Langley Research Center (LaRC)/Volpe Center team at the Federal Aviation Administration/Volpe Center Test Site at JFK International Airport. The primary objective of the test program was to evaluate candidate wake vortex sensors for use in supporting NASA's Aircraft Vortex Spacing System (AVOSS) development under the Terminal Area Productivity (TAP) Program. This was the first effort in more than twenty years to conduct comprehensive testing of a variety of vortex sensors. The comparison testing of some well established sensors with some recent innovative technologies and advanced implementations of some older technologies has proven fruitful in establishing procedural, siting, and testing baselines which will prove useful in conducting similar testing in the future.

A number of organizations participated in the test program and each organization provided personnel to support the testing activity. The participating organizations and the lead person for each organization are identified as follows:

NASA LaRC – Ben Barker

Volpe Center – Steve Abramson

MIT Lincoln Laboratory – Tim Dasey

WLR Research – Bill Rubin

B. F. Goodrich – George Succi

Scientific Technology Inc. – Ting-i Wang

AeroVironment – Ken Underwood

This report was prepared primarily by Dave Burnham of Scientific and Engineering Solutions, Inc. (SESI), a Volpe Center team member, with contributions by George Greene of NASA LaRC, and inputs, comments, and criticism, constructive of course, by members of all the participating organizations.

METRIC/ENGLISH CONVERSION FACTORS

ENGLISH TO METRIC

LENGTH (APPROXIMATE)

1 inch (in) = 2.5 centimeters (cm)
1 foot (ft) = 30 centimeters (cm)
1 yard (yd) = 0.9 meter (m)
1 mile (mi) = 1.6 kilometers (km)

AREA (APPROXIMATE)

1 square inch (sq in, in^2) = 6.5 square centimeters (cm^2)
1 square foot (sq ft, ft^2) = 0.09 square meter (m^2)
1 square yard (sq yd, yd^2) = 0.8 square meter (m^2)
1 square mile (sq mi, mi^2) = 2.6 square kilometers (km^2)
1 acre = 0.4 hectare (ha) = 4,000 square meters (m^2)

MASS - WEIGHT (APPROXIMATE)

1 ounce (oz) = 28 grams (gm)
1 pound (lb) = .45 kilogram (kg)
1 short ton = 2,000 pounds (lb) = 0.9 tonne (t)

VOLUME (APPROXIMATE)

1 teaspoon (tsp) = 5 milliliters (ml)
1 tablespoon (tbsp) = 15 milliliters (ml)
1 fluid ounce (fl oz) = 30 milliliters (ml)
1 cup (c) = 0.24 liter (l)
1 pint (pt) = 0.47 liter (l)
1 quart (qt) = 0.96 liter (l)
1 gallon (gal) = 3.8 liters (l)
1 cubic foot (cu ft, ft^3) = 0.03 cubic meter (m^3)
1 cubic yard (cu yd, yd^3) = 0.76 cubic meter (m^3)

TEMPERATURE (EXACT)

$°C=5/9(°F - 32)$

METRIC TO ENGLISH

LENGTH (APPROXIMATE)

1 millimeter (mm) = 0.04 inch (in)
1 centimeter (cm) = 0.4 inch (in)
1 meter (m) = 3.3 feet (ft)
1 meter (m) = 1.1 yards (yd)
1 kilometer (km) = 0.6 mile (mi)

AREA (APPROXIMATE)

1 square centimeter (cm^2) = 0.16 square inch (sq in, in^2)
1 square meter (m^2) = 1.2 square yards (sq yd, yd^2)
1 square kilometer (km^2) = 0.4 square mile (sq mi, mi^2)
10,000 square meters (m^2) = 1 hectare (ha) = 2.5 acres

MASS - WEIGHT (APPROXIMATE)

1 gram (gm) = 0.036 ounce (oz)
1 kilogram (kg) = 2.2 pounds (lb)
1 tonne (t) = 1,000 kilograms (kg) = 1.1 short tons

VOLUME (APPROXIMATE)

1 milliliter (ml) = 0.03 fluid ounce (fl oz)
1 liter (l) = 2.1 pints (pt)
1 liter (l) = 1.06 quarts (qt)
1 liter (l) = 0.26 gallon (gal)
1 cubic meter (m^3) = 36 cubic feet (cu ft, ft^3)
1 cubic meter (m^3) = 1.3 cubic yards (cu yd, yd^3)

TEMPERATURE (EXACT)

$°F=9/5(°C) + 32$

QUICK INCH-CENTIMETER LENGTH CONVERSION

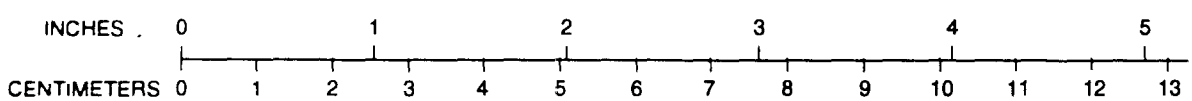

QUICK FAHRENHEIT-CELSIUS TEMPERATURE CONVERSION

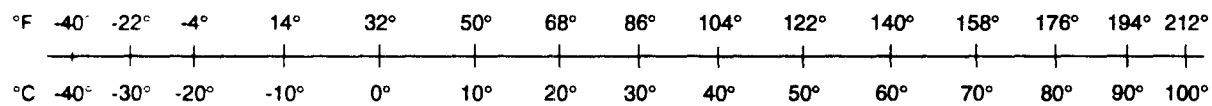

For more exact and or other conversion factors, see NIST Miscellaneous Publication 286, Units of Weights and Measures Price $2.50. SD Catalog No. C13 10286.

Updated 6/1/96

TABLE OF CONTENTS

Section — Page

1. INTRODUCTION 1

1.1 OBJECTIVES 1

1.1.1 Primary Objectives 1

1.1.2 Secondary Objectives 2

1.1.3 Evaluation Methodology 2

1.2 TEST PARTICIPANTS 2

2. TEST DESCRIPTION 3

2.1 APPROACH 3

2.1.1 Responsibilities 3

2.1.2 Data Recording 3

2.1.3 Pre-Test Checkout 3

2.1.4 Test Procedure 5

2.2 AIRPORT LAYOUT 5

2.3 SITE DESCRIPTION 6

2.4 VORTEX SENSOR COVERAGE 7

2.5 COORDINATE SYSTEM 8

3. SENSOR DESCRIPTIONS 9

3.1 ANEMOMETER ARRAY 9

3.1.1 Data Recording Formats 10

3.1.2 Measurement Capabilities 10

3.1.2.1 Wind and Turbulence 10

3.1.2.2 Lateral Vortex Locations 11

3.1.2.3 Height and Circulation 14

3.2 SONIC ANEMOMETERS 16

3.2.1 Metek Measurement Capabilities 16

3.2.2 Metek Data Reduction 17

3.2.3 ATI Measurement Capabilities 18

3.2.4 ATI Data Reduction 18

3.3 WIND PROFILE SODARS 19

3.3.1 Wind Profile Measurements 19

TABLE OF CONTENTS (cont.)

Section		Page
	3.3.2 Data Recording	20
	3.3.3 Data Reduction	20
	3.3.4 Wake Vortex Measurements	20
	3.4 MIT/LL LIDAR	20
	3.4.1 Signal Processing	22
	3.4.2 Measurement Method	23
	3.4.3 Real-Time Vortex Tracking	23
	3.4.4 Data Reduction	24
	3.4.5 Vortex File Format	24
	3.4.6 Crosswind Profiles	24
	3.5 MIT/LL METEOROLOGICAL SENSORS	25
	3.6 WLR RESEARCH RASS	25
	3.6.1 Detection Capabilities	26
	3.6.2 Circulation Estimate	26
	3.6.3 Data Format.	27
	3.7 SCTI SCINTILLOMETER	28
	3.7.1 Real-Time Processing Algorithms	28
	3.7.2 Off-Line Data Processing	29
	3.8 WV SODAR	31
	3.8.1 System Operation	33
	3.8.2 Data Formats	34
	3.8.3 Data Analysis	34
4.	VORTEX SENSOR COMPARISONS	39
	4.1 ANEMOMETER ARRAY - LIDAR	39
	4.1.1 Lateral Position Comparisons	39
	4.1.2 Overlay Plots	39
	4.2 ARRAY - LIDAR - SODAR	40
	4.2.1 Lateral Position	40
	4.2.2 Height	40
	4.2.3 Circulation	42
	4.3 RASS - LIDAR	42

TABLE OF CONTENTS (cont.)

Section — Page

4.3.1 Location ... 42
4.3.2 Circulation ... 44

5. METEOROLOGICAL SENSOR COMPARISONS ... 47

5.1 WIND ... 47
5.1.1 Validation ... 47
5.1.2 Profiles ... 48
5.1.2.1 Time Variation ... 48
5.1.2.2 Lidar-Sodar Comparisons ... 50
5.2 WIND TURBULENCE ... 52
5.3 TEMPERATURE ... 53
5.4 TEMPERATURE FLUCTUATIONS ... 54

6. VORTEX OBSERVATIONS ... 57

6.1 BOUNDARY LAYER UNDER VORTEX ... 57
6.1.1 Sample Vortex Data ... 57
6.1.2 Ambient Wind Profiles ... 59
6.2 SONIC ANEMOMETER MEASUREMENTS INSIDE VORTEX OVAL ... 59

7. EFFECT OF AIRCRAFT ON METEOROLOGY ... 63

8. CONCLUSIONS ... 65

8.1 FIRST TIME OBSERVATIONS ... 65
8.2 VORTEX SENSOR STATUS ... 65
8.2.1 MIT/LL Lidar ... 65
8.2.2 Anemometer Array ... 65
8.2.3 RASS ... 65
8.2.4 WV Sodar ... 66
8.3 WIND MEASUREMENTS BY VORTEX SENSORS ... 66
8.4 METEOROLOGICAL MEASUREMENTS ... 66

9. RECOMMENDATIONS ... 69

9 1 AVOSS VORTEX SENSOR SUITABILITY ... 69
9.1.1 Vortex Sensor Requirements ... 69

TABLE OF CONTENTS (cont.)

Section		Page
	9.1.2 Anemometer Array	69
	9.1.3 RASS	70
	9.1.4 WV Sodar	70
	9.1.5 Scintillometer	70
	9.2 FUTURE TESTS	70
	9.2.1 Test Procedures	70
	9.2.2 Analysis Methods	70
	9.2.3 Anemometer Array	71
	9.2.4 MIT/LL Lidar	71
	9.2.5 RASS	71
	9.2.6 WV Sodar	71
	9.2.7 Sonic Anemometers	71
	9.2.8 Scintillometer	72
	9.2.9 Meteorological Sodars	72
APPENDIX:	COMPARISON OF VORTEX DATA FROM LIDAR AND ANEMOMETER ARRAY	A-1
REFERENCES		R-1

LIST OF ILLUSTRATIONS

Figure Page

Figure 1. Data Collection: Local Area Network and Independent Computers 4
Figure 2. Kennedy Airport Layout 5
Figure 3. Site Layout (not to scale) 6
Figure 4. Cross Track Coverage of Wake Vortex Sensors 7
Figure 5. B-747 Approaching Runway 31R over Anemometer Array (Volpe Trailer on Left, Middle Marker on Right) 9
Figure 6. Sample Plot of Meteorological Variables (November 20, 1996) 12
Figure 7. Sample Output from Least-Square-Fit Analysis 15
Figure 8. Metek Sonic Anemometer 16
Figure 9. Minisodar (Model 4000) 19
Figure 10. Sample Minisodar Wake Vortex Data 21
Figure 11. Layout of MIT/LL Lidar Van 21
Figure 12. Optical Configuration of MIT/LL Lidar 21
Figure 13. Lidar Deployment Scenarios 22
Figure 14. Depiction of Lidar Scan Across a Single Vortex (left) and Spectral Maximum Velocity versus Crossrange (right) from a Scan Across a Pair of Vortices Generated by a Boeing 757 23
Figure 15. RASS (right) near Volpe Trailer (left) 26
Figure 16. Sample RASS Plot 27
Figure 17. LOA Block Diagram 28
Figure 18. LOA Sensing Baselines 29
Figure 19. Sample Wind (m/s) (top) and Turbulence ($m^{-2/3}$) (bottom) LOA Data from November 20, 1996. 30
Figure 20. Sodar Coverage and Resolution (units of feet) 31
Figure 21. Sodar Acoustic Elements 32
Figure 22. Wake Vortex Sodar Mounted on Trailer 33
Figure 23. Beam-Formed Spectra (Ages 2-20 seconds) for B-747 Run 156 on November 13, 1996) 36
Figure 24. Beam-Formed Spectra (Ages 23-41 seconds) for B-747 Run 156 on November 13, 1996) 37

LIST OF ILLUSTRATIONS (cont.)

Figure | Page

Figure 25. Beam-Formed Spectra (Ages 0-18 seconds) for L-1011 Run 163 on November 13, 1996) 38

Figure 26. Histogram of Lateral Position Differences 39

Figure 27. Response of Crosswind Anemometers (0830-0930, November 22, 1996) 40

Figure 28. Lateral Position Measured by Anemometer Array, Lidar and Sodar (Runs 150, 156 on November 13, 1996) 41

Figure 29. Height Measured by Anemometer Array, Lidar, and Sodar (Runs 150, 156 on November 13, 1996) 41

Figure 30. Circulation Measured by Anemometer Array and Lidar (Runs 150, 156 on November 13, 1996) 42

Figure 31. RASS Data for B-747 Run 284 on November 20, 1996 43

Figure 32. Comparison of Lidar Vortex Trajectory to RASS Range Bins 43

Figure 33. Comparison of RASS and Lidar Circulations 45

Figure 34. Sonic Anemometer Crosswind and Headwind Components for November 20 (5-minute average) 47

Figure 35. Comparison of Sodar Crosswind and Headwind at 50 Meters Altitude (5-minute average) 48

Figure 36. Lidar Crosswind Profile (one-minute average) 49

Figure 37. M3000 Sodar Crosswind and Headwind Profiles(5-minute average) 49

Figure 38. M4000 Sodar Crosswind and Headwind Profiles (5-minute average) 50

Figure 39. Sample Plot Comparing Crosswind Profiles: Lidar and One-Minute Sodar Data 51

Figure 40. Sample Plot Comparing Crosswind Profiles: Lidar and Five-Minute Sodar Data 51

Figure 41. Metek Sonic Anemometer Turbulence 53

Figure 42. Propeller Anemometer (Pole 15) Turbulence 53

Figure 43. Temperature Comparisons for November 20 54

Figure 44. Variations in log C_n^2 on November 20, 1996 55

Figure 45. Variations in Metek Sonic Anemometer Temperature on November 20, 1996 55

Figure 46. Crosswind Profile under B-747 Vortex, Run 242 on November 17, 1996 57

LIST OF ILLUSTRATIONS (cont.)

Figure Page

Figure 47. Crosswind Ratios, Run 242 57
Figure 48. Vertical Wind Profile, Run 242 57
Figure 49. Crosswind Profile for Run 248 on November 17, 1996 58
Figure 50. Crosswind Ratios for Run 248 on November 17, 1996 58
Figure 51. Vertical Wind Profile for Run 248 on November 17, 1996 58
Figure 52. Crosswind Profile for Run 251 on November 17, 1996 58
Figure 53. Crosswind Ratios for Run 251 on November 17, 1996 58
Figure 54. Vertical Wind Profile for Run 251 on November 17, 1996 58
Figure 55. Ambient Crosswind at 28 feet on November 15, 1996 59
Figure 56. Ambient Crosswind Ratios on November 15, 1996 59
Figure 57. Crosswind and Vertical Wind from Propeller Anemometers on Pole 7 (-50 feet) 60
Figure 58. Crosswind Comparison 61
Figure 59. Vertical Wind Comparison 61
Figure 60. Temperature 61
Figure 61. Headwind 61
Figure 62. Temperature, Relative Humidity on November 18, 1996 63
Figure 63. Runway Centerline Vertical Wind Standard Deviation on November 18, 1996 63

LIST OF TABLES

Table | Page

Table 1. Participating Organizations 2
Table 2. Sensor Responsibilities 3
Table 3. Operational Test Periods 5
Table 4. Sensor Locations (feet) 7
Table 5. Terminology for Wind and Turbulence Components 11
Table 6. Midisodar (M3000) Characteristics 19
Table 7. Minisodar (M4000) Characteristics 19
Table 8. RASS Range Bin Characteristics 27
Table 9. Vortex Locations in Figures 23 and 24 35
Table 10. Anemometer Processing 47
Table A-1. Summary of Anemometer Array - Lidar Comparison A-1
Table A-2. Run by Run Comparison of Lidar and Anemometer Array Measurements A-3

LIST OF ACRONYMS

AVOSS	Aircraft Vortex Spacing System
CATER	Collection & Analysis of Terminal Records
cw	Continuous Wave
DAS	Data Acquisition System
DOT	Department of Transportation
DSP	Digital Signal Processor
FFT	Fast Fourier Transform
GPS	Global Positioning System
JFK	New York's Kennedy International Airport
LAN	Local Area Network
LaRC	Langley Research Center
LED	Light Emitting Diode
lidar	light detection and ranging
LO	Local Oscillator
LOA	Long-Baseline Optical Anemometer
MAVSS	Monostatic Acoustic Vortex Sensing System
MIT/LL	Massachusetts Institute of Technology's Lincoln Laboratory
MO	Master Oscillator
NASA	National Aeronautics and Space Administration
RASS	Radar Acoustic Sensing System
RG	Range Gate
SBIR	Small Business Innovative Research
ScTI	Scientific Technology, Inc.
sodar	sound detection and ranging
SOR	Start of Run
TAP	Terminal Area Productivity
TII	Technology Integration, Inc.
US	United States
UTC	Universal Time Clock
WV	Wake Vortex

1. INTRODUCTION

The NASA Langley Research Center's (LaRC) Terminal Area Productivity (TAP) Program is investigating new sensor technologies for measuring aircraft wake vortices. The new technologies will be evaluated by comparison with more established sensor technologies.

In June 1994, under the aegis of the Federal Aviation Administration (FAA), the US Department of Transportation (DOT) Volpe National Transportation Systems Center (Volpe Center) established[1] a wake vortex test site in the approach region to Runway 31R at New York's Kennedy International Airport (JFK). An array of anemometers is used to track the lateral position of wake vortices from landing aircraft at a point nominally 3100 feet from touchdown. Such an array is an all-weather system, which has been shown[2] to give accurate lateral vortex positions but has not provided vortex strength information. Recently developed[1] processing algorithms show promise of also measuring vortex height and circulation, but they need validation by comparison with a remote sensor known to measure height and circulation.

The utility of the FAA/Volpe Center JFK Test Site in meeting NASA LaRC's sensor testing requirements led to in a cooperative effort between NASA LaRC and the Volpe Center. In addition to the advantage of the Volpe anemometer line serving as ground truth, another factor which made the site attractive for this effort is the abundance of Heavy aircraft, including the largest civilian jet transport (B-747-400) operating into JFK airport and frequently using runway 31R under a variety of meteorological conditions. Testing commenced on November 13, 1996 and continued through November 22, 1996.

1.1 OBJECTIVES

1.1.1 Primary Objectives

The original objectives for the November 1996 JFK wake vortex test were to:

1. Test and refine performance of the LaRC pulsed lidar system,
2. Correlate performance of the LaRC pulsed lidar system with the Massachusetts Institute of Technology's Lincoln Laboratory (MIT/LL) cw lidar system,
3. Evaluate and compare the capabilities of the lidar systems with other candidate wake vortex detection systems, and
4. Collect meteorological data from both dedicated meteorological instruments and wake vortex detection instruments that will add to our understanding of the relationship between meteorological condition and vortex behavior.

Since the LaRC pulsed lidar was not available during the time frame of the test, the first two objectives were deferred until the spring of 1997, when an additional JFK test was planned. This new test implied a fifth objective, namely to learn from the November 1996 test how to improve the spring 1997 test.

Objectives 3 and 4 will be addressed in this report. The MIT/LL cw lidar will serve as the reference sensor for Objective 3. The focus of this report is sensor evaluation; the use of the data

collected for understanding wake vortex behavior as a function of meteorological conditions (second part of Objective 4) will be deferred to a future report.

1.1.2 Secondary Objectives

Several specific secondary objectives were of interest to both NASA and the Volpe Center.

1. Assess height and circulation accuracy of anemometer array,
2. Measure thickness of boundary layer under a wake vortex,
3. Compare turbulence measurements of propeller and sonic anemometers, and
4. Assess feasibility of using ground-based measurements inside the vortex oval to infer the vertical variation of potential temperature and headwind.

Sample data will be presented to address these objectives.

1.1.3 Evaluation Methodology

The following sensors will be used as wake vortex reference sensors:

1. Lateral position - cw lidar, anemometer array.
2. Height - cw lidar.
3. Circulation - cw lidar.

The anemometer array normally tracked both vortices. The cw lidar usually tracked only one vortex; when both vortices were close together the data provided an approximate location for the other vortex. Simultaneous tracks for both vortices usually lasted for only a short time (typically 10-20 seconds).

The following sensors will be used as meteorological reference sensors:

1. Wind Component - anemometer array, two sodars.
2. Turbulence - sonic anemometer, propeller anemometer.
3. Temperature - sonic anemometer

The report will not analyze the data collected by the MIT/LL weather station.

1.2 TEST PARTICIPANTS

Table 1 lists the organizations participating in this test and the sensors for which they were responsible. NASA/LaRC and the Volpe Center assisted all participants with coordinating approvals, logistics, and system installation.

Table 1. Participating Organizations

Organization	Sensor
Volpe Center	Anemometer Array Sonic Anemometers
AeroVironment	Sodars
MIT/LL	Lidar (cw, 10-micron) Weather Station Sonic Anemometer
Scientific Technology, Inc.	Optical Anemometer
WLR Research	RASS
B. F. Goodrich (TII)	Wake Vortex Sodar

2. TEST DESCRIPTION

2.1 APPROACH

2.1.1 Responsibilities

The Volpe Center and NASA/LaRC each appointed a test director and they were authorized to modify test procedures and plans as necessary to achieve test objectives. Their responsibilities included:

1. Coordination: e.g., time sharing or relocating sensors that interfere with each other
2. Test Schedule
3. Logistics: transporting personnel, visitors, equipment, and fuel to and from the test site.

Responsibilities for acquisition, installation and operation of the various instruments and systems are shown in Table 2.

Table 2. Sensor Responsibilities

Sensor	Sponsor	Installation/Operation
CW Lidar	LaRC	Lincoln Laboratory
Anemometer Array	Volpe Center	Volpe Center
Wake Vortex Sodar	LaRC	BF Goodrich/TI
Wake Vortex RASS	Volpe Center	WLR Research
Weather Station	LaRC	Lincoln Laboratory
Sonic Anemometer	LaRC	Lincoln Laboratory
Meteorological Sodars	Volpe Center	Volpe Center
ScTI Scintillometer	LaRC	Volpe Center
Sonic Anemometers	Volpe Center	Volpe Center

2.1.2 Data Recording

The data recording made use of the Volpe Local Area Network (LAN) and a number of independent data collection computers, as detailed in Figure 1. For simplification, the Lincoln Laboratory data collection systems are omitted from Figure 1. The MIT/LL Node in Figure 1 was located in the MIT/LL Lidar Van to provide real-time displays of the data from the Volpe anemometer array.

At the beginning of each test period the clocks were synchronized among most of the independent recording systems. Because of the complex interactions between the different recording systems, this synchronization was not totally successful.

The aircraft arrivals and aircraft identifications were recorded for a number of the data systems. The FAA Eastern Region provided Collection & Analysis of Terminal Records (CATER) data for part of the test period (November 12-15, 1996). The CATER file lists aircraft type with approximate landing times for Runway 31R arrivals.

2.1.3 Pre-Test Checkout

Each test participant was responsible for completely checking the performance of their equipment prior to test and certifying to the test directors that it was ready for inclusion in the test. Checks were run to determine if there were any detrimental interference between systems which would preclude simultaneous operations. The Wake Vortex Sodar was moved farther down the road towards the runway to eliminate interference from the RASS System. MIT/LL moved their electrical generator system to reduce possible noise interference with the meteorological

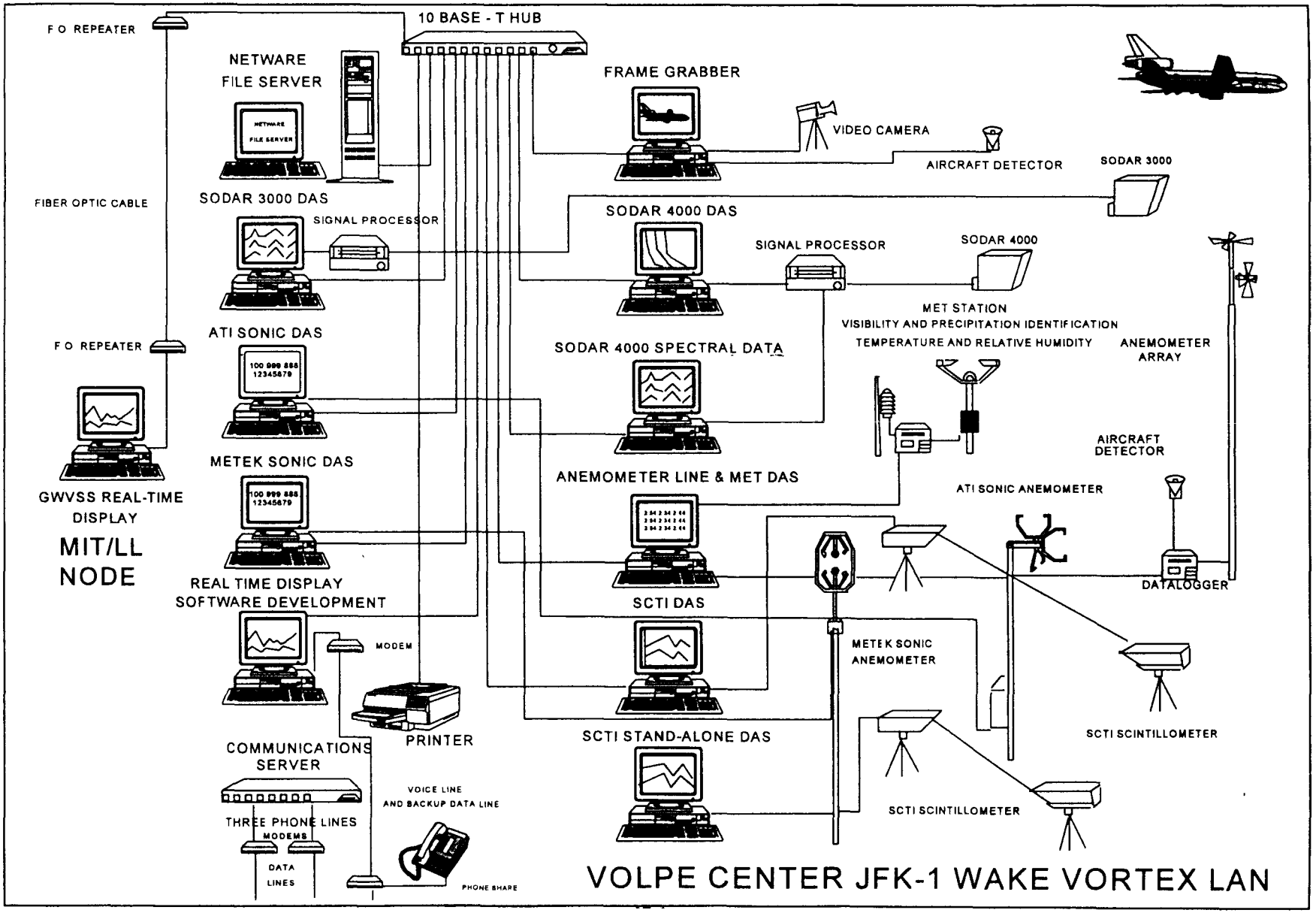

Figure 1. Data Collection: Local Area Network and Independent Computers

minisodar. It was later determined that the interference was an internal problem within the sodar and not due to any external objects or systems.

2.1.4 Test Procedure

In 1994 and 1995, the Volpe data collection at the site was automatic and continuous, apart from a number of failures in the data acquisition equipment and aircraft noise detectors. When the site was reactivated in August 1996, a lightning strike destroyed much of the data acquisition equipment. After the strike, the equipment was repaired or replaced and additional lightning protection was installed. However, to assure that the site would be available for the test described in this report, a more conservative approach to site operation was adopted. Whenever personnel were not at the site, all data acquisition equipment was deactivated and disconnected. Thus, data were collected only during short periods of November 1996.

After pre-test checkout of all systems, practice data recording began on November 12, 1996. At the beginning of each day all clocks were synchronized using a Global Positioning System (GPS) receiver to derive UTC clock time. Volpe Center personnel called the Air Traffic Control Tower Chief to ascertain current and future traffic patterns and to request the use of Runway 31R for arrivals, if at all possible. Personnel in the Volpe trailer recorded aircraft type and passage time over the anemometer array whenever testing was operational. Table 3 shows the time periods when testing was operational.

Table 3. Operational Test Periods

Date	Hours
11/12/96	19:24:43 - 22:18:37
11/13/96	14:08:46 - 22:27:48
11/14/96	12:52:00 - 22:32:46
11/15/96	11:43:22 - 20:03:14
11/20/96	14:21:31 - 22:08:00

2.2 AIRPORT LAYOUT

Figure 2 shows the airport layout, which shows the location of Runway 31R.

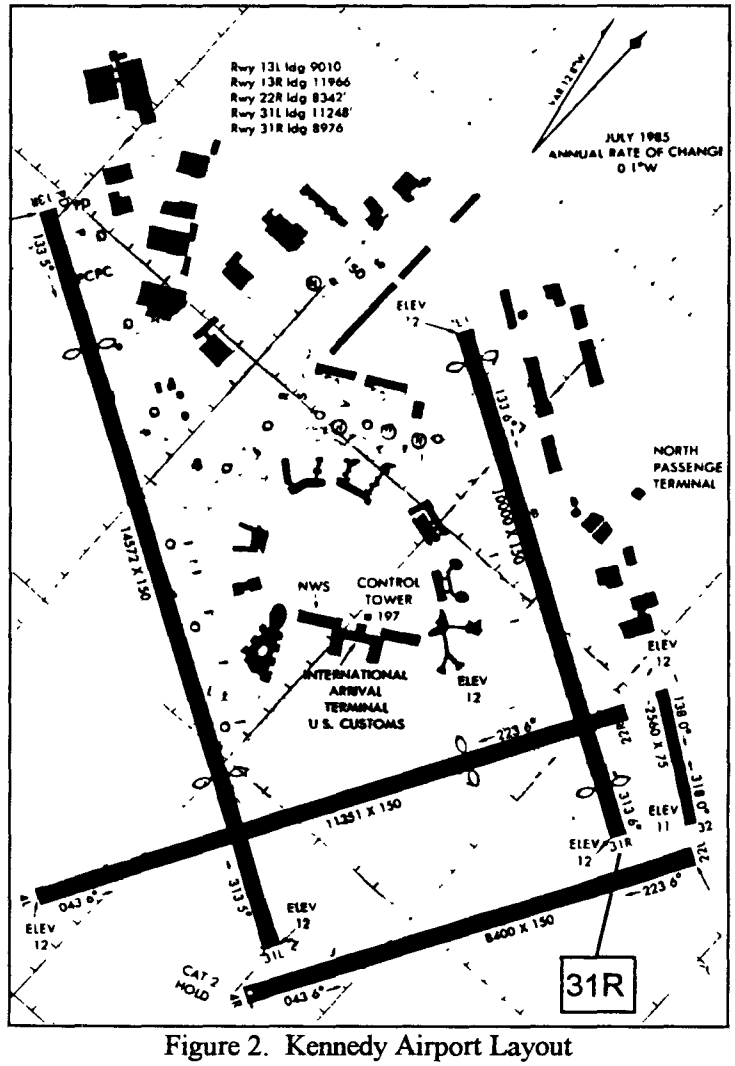

Figure 2. Kennedy Airport Layout

2.3 SITE DESCRIPTION

Figure 3 shows the detailed layout of the test site in the middle marker region of Runway 31R.

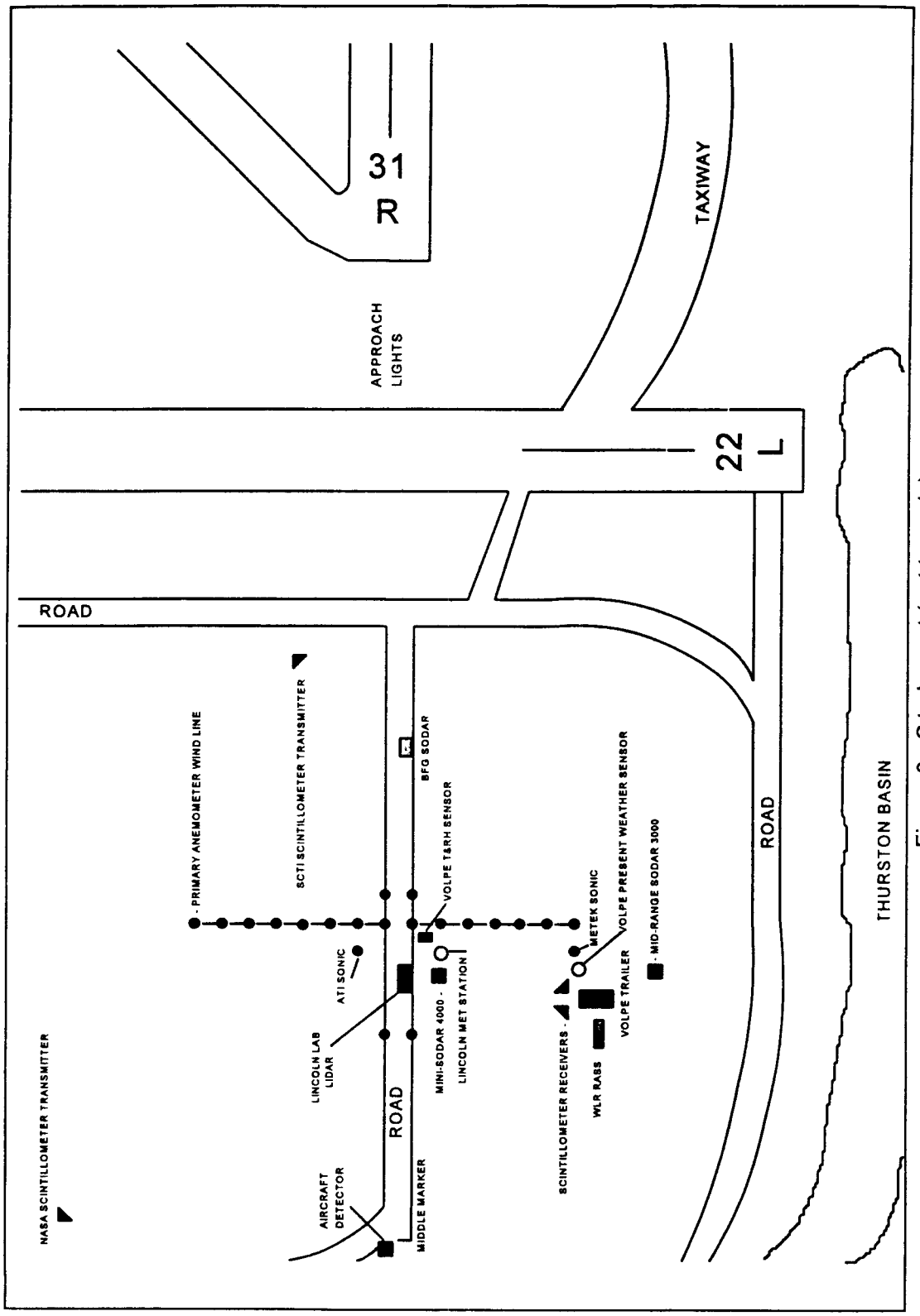

Figure 3 . Site Layout (not to scale)

Table 4 shows the exact sensor locations with respect to the Runway 31R extended centerline (lateral position) and the 31R middle marker (longitudinal position). The middle marker is 2300 feet from the threshold of Runway 31R. The scintillometer locations are those at the beginning of the test. With respect to the extended runway centerline, positive lateral position is towards the northeast (the pilot's right or starboard on approach) and negative lateral position is towards the southwest (the pilot's left or port on approach). With respect to the middle marker location, positive longitudinal position is towards the runway (northwest) and negative direction is away from the runway (southeast).

Table 4. Sensor Locations (feet)

Sensor Name	Lateral Position	Longitudinal Position
Anemometer Array	±350	400
Lidar	+45	300
MIT/LL Tower	+70	300
RASS	+380	200
Wake Vortex Sodar	+45	600
SCTI Scintillometer (R)	+350	250
SCTI Scintillometer (T)	-200	1000
NASA Scintillometer (R)	+350	250
NASA Scintillometer (T)	-300	-200
Mini-Sodar 4000	+100	300
Mini Sodar 3000	+600	300
Metek Sonic	+350	350
ATI Sonic	-50	350

2.4 VORTEX SENSOR COVERAGE

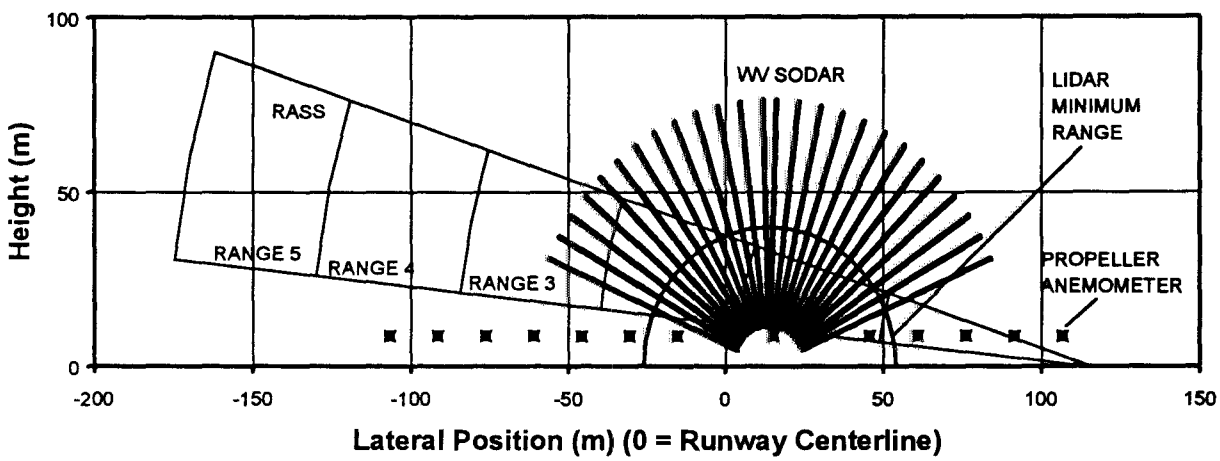

Figure 4. Cross Track Coverage of Wake Vortex Sensors

The relative coverage of the vortex sensors is critical to the feasibility of the planned sensor inter-comparisons. Figure 4 shows the relative coverage of the various vortex sensors. Note that, only a small portion of space was covered by all four sensors. The following assumptions were made in generating Figure 4:

1. The RASS range gates are defined by the operating software. Comparisons with lidar data suggested that the RASS range gates were about one-range gate width farther from the RASS than the ranges specified by the software. Subsequent checking of the radar with a range calibration unit showed that the ranges should be increased by 1.16 range gates beyond the nominal values. The corrected values are plotted in Figure 4.
2. The lidar range limits are taken as 40 to 250 meters. The 40-meter minimum range value was based on the data collected during the test.

3. The sodar range limits are taken as the lower limit of range gate 2 (37 feet) and the middle of range gate 10 (250 feet). The 26 sodar beams are shown.

4. The positions of the propeller anemometers in the array are shown; the vortex detection coverage may extend to perhaps 30 or 40 meters above each anemometer, depending upon the vortex strength.

2.5 COORDINATE SYSTEM

The coordinate system used to describe the test and its results is based on Runway 31R landings:

1. Lateral position: zero at extended runway centerline, positive to right for landing aircraft.
2. Longitudinal position: zero at middle marker, positive toward runway.
3. Headwind: Positive for wind blowing from runway.
4. Crosswind: Positive for wind blowing to right for landing aircraft.
5. Vertical wind: Positive is up.

3. SENSOR DESCRIPTIONS

The following sections describe the sensors installed for the test, discuss the data recording formats, and present sample data from the sensors.

3.1 ANEMOMETER ARRAY

The details of the anemometer array installation (see Figure 5) and processing algorithms are contained in Reference 1 and in a separate report[3]. A summary description will be presented here.

Figure 5. B-747 Approaching Runway 31R over Anemometer Array (Volpe Trailer on Left, Middle Marker on Right)

The primary anemometer array was installed on a baseline:

1. Oriented perpendicular to the extended runway centerline,
2. Located 400 feet inside the Runway 31R middle marker, and
3 Extended ± 350 feet from the extended runway centerline.

Vertical wind and crosswind propeller anemometers (R. M. Young Model 27106R) were mounted on 27-foot fiberglass poles spaced 50 feet apart, the actual height is about 28 feet to the crosswind anemometer and 29 feet to the vertical anemometer. A nominal height of 30 feet or 10 meters is sometimes assumed.

The primary anemometer array was augmented by:

1 Headwind anemometers at both ends of the primary array (± 350 feet) and near the middle (+50 feet).

2. Two additional short arrays (centerline and +50 feet) at distances of 200 and 450 feet from the middle marker. Prior tests generally measured a single cross-section through a vortex and hence could not detect vortex distortion (i.e., Crow instability) which may reduce the vortex hazard. This installation has made a limited effort to detect distortion for stalled vortices by installing two additional short arrays near the runway centerline. (Airport obstruction rules would mandate shorter poles at locations closer to touchdown.)

3 At one location (+100 feet) three additional, shorter poles were installed (14, 7 and 3.5 feet) to assess the thickness of the boundary layer under a wake vortex. Both vertical wind and crosswind anemometers were mounted on each pole.

3.1.1 Data Recording Formats

The signal from each anemometer is sampled at 10 Hz and averaged for 2 seconds in a Campbell Scientific data acquisition system (DAS) before being transmitted to the central data acquisition system. Data collection is completely automatic and runs unattended. Aircraft arrivals are detected by a noise sensor (vertical pointing horn-type loudspeaker) which, after amplification, rectification and low-pass filtering, is also averaged for 2 seconds. A peak in the noise level above a specified noise level triggers the start-of-run (SOR) procedure for data collection and real-time processing/display. The following files are recorded when the system is in operation:

1. Run files, which start ten seconds before SOR (using a one-minute data buffer) and terminate at the next SOR or after three minutes, whichever comes first.
2. Complete daily files, which contain all data received by the central DAS.
3. Reduced daily files, which contain all data received by the central DAS from one minute before SOR until five minutes after SOR.
4. Daily meteorological data files, which consist of one-minute data blocks containing reports from each meteorological sensor and the mean and standard deviation for each anemometer (from two-second measurements).

Two additional files are updated continually for real-time analysis. One file saves the last two-second block of wind measurements. Another file saves the data from the last aircraft arrival.

3.1.2 Measurement Capabilities

3.1.2.1 Wind and Turbulence

The anemometer array provides detailed information about wind and turbulence[4] at 30 feet above the ground. The wind components can be estimated from one-minute means, which can be obtained from (a) the daily meteorological data files or (b) the first 60 seconds of the run files. The wind component turbulence can be estimated using one-minute standard deviation values, from either data source, (a) or (b). One-minute turbulence values can have fluctuations of more than a factor of two and hence are not very satisfactory. Longer time averages (e.g., 15 minutes) can be obtained by processing the daily meteorological files.

The presence of wake vortices is the primary limitation on using anemometer array data for assessing ambient wind and turbulence. The influence of wake vortices can generally be excluded by taking the wind measurements from the upwind end of the array with respect to the crosswind Two algorithms were used to assess ambient wind:

1. The sum of the crosswinds is used to determine which direction the crosswind is blowing. The data from the upwind end is then taken as the ambient wind.

2. The crosswind turbulence values from the ends of the array are compared. The lower value is used to characterize the crosswind turbulence (which is the primary limitation on tracking wake vortices with the anemometer array).

Figure 6 shows a sample 24-hour plot of the meteorological parameters, showing both ends of the anemometer array (poles 01 and 15). The wind parameters are named as indicated in Table 5 (pole number = nn). The temperature is labeled TMPC and the relative humidity HUMD. Note that C15 and H15 have spikes at 1410 hours; such spikes are caused by transmission errors between the field DAS and the central DAS.

Table 5. Terminology for Wind and Turbulence Components

Component	Mean Wind	Standard Deviation
Headwind	Hnn	THnn
Crosswind	Cnn	TCnn
Vertical	Vnn	TVnn

The influence of wake vortices on the measurements can be noted from 1100 to 1245 hours. Since the crosswind is positive in this time period, the wind is blowing toward Pole 15. All three wind components show much higher turbulence values for Pole 15 than for Pole 01.

3.1.2.2 Lateral Vortex Locations

The first step in analyzing the anemometer array measurements uses the traditional crosswind tracking algorithm[2] which assigns the lateral position of the two wake vortices to the anemometers showing the maximum and minimum crosswind components. A number of refinements are required to provide reliable data under all conditions:

1. The median crosswind across the array is taken as an estimate of the ambient crosswind; using the median crosswind value usually eliminates the effects of the wake vortices. This algorithm would work better if the array were longer, so that a smaller fraction of the array would be influenced by the vortices. The vortex crosswinds for the two vortices are taken as the difference between the maximum or minimum crosswind and the median crosswind.

2. The value of the vortex crosswind is used to start and stop the vortex trajectory. Fixed starting and stopping thresholds of 2.0 and 1.0 m/s, respectively, were used in prior studies[3] and worked reasonably well under low turbulence conditions. Since the turbulence levels were higher for most of the November 1996 runs available for sensor inter-comparisons, the starting and stopping thresholds had to be adjusted for the measured turbulence levels. To provide a stable turbulence value for this purpose, a 15-minute average of the minimum crosswind standard deviation (Section 3.1.2.1) was used. The average was taken prior to the aircraft arrival so that the algorithm could be used for real-time analysis in the future. A longer averaging time will provide a more stable value, but a shorter averaging time will better follow changes in turbulence levels. The analysis (presented in Appendix A) suggested that 15 minutes was long enough to give a stable value, but may have given a crosswind variance value that was not always appropriate for a given run. Future work will study shorter averaging times. The selection of starting and stopping threshold values is a tradeoff between false detections (values too low) and missed detections (values too high). After evaluating a variety of values, the starting threshold was set at 6.0 times the minimum crosswind standard deviation (minimum threshold of 2.7 m/s) and the stopping threshold was set at 4.0 times the minimum crosswind standard deviation (minimum threshold of 1.6 m/s).

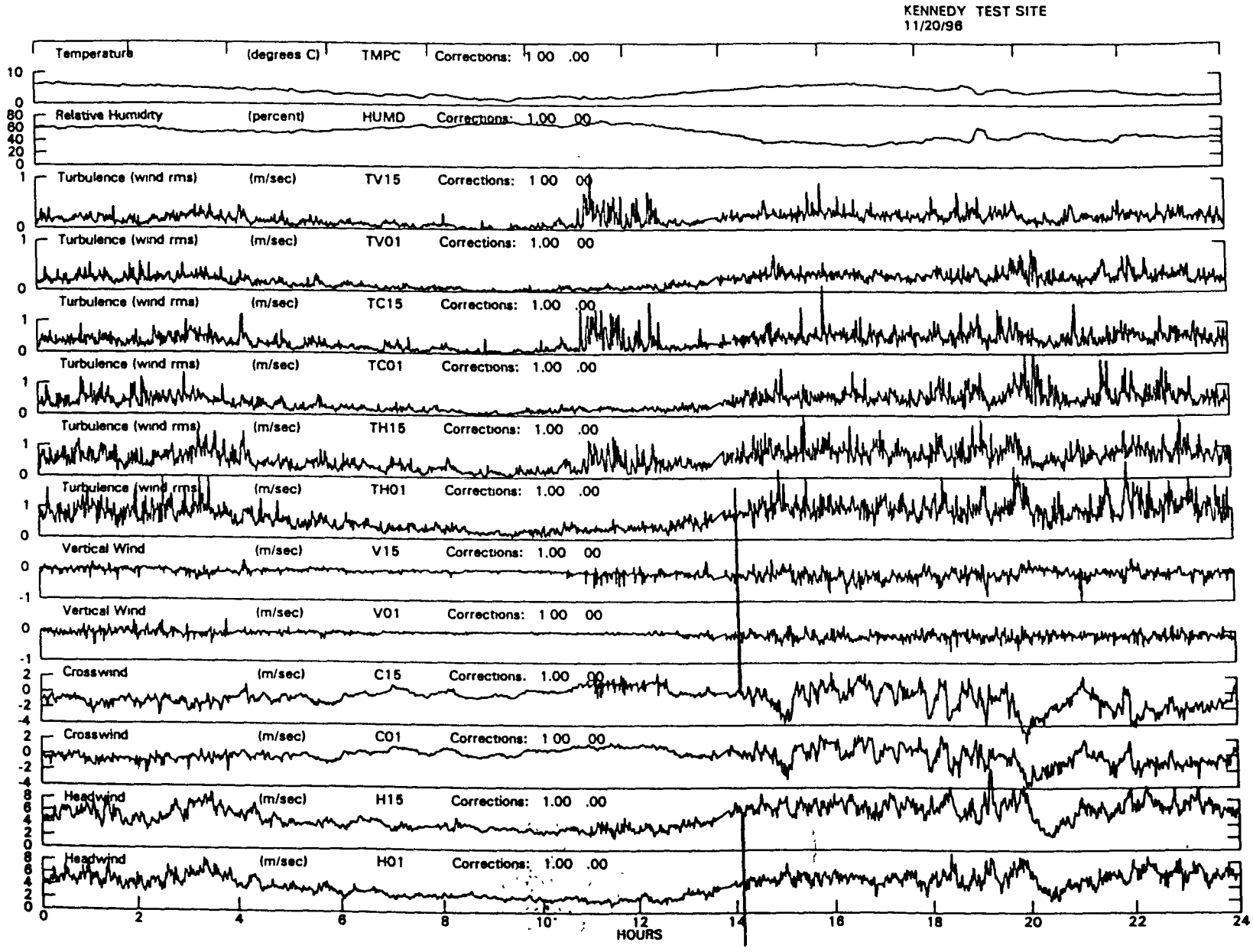

Figure 6. Sample Plot of Meteorological Variables (November 20, 1996)

3. The traditional anemometer array tracking algorithm terminated the vortex trajectory whenever the lateral position determination became unreliable. This approach is reflected in the current processing by terminating a vortex track when the vortex location jumps by more than three poles.

4. The finite length of the anemometer array poses tracking problems when a vortex moves off the end of the array. In this case, the apparent vortex lateral position remains fixed at the last anemometer even though the actual location may lie far beyond the array. The maximum duration of the vortex track at the last anemometer is set[3] at 1.5 times the time it spent at the next to last anemometer. The existing algorithm[3] had to be refined for the analysis of Appendix A to account for a) vortices first detected at the last anemometer, and b) vortex locations moving toward the runway centerline after reaching the next to last anemometer.

The analysis of Appendix A examined the question of whether a vortex track should be restarted after it is terminated. In most cases, it was found to be better to restart the trajectory when the starting threshold was exceeded and rely on the difference between starting and stopping thresholds to eliminate false restarts. The one exception was when the vortex had traveled off the end of the array; if the vortex is lost off the end and its age is 12 seconds or greater, then the track is never restarted. The early age vortex data can be influenced by the wake vortices from the previous arrival; the algorithms must be designed to prevent such vortices from dominating the analysis of the current run.

The algorithm described above was used to start the height and circulation algorithms described in the next section. An alternative analysis was used to provide the lateral position data distributed to the other test participants:

1. The wind field was averaged with a six-second running average (i.e., averaging three consecutive 2-second averages).

2. The maximum and minimum crosswind values were determined across the array during the ten seconds prior to SOR; the max-min difference was used to set the vortex crosswind tracking threshold. This difference may be greater than ambient because of the residual wake vortices from the prior aircraft. High thresholds will result in missed vortices.

3 The same vortex crosswind threshold was used for starting and stopping; it was set at 0.50 times the max-min difference.

4. When the vortex position jumped more than one pole position, the track was terminated if the vortex crosswind was less than 0.75 times the max-min difference.

5. Once a track was terminated, it was not restarted. The use of the six-second running average on the measured wind field reduced the chances of a momentary vortex dropout.

6. No attempt was made to limit the length of time a vortex was apparently located at the end of the anemometer array.

3.1.2.3 Height and Circulation

A least-square-fit algorithm was developed[1,3] to extend the analysis of the anemometer array data to estimate vortex height and circulation and refine the lateral position given by the min-max crosswind algorithm. The parameters of the fit are:

1. Ambient crosswind,
2. Height of each vortex included in fit,
3. Lateral position of each vortex included in fit, and
4. Circulation of each vortex included in the fit.

The classical image model is used to represent the interaction of the vortices with the ground; image vortices are included to satisfy the boundary condition of no vertical wind at the ground. The horizontal and vertical wind at each anemometer location is calculated by adding the vortex induced winds to the ambient crosswind. The stall response of the propeller anemometer is modeled by setting the calculated horizontal and vertical winds to zero if both are less than 0.5 m/s.

The results of the conventional tracking algorithm (Section 3.1.2.2) are used to decide how many vortices to include in the fit (i.e., those being tracked) and to obtain initial estimates of the vortex parameters:

1. The ambient crosswind is taken as the median crosswind.
2. The lateral positions are used directly.
3. The ratio of circulation to height is taken from the measured vortex crosswind (correct for an isolated vortex).
4. The vortex height is the least sensitive parameter and is taken as 30 meters.

The ratio of circulation to height is used as one parameter of the fit to avoid the strong interaction between height and circulation in specifying the measured vortex velocity. Once the largest measured vortex crosswind is specified, the height of the vortex determines the width of the observed crosswind peak; an intermediate value of 30 meters is used for the initial vortex height. The parameters of the fit are varied by specified increments (0.7 m/s for ambient crosswind, 8 meters for lateral position and 20 percent for circulation/height and height) until a minimum sum of squares of the 30 errors (i.e., the difference between calculated and measured horizontal or vertical wind component at each of the 15 lateral positions) is obtained. The increments are then divided by two and the minimization repeated. After three divisions, the process is terminated. The fit is abandoned if it does not converge after 30 incremental changes.

Figure 7 shows sample output from the least-square-fit algorithm. A low turbulence run was selected since the runs presented in Appendix A are high turbulence runs. The crosswind is zero and the vortices exhibit the classic descent into ground effect with subsequent separation. Fixed start and stop thresholds of 2.0 and 1.0 m/s were used. The vortices appear to be tracked in lateral position even after the vortex-induced crosswind drops below the 1.0 m/s threshold.

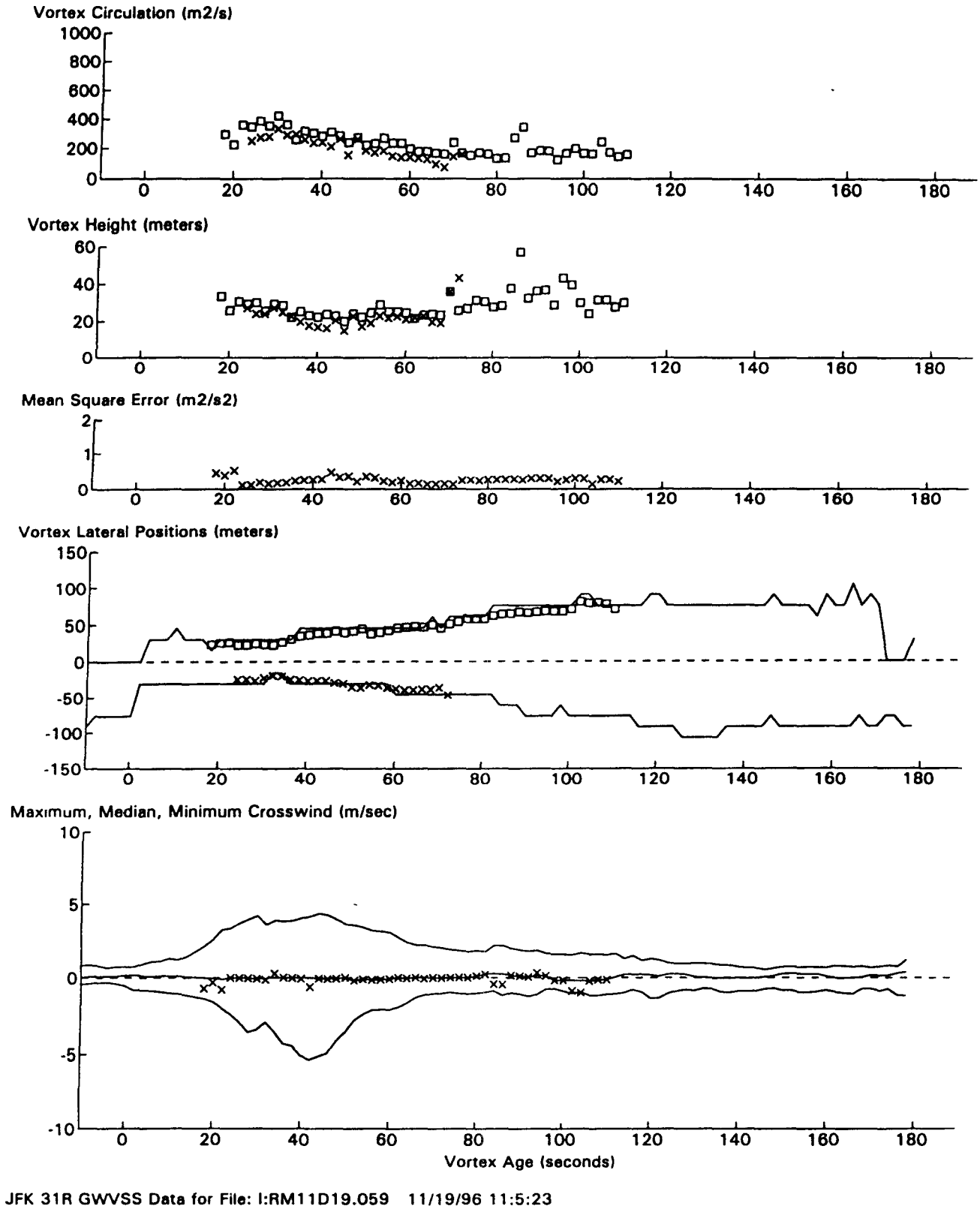

Figure 7. Sample Output from Least-Square-Fit Analysis

Five different plots are shown in Figure 7; starting from the bottom they present the following parameters as a function of vortex age:

1. Crosswind: Solid lines are minimum, median and maximum from min-max-crosswind analysis. Crosses are fitted ambient crosswind.

2. Lateral Position: Solid lines are locations of minimum and maximum crosswinds. Crosses and boxes are the fitted lateral positions for the minimum-crosswind (port) and maximum-crosswind (starboard) vortices, respectively.

3. Mean Square Error: Minimum total sum of errors (both vertical and crosswind) divided by the number of poles (15).

4. Height: Crosses and boxes are the fitted heights for the minimum-crosswind (port) and maximum-crosswind (starboard) vortices, respectively.

5. Circulation: Crosses and boxes are the least-square-fit circulations for the minimum-crosswind (port) and maximum-crosswind (starboard) vortices, respectively.

3.2 SONIC ANEMOMETERS

Sonic anemometers obtain wind measurements by transmitting and receiving short ultrasonic pulses between pairs of sensor probes and measuring the propagation delay times. Advantages of the sonic anemometer over propeller or cup anemometers include high response speed, no moving parts, and high durability/reliability under severe weather conditions. The JFK Wake Vortex Test deployed three sonic anemometers, one produced by Metek, Inc., and two by ATI, Inc. One sensor of each type was operated by the Volpe Center and will be described here. The second ATI was operated by MIT/LL (see Section 3.5). See Section 5.1.1 to relate the sonic anemometer measurements to the test coordinate system specified in Section 2.5.

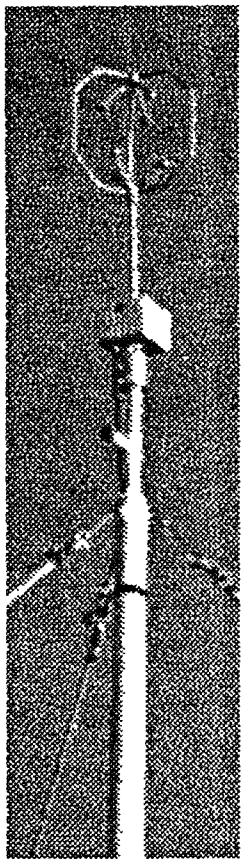

Figure 8. Metek Sonic Anemometer

3.2.1 Metek Measurement Capabilities

The Metek sonic anemometer (see Figure 8), positioned 350 feet to the northeast side of the runway centerline, and 50 feet from the anemometer array, was primarily deployed for measuring atmospheric turbulence. The unit was set at a data rate of 10 Hz with a two-second averaging time. The following parameters were provided in an hourly ASCII file format:

x — Mean x wind component in the sensor-related orthogonal coordinate system (parallel to the index mark on the sensor head) (m/s)

y — Mean y wind component in the sensor-related orthogonal coordinate system (horizontally perpendicular to x) (m/s)

z Mean z wind component in the sensor-related orthogonal coordinate system (vertical) (m/s)

T Mean temperature (°C)

xsig Standard deviation of x (m/s)

ysig Standard deviation of y (m/s)

zsig Standard deviation of z (m/s)

Tsig Standard deviation of T (°C)

xycov Covariance of x and y (m^2/s^2)

xzcov Covariance of x and z (m^2/s^2)

xTcov Covariance of x and T (°Cm/s)

yzcov Covariance of y and z (m^2/s^2)

yTcov Covariance of y and T (°Cm/s)

zTcov Covariance of z and T (°Cm/s)

psig Standard deviation of the wind component parallel to the mean wind direction (m/s)

qsig Standard deviation of the wind component horizontally perpendicular to the mean wind (m/s)

rsig Standard deviation of the wind component vertically perpendicular to the mean wind (m/s)

tp Longitudinal turbulence intensity

tq Transversal turbulence intensity

tr Vertical turbulence intensity

ustar Friction velocity u (m/s)

Tstar Characteristic temperature

Cd Drag coefficient

Mos Monin-Obukhov stability parameter (1/m)

mf Vertical momentum flux (kg/m s^2)

hf Vertical heat flux (W/m^2)

u Mean west-east wind component (m/s)

v Mean south-north wind component (m/s)

w Mean vertical wind component (m/s)

vel Mean horizontal wind velocity (m/s)

dir Mean horizontal wind direction (deg)

3.2.2 Metek Data Reduction

An averaging algorithm was used on selected variables to create one- and five-minute averages for comparison with the other meteorological sensors. The Metek unit was operational for most

of the test period. However, measurements were valid only after 22:00 UTC on November 16, when a malfunction generated during shipping was corrected.

3.2.3 ATI Measurement Capabilities

The ATI sonic anemometer was positioned 50 feet to the southwest side of the runway centerline and 50 feet from the anemometer array (see Figure 3 and Table 4). This location was selected primarily for recording high speed velocity and temperature measurements of wake vortices. The unit was set at a data rate of 10 Hz with no averaging time. The following parameters were recorded in ASCII format in a file which was manually opened and closed at no set time intervals:

1. Mean x wind component in the sensor-related orthogonal coordinate system (parallel to the index mark on the sensor head) (m/s)
2. Mean y wind component in the sensor-related orthogonal coordinate system (horizontally perpendicular to x) (m/s)
3. Mean z wind component in the sensor-related orthogonal coordinate system (vertical) (m/s)
4. Temperature (° C)

3.2.4 ATI Data Reduction

Because the ATI sonic anemometer recorded data at 10 Hz, additional processing was required to extract average parameters. The analysis was complicated by the absence of time tags in the data files. The files remained open for an indefinite period of time, often for many hours. (At least one file contained over one million lines of data.) One file was closed and a new file usually opened around 13:00 UTC each day (08:00 local time when systems were rebooted). Times had to be calculated by noting the time the file closed and counting the number of records in the file. Then, assuming a perfect 10 Hz data rate, a start time was calculated to within a few seconds, and time tags were added to the records. An averaging algorithm was then used to create files of different averaging periods:

1. Unaveraged data were used to examine turbulence levels inside the vortex oval (see Section 6.2).
2. Two-second averages were used to compare to the vortex data from the anemometer array (however, only unaveraged data are presented in this report).
3. One- and five-minute averages were used to compare with averaged winds from other sensors (see Section 5.1).

3.3 WIND PROFILE SODARS

Two sodars (see Figure 9) manufactured by AeroVironment were installed at the test site. A phased array antenna generates three beams, one vertical and two displaced by 15° in the headwind and crosswind directions. After an acoustic pulse is transmitted, the received signal is mixed with the transmit frequency and then processed with a fast fourier transform (FFT) to determine the Doppler spectrum. The three wind components and their variances are determined by suitable processing algorithms that are designed to avoid contamination from ambient noise (such as aircraft operations). See Section 5.1.1 to relate the sodar measurements to the test coordinate system specified in Section 2.5.

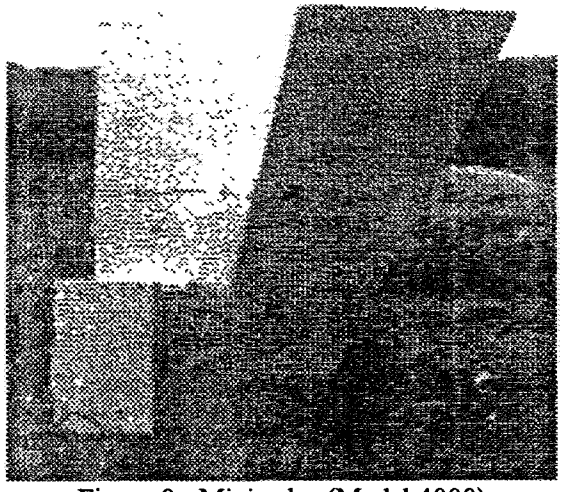

Figure 9. Minisodar (Model 4000)

3.3.1 Wind Profile Measurements

Tables 6 and 7 list the characteristics of the midisodar (Model 3000) and minisodar (Model 4000), respectively. The minisodar is designed for higher resolution (5 m vs. 10 m) and lower minimum range (15 m vs. 30 m), but has a lower maximum range (200 m vs. 400 m).

Table 6. Midisodar (M3000) Characteristics

Maximum Altitude	400 meters
Minimum Altitude	30 meters
Height Resolution	10 meters
Transmit Frequency (approximate)	2800 Hz
Selectable Averaging Interval	1 to 60 minutes
Wind Speed Range	0 to 45 meters / second
Wind Speed Accuracy	< 0.25 meters / second
Wind Direction Accuracy	+ 2 degrees
Weight	500 lbs (227 kg)
Antenna Height	4 ft (1.2 meter)
Antenna Width	4 ft (1.2 meter)
Antenna Length	5 ft (1.5 meter)

Table 7. Minisodar (M4000) Characteristics

Maximum Altitude	200 meters
Minimum Altitude	15 meters
Height Resolution	5 meters
Transmit Frequency (approximate)	4500 Hz
Selectable Averaging Interval	1 to 60 minutes
Wind Speed Range	0 to 45 meters / second
Wind Speed Accuracy	< 0.25 meters / second
Wind Direction Accuracy	+ 2 degrees
Weight	255 lbs (116 kg)
Antenna Height	4 ft (1.2 meter)
Antenna Width	4 ft (1.2 meter)
Antenna Length	5 ft (1.5 meter)

The two sodars were positioned differently (see Figure 3 and Table 4) to provide different information:

1. The minisodar was located 100 feet from the runway centerline where it can be used to assess vortex height as well as wind profiles. This location mandates that the influence of wake vortices must be filtered out of the minisodar wind profiles to assess the ambient wind profile. The minisodar is very similar to the monostatic acoustic vortex sensing system[5] (MAVSS) that has been used by the Volpe Center to measure wake vortex decay at airports. (The Volpe Center MAVSS hardware is antiquated and cumbersome; the minisodar hardware may be a viable option for reviving the MAVSS for future tests.)

2. The midisodar was located well beyond the end of the anemometer array to minimize the influence of wake vortices on its measurements. Since its measurements pertain to higher altitudes, wake vortices are less important and the wind field is likely to be more uniform over the test site.

Both sodars were lined up with the MIT/LL lidar to facilitate sodar-lidar comparisons of crosswind measurements.

3.3.2 Data Recording

The sodar data was sent to the data recording computer via a serial data link with limited capacity. Two different recording modes were used:

1. The normal mode where only velocity and velocity variance data were recorded, and
2 The spectral recording mode where spectra from each pulse were recorded. The sodar pulse repetition period had to be reduced to six seconds when spectra were being recorded.

The first mode was used for wind profiles and the second for wake vortex measurements where one-minute averages would smear out the detailed vortex wind fields.

3.3.3 Data Reduction

The sodars can be set to any averaging period between 1 and 60 minutes. From November 13 to approximately 10:00 UTC on November 15 the averaging period for both instruments was five minutes. After 10:00 UTC on November 15, both instruments switched to recording one-minute averages. To simplify plotting and comparisons, the one-minute averages for the November 13-15 data were converted to five-minute averages.

3.3.4 Wake Vortex Measurements

The minisodar is very similar in characteristics to the monostatic acoustic vortex sensing system[5] (MAVSS) and may be operated in a MAVSS mode in future tests. The vertical pointing acoustic beam of the MAVSS responds to the vertical component of the wake vortex flow field, but is insensitive to the ambient wind, which is horizontal near the ground. Some sodar spectral data for the vertical beam were processed for November 13, 1996. A sample plot is shown in Figure 10, along with aircraft arrival information. Only range gates above 25 meters were used to assure valid data. In Figure 10, the solid line plots the largest vertical wind component for ranges 30, 35 and 40 meters; the dashed line plots the average vertical wind component for the three ranges. Large vertical winds from the wake vortices are evident.

3.4 MIT/LL LIDAR

A detailed discussion of the Lincoln Laboratory lidar can be found elsewhere.[6,7] The following is a brief description of the lidar configuration and operation.

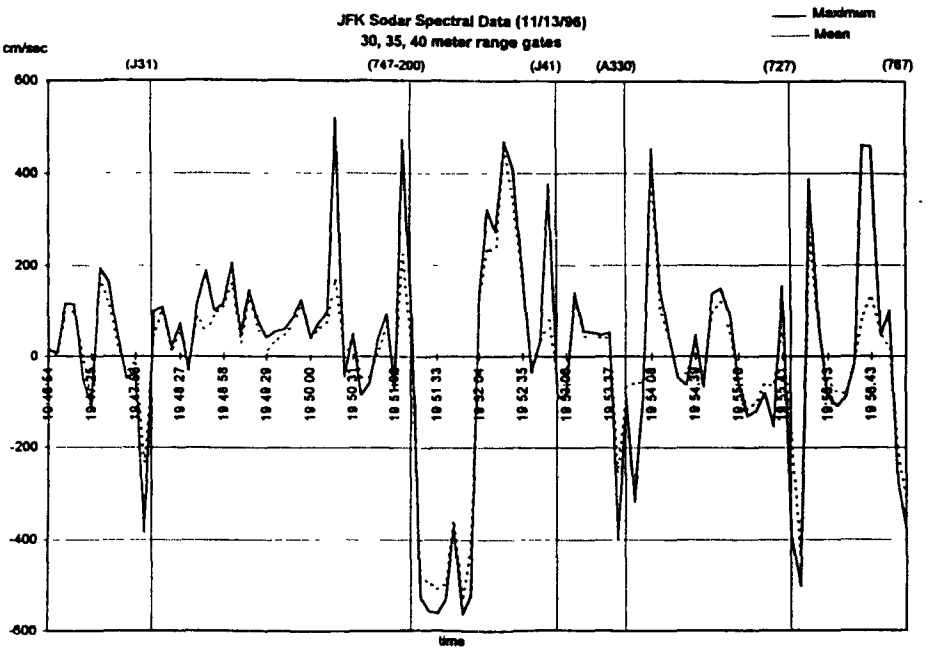

Figure 10. Sample Minisodar Wake Vortex Data

The general layout of the transportable, self-contained, MIT/LL coherent laser radar is shown in Figure 11, and a diagram of the optical configuration is shown in Figure 12. This lidar is similar to previous cw systems developed for measuring aircraft wake vortices.[8,9,10,11] The lidar is composed of a 20-Watt cw CO_2 master oscillator (MO), operating at 10.6 μm, and a 0.5-Watt CW CO_2 local oscillator (LO) laser. The lasers, which operate in a single mode, were built at MIT/LL and have been demonstrated to have extremely high frequency stability The LO and MO laser outputs are sampled and directed onto a room-temperature HgCdTe detector, whose output is used to frequency lock the MO to the LO with a difference frequency of 10 MHz, which corresponds to a 50-m/s Doppler shift This allows the discrimination between Doppler shifts from aerosols moving towards and away from

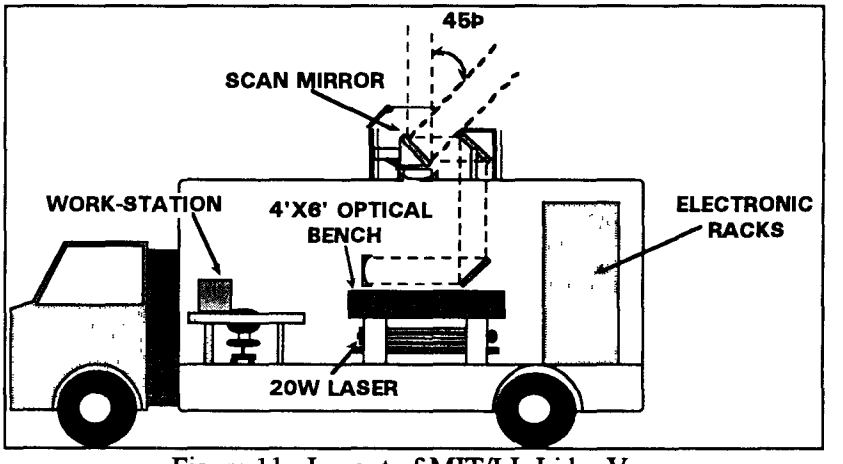

Figure 11. Layout of MIT/LL Lidar Van

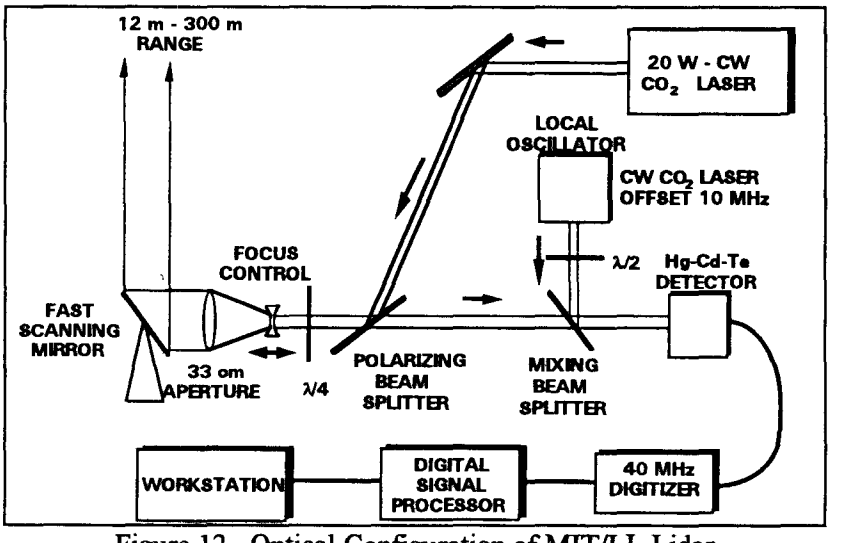

Figure 12. Optical Configuration of MIT/LL Lidar

the lidar. The outputs of both the LO and MO are linearly polarized, and a quarter-wave plate is used for polarization discrimination of transmitted beam from backscattered radiation in a monostatic configuration.

The primary aperture size is determined by a 33-cm diameter off-axis parabolic mirror, and the transmitted beam has a Gaussian intensity distribution at this mirror, with a $1/e^2$ intensity diameter of 22 cm The transmit/receive radiation passes through a variable focusing system composed of a stationary primary mirror and correction lens, and a movable focusing-lens doublet. This optical configuration was designed to maintain an optical beam quality of better than one quarter-wave, peak-to-peak, over the full focus range of 30 m to infinity, as well as to maintain a constant transmit beam diameter on the primary mirror. The transmitted and return beams are directed by a two-axis scanning mirror, which allows 180° coverage along the axis perpendicular to the lidar vehicle axis and 45° coverage along the orthogonal axis.

Typical deployment scenarios are shown in Figure 13, with the vehicle at various locations under or next to the approach path to a runway and the laser scanning perpendicular to it. Data collection at JFK corresponded to the near-ground-effect situation.

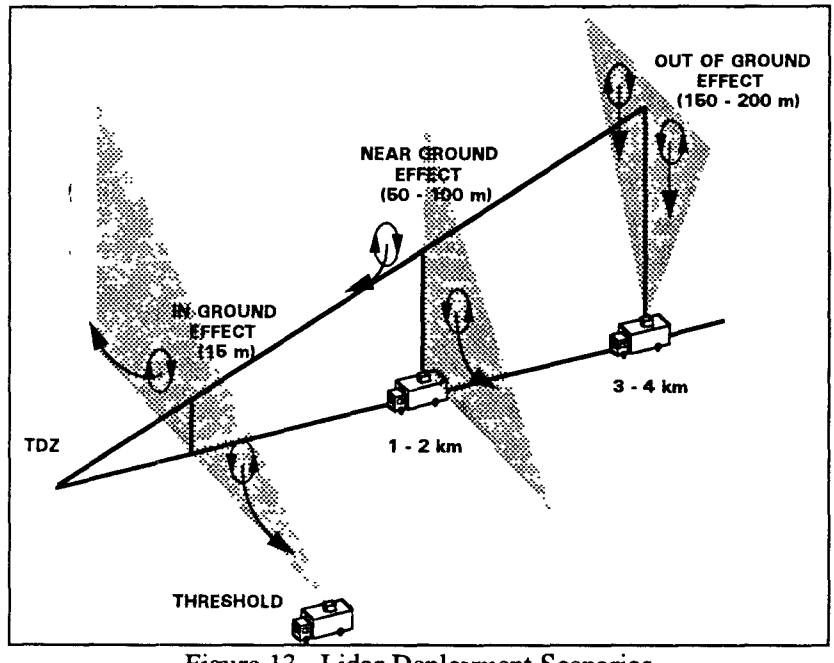

Figure 13. Lidar Deployment Scenarios

3.4.1 Signal Processing

The primary detector is a 100-μm square HgCdTe p-i-n photodiode, cooled to 77 K. The amplified and filtered electrical signal from the detector is digitized by a 40-MHz, 10-bit digitizer, which determines a velocity dynamic range of -50 to +50 m/s. The low-level signal processing consists of FFT calculation from input time sequences and power spectra accumulation, and is performed by a Sharp LH9124 digital signal processor (DSP). The FFT-velocity-bin size and number of accumulated spectra are variable. During the JFK deployment, detector output time sequences were continuously digitized to generate 20, 256-point, velocity power spectra which were then averaged together. The system could repeat this procedure at a rate of about 300 Hz. The averaged spectra were then processed by a pair of Sun Sparc-10 workstations, which save the raw spectra to disk and perform vortex identification. The workstations also control the motion of the scan mirror and variable focus control. A third workstation provides a graphical user interface which allows a controller to view the processed and low-level data in real time and to actively adjust system operation parameters.

3.4.2 Measurement Method

As illustrated in Figure 14, the backscattered return signal detected by the lidar comes primarily from the focal region of the transmitted beam and can be characterized by a lidar sensitivity function which is peaked at the focus of the transmitted laser and has broad tails. The full-width at half maximum of this function is proportional to the square of the focal range; for the wake vortex lidar the width is about 6-m at a focal range of 100-m. Velocity spectra are typically processed by extracting the maximum velocity above a predefined noise threshold and correcting for the spectral spread due to time-series windowing. A plot of the maximum velocity versus crossrange measured from a pair of vortices generated by a Boeing 757 is shown in Figure 14.

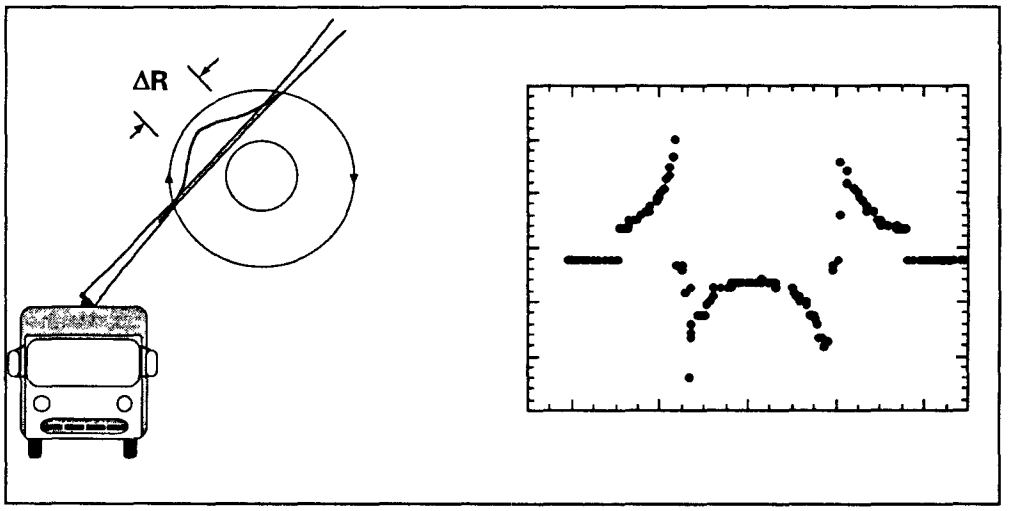

Figure 14. Depiction of Lidar Scan Across a Single Vortex (left) and Spectral Maximum Velocity versus Crossrange (right) from a Scan Across a Pair of Vortices Generated by a Boeing 757.

3.4.3 Real-Time Vortex Tracking

An algorithm has been developed that allows the active tracking of a vortex of chosen circulation (either port or starboard or both) and actively varies the focus and scan angle to continuously scan in the region of the detected vortex. A typical data collection event will then involve the lidar first performing a series of arc-scans across an angle and range neighborhood where an approaching aircraft is expected to pass. The maximum velocities versus scan angle are extracted from the collected spectra and are searched for a vortex signature by convolving them with a matched filter function. If the peak of the convolution exceeds a vortex detection threshold, then the system takes the corresponding scan angle and laser focal range as an initial guess for the vortex angle. The vortex range is estimated as an intelligent interpolation of focus ranges using the last three focus ranges for which vortex signatures were seen. The system then repeatedly scans in the region where the vortices are expected to be located, modifying the scan angle extent and focal range in order to maintain a bracket around the vortex as determined by the location and values of peaks of the matched filter convolutions. The system can be set to track the vortices as they descend and are advected by the ambient crosswind, and it has the capability of adjusting the bracketing region around the vortices based on previous measurements of the crosswinds, that the lidar itself made, as well as on a predicted vortex descent rate.

3.4.4 Data Reduction

Vortex circulation profiles are given by $2\pi r V_{max}(r)$, where r is the crossrange distance (angle from vortex core in radians times the vortex range) to the vortex core and $V_{max}(r)$ is the spectral spread corrected maximum velocity from each measured velocity spectra[12]. Average circulations are calculated by averaging the circulation profiles over a given radius range. Both vortex position estimation and average circulation calculation are performed in real time and presented to the lidar controller.

The lidar data collected at JFK was post-processed for vortex position and circulation. The first step in the post-processing involved a manual verification of the vortex angular position and a quality check of the vortex data for accurate circulation determination. This was done on a scan-by-scan basis in which the automatic vortex angular position determination was verified. Vortex scans were rejected when the vortex data quality was poor because of a large mismatch between lidar focus range and vortex range. An algorithm for vortex position determination was then employed which is based on an expected power law relationship between the signal in each spectral bin, integrated over scan angle, and the corresponding velocity[13]. The vortex ranges generated from this algorithm were then employed in the post-processing of the vortex circulation for the selected scans using the spectral maximum velocities described above.

3.4.5 Vortex File Format

Lines beginning with # indicate a comment line. The first data line specifies the vortex, airport, site, aircraft type, and aircraft model. The second data line specifies the algorithm version number, and the data format version number. The third data line specifies the time of aircraft passage (UTC) as year, month, day, hour, minute, and second. Subsequent data lines indicate a vortex detection and specify the vortex location and circulation estimate as rt, y, dely, z, delz, fd, r0, gam(4.5,14.5), gam(4.5,9.5), and gam(9.5,14.5), where

1. rt = seconds relative to aircraft passage
2. y = distance of vortex from lidar truck laterally (m)
3. dely = relative y estimation error (m)
4. z = altitude of vortex relative to height to lidar truck (m)
5. delz = relative z estimation error (m)
6. fd = lidar focus range - vortex range (m)
7. r0 = cross-range distance between highest positive and negative vortex velocities (m)
8. gam(A,B) = two-sided average circulation estimate for all measurement points from A to B meters in crossrange distance from the vortex center (m^2/s)

Data elements with values of 9999.0 are invalid.

3.4.6 Crosswind Profiles

The MIT/LL lidar can measure crosswind profiles by performing 180° scans at a series of laser focal ranges during times when no vortices are present. The line-of-sight component of the

ambient wind at the altitude of the laser focus is then extracted from the center of the non-zero peak in the velocity spectra. These values are geometrically transformed into a crosswind velocity profile with the assumption that the vertical component is zero. At JFK, crosswind profiles (altitudes of 20 to 250 meters at 10-meter increments) were typically measured between vortex tracking periods.

3.5 MIT/LL METEOROLOGICAL SENSORS

Lincoln Laboratory installed a 30-foot instrumented tower at approximately +70 feet from the runway centerline:

1. A package of sensors manufactured by R.M. Young, collectively referred to as a SAVPAK, was mounted at a height of 6 m and measured standard atmospheric variables: temperature, relative humidity, wind speed, and wind direction. The sensors were sampled at 1 Hz and were typically averaged for one minute.

2. A sonic anemometer, manufactured by Applied Technologies, was mounted at a height of 7 m on the instrument tower. This unit provides flux data from which turbulence values can be derived (see Section 3.2). In the files distributed to the test group, the 10-Hz data were processed to obtain turbulent fluxes and averaged for one minute.

3. The last instrument mounted on the tower was a barometer, manufactured by R.M. Young. This unit was located at a height of 2 m. To match the height of the SAVPAK data, the measurements from this instrument were interpolated to a height of 6 m using equations based on a U.S. standard atmosphere.

Two ASCII data files are recorded for each day. One contains the data from the R.M. Young (SAVPAK) sensors and the other has the flux data from the sonic anemometer. The naming convention for the flux data files is: **fx**date of data collection.version number_date of file creation_hour minute and second of file creation. The SAVPAK files use the same naming convention with **fx** being replaced by **sv.**

3.6 WLR RESEARCH RASS

The WLR Radio Acoustic Sounding System (RASS) (see Figure 15) is based on a commercial 915-MHz radar wind profiler which can be augmented with an acoustic transmitter to measure temperature profiles. WLR Research developed[14] the methodology of using this sensor to detect and measure wake vortices in two configurations: a) beam transverse to aircraft path, where Doppler shifts are related to the vortex tangential velocities, and b) beam along aircraft path where the Doppler shifts are related to axial flow and turbulence in the vortices. The first configuration provides more robust vortex detection and was selected for this test. A RASS uses (Bragg) radar reflection from sound waves. The speed of sound depends upon temperature; however, the radar line-of-sight sound speed increases or decreases directly with the line-of-sight wind velocity component. As the speed of sound changes, acoustic wavelength changes while acoustic frequency remains constant. Since Bragg detection requires the acoustic wavelength to

be one-half the rf wavelength, radiating a band of acoustic frequencies enables Bragg detection of vortex wind speeds from -16.4 m/s to +16.4 m/s.

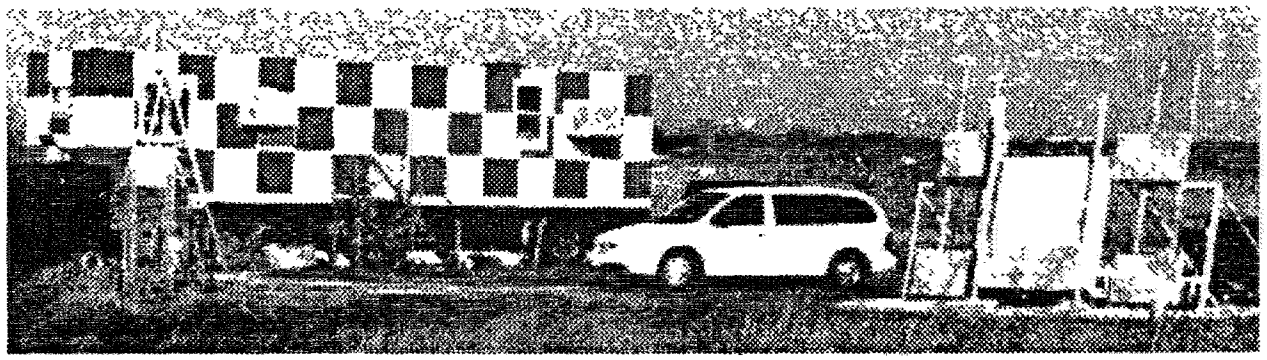

Figure 15. RASS (right) near Volpe Trailer (left)

3.6.1 Detection Capabilities

A RASS has many advantages over a conventional radar system for the study of wake vortices:

1. The coherent reflection from a spherical sound wave is much greater than the conventional radar return from index of refraction inhomogeneities. The RASS tested at JFK produces radar vortex returns at a range of 200 meters that are at least 40 dB stronger than vortex echoes without acoustic enhancement.
2. Apart from wave front distortion effects, the radar reflectivity of the sound waves throughout a vortex is equally strong, while reflectivity due to variations in pressure, temperature, and moisture seen by a conventional radar are expected to vary significantly throughout a vortex.
3. Using acoustic power to increase radar reflectivity is a much less expensive way to increase S/N ratio than increasing rf power.
4. RASS atmospheric returns, which are Doppler shifted by the speed of sound, are not affected by ground clutter. For example, if the radar frequency is 915 MHz and the speed of sound is 343 m/s, the RASS spectrum will be centered at 2093 Hz. Ground clutter, on the other hand, does not experience a Doppler shift and is centered at 0 Hz. Ground clutter is a major problem for a conventional radar.

The RASS provides a simple, all-weather means for detecting wake vortices. Each RASS return detects the entire spectrum of vortex wind velocities within the radar beam. (Real-time) signal processing the wide RASS spectrum yields 100% detection of vortices from large and heavy aircraft with very few false alarms[5]. Detection range should improve in rain and fog due to reduced acoustic attenuation.

3.6.2 Circulation Estimate

When a RASS is positioned to one side of the runway extension, (real-time) calculation of the second moment of each RASS spectrum yields an absolute estimate of vortex circulation. The strength estimate assumes that the vortex is centered in the radar beam and that the reflectivity is uniform over the vortex, as discussed above.

When RASS looks up the glide slope, the second moment is a measure of relative vortex strength which can be converted to absolute strength by a one-time calibration, if the longitudinal scattering characteristics of a vortex are proportional to vortex strength.

3.6.3 Data Format

RASS spectra are reported every 2-3 seconds in each of six 45 meter range bins. The radar beam elevation angle was set at 12°; the beam width is also 12°. Table 8 shows the nominal characteristics of the first five range bins, which were used in the analysis. The RASS measurements were provided in data plots (GIF format) and therefore could not be processed automatically. Figure 16 shows a sample plot, showing the circulation estimates for the first five range bins.

Table 8. RASS Range Bin Characteristics

Range Bin	Range Limits (ft)	Center Range (ft)	Beam Width at Range Bin Center (ft)	Height of Beam Center at Range Bin Center (ft)
1	221-368	295	61	61
2	368-513	441	92	92
3	513-660	587	122	122
4	660-811	736	153	153
5	811-958	885	184	184

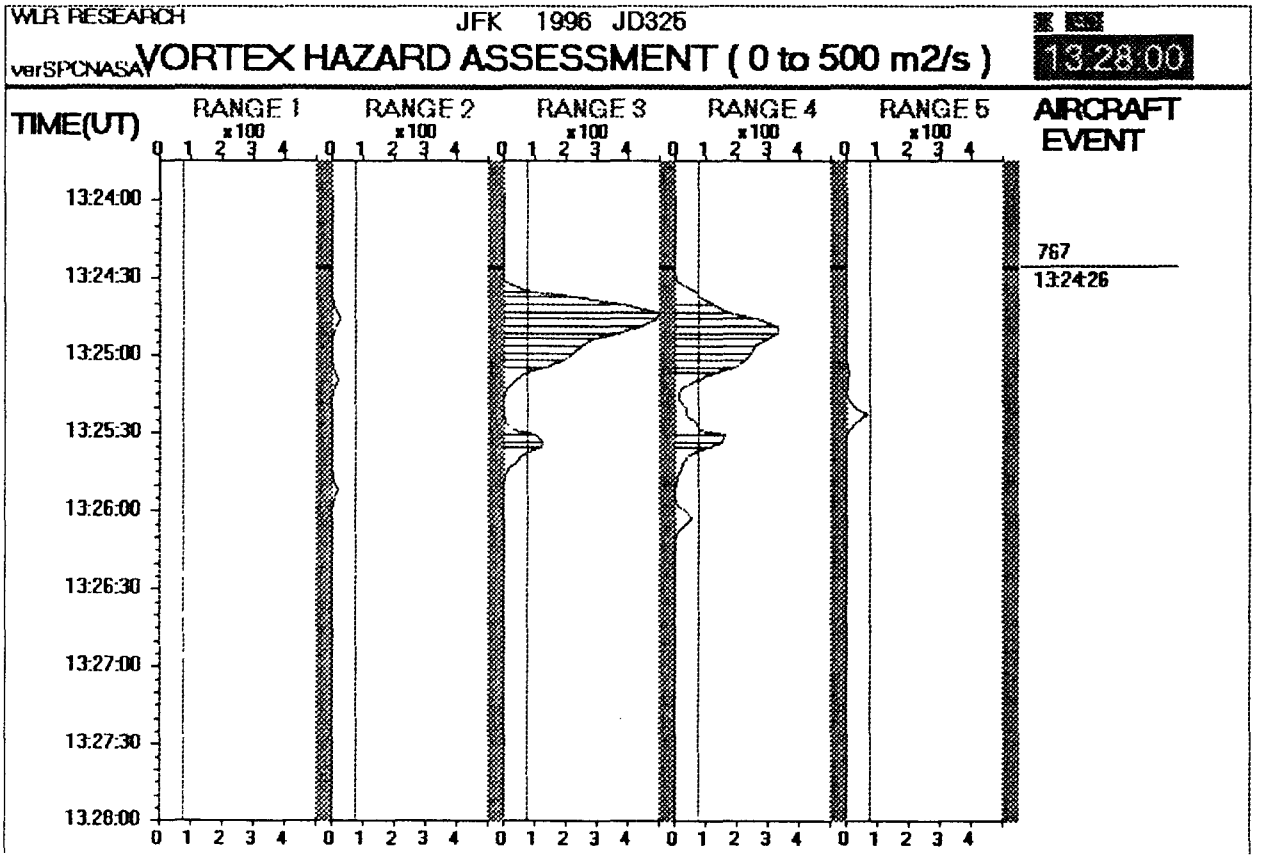

Figure 16. Sample RASS Plot

3.7 SCTI SCINTILLOMETER

The Scientific Technology, Inc. (ScTI) Long-Baseline Optical Anemometer (LOA) uses optical scintillation to measure wind and turbulence. Scintillation is a general term which describes changes in the apparent position or brightness of an object when viewed through the atmosphere. Starlight twinkling is a common example of scintillation. Scintillation effects are caused by optical refraction occurring in small parcels of air whose temperature and density differ from their surroundings. Parcels as small as several centimeters may be detected by the LOA. The strength of the atmospheric turbulence is commonly represented as a refractive index structure constant, expressed by the term: C_n^2 ($m^{-2/3}$).

Figure 17 presents a block diagram of the LOA. The LOA transmitter emits a modulated beam of infrared light. The receiver detects this beam and reconverts it to an electronic signal. Variations measured between the transmitted and detected signals caused by the scintillating air parcels provide the basis of the turbulence measurement (C_n^2). The amplitude of the scintillation is related to the turbulence. The twin modules in the receiver furnish the capability of measuring crosswind by detecting the temporal correlation between the two signals as the air parcels move across the beam path (covariance). The movement of the scintillation from one receiver to the next is related to the crosswind speed.

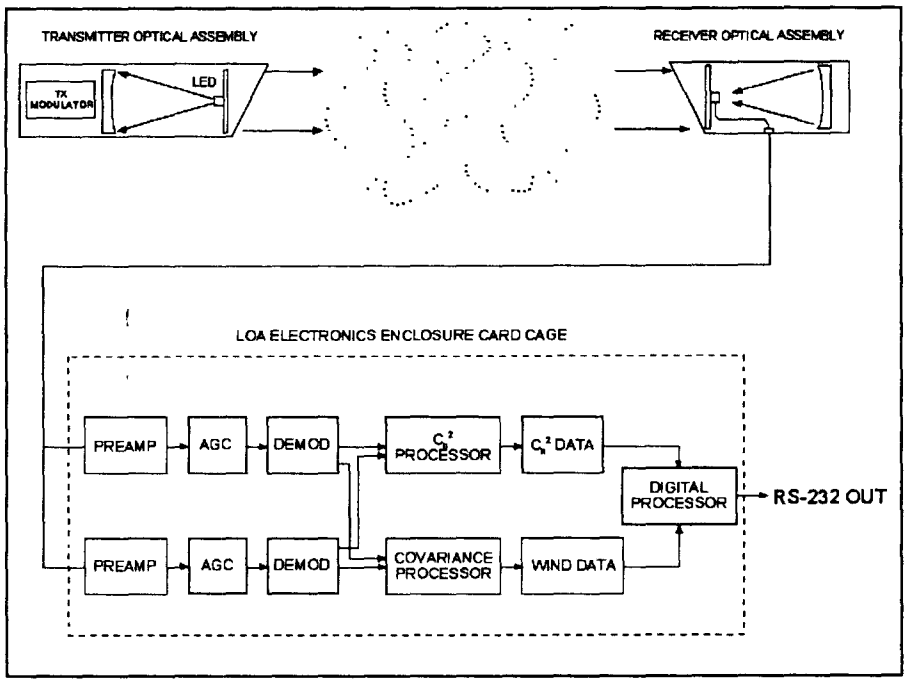

Figure 17. LOA Block Diagram

3.7.1 Real-Time Processing Algorithms

The LOA performs rudimentary real-time processing of the data that consists of sampling, averaging, engineering conversions, and formatting. The LOA digital-to-analog converter samples the output of the two receiver preamps once per second. Ten samples are block averaged to obtain ten-second samples from each receiver. Once averaged, the data is converted into the correct engineering units, formatted into the output string, and recorded. The following data are recorded with the indicated ASCII formats:

1. Crosswind ±ww.w (m/s)
2. Turbulence c.cc e-cc ($m^{-2/3}$)
3. Two detector carrier levels a.aa

3.7.2 Off-Line Data Processing

Post processing was performed with a spreadsheet program. The data presented here were collected using LOA Path # 2, shown in Figure 18; this path gave the highest sensitivity to wake vortices. The crosswind and turbulence results for a 30-minute interval on November 20, 1996 are shown in Figure 19. The influence of wake vortices on both wind and turbulence is clearly indicated.

Crosswind Analysis - Detailed measurements of the crosswind and the wind-induced acceleration (dW/dt) for the test period are shown in the top graph of Figure 19. The thick upper trace on the graph represents a one-minute average and the thin upper trace is the 10-second raw wind data. The lower trace on the graph is the wind-induced acceleration.

Turbulence Analysis - Detailed measurements of the turbulence and the turbulence-induced dynamic impulse ($d^2 (C_n)/dt^2$) for the test period are shown in the bottom graph of Figure 19. The upper trace on the graph represents the 10-second average turbulence. The lower trace on the graph is the turbulence-induced dynamic impulse. Large amplitude signals represent strong dynamic impulses. The correlation of the dynamic impulse with the passage of aircraft (shown as triangles) is excellent with clearly identified spikes immediately following the passage of large aircraft. It is clear that larger aircraft (747, DC10, etc.) induced stronger dynamic impulses than smaller aircraft (727, DC9, etc.).

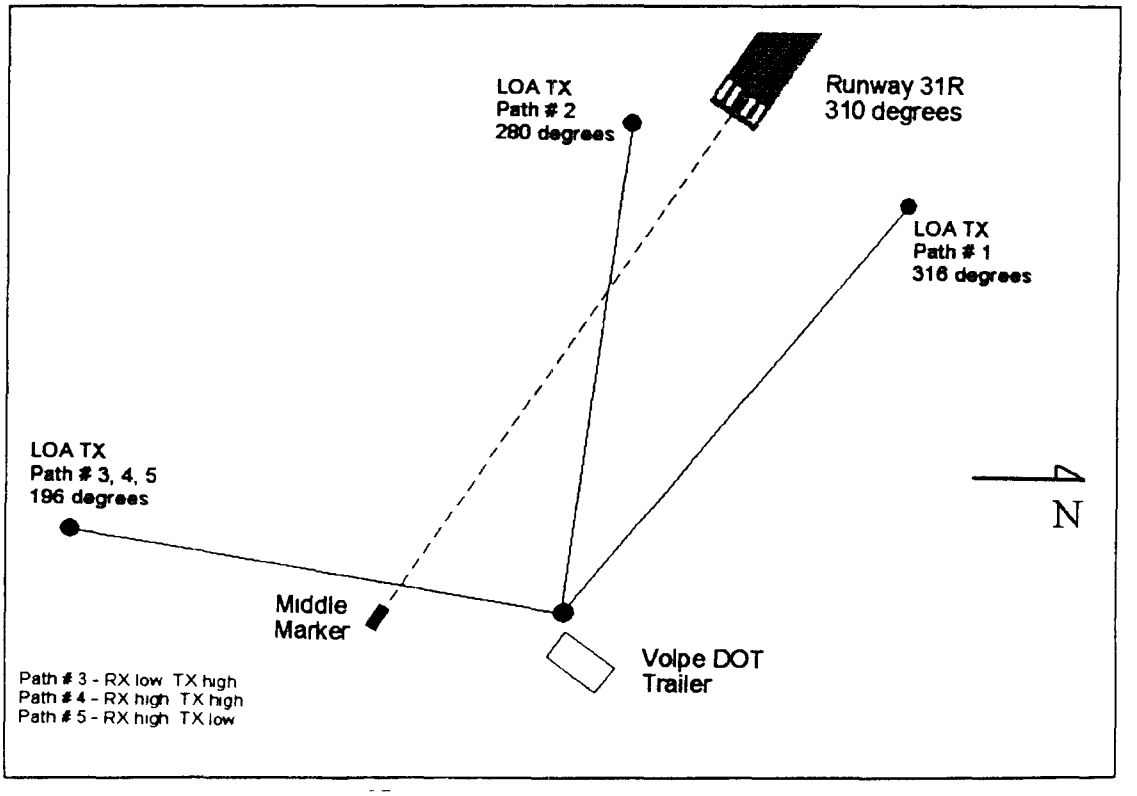

Figure 18. LOA Sensing Baselines

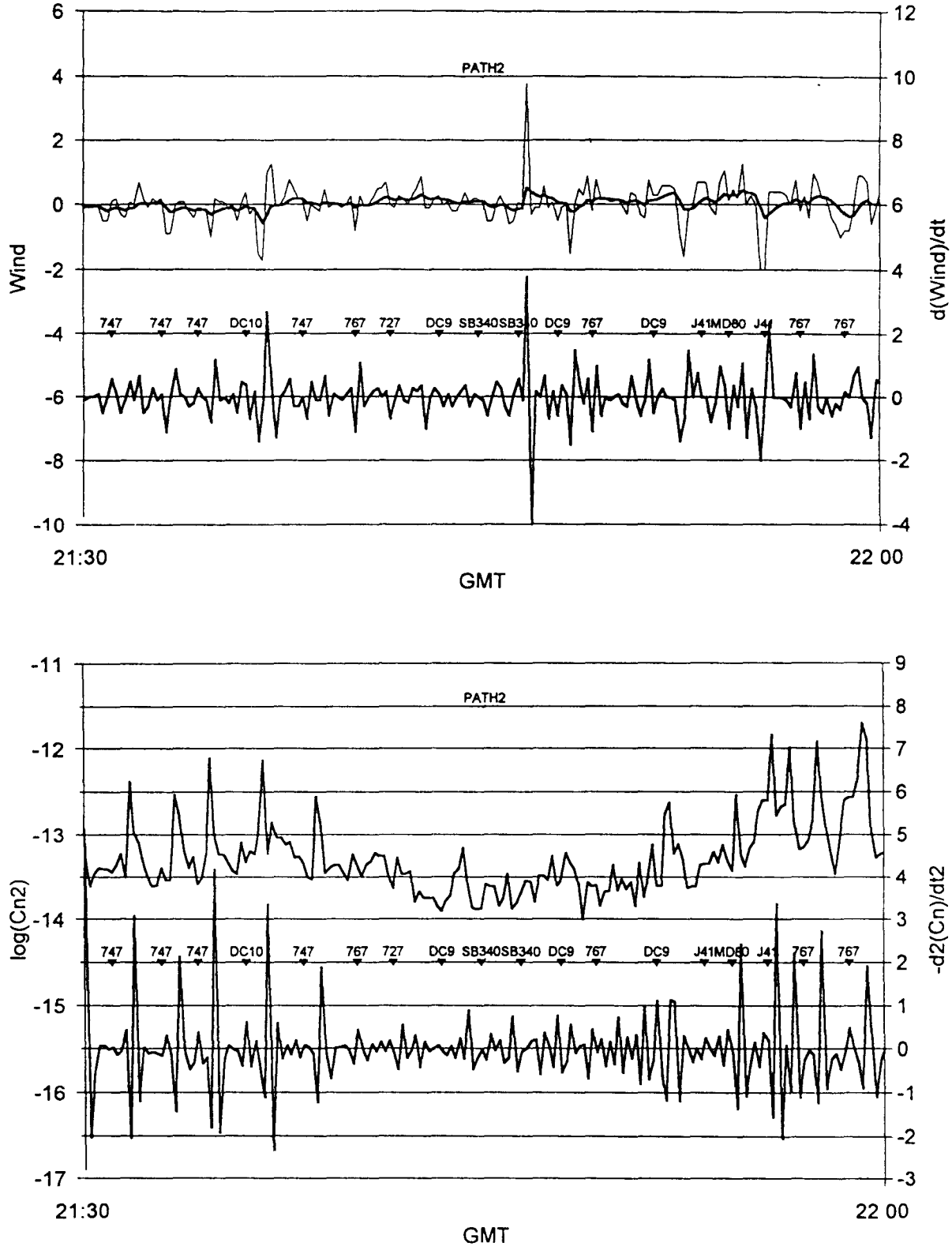

Figure 19. Sample Wind (m/s) (top) and Turbulence ($m^{-2/3}$) (bottom) LOA Data from November 20, 1996.

The next generation of LOA software will include a real-time display of the wake vortex induced dynamic impulse, updated at least once every 5 seconds.

3.8 WV SODAR

The wake vortex (WV) sodar was developed by Technology Integration (now owned by B. F. Goodrich) under the NASA SBIR program. The November 1996 JFK test was the first time it was used to collect wake vortex data with its full capability. Since information about the wake vortex sodar is not readily available from other sources, the description here will be more detailed than for the other sensors.

The WV sodar was designed to monitor wake vortices on final approach to a single runway. To meet this goal, the sodar must be installed near the extended runway centerline at a longitudinal position where the glide slope is located at a height within the sodar's measurement range, which is nominally 25 to 500 feet, but more realistically 37 to 250 feet. The sodar monitors the airflow field over a cross-section perpendicular to the flight path, as illustrated in Figure 20. If the sodar is located near the middle marker of a runway (3500 feet from touchdown), aircraft are at a nominal altitude of 183 feet. The sodar coverage defined in Figure 20 included altitudes from 20 to 350 feet and distances of ±250 feet on either side of the runway centerline.

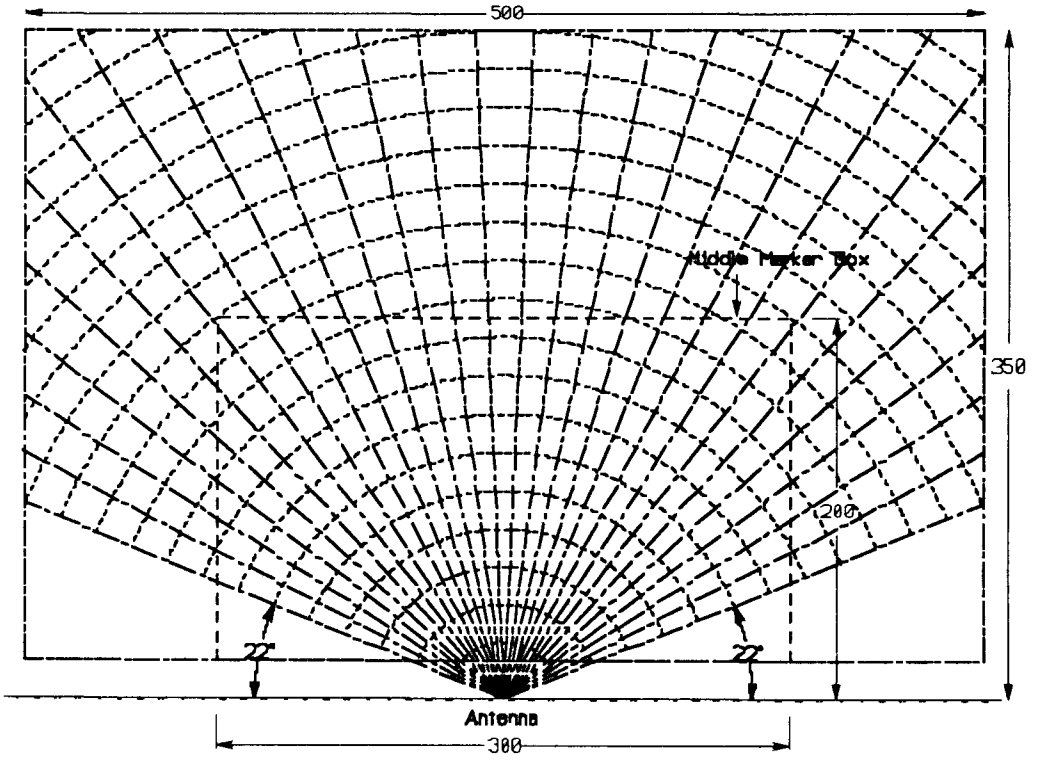

Figure 20. Sodar Coverage and Resolution (units in feet)

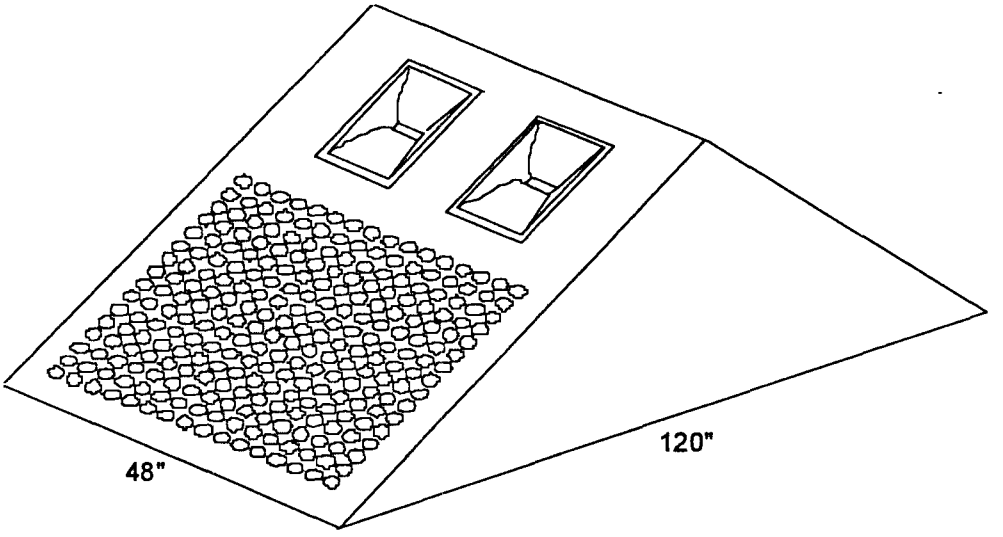

Figure 21. Sodar Acoustic Elements

The WV sodar is a dual antenna, monostatic acoustic radar with 140° coverage, 26 simultaneous beams, and 20 range gates. It incorporates the following features:

1. Separate elements are used for the transmitter and receiver of each antenna, as shown in Figure 2. The transmitter projects a fan-shaped acoustic beam which illuminates all the space of interest. The receiver is a phased array that forms 13 narrow beams, in order to locate the vortex. The reasons for using separate transmit and receive elements are:

   a) The required beam patterns for transmitter and receiver are different.

   b) Using separate elements eliminates a complex phased array transmit/receive switch.

   c) Waiting for transducer ringing to stop when changing from transmit to receive is not necessary; hence, the minimum range is less than would be obtained using the same elements for transmitting and receiving.

2 As shown in Figure 21, each antenna used two transmitter horns, each driven with 300 watts peak power. Each produces a beam which is 30° wide and 65° high. The receive antennas are collocated with the transmitters, and form beams which are 9° by 9°. Each receiving antenna consists of a 16 x 16 matrix of 2-inch diameter transducers. The signals from the elements are combined to form 16 linear arrays. The array can operate up to a frequency of about 3.5 kHz, before aliasing becomes a problem. (Aliasing produces strong side lobes on the opposite side to the main beam.) An array of transducers can have individual elements "shaded", i.e., driven with signals of different amplitude, so as to produce a well formed beam with low side lobes The signal processing combines the 16 linear array signals from an antenna to form 13 beams simultaneously.

3. Personal computer control of the acoustic radar.

4. Real-time signal processing algorithms have been implemented on an array processor inside the personal computer:

   a) Digitization of signals at 12 kHz (16 channels for each antenna).

   b) Real-time spectral analysis using FFT. Consecutive range gates of 512 points (43 msec) are processed.

   c) Spectra from 16 rows of transducers are combined to form 13 beams. The beam forming is performed in the frequency domain. Instead of forming the beams first and then computing their spectrum, the spectrum is computed first. This complex frequency spectrum for all elements is multiplied by a complex beam forming matrix and the rows are summed to form each beam. The complex matrix is pre-computed knowing the element spacing, speed of sound and desired beam directions. This approach is computationally efficient, given that the spectra are needed anyway, and allows the operator to point the beams in any pre-determined direction.

   d) Threshold applied to beam spectra to remove noise. This algorithm is not trivial, since it must eliminate bias due to ambient noise, which is continually changing. An adaptive estimate is made of the ambient noise; the power spectrum for each beam is computed and the 90% probability of the levels calculated. This level is increased by 7 dB and all spectral bins with lower levels are eliminated from subsequent processing.

   e) First and second moments of spectra are generated to give mean velocity and velocity spread. One frequency bin at the transmit frequency (3 kHz) was notched out in an attempt to eliminate clutter The velocity field calculations can keep up with the one-second transmit period to measure the entire 500-foot region approximately once per second.

   f) The data collection software is designed to save data from any step in the processing so that the processing algorithms can be improved using field data.

5 The computer is capable of automatically scanning the velocity flow for wake vortices, but the algorithms have not yet been developed.

3.8.1 System Operation

The wake vortex sodar is mounted on a trailer (see Figure 22) so that it can be

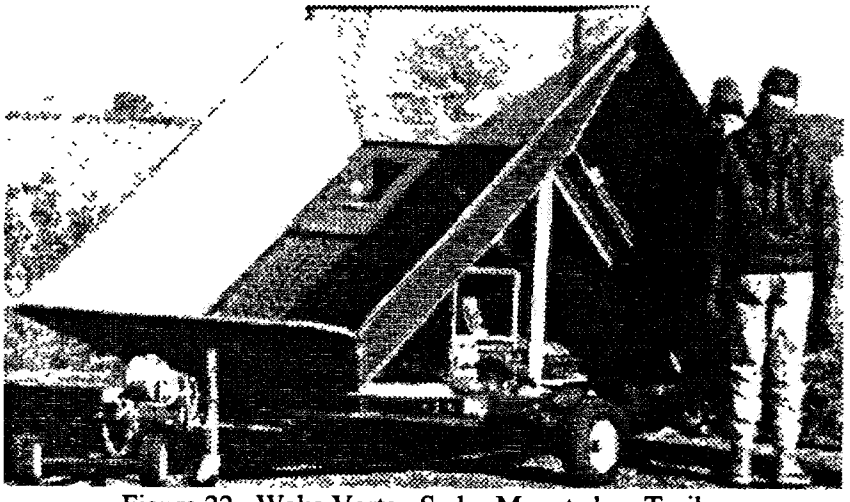

Figure 22. Wake Vortex Sodar Mounted on Trailer

transported to the test site location. A shallow shroud is mounted around each antenna to reduce sidelobes and noise pickup; however, it does not completely shield the transducer matrix from viewing the horizon.

The computer automatically generates the transmitted acoustic waveform and drives both transmitters simultaneously. The reflected signal data is then acquired from both receiving arrays simultaneously. The received signal from each row of transducers is digitized and stored in memory. The Doppler processing, beam forming, noise thresholding, and moment computations are then performed. Finally, the results are transferred from the array processor to the central processing unit for vortex location. When these computations have been completed, the transmitter is ready to pulse again (about 1 second).

3.8.2 Data Formats

Data for different runs were recorded at two different steps of the real-time processing:

1. Beam-formed spectra - Because of processing computer limitations, beam-formed spectra could be recorded only every three seconds. Beam-formed spectra were recorded for less than half the runs.
2. Velocity fields - Velocity fields could be recorded every second and were therefore the dominant form of data recording.

3.8.3 Data Analysis

The original goal of the data analysis was to develop algorithms for automatically reducing velocity field data into vortex location and circulation information. Before this goal could be addressed, a significant data validation effort was required; consequently, the original goal turned out to be beyond the scope of this report. The available WV sodar runs were collected on November 13, 1996. The first step in the data validation process was to display plots of mean velocity and velocity spread versus beam angle and range gate. These plots showed a number of anomalies, which were subsequently explained by analyzing beam-formed spectra:

1. Vortex-like velocity profiles (sign reversal for beams on opposite sides of the vortex core) were observed for the positive pointing antenna but not for the negative pointing antenna. Spectral plots showed that the negative pointing antenna suffered from a large amount of clutter (broader than the one frequency bin rejection filter) at the ranges where vortices were detected. Also, for this antenna only, the data from the range gates were shifted up or down one range gate on alternate transmit pulses.

2. Large velocity spreads were not observed in the center of the vortices. The broad spectra from the vortex core were apparently wiped out by the noise rejection algorithm.

A laser printer display format was developed to view the beam-formed spectral data, which were corrected for the range-gate-shift problem, mentioned above. Figures 23 and 24 show the beam spectra for Run 156 (B-747) on November 13, 1996. The range gates are plotted vertically and the different transmit pulses are plotted horizontally. Within each range-gate box, the 26 beams are plotted horizontally (left to right as viewed from a landing aircraft) and the 44 spectral bins are

plotted vertically (lower to higher frequency). The spectral intensity is indicated by the blackness of the pixel. The blackness of the spectra for age 2 seconds at the left of Figure 23 is caused by aircraft noise. The non-shifted frequency shows up as a horizontal line across a range-gate box. Note the large amount of ground clutter (near-zero Doppler shift) in the left (negative pointing) beam for range gates 5 and above. Positive Doppler shifts (up) in frequency correspond to a wind component toward the antenna, or toward the ground for the middle beams which are pointed almost vertically.

Wake vortices are characterized by a reversal of Doppler shift on either side of the vortex core. The port vortex has a negative Doppler shift on the left and a positive Doppler shift on the right; the starboard vortex has a negative Doppler shift on the right and a positive Doppler shift on the left. Perhaps the clearest vortex signature is the port vortex at age 23 seconds in range gate 5 and beam +7. This signature also shows a strong zero-Doppler reflection at the vortex core; such reflections are typically observed[15] for small vortex cores. For tracking purposes the beams were numbered -13 to +13 from left to right across a range-gate box (no beam 0). Table 9 shows vortex locations in range gate (RG) and beam which were assigned to the spectra in Figures 23 and 24. Some of the assignments required imagination. The resulting vortex trajectories are shown in Sections 4.2.1 and 4.2.2.

Table 9. Vortex Locations in Figures 23 and 24

	Port	Vortex	Starboard	Vortex
Age (s)	RG	Beam	RG	Beam
5	9	-4.5	7.5	5
8	7	-5	5	7.5
11			8	8
14	5.5	-1	9.5	10
17	5	2	9	10.5
20	4	3.5		
23	5	7		
26	5	9.5		
29	5	10		
32	5	10		

The spectra in Figures 23 and 24 also show another characteristic of small core vortices, namely the whistling noise sometimes generated by wake vortices. This noise generates a broad spectral band at all range gates for several beams near the vortex core (see ages 17, 32 and 38 seconds). The noise varies significantly in time and therefore is not seen at all times. The noise band increases in intensity toward higher range gates because the noise level is independent of range gate, while the gain of each range gate is increased linearly with range gate number to compensate for the normal decrease in backscatter with range gate. Figure 25 for an L-1011 aircraft shows noise bands even more dramatic than those in Figures 23 and 24; the noise from both vortices can be seen simultaneously at ages 12 and 15.

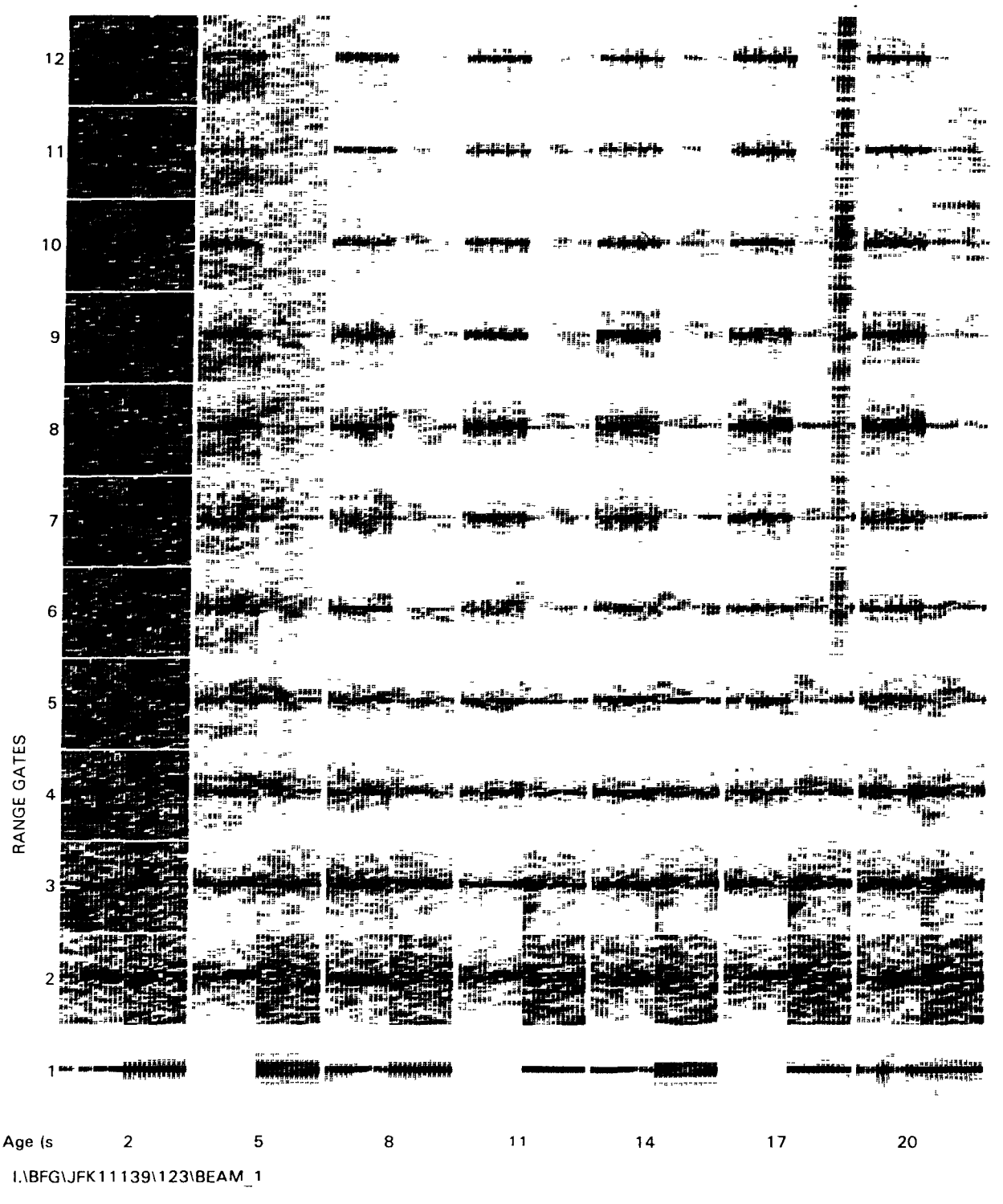

Figure 23. Beam-Formed Spectra (Ages 2-20 seconds) for B-747 Run 156 on November 13, 1996

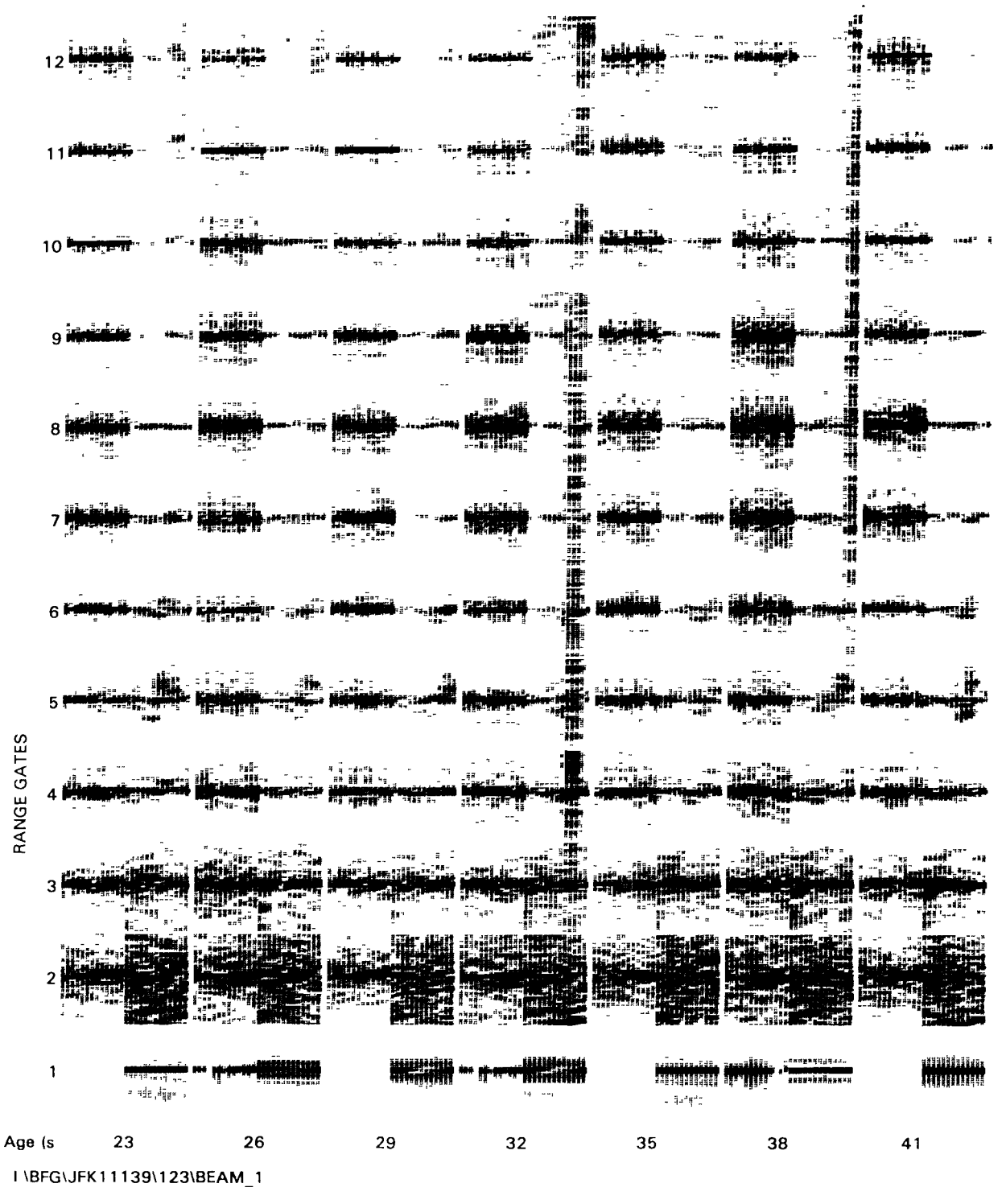

Figure 24. Beam-Formed Spectra (Ages 23-41 seconds) for B-747 Run 156 on November 13, 1996

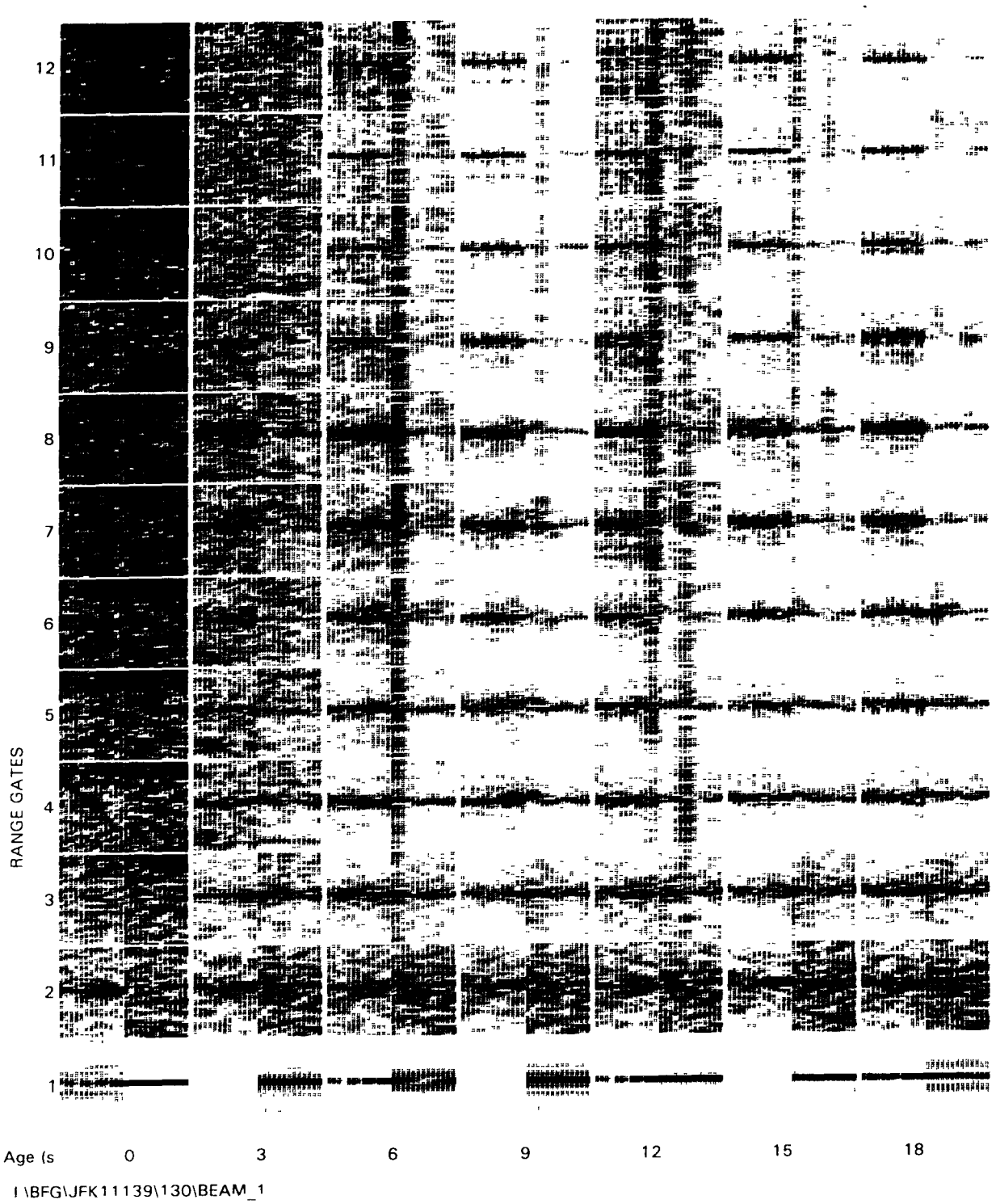

Figure 25. Beam-Formed Spectra (Ages 0-18 seconds) for L-1011 Run 163 on November 13, 1996

4. VORTEX SENSOR COMPARISONS

4.1 ANEMOMETER ARRAY - LIDAR

4.1.1 Lateral Position Comparisons

A statistical comparison of the lidar and anemometer array lateral positions was attempted, using the anemometer array lateral positions distributed to all test participants (see Section 3.1.2.2 for a description of the algorithms). Position differences were determined by comparing each lidar position with the time interpolated anemometer-array position. Lidar positions which required extrapolations of anemometer-array positions were not used. A resulting composite histogram is shown in Figure 26, where 65 runs from November 13, 1996 and November 20, 1996 are combined. In general, the lateral position estimates between the systems compared quite well. It is comforting that the mode of the histogram is at zero error, implying that there are no systematic biases in the sensors. Note that some of the difference is probably due to quantization error from the Volpe algorithm, which assigned the vortex position to the position of an anemometer pole (15-meter pole spacing). The anemometer array least-squares algorithm results (Section 3.1.2.3), which is capable of estimating vortex lateral positions between anemometer poles, was not available for this analysis.

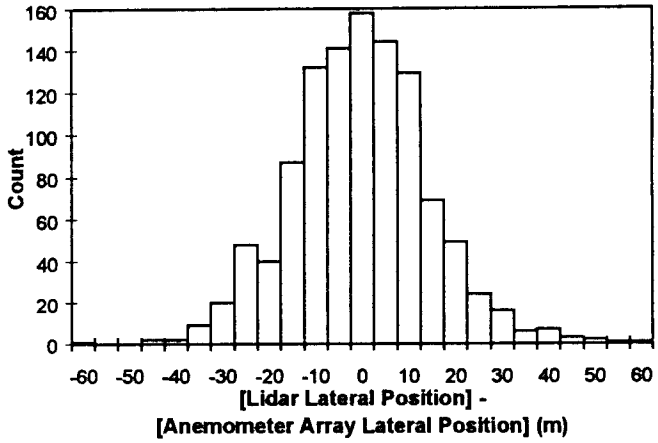

Figure 26. Histogram of Lateral Position Differences

4.1.2 Overlay Plots

Comparison plots (see Appendix A) were generated for 128 runs, overlaying the anemometer least-square-fit values with the lidar values; all vortex parameters were included: lateral position, height and circulation An effort was made to synchronize the lidar and anemometer array data for all runs

As discussed in Appendix A, the overlay plots were visually scanned to assess the agreement between the two sensors. Valid anemometer array measurements were available for 84% of the runs. Invalid anemometer array data points were observed for only 5% of the runs. Invalid lidar data points (incorrect vortex identification or identifying one vortex as two vortices) were observed for only 7% of the runs. The lateral positions from the two sensors were inconsistent for 4% of the runs A significant amount of overlapping data from the two systems was observed for 47% of the runs; of these runs, 18 percent had significantly lower vortex heights from the anemometer array than from the lidar. Since the circulation from the anemometer array is closely correlated with the height, the circulation values were typically low when the height was low.

The general agreement between the anemometer array and lidar was surprisingly good. The high detection starting and stopping thresholds, which were selected to reduce false detections (see Section 3.1.2.2), also served to eliminate data where the lateral positions and/or heights were in disagreement.

One anemometer array anomaly was observed in a number of runs (e.g., runs 284, 330 and 307 on November 22, 1996); the port vortex lateral position never reached the negative end (Pole 01) of the anemometer array even though the lidar showed the vortex to have passed that end of the array. This effect was noted for a small negative ambient crosswind (-1 m/s). A similar negative crosswind without wake vortices was observed on November 22, 1996 and was processed to generate Figure 27, which compares the one-hour averaged crosswind for the 15 anemometers. A number of anemometers appear to have significantly reduced response: C01, C04, and C08; and, to a lesser extend, C05. The reduced response of C01 compared to C02 and C03 (0.6 m/s less) could account for the vortex location being assigned to C02 or C03 rather than C01.

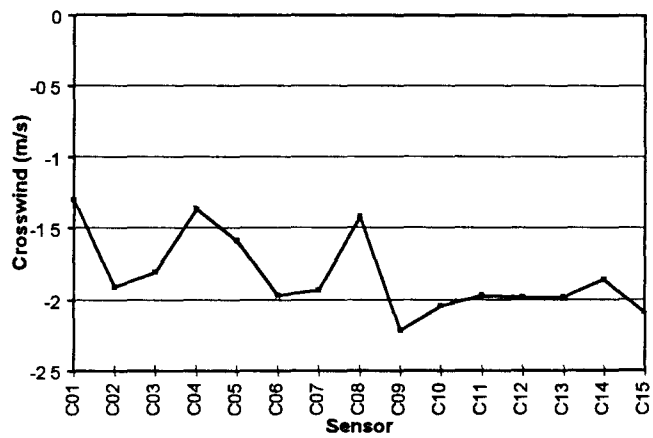

Figure 27. Response of Crosswind Anemometers (0830-0930, November 22, 1996)

4.2 ARRAY - LIDAR - SODAR

The measurements from the anemometer array, lidar, and sodar are compared for two B-747 runs (anemometer-array runs 150 and 156 on November 13, 1996). The raw data for Run 156 was presented in Section 3.8.4. The runs selected were the only B-747 runs with concurrent lidar and sodar beam-formed spectral data.

4.2.1 Lateral Position

Figure 28 shows the lateral positions measured by the three sensing systems; the abbreviation AnAr is used for the anemometer array. All three sensors agree well for Run 156, except for a lidar port (P) vortex deviation at age 60 seconds. The sensor-to-sensor variation is greater for Run 150. The sodar data for the P vortex shows the biggest deviations.

4.2.2 Height

Figure 29 compares the vortex height measurements for the three sensing systems. Again, the height measurements are generally consistent for Run 156, but show greater variations for Run 150. The anemometer array measurements become erratic at the end of both runs.

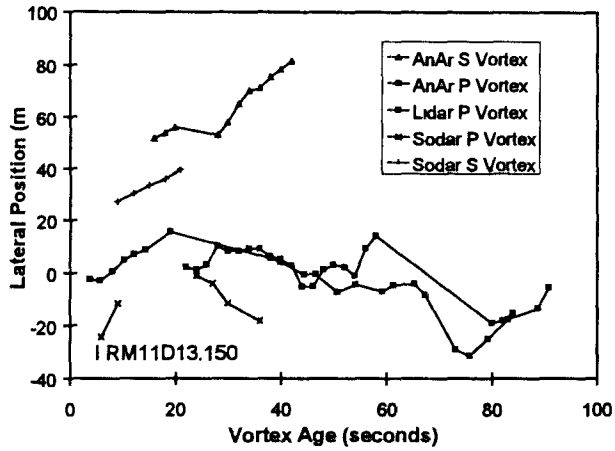

Figure 28. Lateral Position Measured by Anemometer Array, Lidar and Sodar (Runs 150, 156 on November 13, 1996)

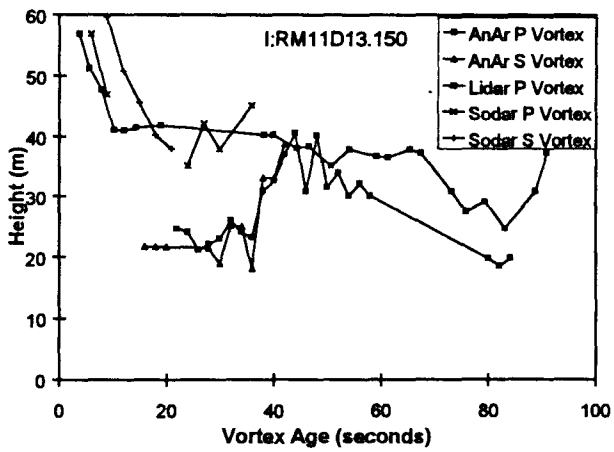

Figure 29. Height Measured by Anemometer Array, Lidar, and Sodar (Runs 150, 156 on November 13, 1996)

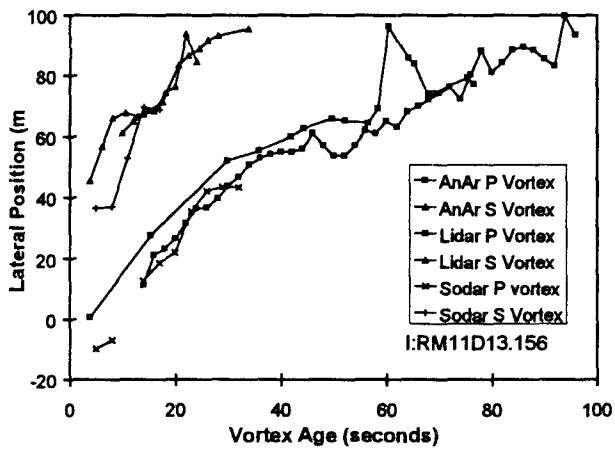

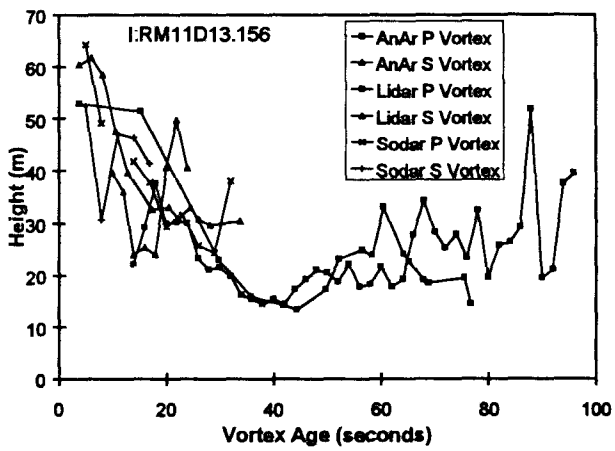

Typically, the height data from the anemometer array are low before age 20 seconds, but become believable after that age when the wake vortices have descended close to the ground. Run 156 exhibits this normal variation. However, for ages 20 to 36 seconds, Run 150 shows a consistent difference of about 20 meters between sodar/lidar heights and anemometer array heights for both vortices.

This height difference could be caused by deficiencies in the lidar and sodar data. The P Vortex is above the lidar at this time period and is therefore constrained by the minimum range capabilities of the lidar. The lidar P Vortex heights suddenly reach a fixed minimum value of 40 meters for ages 10 to 40 seconds, with a measurement dropout between ages 20 and 36 seconds. These lidar measurements are consistent with the actual vortex height being lower. [The lidar did not measure the starboard (S) Vortex.] The sodar measurements reach a similar minimum value for both vortices during this time period. The sodar measurements in this time period were assigned to range gates 5 or 6; vortex signatures were rarely observed at lower range gates, perhaps because of the greater amount of clutter at the lower range gates.

4.2.3 Circulation

The lidar data files provided three circulation values; the circulation was averaged over three ranges of vortex radius: radius averaging of 4.5-14.5, 4.5-9.5, and 9.5-14.5 meters. Since the anemometer array estimates the total vortex circulation, the last circulation value was selected from the lidar files for comparison with the anemometer array measurements. Circulation estimates were not made from the sodar data.

Figure 30 compares the anemometer array and lidar circulation measurements for the two B-747 runs. To facilitate comparisons, S Vortex circulations are assigned positive values and P Vortex circulations negative values.

As in the previous comparisons, the circulation values for the two sensing systems are reasonably consistent for Run 156 after age 20 seconds. The extrapolated initial circulation is near the typical 600 m^2/s value for a B-747. As expected, the anemometer array values are closely correlated with the assigned heights in Figure 29.

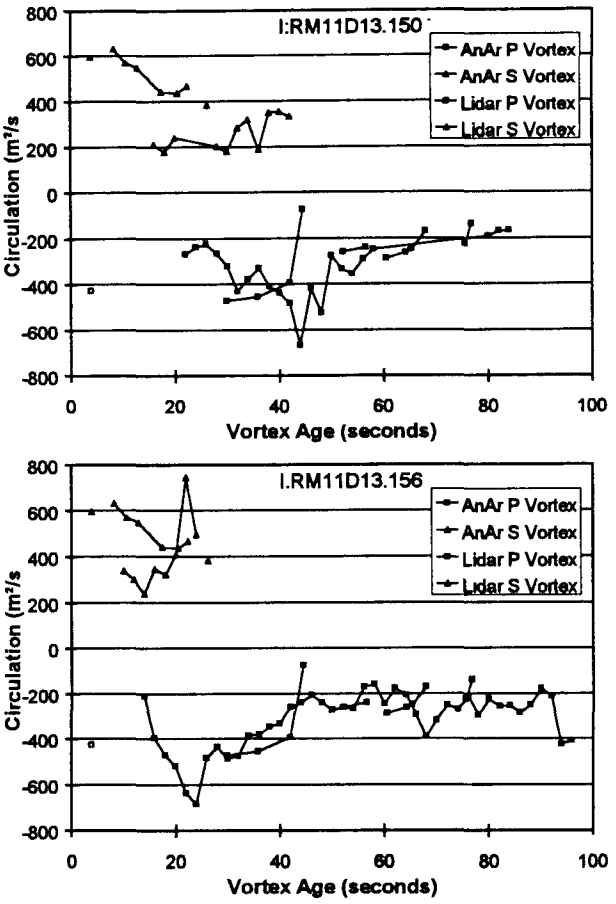

Figure 30. Circulation Measured by Anemometer Array and Lidar (Runs 150, 156 on November 13, 1996)

The circulation measurements for Run 150 show anemometer array values at ages 20 to 36 seconds that are roughly half the values measured after 36 seconds. Since the circulation is not expected to increase with age, this observation suggests that the anemometer array heights in Figure 29 are actually too low and are the cause of the low circulation measurements.

4.3 RASS - LIDAR

4.3.1 Location

A prior test[14] showed that the RASS range vortex signals correlated well with the lateral position given by the anemometer array; the comparison was limited, however, because the vertical position of the vortex in the RASS beam could not be determined from the anemometer array data. In this test the lidar provides the vertical location information missing from the earlier test.

One B-747 run was selected to verify that the RASS signals occurred when the lidar vortex was located in the correct RASS range and angle Figure 31 shows the RASS data for the selected run, which was unique in having signals in Ranges 2 through 5. The lidar vortex locations were

also unique for this run, showing vortex heights above 100 meters (see Appendix A). Figure 32 shows the lidar location data plotted on top of the RASS range bin locations. The vortex age (seconds) is indicated for some of the lidar locations. The sign of the lateral position was reversed from the normal direction so that the range bins are in the same order as in Figure 31.

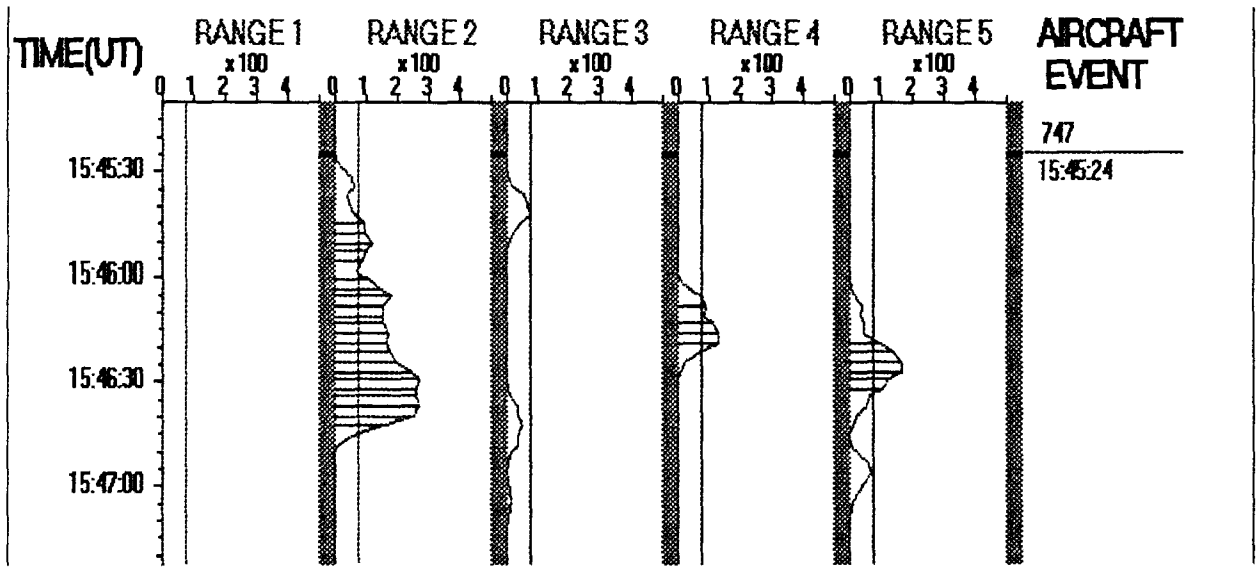

Figure 31. RASS Data for B-747 Run 284 on November 20, 1996

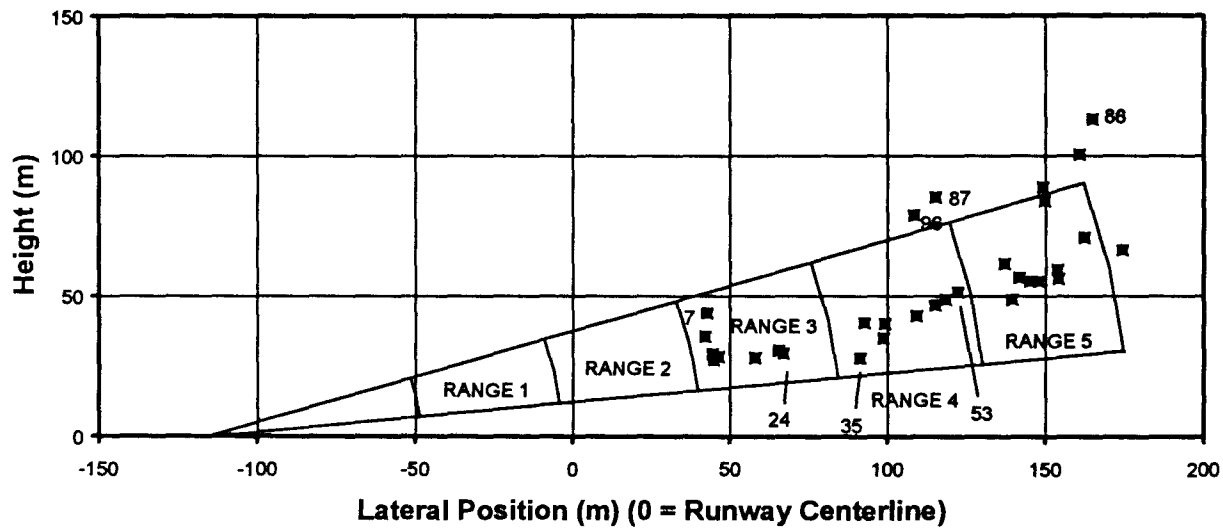

Figure 32. Comparison of Lidar Vortex Trajectory to RASS Range Bins

The interpretation of the consistency between Figures 31 and 32 depends upon a number of assumptions:

1. In contrast to the 12-second correction used for lidar data on November 20, 1996 in Appendix A, no correction was applied here; the first lidar data point had a nominal vortex age of 7 seconds, which is reasonable considering that the initial height is near the nominal aircraft height of 50 meters and the vortex is descending rapidly, as is normally observed just after the vortex pair is created.

2. The lidar measured only the port vortex. The anemometer array (see Appendix A) showed that the starboard vortex remained close to the runway centerline until age 80 seconds.
3. The RASS appears to track the port vortex across Range Bins 3 to 5, making the transition from Range 3 to 4 at about 27 seconds and from Range 4 to 5 at about 54 seconds.

The data from the two sources are consistent (after the range correction mentioned in Section 3.6.3):

1. The starboard vortex near the runway centerline gives the signal observed in Range 2.
2 The transitions for ranges 2-3 and 4-5 occur at the correct ages.
3. The port vortex lingers in Range 5 until it completely decays.
4. The port vortex signal remains small until it is near the range 3-4 boundary. Perhaps the initial signal is small because the vortex is on the boundary between Ranges 3 and 4.

This method of interpreting the RASS data leaves much to be desired. A better approach would be to assume a range and angle response function for the RASS and compare the RASS measurements with the calculations based on the lidar vortex locations.

4.3.2 Circulation

The RASS and lidar circulation measurements were compared using the following procedure:

1. RASS circulation estimates, vortex age and range bin were picked from peaks in the RASS data displays (Figure 16) for 46 arrivals on November 20.
2. Lidar locations and circulations were determined for the vortex ages picked from the RASS plots. Plots of lidar circulation versus age were manually interpolated to give the lidar circulation estimates at the RASS vortex age. Data points were included only if a lidar circulation estimate at a comparable time was available. Care was taken to compare RASS circulations with the circulation from the correct vortex, either port or starboard, as determined by the lidar. The deduction of which vortex the RASS circulation represented was made by comparing the RASS range gate with lidar position estimates.

In general, RASS detections at Range 2 correlated with lidar positions very near the centerline, while Range 3 detections correlate with lidar vortex detections at about -50 m laterally from the centerline, and so on. This result is consistent with the range correction mentioned in Section 3.6.3.

Figure 33 shows a scatter plot comparison of the lidar and RASS circulations. This plot was assembled from RASS and lidar observations of 29 aircraft arrivals (in six cases there was more than one RASS circulation estimate per aircraft). In general, the RASS circulation estimates are underestimates compared to the lidar circulation values. In a few instances where the vortex is at very close range to the lidar truck and the lidar depth of focus is very small, the lidar may not have been able to observe the highest vortex tangential velocities; this effect may result in an

underestimate of the vortex circulation and may account for the few cases where the RASS's circulation estimates are higher than the lidar's.

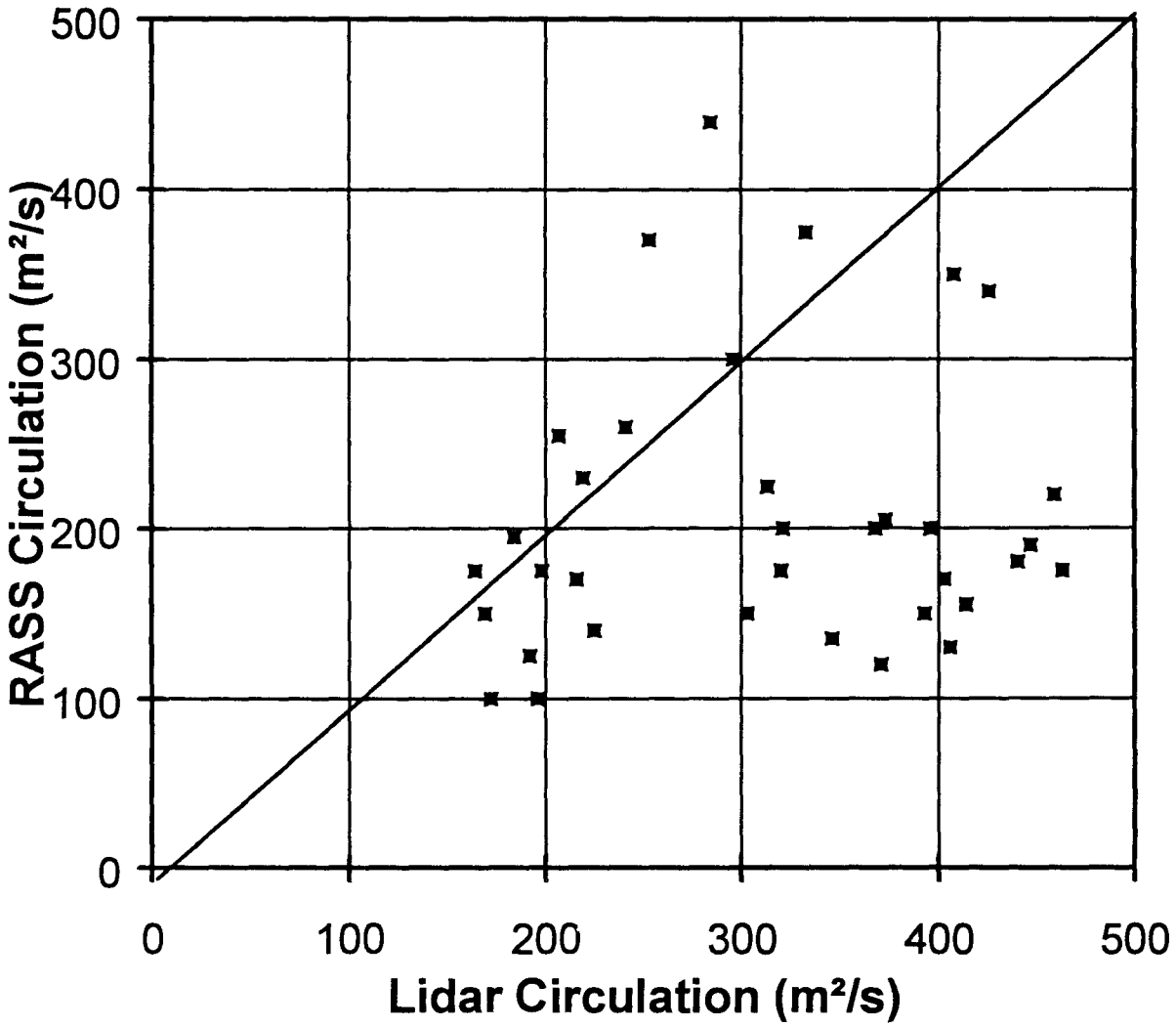

Figure 33. Comparison of RASS and Lidar Circulations

5. METEOROLOGICAL SENSOR COMPARISONS

This chapter presents comparisons of wind, turbulence, and temperature measured using different sensor technologies. The MIT/LL meteorological measurements (Section 3.5) were generally not included since they did not add any additional sensor technologies.

5.1 WIND

Wind component measurements were obtained from propeller anemometers, sonic anemometers, sodars, and the lidar. Table 10 lists the report sections where the data reduction for these measurements is described. All instruments used a coordinate system aligned with the runway to permit direct comparisons of wind components. The propeller anemometers and sodars were running for most of the test period, but the sonic anemometers and lidar each had several days when they were not. The one day when all of these instruments were functioning was on November 20. For this reason, the meteorological sensor comparisons will focus on November 20 data.

Table 10. Anemometer Processing

Type	Section
Propeller	3.1.1/3.1.2.1
Sonic (Metek)	3.2.2
Sonic (ATI)	3.2.4
Sodars	3.3.3
Lidar	3.4.6

5.1.1 Validation

To validate the data being recorded by the different sensors, the data was formatted and plotted. As mentioned above, all measurements were supposed to be oriented with respect to the runway. Headwind was defined as positive parallel to the runway centerline and opposite to the landing aircraft's direction of flight, while crosswind was perpendicular to the runway and positive blowing from the pilot's left to right. In the course of validating the different data sets, it was learned that most of the instruments were oriented in different directions.

1. The headwind propeller anemometers indicated negative headwinds when, in fact, the headwinds were positive throughout the test period. All the headwind data needed to be reversed.

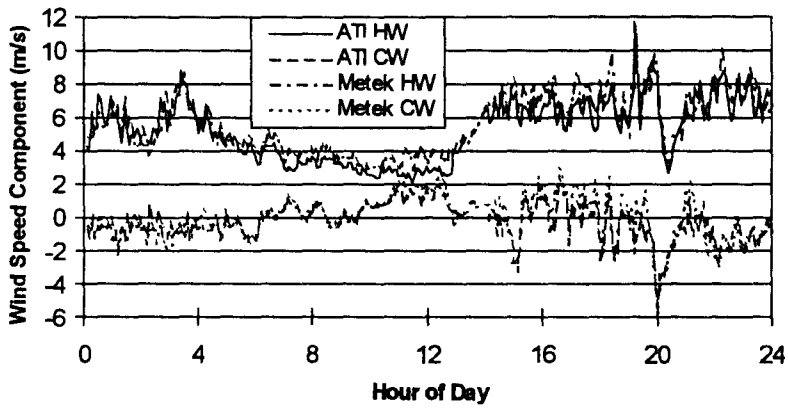

Figure 34. Sonic Anemometer Crosswind and Headwind Components for Nov. 20 (5-minute average)

2. The Metek sonic anemometer's x axis was aligned with negative headwind. The y axis was aligned with the crosswind and therefore needed no correction. The ATI sonic anemometer's u and v components were aligned with negative headwind and negative crosswind, respectively. Both values were reversed to agree with the runway coordinate system. Figure 34 compares the wind component measurements from the

Metek and ATI sonic anemometers after conversion to runway coordinates. The results are quite consistent.

3. The data from the M4000 sodar was observed to be invalid below 30-m altitude. This problem was traced to the clear tedlar cover over the sodar, which was meant to protect the sodar from bad weather and dust. The cover resonated at a frequency which caused problems with the data returned by the lower range gates. The problem was fixed by simply removing the cover, after the test period had concluded.

4. The M3000 sodar u component was aligned with the crosswind and its v component with negative headwind. The M4000 sodar u component was aligned with negative headwind and the v component with negative crosswind Figure 35 shows the sodar headwinds and crosswinds at 50-m height after converting to runway coordinates. The data for M3000 are shifted up by 10 m/s to permit a clearer comparison of the two measurements. The measurements agree reasonably well.

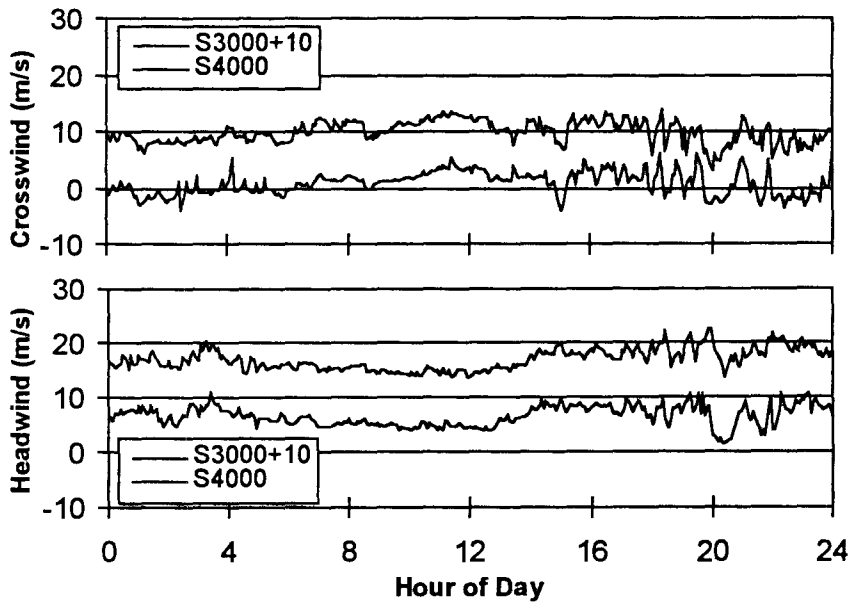

Figure 35. Comparison of Sodar Crosswind and Headwind at 50 Meters Altitude (5-minute average)

5.1.2 Profiles

5.1.2.1 Time Variation

Both the sodars and the lidar measure winds at multiple heights, making it possible to produce wind altitude profiles. The instruments are designed to cover different ranges. The M4000 sodar returns values between 15-m and 200-m at 5-m intervals. The M3000 sodar returns values between 30-m and 400-m with a 10-m interval. The lidar data ranges varied, with a minimum of 20 m and maximum of 250-m range in 10-m increments. Both sodars operated all day on November 20, while the lidar collected data between approximately 18:00 and 22:00 UTC.

Figure 36 shows selected lidar crosswind data between 30-m and 200-m. To give a clear view of each range, the plots have been separated by adding a constant factor which puts zero crosswind on a different line of the plot For instance, the 80-m data has a value of 30 m/s added to each

point, so an 80-m data point plotted at 25 m/s indicates an actual crosswind of -5m/s. (The subsequent sodar plots follow a similar pattern.) The gaps in time were a result of the fact that the lidar alternated between wind mode and vortex mode and did not operate continuously in wind mode.

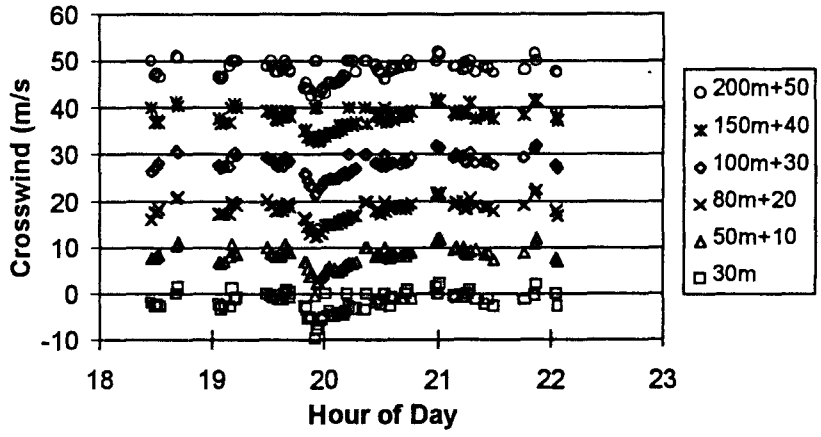

Figure 36. Lidar Crosswind Profile (one-minute average)

Figure 37 shows the crosswind and headwind profiles for the M3000 sodar; Figure 38 shows the corresponding profiles for the M4000 sodar. When viewing these plots it should be noted that values plotted at the zero point for that series may indicate a missing (i.e., invalid) data point rather than a zero value. This can be noticed at the beginning of the M4000 sodar crosswind plot for the 100-m values. These invalid values also appear at the corresponding height and time on the headwind plot. In general, the 50- and 80-m values seem to be the best behaved. The 30-m values from the M3000 sodar (lowest range gate) are definitely inconsistent with the other wind values. The 100-m M4000 sodar values are starting to show missing data (zero values) for 22-24 hours; thus, under these conditions, the M4000 maximum range is less than half the nominal maximum range of 200 meters.

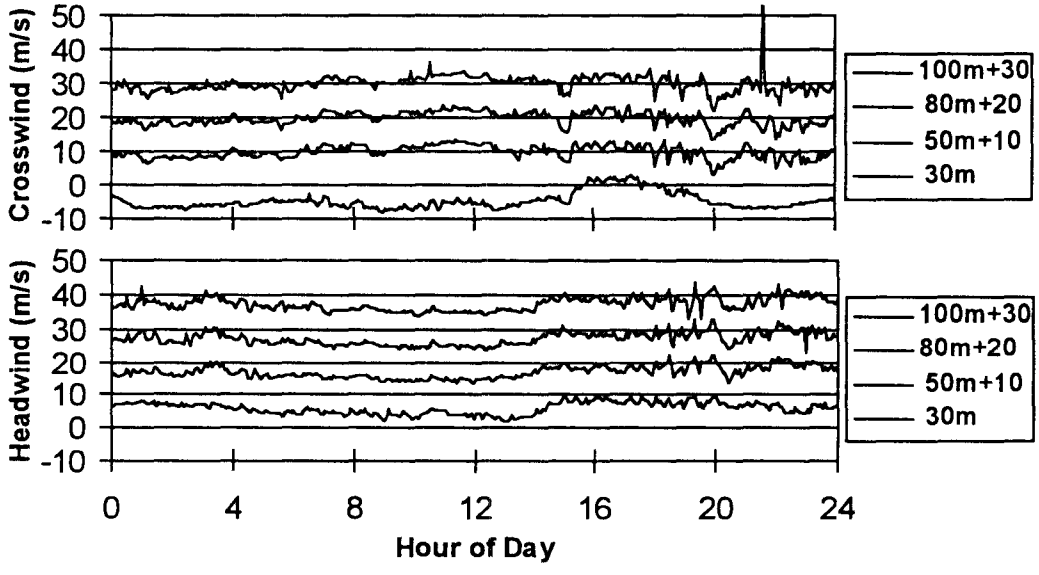

Figure 37. M3000 Sodar Crosswind and Headwind Profiles(5-minute average)

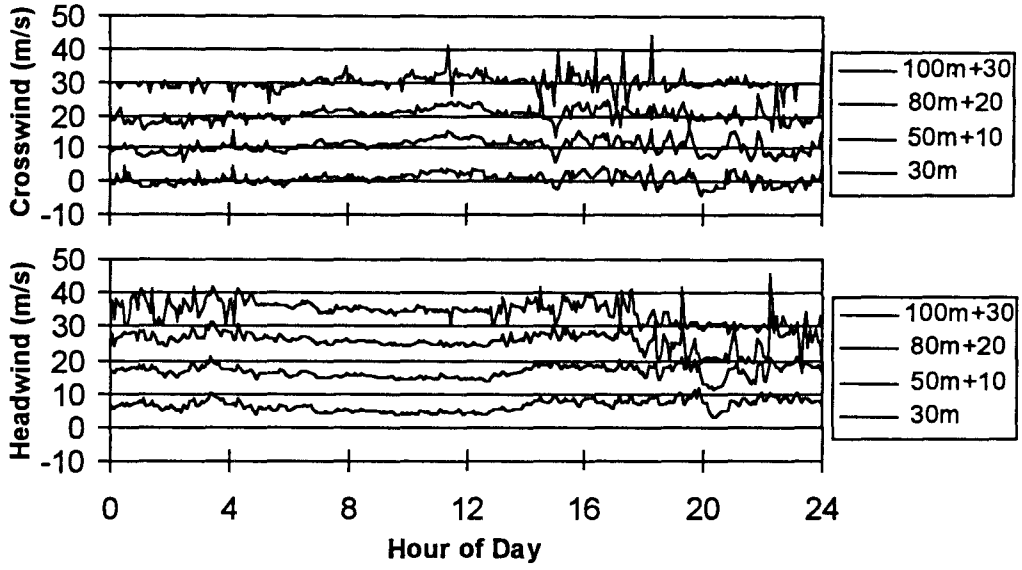

Figure 38. M4000 Sodar Crosswind and Headwind Profiles (5-minute average)

5.1.2.2 Lidar-Sodar Comparisons

A comparative analysis was conducted between the crosswinds measured by the lidar and the AeroVironment M3000 sodar. The M3000 was used since it:

1. Has a higher maximum range than the M4000 (400 versus 200 meters), and
2. Was farther away from the runway centerline and hence should have had less contamination due to stalled wake vortices.

The lidar wind data was collected only when wake vortices were not being tracked and hence the time periods were relatively short. Simultaneous lidar and sodar wind measurements were made on November 13, 1996 from 19:15 to 22:03 UTC, and on November 20, 1996 from 18:03 to 22:04 UTC.

Figures 39 and 40 are examples of plots that were created for November 13 and 20, overlaying crosswind profiles from both sensors. The error bars display the standard deviation of each measurement. The measurements which show no error bars were instances where only one sample point was gathered and no standard deviation could be calculated. The measurement range of the lidar varied both days, but generally extended from 20 m to 250 m. The lidar data are averaged for one minute. It is important to note that the M3000 sodar was set to different averaging periods for the two days. On November 13, a five-minute averaging period was used with a maximum range of 400 m and vertical resolution of 10 m. On November 20, the sodar was set to a one-minute averaging period.

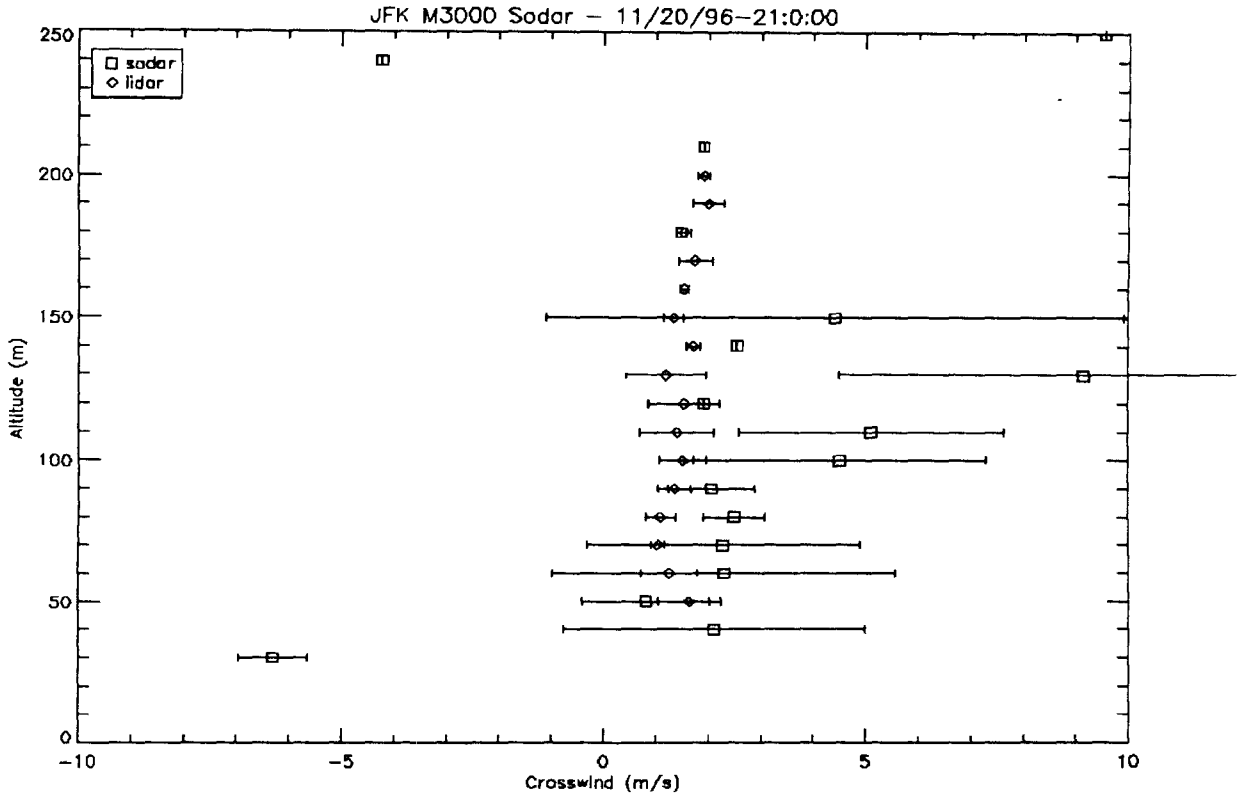

Figure 39. Sample Plot Comparing Crosswind Profiles: Lidar and One-Minute Sodar Data

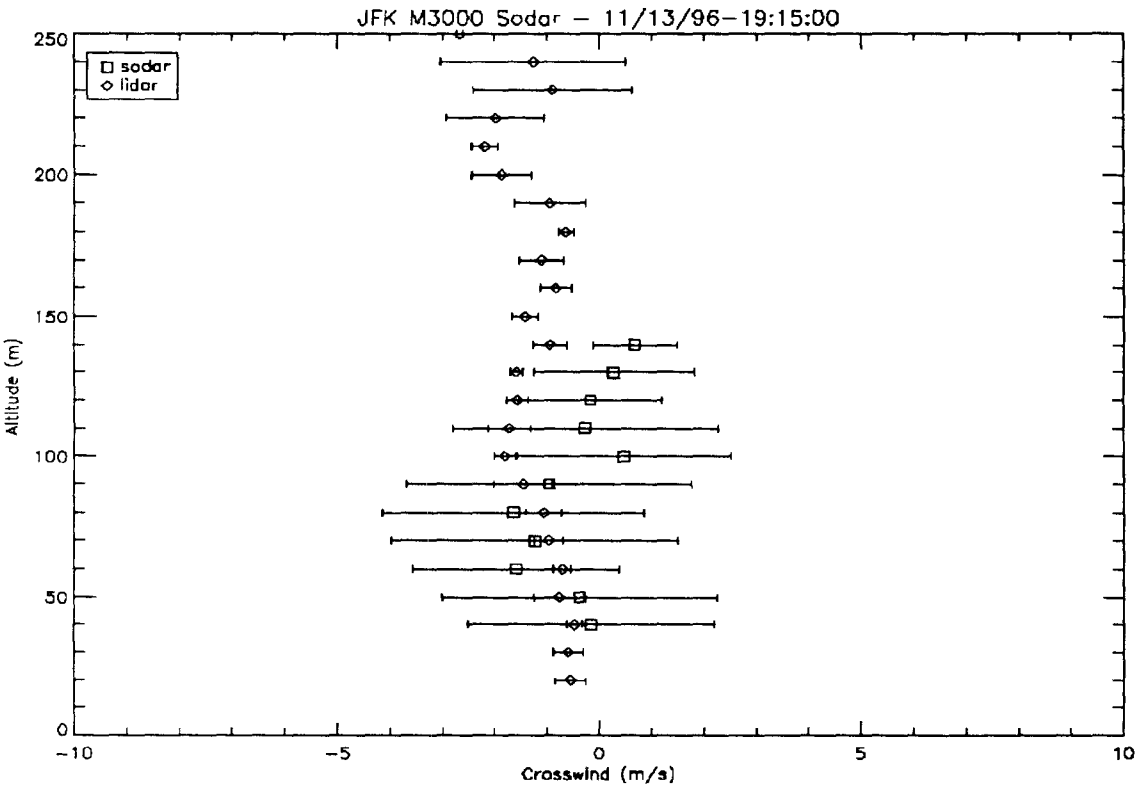

Figure 40. Sample Plot Comparing Crosswind Profiles: Lidar and Five-Minute Sodar Data

It can be seen by comparing Figures 39 and 40 that the changes in the sodar averaging time have a substantial effect on the sodar data and their comparison with the lidar measurements. Figure 39 shows that the one-minute sodar data vary greatly with height and do not compare well with the lidar, especially above 100 meters. In Figure 40, a significant improvement can be seen not only in the sodar's comparison with the lidar, but also in its consistency with height.

In a very limited analysis, an effort was made to generate five-minute averages from the one-minute data on November 20 to examine whether there was any improvement in comparison with the lidar. Although the range in values seemed to decrease somewhat, there was still very little consistency with height and the overall comparison with the lidar remained poor.

The conclusion drawn from the analysis between the sodar and lidar crosswinds is that the sodar seems to perform better when a longer averaging period is used. This is most likely due to the fact that during a longer averaging period, more sample points can be gathered for each measurement, which significantly improves the quality of the data.

5.2 WIND TURBULENCE

Among the Metek sonic anemometer's many recorded parameters (Section 3.2.1), there are several having to do with turbulence. Figure 41 shows xsig, ysig and zsig which are the one-minute averaged standard deviations of the wind in the x, y, and z directions. This turbulence parameter responds to turbulent frequencies with periods shorter than two seconds. To be more precise, these parameters are the standard deviation calculated over two seconds and then averaged for one minute. The Metek x, y, and z components were aligned with the headwind, crosswind and vertical wind on the runway.

Turbulence can also be obtained from the propeller anemometers. Figure 42 shows the propeller anemometer turbulence data from Pole 15, which was located 50 feet away from the Metek sonic anemometer. These parameters are the standard deviation of two-second wind averages, calculated over one minute. These parameters respond to frequencies with periods between 2 and 60 seconds. Thus, there is essentially no overlap in frequency spectrum for the sonic anemometer and propeller anemometer turbulence values.

The difference in frequencies results in substantial differences between the sonic and propeller anemometer turbulence parameters:

1. The sonic anemometer (high frequency) gives vertical turbulence values that are very slightly lower than the horizontal turbulence values. The propeller anemometer turbulence values (lower frequencies) are substantially lower for the vertical component than for the horizontal wind components. These results are reasonable since the proximity to the ground suppresses the low frequencies of vertical turbulence but has no effect on horizontal turbulence. Isotropic turbulence is expected for turbulent wavelengths much shorter than the height of measurement.
2. Wake vortices show up clearly in the propeller anemometer turbulence measurements (e.g., 1100-1300 hours), but have a much smaller effect on the sonic anemometer turbulence measurements The vortex winds vary relatively little over the two-second

period measured by the sonic anemometer values, but vary strongly over the one-minute period of the propeller anemometer analysis.

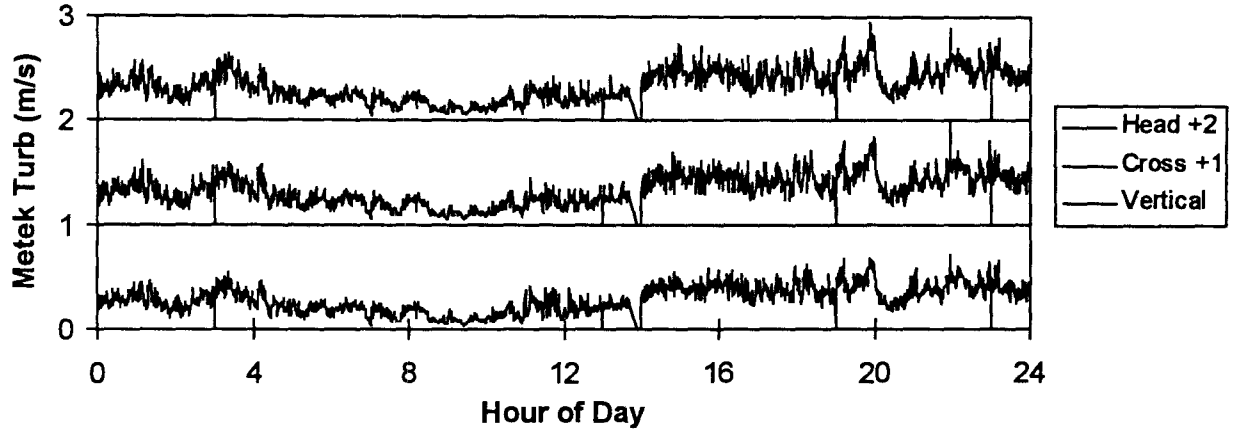

Figure 41. Metek Sonic Anemometer Turbulence

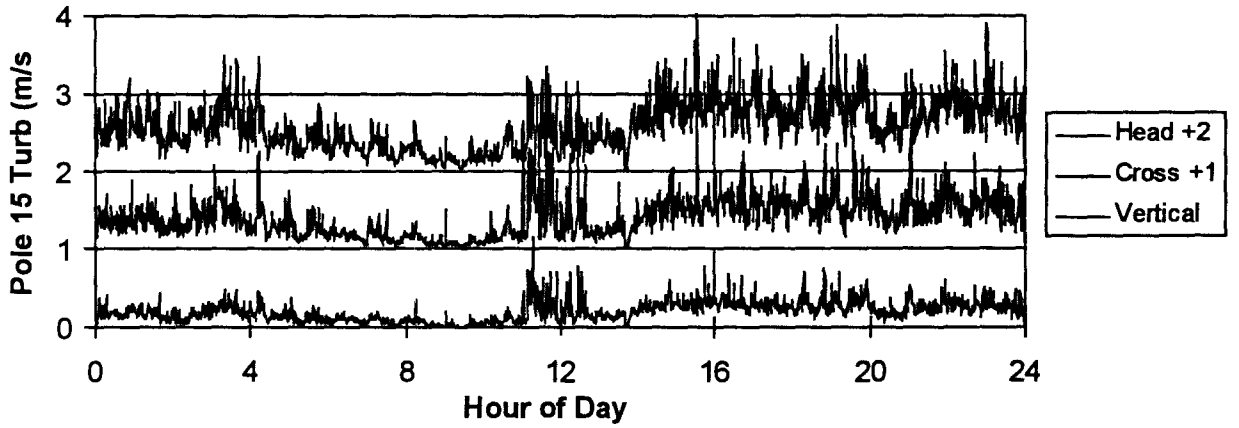

Figure 42. Propeller Anemometer (Pole 15) Turbulence

5.3 TEMPERATURE

Multiple instruments were used to record temperatures during the test period: two sonic anemometers, and two R. M. Young temperature sensors. The ATI and Metek sonic anemometer were located at 10 m heights while the Volpe Center and MIT/LL R. M. Young temperature sensors were located at 2.5 m and 6 m heights, respectively. Figure 43 shows the temperature variation for November 20. The Volpe sensor seems to agree most closely with the surface observations. However, these were only reported once per hour and only to within a degree. The MIT/LL sensor data was only available from the times between about 18:00 and 22:00 UTC, when it agreed with the Volpe sensor. The two sonic temperatures also agreed quite well. The differences between the Volpe and sonic temperatures are likely due to two effects:

1. The R. M. Young sensor appears to have a one-degree bias toward lower temperature.

2. The rest of the differences appear to be related to the lower measurement height of the Volpe sensor. When there is a nocturnal inversion (perhaps 0400-1300 hours), the lower sensor should read colder air. On the other hand, when the ground is strongly heated by sunlight (e.g., 1500-1800), the lower sensor should read the same or slightly higher.

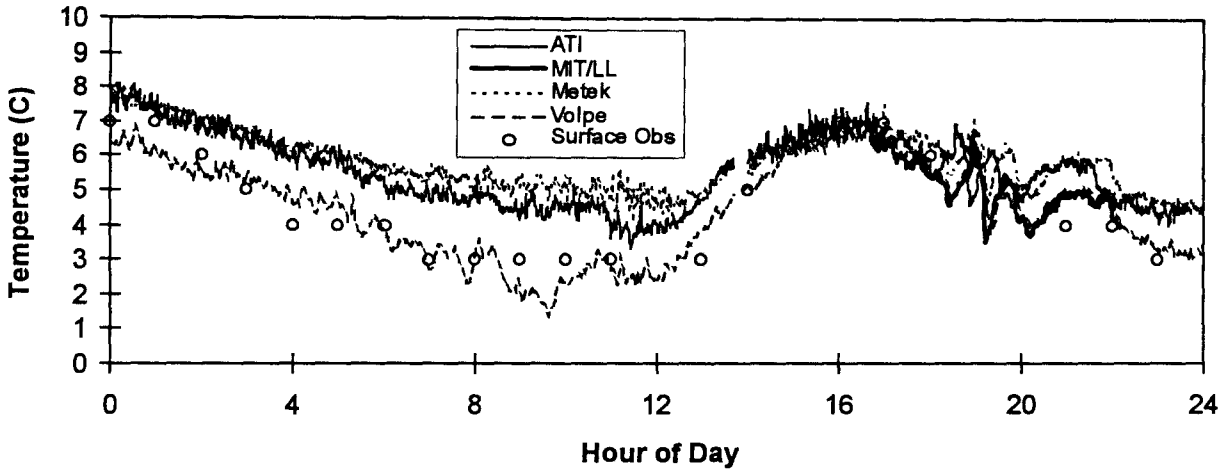

Figure 43. Temperature Comparisons for November 20

5.4 TEMPERATURE FLUCTUATIONS

The scintillometer responds to variations (C_n^2) in the index of refraction, which are predominately related to temperature fluctuations (humidity fluctuations may also play a role). Since the sonic anemometer is capable of measuring temperature fluctuations, some correlation would be expected between the sonic anemometer parameters and the measured C_n^2. Figure 44 shows the measured log C_n^2 for 1200-2400 hours on November 20, 1996; considerable variation is observed. Two sonic anemometer parameters were plotted for the same period in an attempt to find some correlation:

1. The standard deviation of temperature (sigT) showed almost no variation with time of day. At first sight, this result appears to be unreasonable since one would expect sigT to increase with thermal activity during the middle of the day (1500-1800 hours, as indicated in Figure 43). The likely explanation for this apparent anomaly is the short analysis time (two seconds) used to calculate sigT.

2. When the temperature was plotted versus time of day (see Figure 45), the variation appeared to be correlated with the variation in log C_n^2. A closer examination showed that the correlation is not simple; although the shapes of the curves are similar, the peaks and dips do not occur at exactly the same times. One would not expect a perfect correlation since the temperature fluctuations should perhaps be proportional to solar heating, which could perhaps be related to the slope of the temperature versus hour-of-day curve.

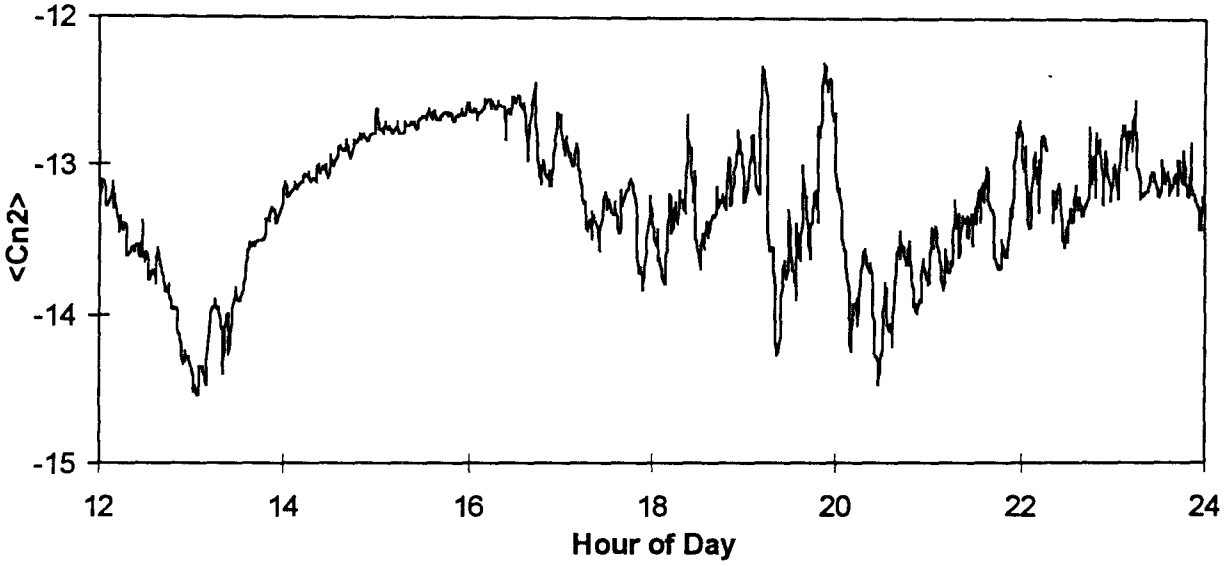

Figure 44. Variations in log C_n^2 on November 20, 1996

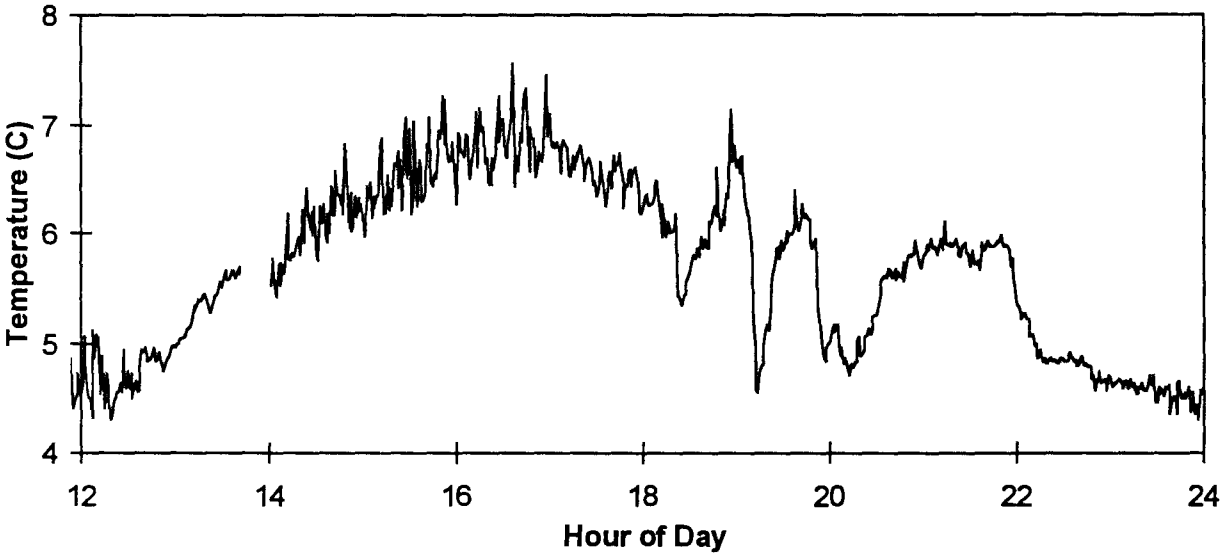

Figure 45. Variations in Metek Sonic Anemometer Temperature on November 20, 1996

6. VORTEX OBSERVATIONS

6.1 BOUNDARY LAYER UNDER VORTEX

6.1.1 Sample Vortex Data

Vertical wind and crosswind anemometers were installed at four heights (28, 14, 7, and 3.5 feet) on the anemometer array at lateral position +100 feet. Runs where the wake vortices linger over this location were selected by viewing the lateral transport plots from the anemometer array. Figure 46 shows the crosswinds measured under a B-747 vortex under low turbulence conditions. The three higher anemometers give equal readings for all ages. The lowest anemometer (C22) starts to read lower but jumps to match the other sensors at age 14 seconds, when the vortex core passes overhead, as indicated by a reversal in the vertical wind (see Figure 48). Figure 47 compares the measurements as ratios; the crosswinds of the lower anemometers are divided by the measurement of the highest anemometer.

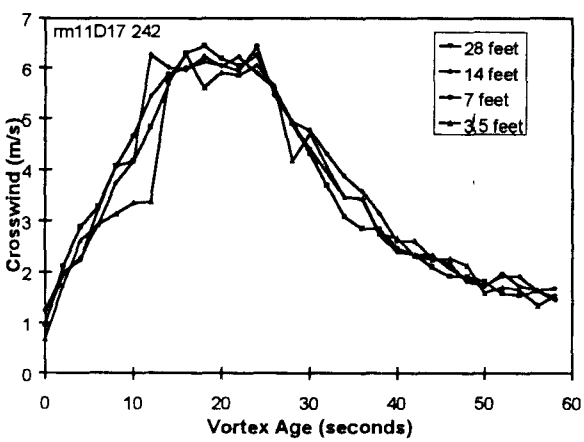

Figure 46. Crosswind Profile under B-747 Vortex, Run 242 on November 17, 1996

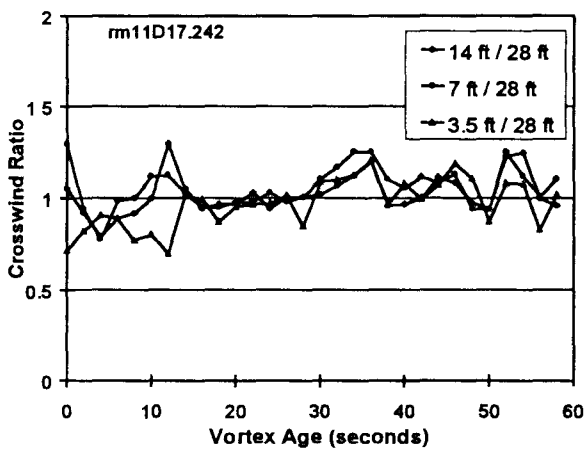

Figure 47. Crosswind Ratios, Run 242

Figure 48 compares the vertical winds measured at the four levels. The results are not as simple as for the horizontal winds. The vertical wind reverses sign when the vortex passes over the anemometer location age 14 seconds. Note that after the reversal, the 14-foot anemometer shows a larger crosswind than the 28-foot anemometer until vortex age 24 seconds. This difference may be the result of a secondary vortex. The vertical wind at the two lowest anemometers is very small and shows little correlation with the vertical wind at higher levels

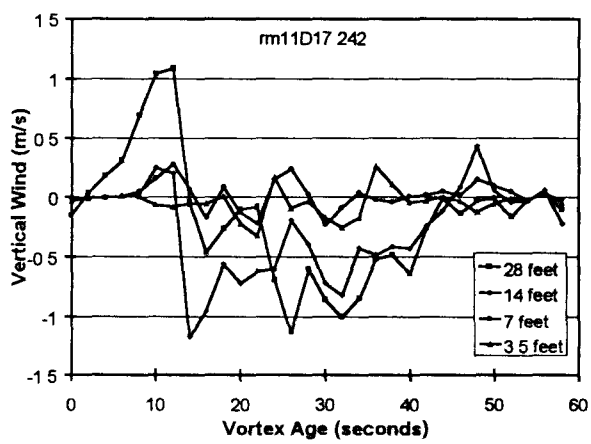

Figure 48 Vertical Wind Profile, Run 242

Figures 49-54 present data for two runs for smaller aircraft; the observed boundary layer thickness is greater for these runs.

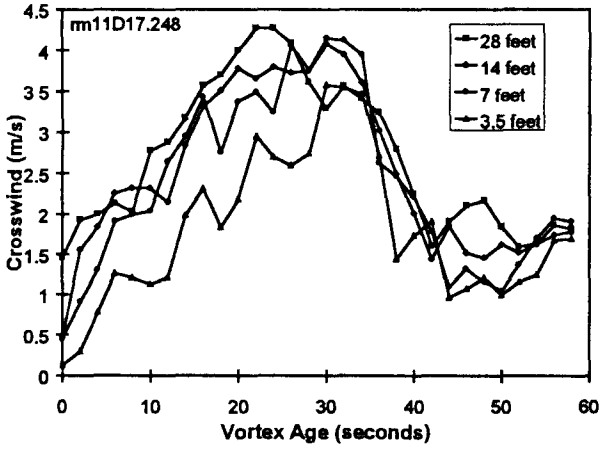

Figure 49. Crosswind Profile for Run 248 on November 17, 1996

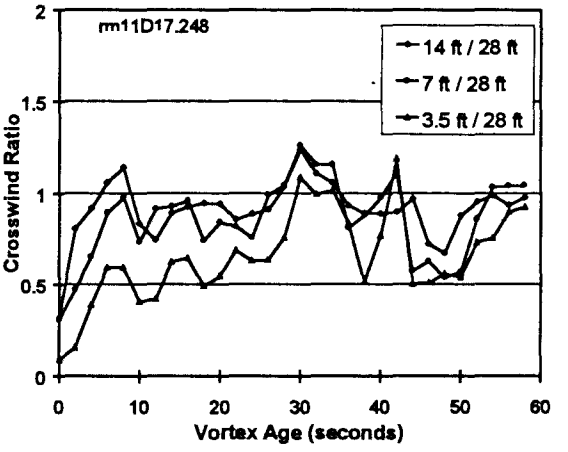

Figure 50. Crosswind Ratios for Run 248 on November 17, 1996

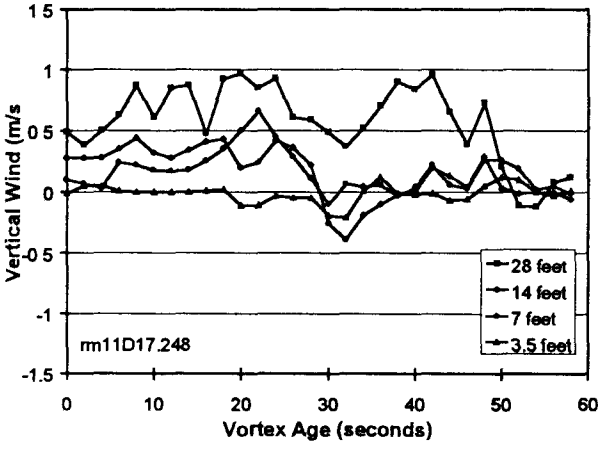

Figure 51. Vertical Wind Profile for Run 248 on November 17, 1996

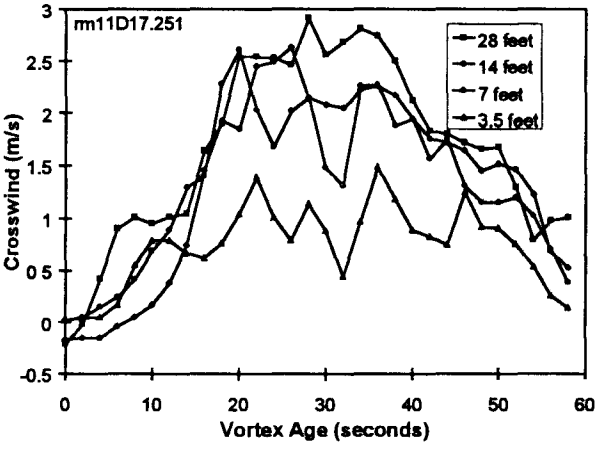

Figure 52. Crosswind Profile for Run 251 on November 17, 1996

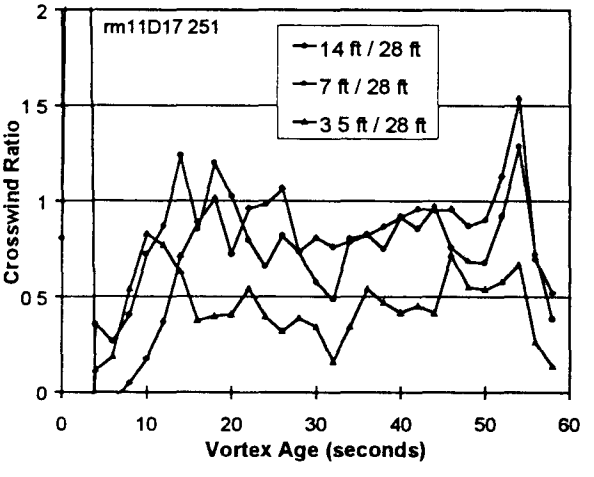

Figure 53. Crosswind Ratios for Run 251 on November 17, 1996

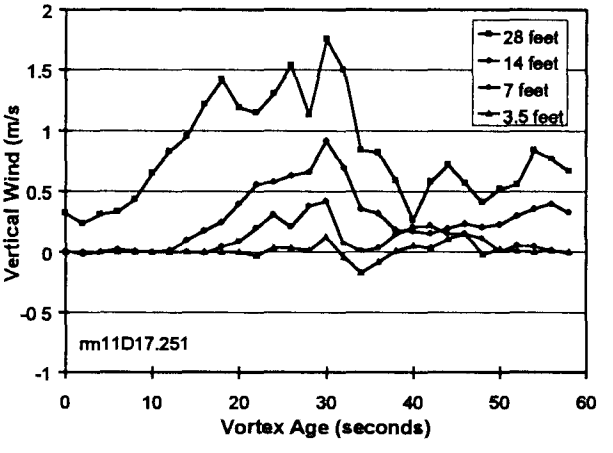

Figure 54. Vertical Wind Profile for Run 251 on November 17, 1996

6.1.2 Ambient Wind Profiles

The same crosswind anemometers used to measure the boundary thickness in Section 6.1.1 can be used to estimate the ambient wind boundary layer thickness. Figure 55 shows the crosswind at 28-foot height (Pole 10) for November 15, 1996. The values plotted are one-minute averages. Note the large amount of turbulence in the middle of the daylight period (1300-2200 hours).

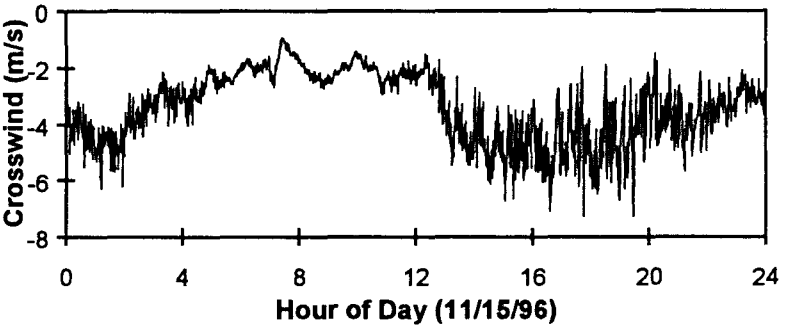

Figure 55. Ambient Crosswind at 28 feet on November 15, 1996

Figure 56 shows the ratios of the crosswind at 14, 7 and 3.5 feet to the crosswind at 28 feet. To keep the plots from overlapping, the ratios have been smoothed with a seven-minute running average. The thickness of the ambient wind boundary layer is much greater than the vortex boundary layer thickness noted in Figures 47, 50 and 53.

Under some conditions the wind is expected to vary logarithmically with height above the ground. Since the heights of the four anemometer poles varied by factors of two, a logarithmic profile would give equal wind increments between the readings of the four anemometers. The ratio values in Figure 56 should vary the same way, with the top ratio being one. At some times of the day, roughly equal wind increments are noted between the sensors at 3.5, 7 and 14 feet; however, a larger increment is always noted for the wind difference between 14 and 28 feet. Thus, the ambient crosswind profile is not well represented by a logarithmic form.

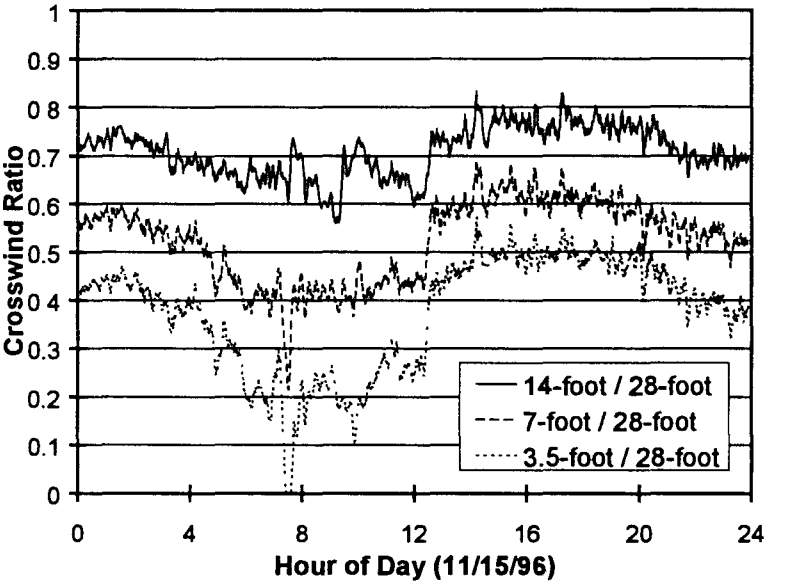

Figure 56. Ambient Crosswind Ratios on November 15, 1996

6.2 SONIC ANEMOMETER MEASUREMENTS INSIDE VORTEX OVAL

The ATI sonic anemometer was located at lateral position -50 feet (same lateral position and height as Pole 7), displaced 50 feet toward the middle marker from the main anemometer array. Since the goal of the sonic anemometer measurements was to measure the temperature and headwind inside the vortex oval, runs were selected where:

1. The turbulence level measured by the propeller anemometers was low and hence the atmosphere was likely stratified. The potential temperature increases with height in a stratified atmosphere; thus, the temperature inside of the vortex oval would be expected to be higher than ambient when the oval reached the ground.

2. The anemometer array showed that a vortex remained above Pole 6 (lateral position at -100 feet) for some period of time. When the runs were selected, the location of the ATI sonic anemometer was mistakenly thought to be at lateral position -100 feet rather than its actual value of -50 feet.

Figures 57-61 show typical data from such a run. Figure 57 shows the time variation of the two wind components measured at Pole 7. The vortex-induced crosswind is negative since the Pole 7 is under the Port vortex. Since the Port vortex is being transported away from the runway centerline, Pole 7 is located between the two vortices and hence the vertical wind is down or negative. Figures 58 and 59 compare the crosswind and headwind measured by the sonic (10 Hz) and propeller (0.5 Hz) anemometers, which are displaced by 100 feet along the flight path. Because the time synchronization between the data from the two anemometers was not perfect, the relative time scales for the two measurements was adjusted to give the best crosswind and headwind agreements. The time difference was 9 seconds for the run shown in Figures 57-61. Figures 60 and 61 show the sonic anemometer measurements of headwind and temperature.

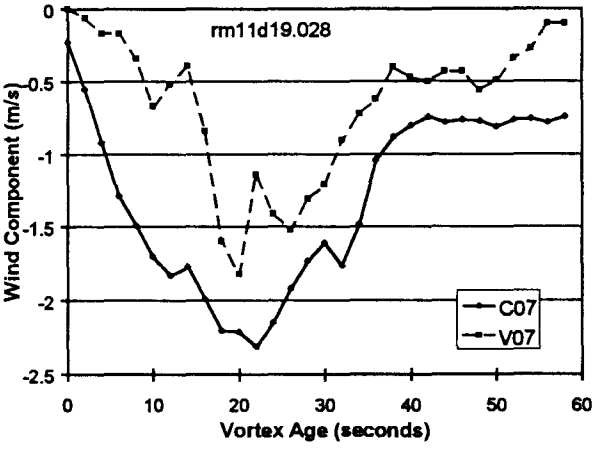

Figure 57. Crosswind and Vertical Wind from Propeller Anemometers on Pole 7 (-50 feet)

The agreement between the crosswind and vertical wind measurements in Figures 58 and 59 is reasonable; the details are different, however, after the turbulent part of the vortex reaches the sonic anemometer. Runs often showed significant differences in the arrival times of turbulence spikes at the two anemometers, which were separated by 50 feet along the flight path; this difference was typically more notable for the vertical wind component.

The results generally agree with the concept of the vortex oval descending to the ground and bringing down a sample of the atmosphere from the height of the flight path. The vortex oval appears to reach the sonic anemometer at about 11 seconds. The arrival of the oval is signaled by a dramatic increase in turbulence for all three wind components and a sharp increase in temperature and headwind. Such high turbulence levels at the edge of the vortex oval are noted in calculations of vortex decay in a stratified atmosphere and observed as enhanced backscatter near the edge of the vortex oval in MAVSS vortex measurements in a stratified atmosphere.

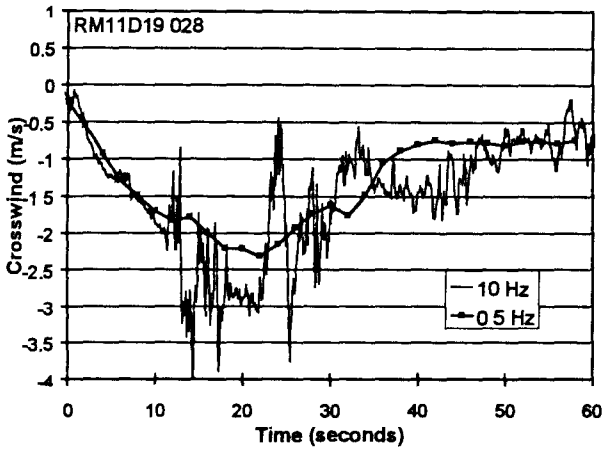

Figure 58. Crosswind Comparison

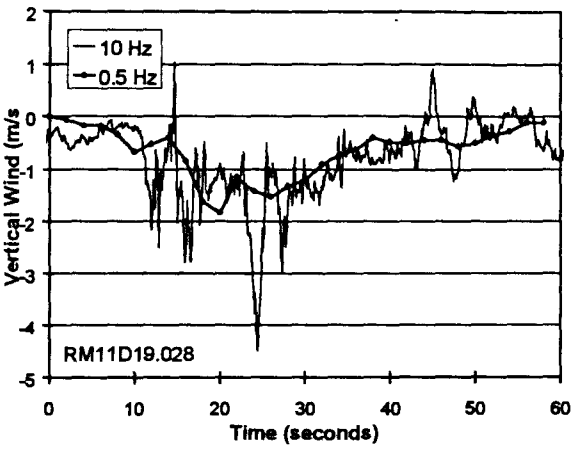

Figure 59. Vertical Wind Comparison

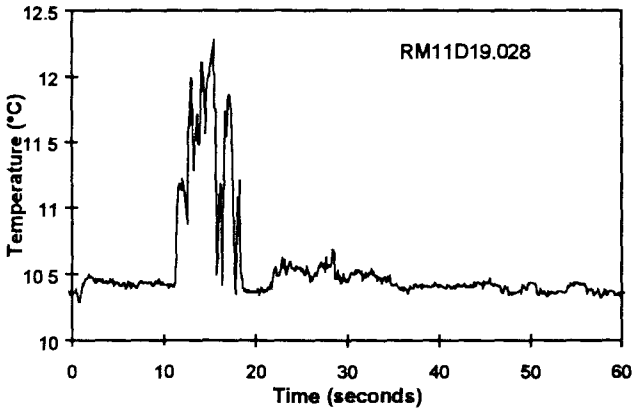

Figure 60. Temperature

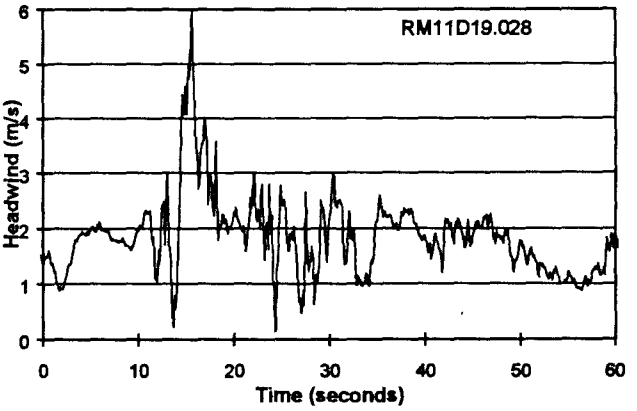

Figure 61. Headwind

7. EFFECT OF AIRCRAFT ON METEOROLOGY

Although the general idea that aircraft affect the ambient meteorological conditions has been known for a long time, the actual observation of such an effect has not been documented (apart from the well-known influence of wake vortices on wind measurements.). The November 1996 JFK test provided several clear cut examples of aircraft arrivals influencing the measured temperature and relative humidity; the effect was noted under conditions of nocturnal inversion. Since the Volpe temperature and relative humidity sensors were located near the runway centerline under the arriving aircraft, this observation is not surprising.

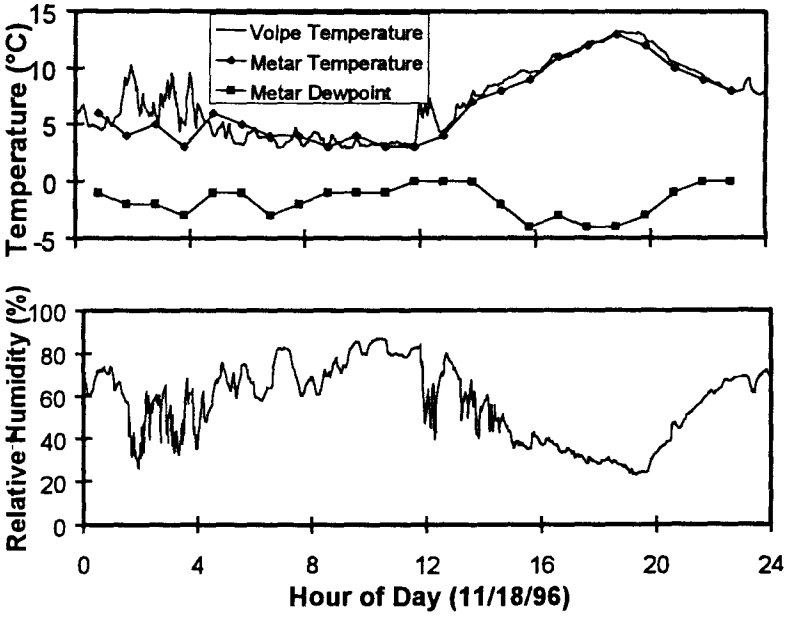

Figure 62. Temperature, Relative Humidity on November 18, 1996

Figure 62 shows the Volpe temperature and relative humidity for November 18, 1996; the surface observation (Metar) temperature and dewpoint are also plotted. Normal daytime heating (increasing temperature, decreasing relative humidity) is observed from 12:00 to 19:00 hours (UTC); cooling is observed from 19:00 to 24:00 hours.

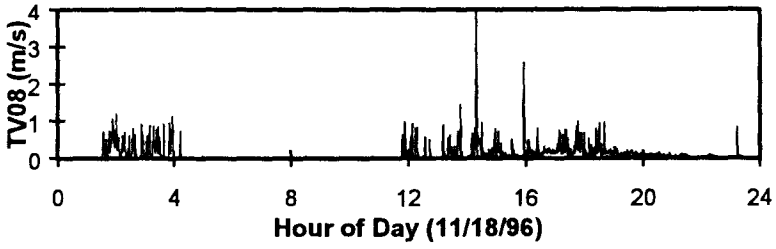

Figure 63. Runway Centerline Vertical Wind Standard Deviation on November 18, 1996

Aircraft arrivals are indicated in Figure 63, which plots the standard deviation of the vertical wind on the runway centerline. The night (01:00-04:00 UTC) and early morning (12:00-13:00 UTC) (local time is UTC minus five hours) aircraft arrivals are correlated with noticeable increases in temperature above the Metar values and decreases in relative humidity. Arrivals later in the morning show smaller or negligible effects on temperature and relative humidity. This observation is consistent with a nocturnal inversion where the potential temperature increases with height; the descending vortex ovals bring warmer air down to the temperature and humidity sensors that are installed at a height of 8 feet.

8. CONCLUSIONS

8.1 FIRST TIME OBSERVATIONS

This test provided a surprising number of first time observations:

1. Boundary layer thickness under wake vortex in ground effect.
2. High time resolution *in situ* temperature and velocity data inside vortex oval. [Note that hot-wire anemometer data in tower fly-by tests usually did not resolve velocity components and did not measure temperature.]
3. Directional measurements of vortex generated sound.
4. Influence of aircraft on meteorological conditions.

8.2 VORTEX SENSOR STATUS

8.2.1 MIT/LL Lidar

After extensive development work at the Memphis, TN Airport, the MIT/LL lidar was in an operational state for the November 1996 JFK test. The analysis presented in Appendix A suggested two areas where algorithm improvement is warranted:

1. Sometimes a vortex is misidentified.
2. Sometimes both vortices are located too close together to be the two primary wake vortices; one is likely a secondary vortex, which should be identified as such.

8.2.2 Anemometer Array

This test provided the first opportunity for serious comparisons of anemometer and lidar data; 60 runs of simultaneous lidar and anemometer array measurements were studied. The agreement between the two sensors was surprisingly good after vortex age 20 seconds, although the anemometer array sometimes gave lower vortex heights than those measured by the lidar.

Prior analysis of anemometer array data used fixed crosswind thresholds for starting and ending vortex trajectories; these analyses were valid for low turbulence conditions, but became invalid for higher turbulence levels. Since most of the lidar-anemometer comparison runs had significant turbulence levels, the anemometer processing algorithms had to be refined to reflect the reduced vortex detection sensitivity as the turbulence level increases. Although not yet perfect, the anemometer array processing algorithms can now operate successfully under various turbulence conditions.

8.2.3 RASS

This test provided the first comparisons between lidar and RASS measurements:

1. Position comparisons suggested a one-range-bin error in range for the RASS. This error was subsequently verified using a range calibration unit.

2. One run was analyzed to correlate RASS signatures with lidar vortex locations. RASS signals were noted when the lidar vortex locations were near the center of the RASS beam. The format of the RASS data did not permit a more systematic analysis.
3. Comparison with lidar circulations: The peak RASS measurements showed some correlation with the lidar measurements; the RASS values were generally somewhat lower.

8.2.4 WV Sodar

This test provided the first satisfactory wake vortex data from this sensor. The real-time processing algorithms, which had been developed on the basis of wind data, were not adequate for wake vortex tracking and measurement. The data suffered from ground clutter. Wake vortices were sometimes lost between range gates; overlapping range gates are needed. Processing had to start with beam-formed spectra (about half the runs) since the velocity and variance algorithms applied in real-time were not robust.

8.3 WIND MEASUREMENTS BY VORTEX SENSORS

Consistent crosswind measurements can be collected in a shorter time with the lidar than with a sodar. However, the lidar is currently used for wind monitoring only when the system is not actively tracking vortices. In wind mode, the spectral velocity resolution is increased at the cost of spatial resolution. If there is a high traffic density, then there may not be time between aircraft for wind estimations. Estimating winds while tracking vortices are mutually exclusive operations for a cw lidar.

The lidar is physically capable of scanning both in a direction perpendicular to the flight path and in a direction along the flight path down to about 45 degrees with respect to vertical. The wind software used in November 1996 did not use the second scanning axis for estimation of headwind. Since that time, the lidar has been upgraded with a wind scanning and processing system which should allow the system to estimate both crosswind and headwind components approximately every minute.

Although the WV sodar has been used to measure wind profiles in the past, this function was not pursued in the current analysis where the available resources were applied to analyzing vortex data.

8.4 METEOROLOGICAL MEASUREMENTS

Although atmospheric turbulence is expected to be an important parameter in defining the rate of wake vortex decay, the analysis of atmospheric turbulence data from the test raised as many questions as it answered:

1. The averaging method strongly affected the anemometer measurements of turbulence. Short-time averages responded to isotropic turbulence. Longer-time averages showed reduced vertical wind component variations and responded to wake vortices.

2. Scintillometer measurements of C_n^2 showed no correlation with short-time measurements of temperature variation, but showed some relationship with average temperature measurements. Further work will be needed to establish a valid correlation between scintillometer and sonic anemometer measurements of C_n^2.

9. RECOMMENDATIONS

9.1 AVOSS VORTEX SENSOR SUITABILITY

The Aircraft Vortex Spacing System (AVOSS) is being developed[16] by NASA to specify dynamic aircraft spacing in the terminal area environment. Wake vortex sensors are required for two purposes:

1. Research on vortex behavior for developing safe spacing algorithms based on meteorological measurements, and
2. Real-time vortex measurements to validate predictions based on meteorological measurements.

The goal of the AVOSS is to protect a defined approach corridor against inadvertent unacceptable wake vortex encounters.

9.1.1 Vortex Sensor Requirements

Although detailed vortex sensor requirements have not yet been defined, general requirements can be based on required system functionality:

1. Real-time, automatic, unmanned, all-weather - These requirements are almost mandatory for real-time system purposes and are desirable for increasing the efficiency of wake vortex research studies. The anemometer array, RASS and scintillometer come closest to meeting these requirements.
2. Environmentally acceptable - The sensor must not annoy the airport neighbors, i.e., RASS could be a problem.
3. Coverage, sensitivity - The entire protected approach corridor must be covered with enough sensitivity that hazardous vortices are reliably detected. Coverage is most difficult near the outer marker; only a pulsed lidar or a RASS have the capability to measure to 500 meters altitude.
4. Location accuracy, resolution - Accuracy and resolution requirements are generally higher for vortex height than lateral position because the protected corridor is effectively wider than it is high.
5. Circulation accuracy - Accuracy in measuring circulation is probably not important now, but may become more important if hazard definition efforts are successful.

9.1.2 Anemometer Array

The main limitation of the anemometer array is height coverage. Vortices that bounce back up into the flight path may not be detected.

9.1.3 RASS

Although the RASS resolution in space and circulation is relatively poor, its capabilities may be adequate for AVOSS. The long range capabilities of the RASS (e.g., at outer marker) appear promising, but are untested at present.

9.1.4 WV Sodar

The intended coverage of the WV sodar is appropriate for protecting the part of the approach corridor near the ground. Considerable additional development and testing will be required to assess its ultimate capabilities.

9.1.5 Scintillometer

The scintillometer is akin to the anemometer array, but with more longitudinal coverage and less longitudinal resolution. Even if the longitudinal resolution issue can be resolved, the height sensitivity remains to limit the capability of the scintillometer in monitoring the approach corridor.

9.2 FUTURE TESTS

9.2.1 Test Procedures

1. Determine causes for time synchronization problems and rectify. As backup, have each recording system keep its own aircraft arrival time.

2. Some of the anemometer array run files are very short (see Appendix A); in some cases the data for one arrival is split into two run files, perhaps by a spurious aircraft detection. Provision should be made for overlapping run files. A run file should be closed only after the second subsequent aircraft detection. This change will also handle the cases where wake vortices are still active when the next aircraft arrives.

3 Run files, like the anemometer array run files, should be generated for any sensors used to study wake vortices. Such files make post processing much more convenient. Extracting vortex data from long-time data files is tedious and highly dependent upon clock synchronization.

4 All manned sensor measurements were conducted under unstratified, turbulent conditions. Future tests should schedule some manned data collection under stratified, low turbulence conditions (night or early morning). The cooperation of Air Traffic Control in scheduling runway usage would be necessary to facilitate such data collection.

9.2.2 Analysis Methods

1. Several sensors (lidar and anemometer array) can detect the presence of secondary wake vortices, which can be generated by the interaction of a wake vortex with the boundary layer at the ground. Since secondary wake vortices may have an important influence on vortex decay, they should be considered in more detail in future analyses of field data

9.2.3 Anemometer Array

1. Since the boundary layer is thinner than 3.5 feet under some wake vortices and the lowest vertical anemometer shows little of interest, the 3.5-foot vertical anemometer should be reinstalled at 1.75 feet to measure the crosswind. Since the boundary layer is so thin, the grass within 100 feet of these anemometers must be kept short during future tests.

2. The November 1996 results show signs of nonuniform anemometer response (Section 4.1, Figure 27). All anemometers should be refurbished before the next test.

9.2.4 MIT/LL Lidar

1. Relocate to 100 meters from runway centerline so that stalled vortices can be tracked to low altitudes. May require some gravel to make van movement safe.

2. Improve tracking and analysis algorithms for in-ground-effect data collection.

3. During this first JFK test, real-time wind profiles were at a lower priority than good lidar vortex tracks. The lidar system is being upgraded so that the transition between vortex tracking and wind measurement is more automated.

9.2.5 RASS

1. Provide output data in measurement, not picture format. Process November 1996 data in this form to develop sensor response model before collecting more data at current RASS location.

2. Test at outer marker location.

9.2.6 WV Sodar

1. Locate on runway centerline to best measure stalled wake vortices.

2. Install clutter fence to reduce noise and clutter.

3 Record some raw digitized data to develop improved real-time processing (specifically interleaved range gates).

4. Use faster data acquisition computer so that beam-formed data can be recorded once per second.

5. Consider using shorter maximum range for faster update rate.

9.2.7 Sonic Anemometers

1. Install ATI unit farther from runway centerline to see larger vortex winds.

2. Deploy more than one high-data-rate sonic anemometer on same side of runway to assess how the vortex recirculation oval evolves in time and space.

9.2.8 Scintillometer

1. Install on extended runway centerline to test capability for monitoring when approach corridor is clear of wake vortices. Since maximum response is near midpoint of transmitter and receiver, should install with midpoint near the anemometer array.

2. Test with reflected beam from tower to measure turbulence away from the ground.

9.2.9 Meteorological Sodars

1. Fix cover problem with minisodar to recover low altitude measurement capability.

2. Relocate minisodar to runway centerline to better measure stalled vortex height. Reduce maximum range from 200 to 70 or 100 meters to increase repetition rate for vortex measurements.

3. Speed up data recording by writing directly to fileserver over Ethernet rather than serial line; need to replace computer board in minisodar signal processor.

APPENDIX: COMPARISON OF VORTEX DATA FROM LIDAR AND ANEMOMETER ARRAY

This appendix compares the vortex data from all the concurrent runs (128) with lidar and anemometer array measurements. The comparison makes use of the anemometer array plot format shown in Figure 7. The lidar measurements for vortex location and circulation are plotted on top of the anemometer array data points (X and ▯) using somewhat larger symbols for the lidar data.

These overlay plots were then analyzed visually for the criteria listed in Table A-1, which also summarized the results. Table A-2 provides details for the 128 runs. The column code (A-F) in Table A-1 is used to identify the runs in Table A-2 which met each criterion in Table A-1 ("X" in corresponding column of Table A-2).

Table A-1. Summary of Anemometer Array - Lidar Comparison

Criterion	Column	Runs	Percent *
No Anemometer array data.	A	21	16
False detections by anemometer array.	B	7	5
Lidar gives data from one vortex as two vortices or misidentifies vortex. Some of the incorrect vortices appear to be secondary vortices of opposite sign circulation, which can be generated by detachment of the boundary layer at the ground. Such vortices can also be seen[1] in the anemometer array data, but were not looked for in the current analysis.	C	9	7
Lateral position disagrees between lidar and anemometer array. This disagreement is typically for the vortex not being tracked by the lidar; since the lidar range scan does not bracket the vortex location for the vortex not being tracked, large range errors are likely and probably account for most lateral position disagreements.	D	5	4
Simultaneous lateral positions for a long time.	E	60	47
For E cases, heights disagree: L = anemometer array low, H = anemometer array high (no H's noted). The points before 20 seconds are generally low for the anemometer array and were excluded from this analysis.	F	11	18**

* Percent total runs ** Percent 'E' runs

Table A-2 starts with the day, hour, minute and second of the arrival time recorded by the anemometer array, followed by the anemometer array file name. Two columns then list the aircraft types from: a) Lincoln Laboratory (used to label the overlay plots), and b) Volpe spotter. The spotter type list a) corrects two types on November 13, 1996, b) adds two unknown types on November 20, 1996, and c) provides the series for most B-747 arrivals. Two crosswind turbulence parameters follow: a) one-minute value derived from the run file, and b) value

obtained from a 15-minute average prior to the aircraft arrival. Because of the fluctuations in the one-minute values, the anemometer array analysis was governed by the 15-minute average value.

Following Table A-2, the overlay plots for all runs are included.

Table A-2. Run by Run Comparison of Lidar and Anemometer Array Measurements

Day	Hour	Min	Sec	File name	Type	Type	MinTC	MTC-15	A	B	C	D	E	F
13	18	48	25	RM11D13.067	B767	767	0.82	0.57		X				
13	18	54	11	RM11D13.070	B767	767	0.20	0.60			X			
13	18	55	59	RM11D13.072	B767	757	0.30	0.58	X					
13	19	5	43	RM11D13.076	B767	767	0.23	0.50						
13	19	8	56	RM11D13.077	B767	767	0.37	0.44						
13	19	10	33	RM11D13.078	B767	767	0.34	0.45					X	
13	19	19	8	RM11D13.079	B767	A300	0.56	0.41					X	L
13	19	24	4	RM11D13.081	B767	767	0.27	0.41						
13	19	26	18	RM11D13.082	B757	757	0.48	0.40					X	
13	19	28	26	RM11D13.083	B767	767	0.65	0.38					X	
13	19	31	0	RM11D13.084	B747	747-200	0.52	0.41					X	
13	20	6	7	RM11D13.099	B767	767	0.61	0.43						
13	20	32	48	RM11D13.112	B767	767	0.57	0.53					X	
13	20	36	47	RM11D13.114	B767	767	0.51	0.53					X	
13	20	40	57	RM11D13.117	EA33	A330	0.68	0.52	X	X				
13	20	56	10	RM11D13.126	B767	767	0.5	0.54						
13	21	9	6	RM11D13.132	B767	767	0.29	0.50						
13	21	15	8	RM11D13.134	DC10	DC10	0.54	0.39						
13	21	21	11	RM11D13.137	DC9	DC9	0.5	0.43	X					
13	21	23	45	RM11D13.138	B727	727	0.38	0.42					X	
13	21	26	39	RM11D13.140	B727	727	0.73	0.45						
13	21	37	45	RM11D13.144	B747	747-200	1.00	0.58					X	
13	21	39	57	RM11D13.145	EA30	A300	0.69	0.61					X	
13	21	43	37	RM11D13.147	MD80	MD80	0.57	0.57	X					
13	21	45	21	RM11D13.148	EA30	A300	0.51	0.52					X	
13	21	47	3	RM11D13.149	DC8	DC8	0.40	0.53						
13	21	49	11	RM11D13.150	B747	747-200	0.55	0.52					X	L
13	21	52	41	RM11D13.152	B767	767	0.25	0.44					X	
13	21	55	3	RM11D13.153	B767	767	0.35	0.39					X	
13	21	59	55	RM11D13.156	B747	747-200	0.52	0.38					X	
13	22	4	4	RM11D13.158	B767		0.34	0.37	X					
13	22	6	14	RM11D13.159	Prop		0.24	0.36	X					
13	22	11	46	RM11D13.162	L101	L1011	0.46	0.38					X	
13	22	14	18	RM11D13.163	L101	L1011	0.44	0.37						
13	22	16	16	RM11D13.164	DC10	DC10	0.37	0.35					X	
13	22	20	16	RM11D13.166	B767		0.44	0.36						
13	22	27	48	RM11D13.170	B747	747	0.51	0.41					X	
14	14	11	39	RM11D14.109	DC10	DC10	0.39	0.38						
14	14	25	23	RM11D14.114	Conc	Concord	0.45	0.40					X	
14	14	31	20	RM11D14.117	B767	767	0.48	0.41						
14	15	15	49	RM11D14.126	B747	747-400	0.37	0.40			X			
14	15	35	57	RM11D14.132	B747	747-400	0.83	0.43			X		X	
14	15	39	11	RM11D14.134	B767	767	0.65	0.44			X		X	
14	20	18	14	RM11D14.203	B747	747-200	0.39	0.36					X	
14	20	33	46	RM11D14.212	B767	767	0.62	0.46						
14	20	38	25	RM11D14.215	B767	767	0.54	0.55						

Day	Hour	Min	Sec	File name	Type	Type	MinTC	MTC-15	A	B	C	D	E	F
14	20	39	43	RM11D14.216	EA34	A340	0.91	0.56						
14	20	43	13	RM11D14.218	B767	767	0.38	0.54						
14	20	53	25	RM11D14.222	B747	747-200	1.05	0.47					X	
14	20	58	25	RM11D14.224	B767	767	0.43	0.48						
14	21	11	53	RM11D14.231	EA30	A300	0.70	0.51	X					
14	21	16	16	RM11D14.233	MD80	MD80	0.66	0.55	X					
14	21	18	40	RM11D14.234	B767	767	0.42	0.59	X					
14	21	28	50	RM11D14.239	DC9	DC9	0.54	0.56	X					
14	21	31	42	RM11D14.240	B727	727	0.42	0.53	X					
14	21	34	40	RM11D14.242	B747	747-200	0.9	0.51						
14	21	36	52	RM11D14.243	B747	747-200	0.61	0.55						
14	21	40	24	RM11D14.245	MD80	MD80	0.76	0.54	X					
14	21	49	13	RM11D14.250	B767	767	0.57	0.52						
14	21	53	8	RM11D14.252	EA34	A340	0.63	0.49						
14	21	55	43	RM11D14.254	B767	767	0.53	0.47						
14	21	57	1	RM11D14.255	B767	767	0.46	0.46						
15	12	4	44	RM11D15.025	B767	767	0.20	0.21	X					
15	12	17	44	RM11D15.030	MD11	MD11	0.30	0.20	X					
15	12	21	47	RM11D15.031	DC8	DC8	0.19	0.19						
15	12	50	10	RM11D15.036	B747	747	0.35	0.38						
15	13	3	20	RM11D15.043	EA30	A300	0.55	0.44						
15	20	5	4	RM11D15.141	B767		0.59	0.62						
15	20	14	16	RM11D15.147	B747		1.03	0.64					X	
20	18	47	50	RM11D20.228	B747	747-200	0.56	0.43					X	
20	19	4	56	RM11D20.235	B767	767	0.73	0.52						
20	19	7	0	RM11D20.236	B757	757	0.68	0.59					X	
20	19	11	26	RM11D20.238	B747	747-400	0.62	0.63					X	L
20	19	25	43	RM11D20.242	B757	757	0.46	0.47			X		X	
20	19	27	29	RM11D20.243	EA30	A300	0.37	0.42					X	
20	19	29	25	RM11D20.244	B757	757	0.33	0.39					X	
20	19	32	55	RM11D20.246	B747	747-200	0.61	0.37					X	L
20	19	36	9	RM11D20.247	B757	757	0.40	0.43					X	
20	19	39	5	RM11D20.248	B767	767	0.51	0.46					X	
20	19	43	39	RM11D20.249	B767	767	0.38	0.48		X	X			
20	19	47	33	RM11D20.250	B727	727	1.04	0.52						
20	19	54	13	RM11D20.253	B767	767	0.91	0.59		X				
20	19	56	39	RM11D20.254	B727	727	0.70	0.64	X					
20	19	59	12	RM11D20.257	B767	767	0.77	0.68	X					
20	20	1	34	RM11D20.258	EA34	A340	1.05	0.69					X	
20	20	3	48	RM11D20.259	B747	747-400	0.38	0.66			X		X	
20	20	12	15	RM11D20.265	L101	L1011	0.29	0.52			X		X	L
20	20	13	48	RM11D20.266	EA33	A330	0.28	0.51						
20	20	18	8	RM11D20.268	B747	747-200	0.56	0.49				X	X	
20	20	25	24	RM11D20.271	L101	L1011	0.24	0.44				X	X	
20	20	30	44	RM11D20.274	B747	747-400	0.58	0.38					X	
20	20	33	56	RM11D20.276	MD11	MD11	0.45	0.38					X	
20	20	37	46	RM11D20.278	B757	757	0.30	0.39				X	X	
20	20	41	16	RM11D20.280	B747	747-200	0.29	0.37					X	

Day	Hour	Min	Sec	File name	Type	Type	MinTC	MTC-15	A	B	C	D	E	F
20	20	43	20	RM11D20.281	B767	767	0.21	0.36					X	
20	20	45	6	RM11D20.282	DC9	DC9	0.46	0.35	X		X			
20	20	47	15	RM11D20.284	B747	747-200	0.69	0.35					X	L
20	20	49	32	RM11D20.285	B757	757	0.35	0.35				X	X	L
20	20	51	8	RM11D20.286	Braz	Braz	0.35	0.35	X					
20	20	52	5	RM11D20.287	MD80	MD80	0.30	0.35						
20	20	53	37	RM11D20.288	B767	767	0.27	0.35					X	
20	20	56	57	RM11D20.290	L101	L1011	0.52	0.38					X	
20	21	0	23	RM11D20.292	N/A	DC10	0.45	0.71						
20	21	2	15	RM11D20.293	B767	767	0.46	0.42					X	
20	21	3	59	RM11D20.294	B767	767	0.54	0.40	X	X				
20	21	7	53	RM11D20.296	B767	767	0.31	0.43						
20	21	11	57	RM11D20.297	B747	747-200	0.25	0.42					X	
20	21	15	45	RM11D20.299	B727	727	0.36	0.41						
20	21	19	1	RM11D20.300	MD80	MD80	0.62	0.39		X				
20	21	25	53	RM11D20.303	B747	747-200	0.56	0.44					X	L
20	21	28	9	RM11D20.304	B727	727	0.33	0.44						
20	21	29	13	RM11D20.305	B747	747-200	0.34	0.44					X	L
20	21	31	5	RM11D20.306	B747	747-200	0.57	0.43					X	
20	21	32	49	RM11D20.307	B747	747-200	0.30	0.45					X	
20	21	34	16	RM11D20.308	B747	747-200	0.34	0.45					X	
20	21	36	7	RM11D20.309	DC10	DC10	0.41	0.44					X	
20	21	38	16	RM11D20.310	B747	747-200	0.42	0.43				X	X	
20	21	40	10	RM11D20.311	B767	767	0.80	0.44					X	L
20	21	43	26	RM11D20.313	DC9	DC9	0.36	0.45						
20	21	47	56	RM11D20.316	DC9	DC9	0.93	0.44						
20	21	49	18	RM11D20.317	B767	767	0.45	0.48					X	L
20	21	51	34	RM11D20.318	DC9	DC9	0.45	0.46		X				
20	21	57	4	RM11D20.322	B767	767	0.43	0.54						
20	21	58	42	RM11D20.323	N/A	767	0.44	0.55					X	
20	22	1	30	RM11D20.325	B747	747-200	0.85	0.58					X	
20	22	4	40	RM11D20.327	EA32	A320	0.54	0.60					X	
20	22	6	19	RM11D20.328	B727	727	0.81	0.63	X					
20	22	8	0	RM11D20.330	B767	767	0.69	0.66	X					

OVERLAY PLOTS FOR ALL RUNS

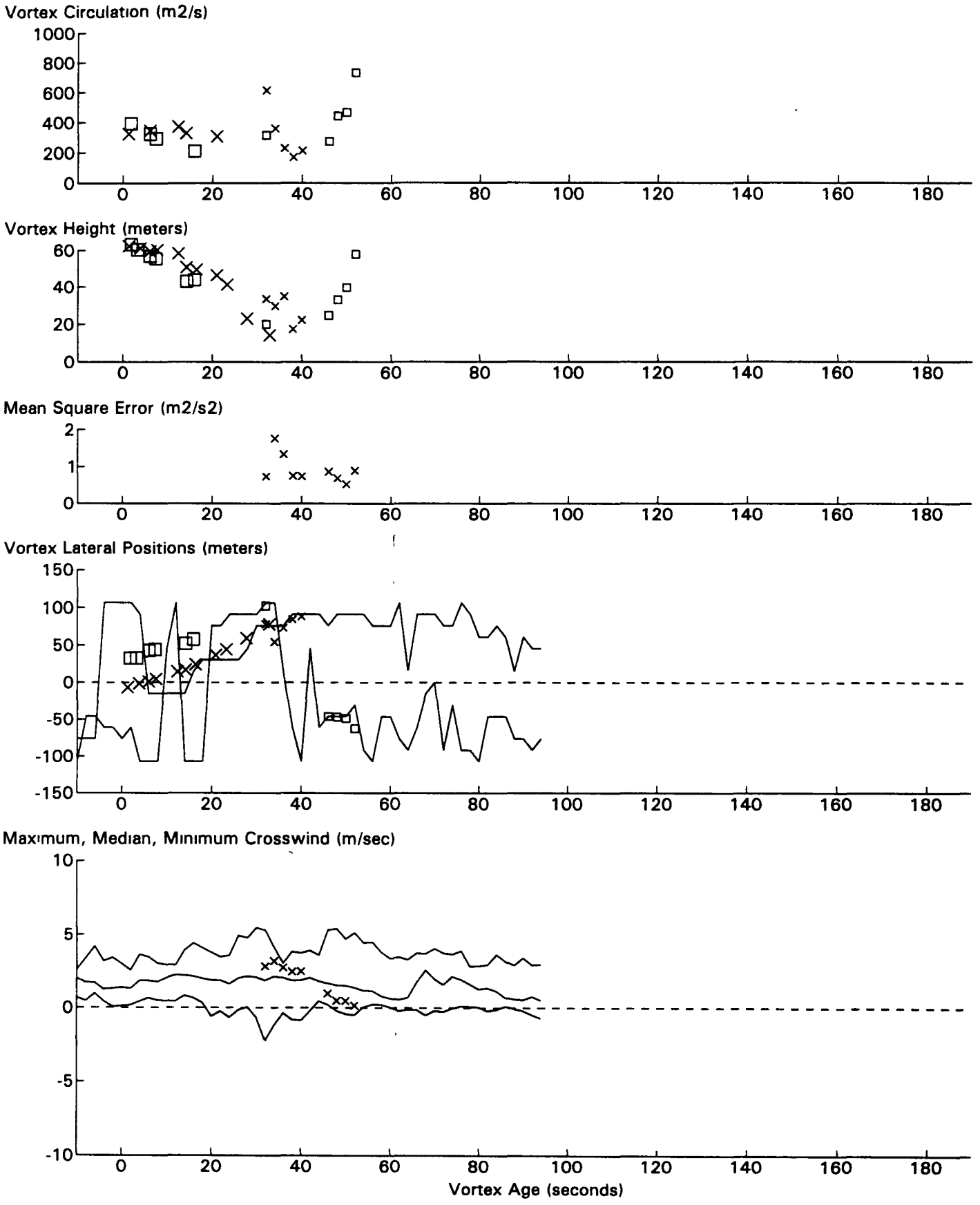

B767 JFK 31R GWVSS Data for File: I:RM11D13.067 11/13/96 18:48:25 dt= 44 CWturb=0.57

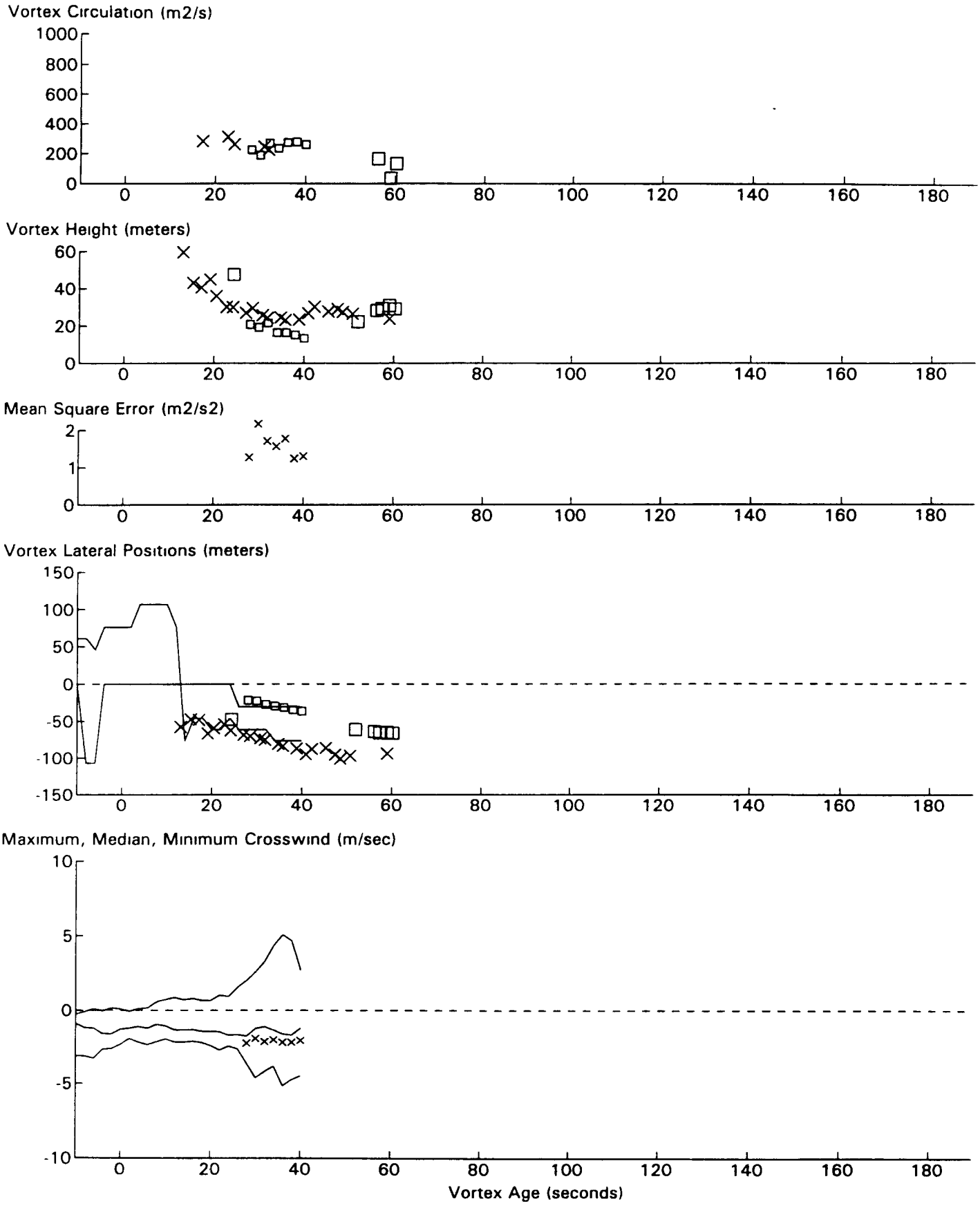

B767 JFK 31R GWVSS Data for File: I:RM11D13.070 11/13/96 18:54:11 dt= 44 CWturb=0.60

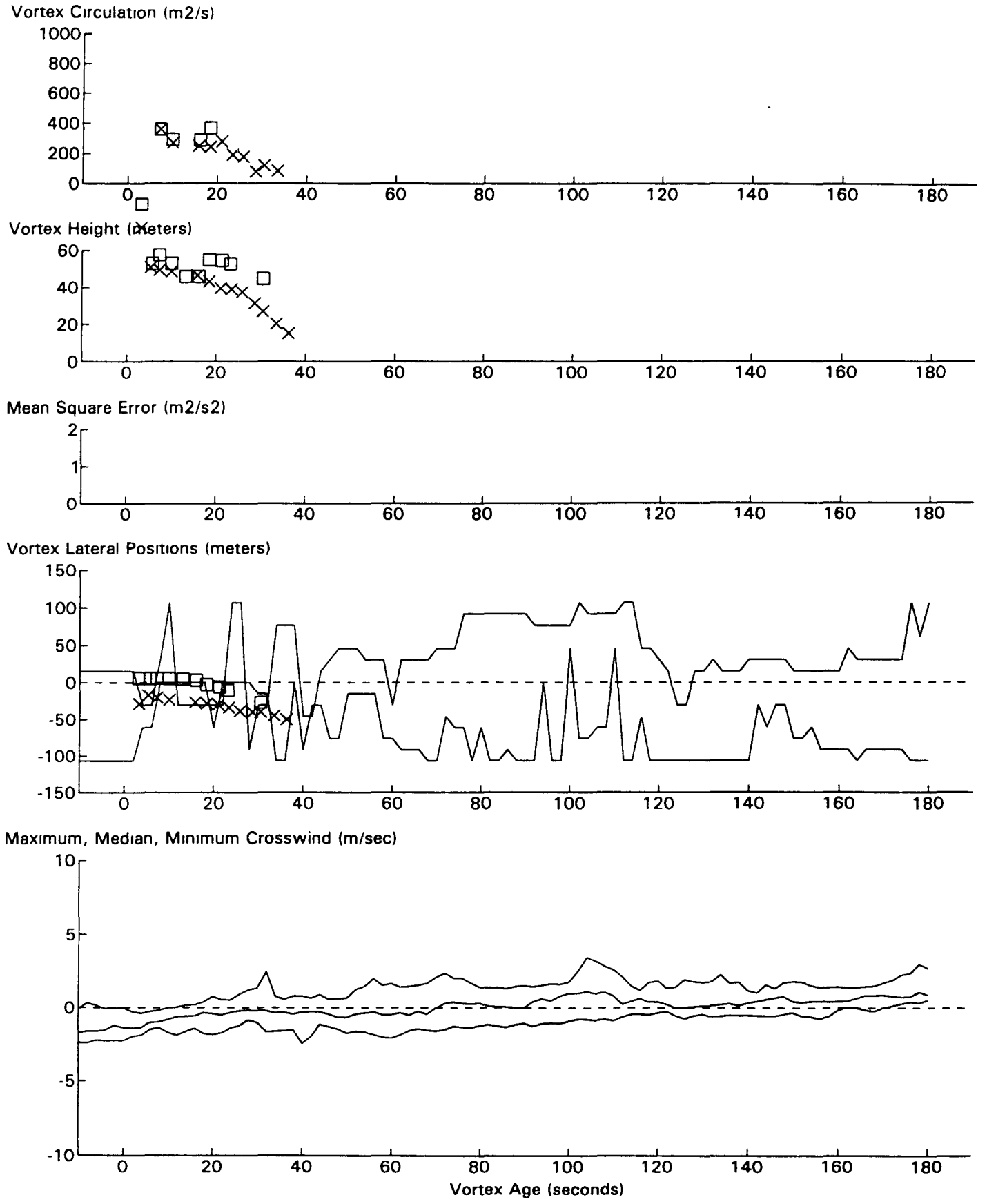

B767 JFK 31R GWVSS Data for File: I:RM11D13.072 11/13/96 18:55:59 dt= 44 CWturb=0.58

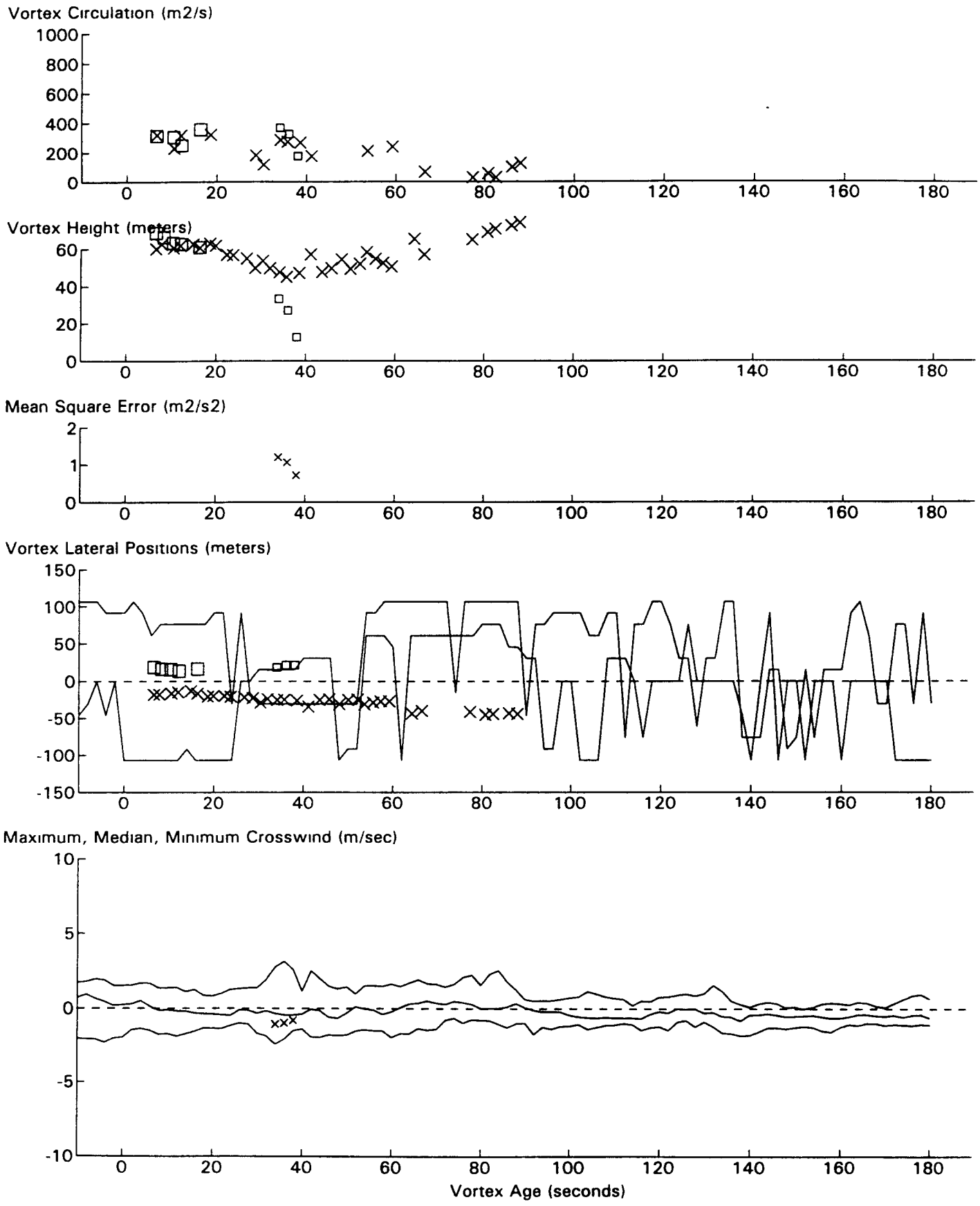

B767 JFK 31R GWVSS Data for File: I:RM11D13.076 11/13/96 19:5:43 dt= 44 CWturb=0.50

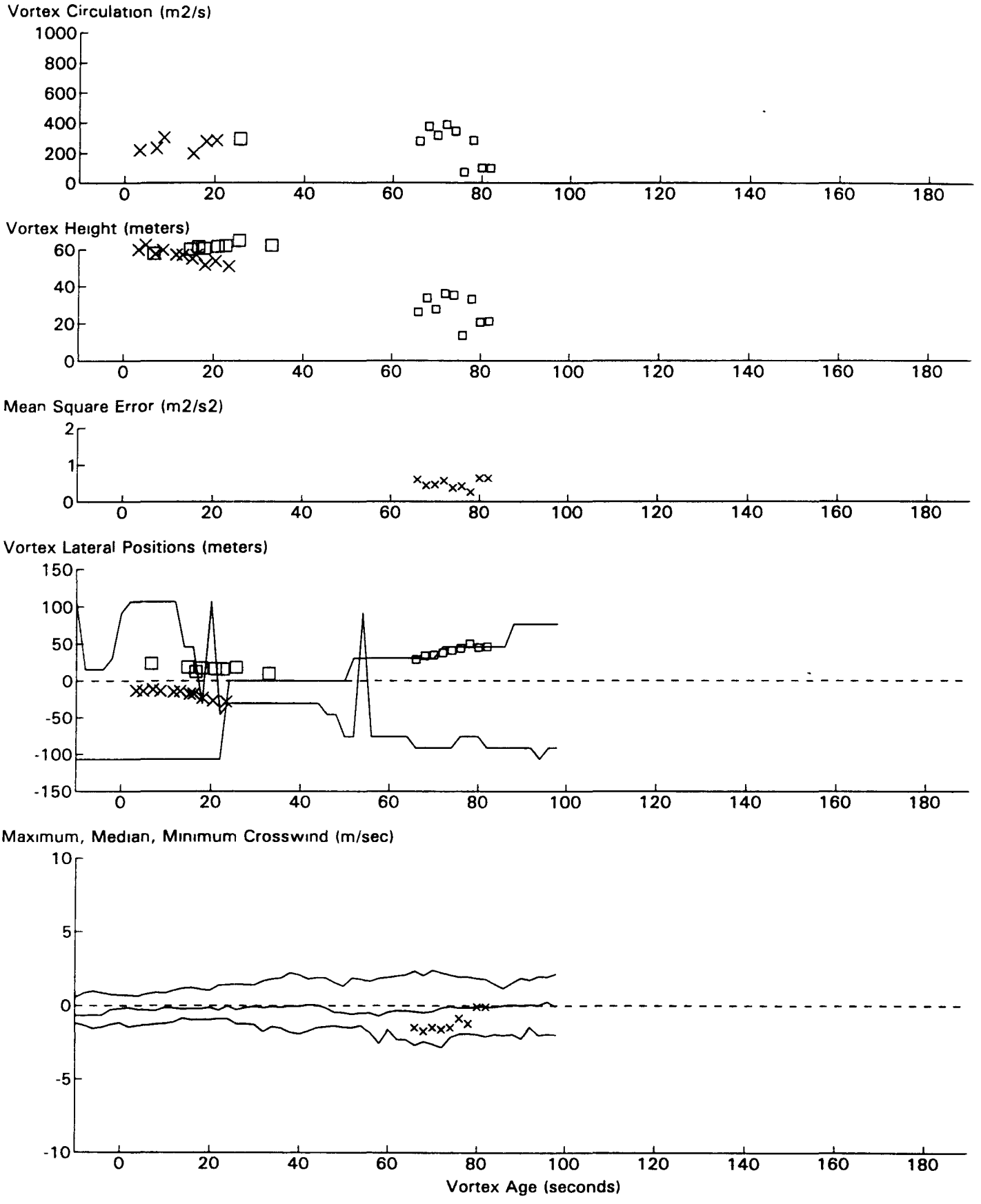

B767 JFK 31R GWVSS Data for File: I:RM11D13.077 11/13/96 19:8:56 dt= 42 CWturb=0.44

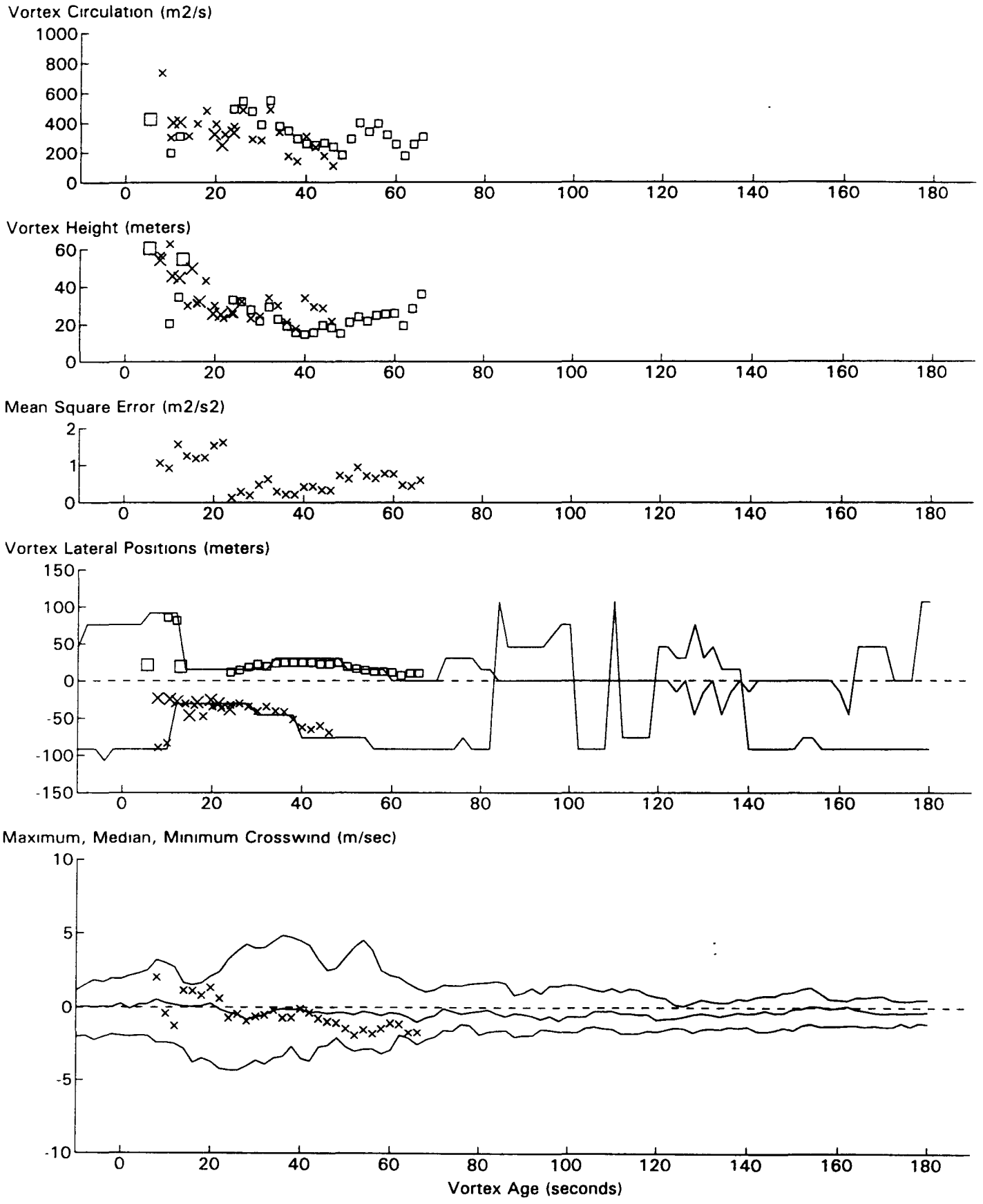

B767 JFK 31R GWVSS Data for File: I:RM11D13.078 11/13/96 19:10:33 dt= 45 CWturb=0.45

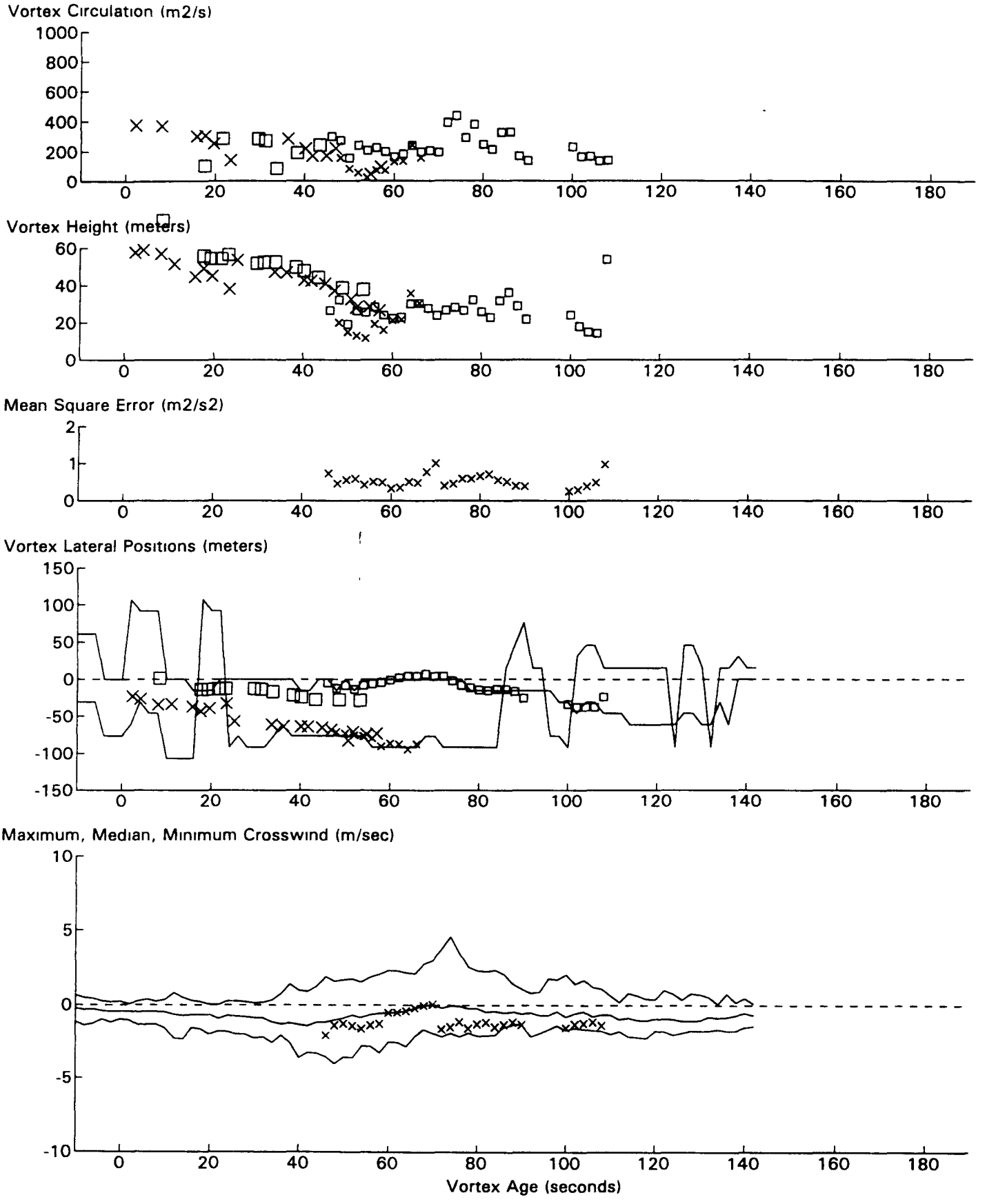

B767 JFK 31R GWVSS Data for File: I:RM11D13.079 11/13/96 19:19:8 dt= 44 CWturb=0.41

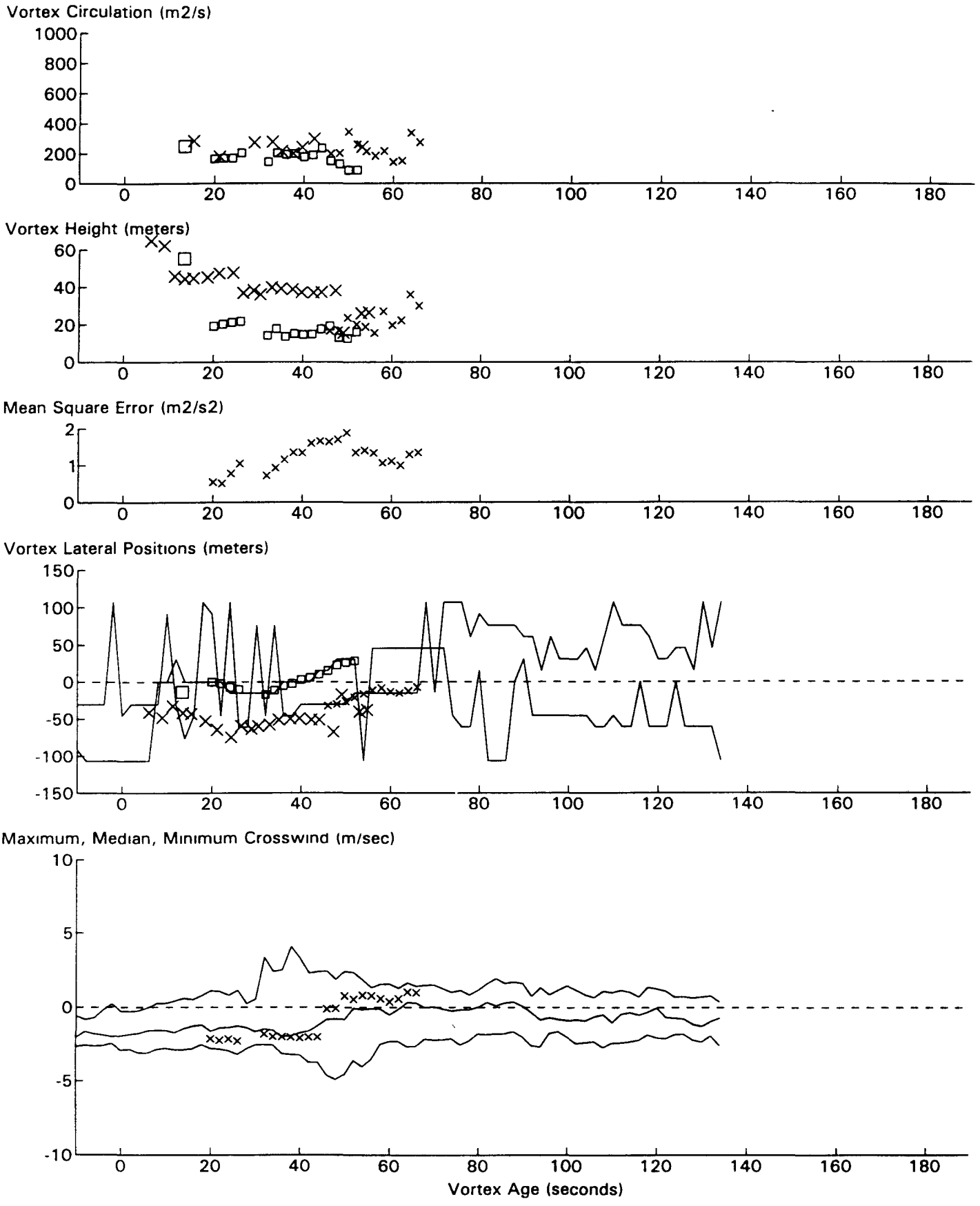

B767 JFK 31R GWVSS Data for File: I:RM11D13.081 11/13/96 19:24:4 dt= 43 CWturb=0.41

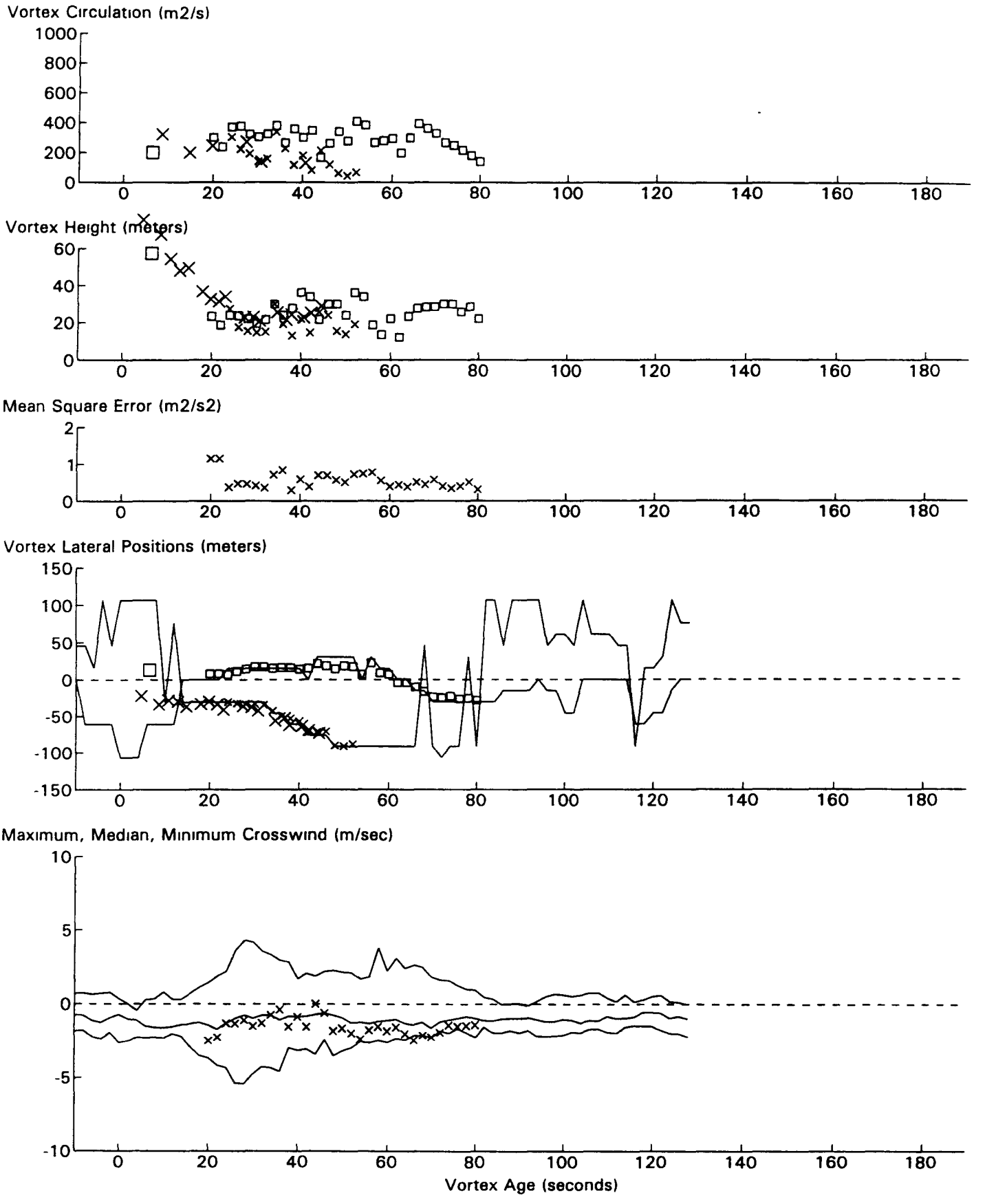

B757 JFK 31R GWVSS Data for File: I:RM11D13.082 11/13/96 19:26:18 dt= 43 CWturb=0.40

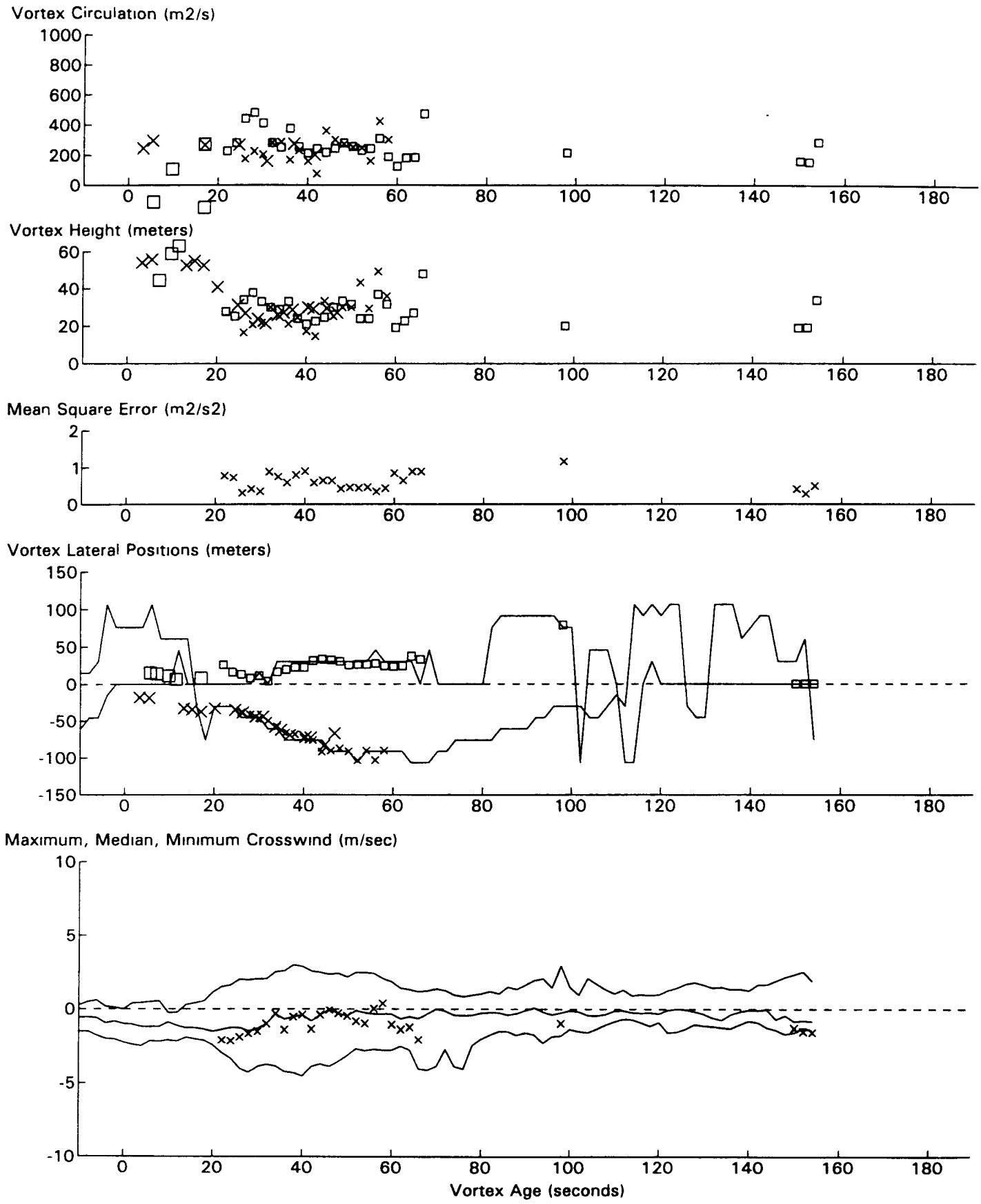

B767 JFK 31R GWVSS Data for File: I:RM11D13.083 11/13/96 19:28:26 dt= 43 CWturb=0.38

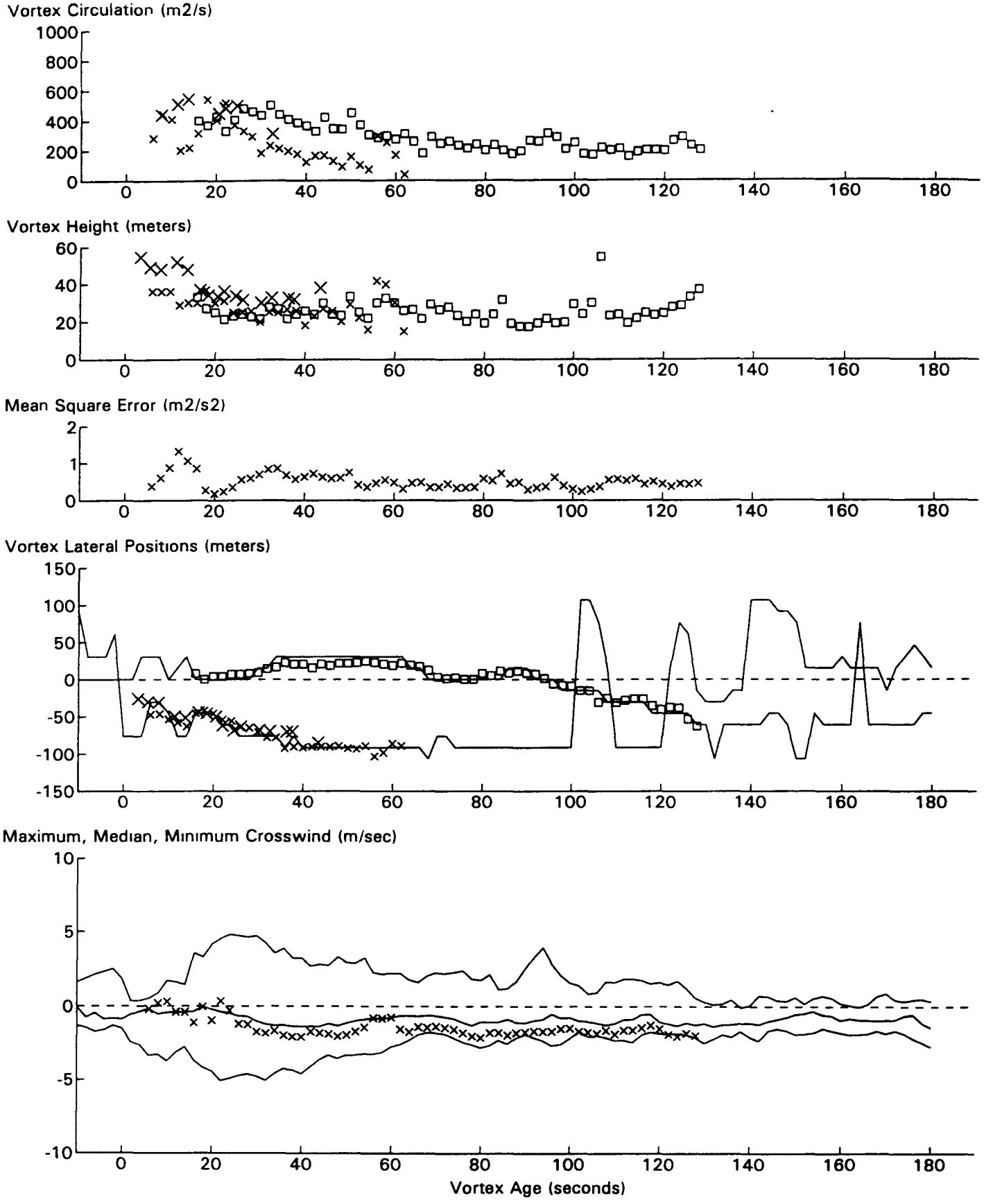

B747 JFK 31R GWVSS Data for File: I:RM11D13.084 11/13/96 19:31:0 dt= 43 CWturb=0.41

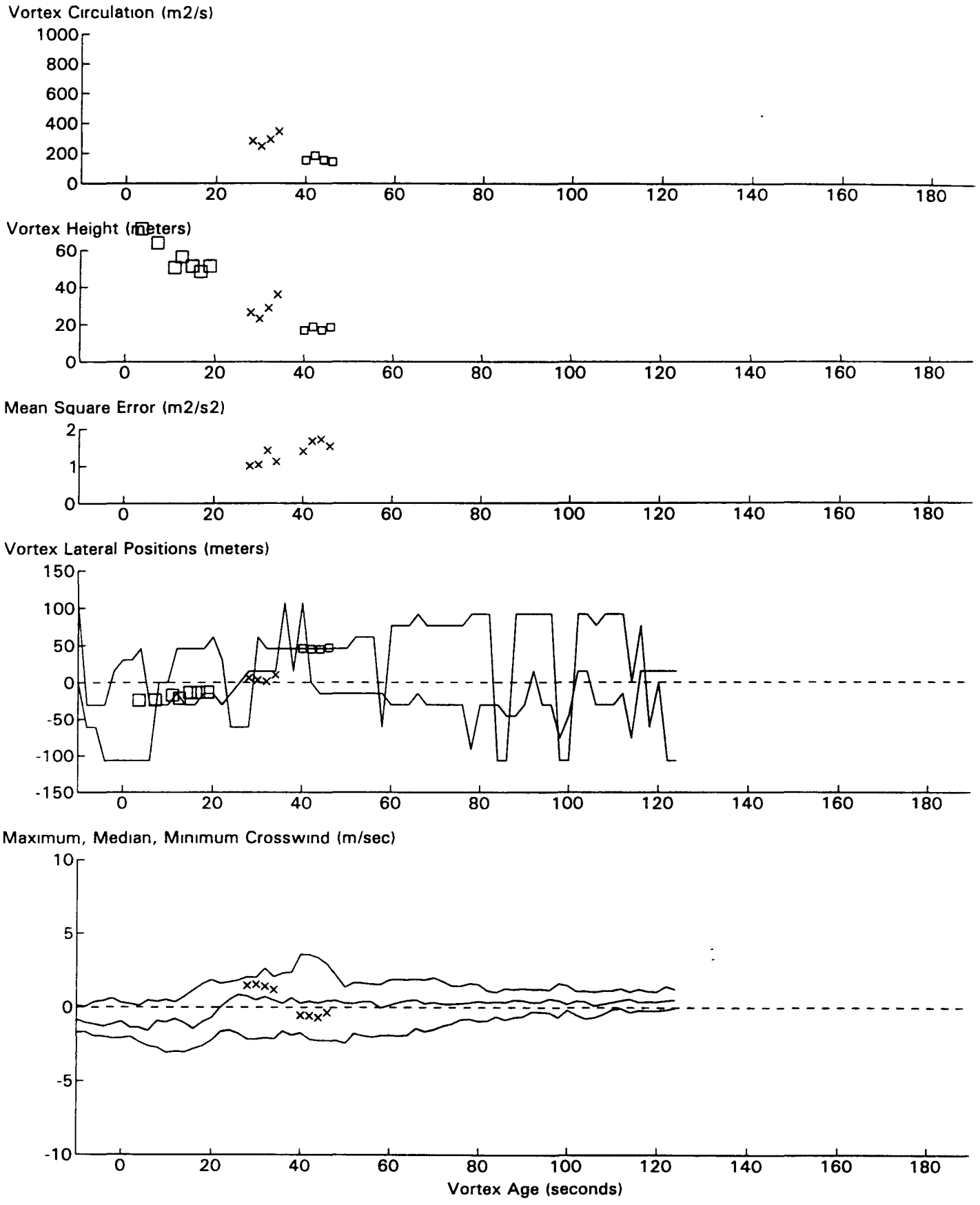

B767 JFK 31R GWVSS Data for File: I:RM11D13.099 11/13/96 20:6:7 dt= 42 CWturb=0.43

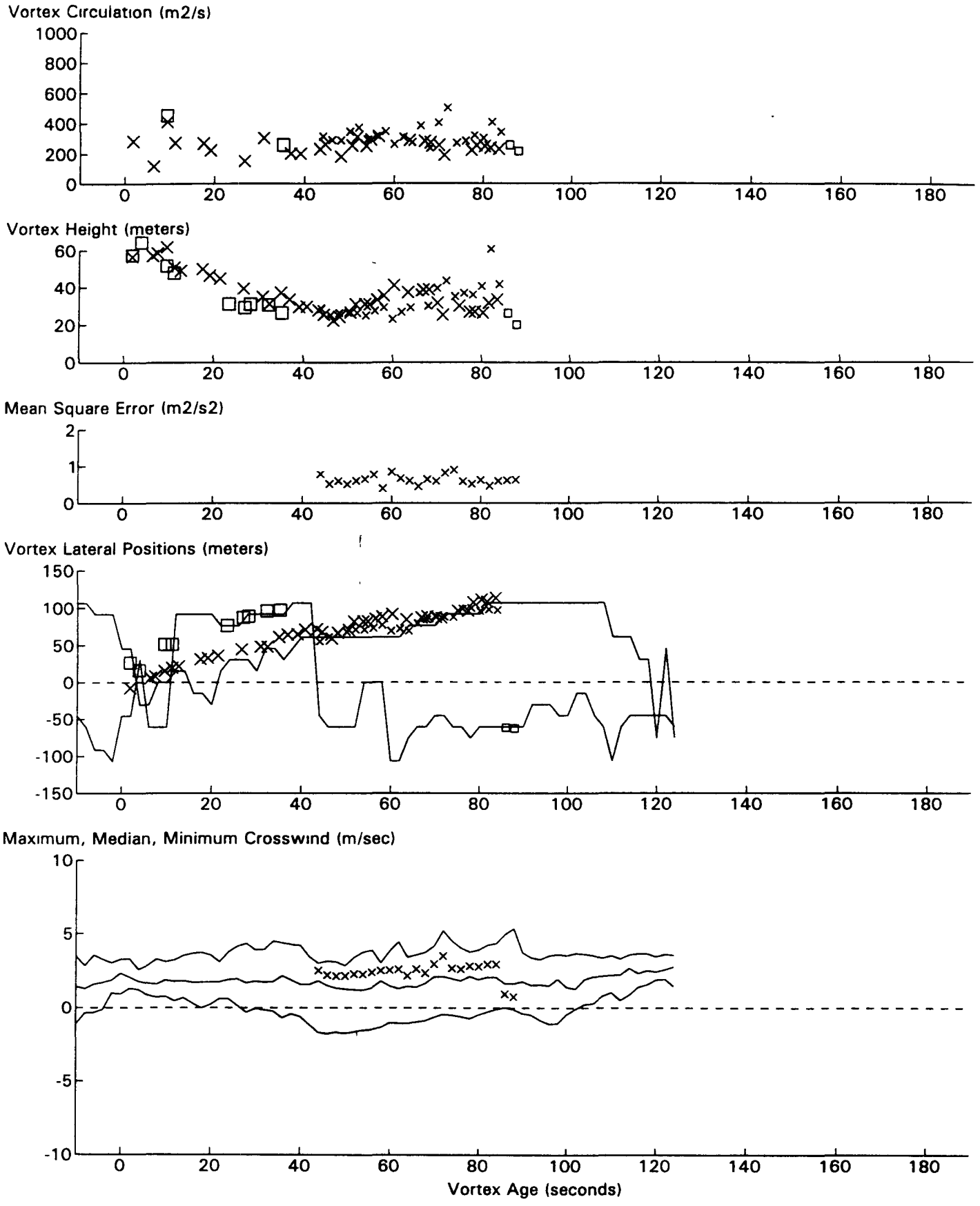

B767 JFK 31R GWVSS Data for File: I:RM11D13.112 11/13/96 20:32:48 dt= 42 CWturb=0.53

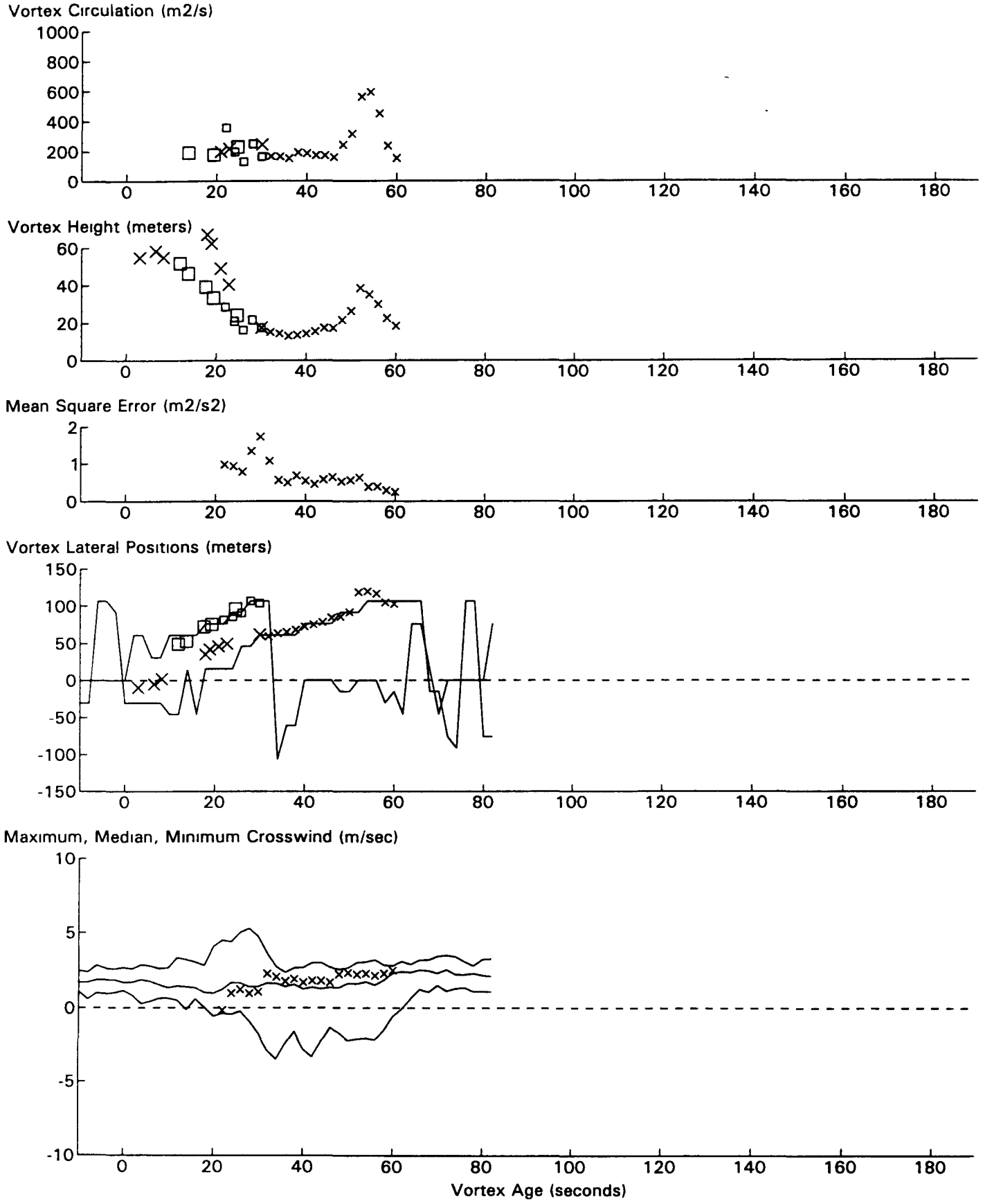

B767 JFK 31R GWVSS Data for File: I:RM11D13.114 11/13/96 20:36:47 dt= 42 CWturb=0.53

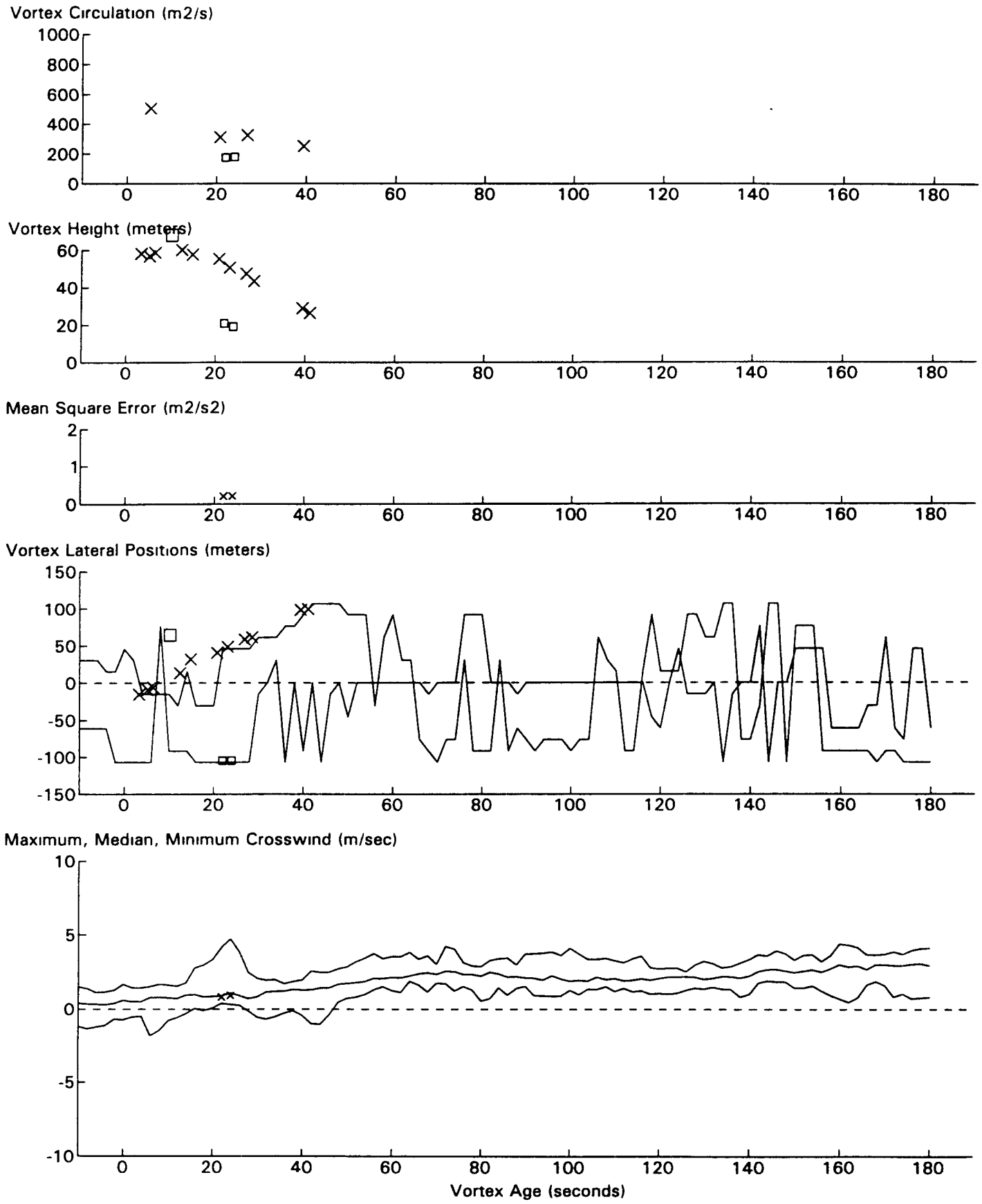

EA33 JFK 31R GWVSS Data for File: I:RM11D13.117 11/13/96 20:40:57 dt= 42 CWturb=0.52

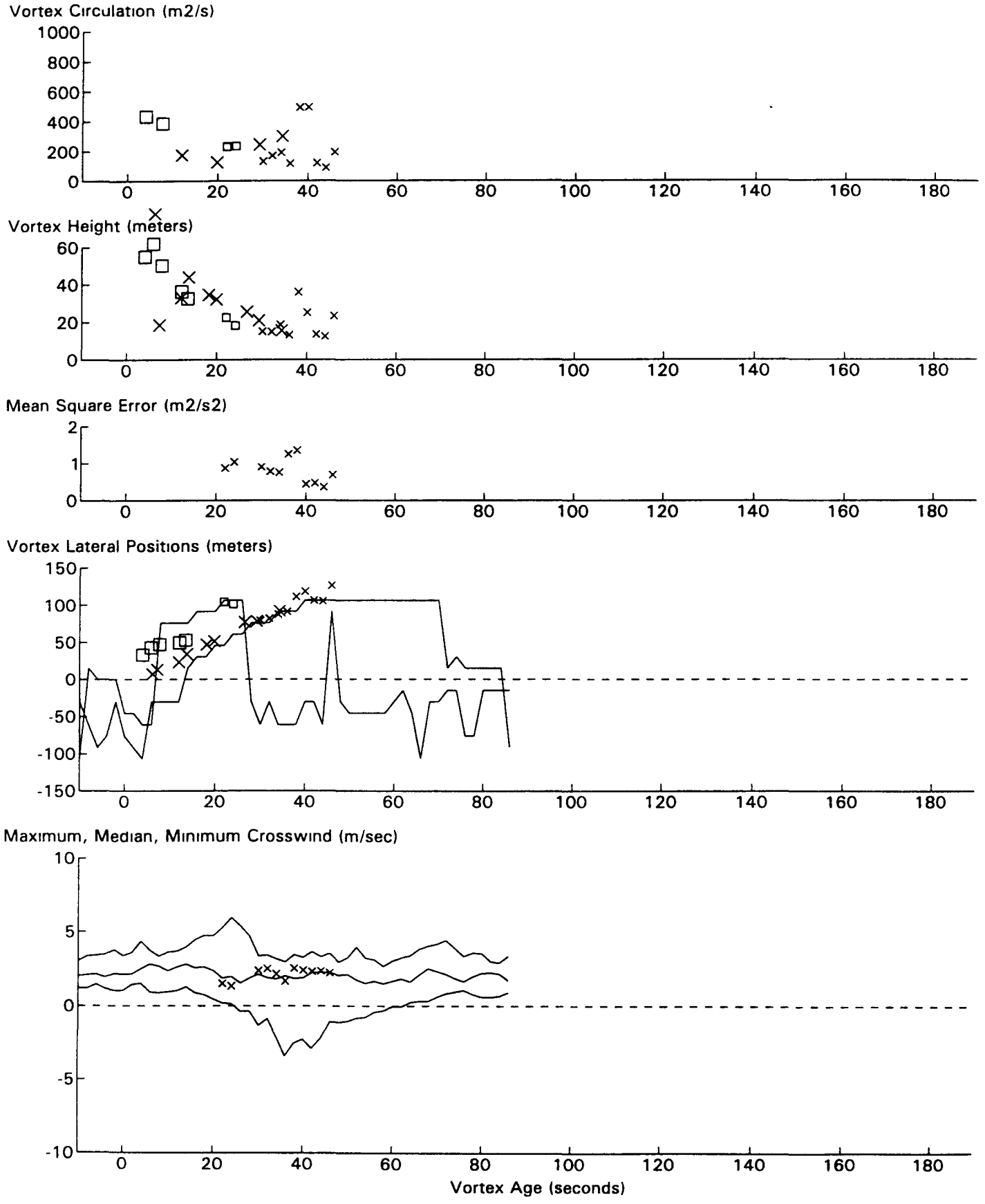

B767 JFK 31R GWVSS Data for File: I:RM11D13.126 11/13/96 20:56:10 dt= 41 CWturb=0.54

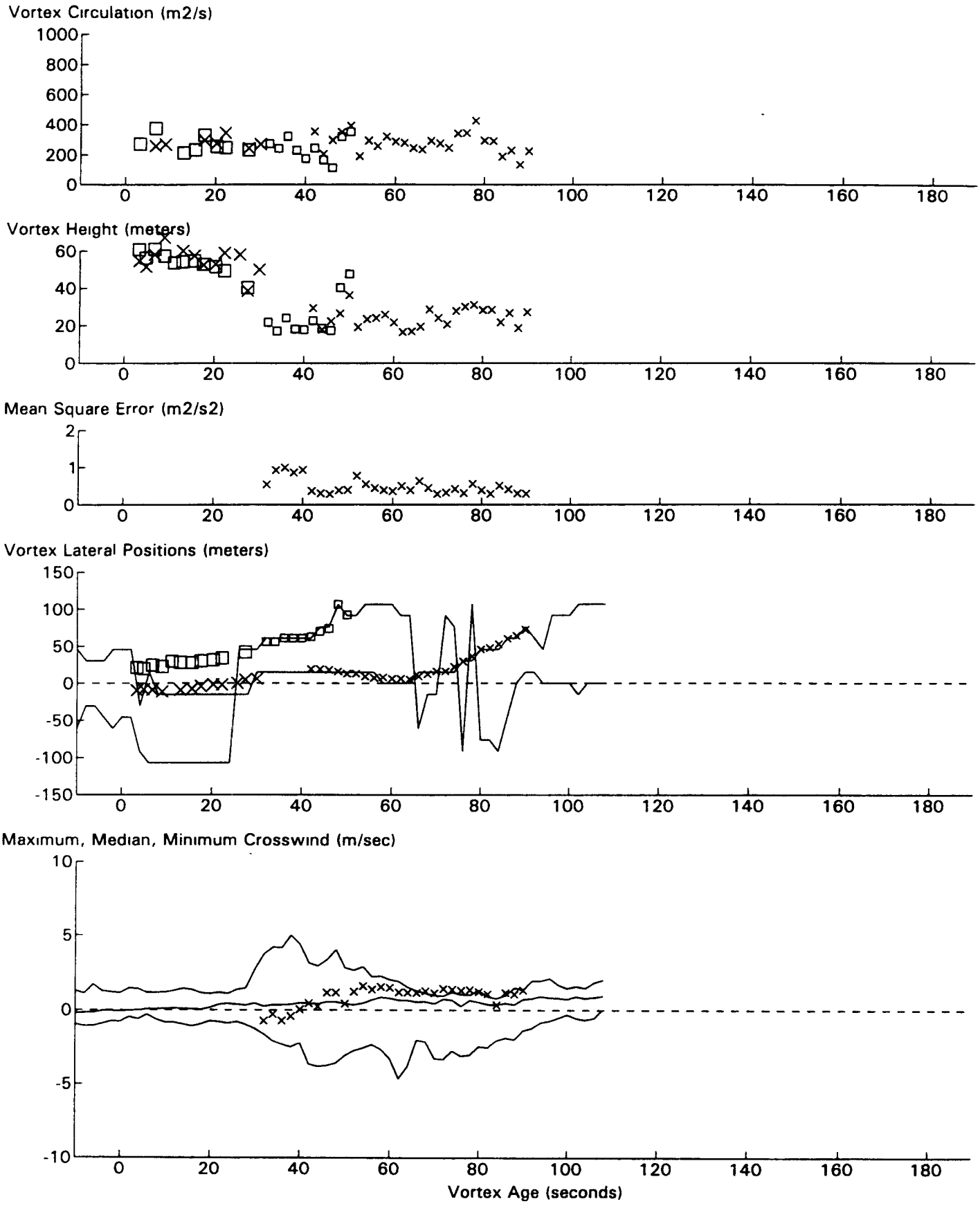

B767 JFK 31R GWVSS Data for File: I:RM11D13.132 11/13/96 21:9:6 dt= 42 CWturb=0.50

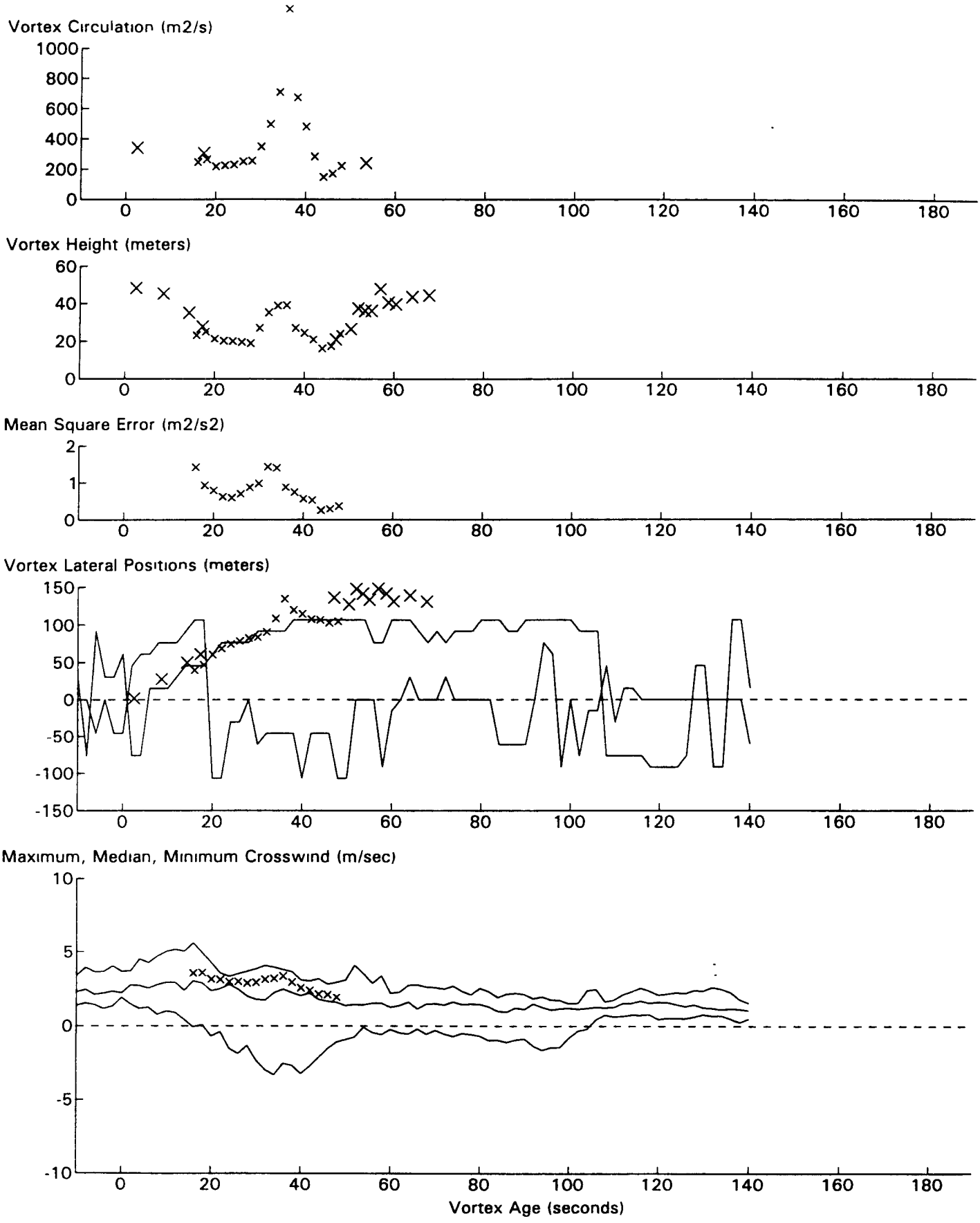

DC10 JFK 31R GWVSS Data for File: I:RM11D13.134 11/13/96 21:15:8 dt= 40 CWturb=0.39

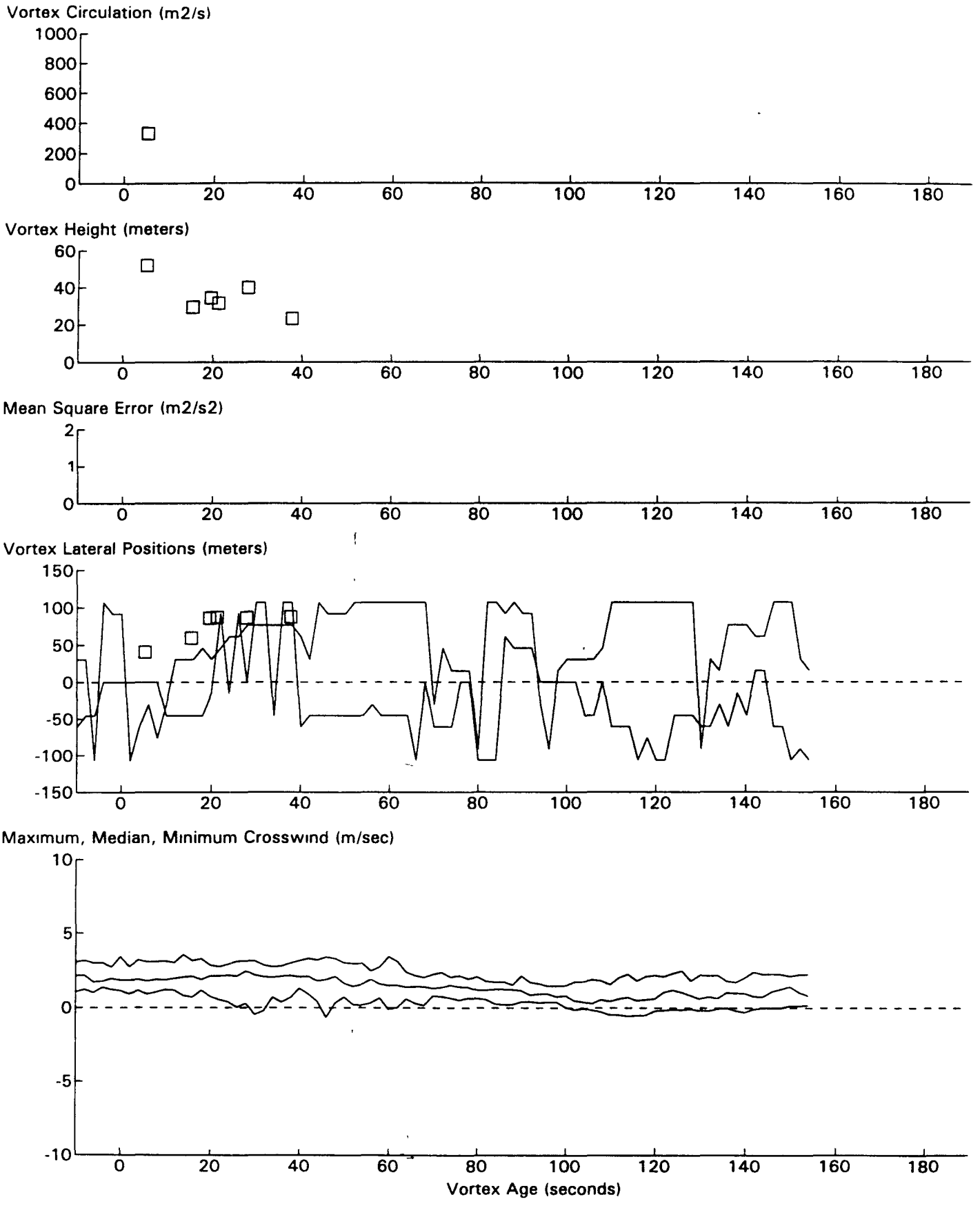

DC9 JFK 31R GWVSS Data for File: I:RM11D13.137 11/13/96 21:21:11 dt= 40 CWturb=0.43

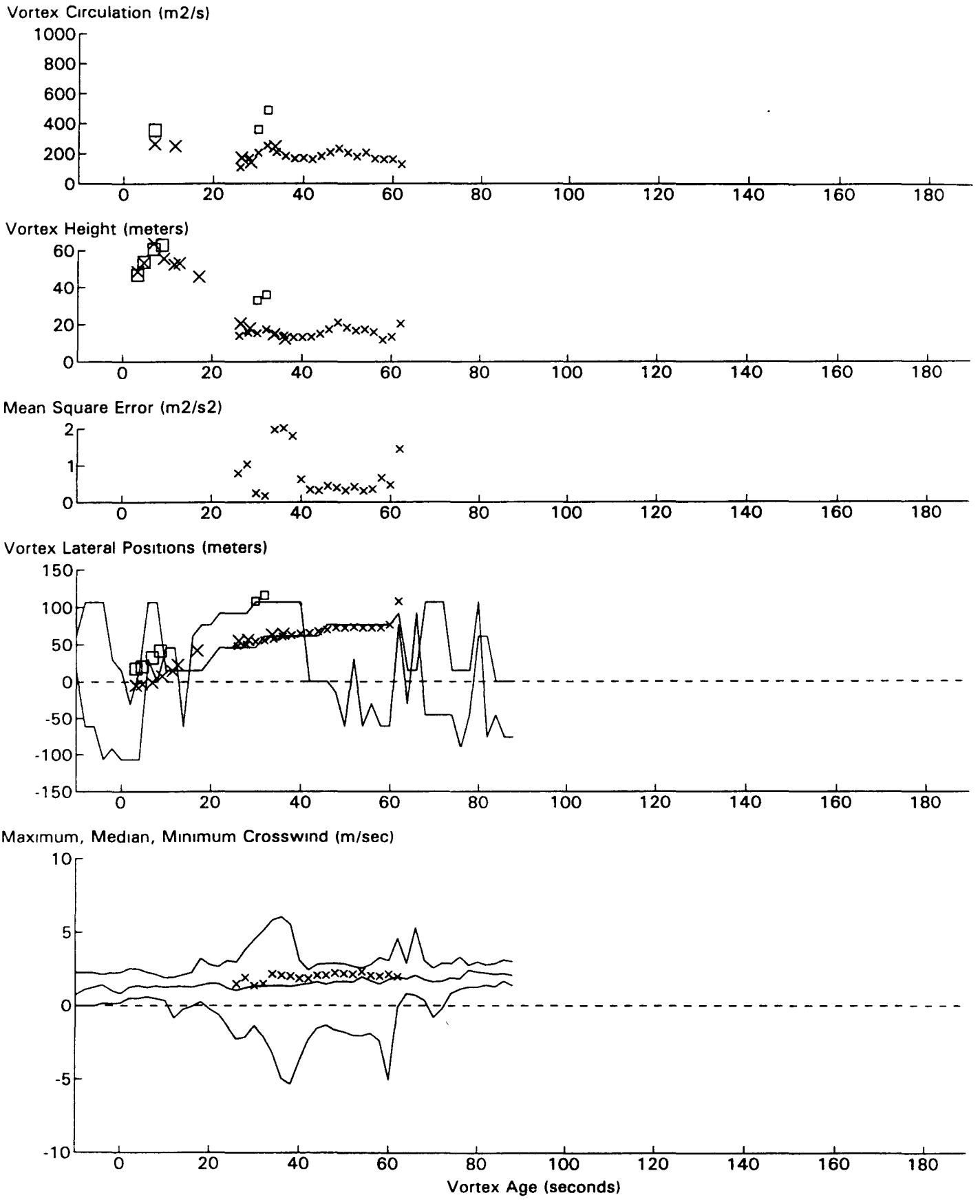

B727 JFK 31R GWVSS Data for File: I:RM11D13.138 11/13/96 21:23:45 dt= 39 CWturb=0.42

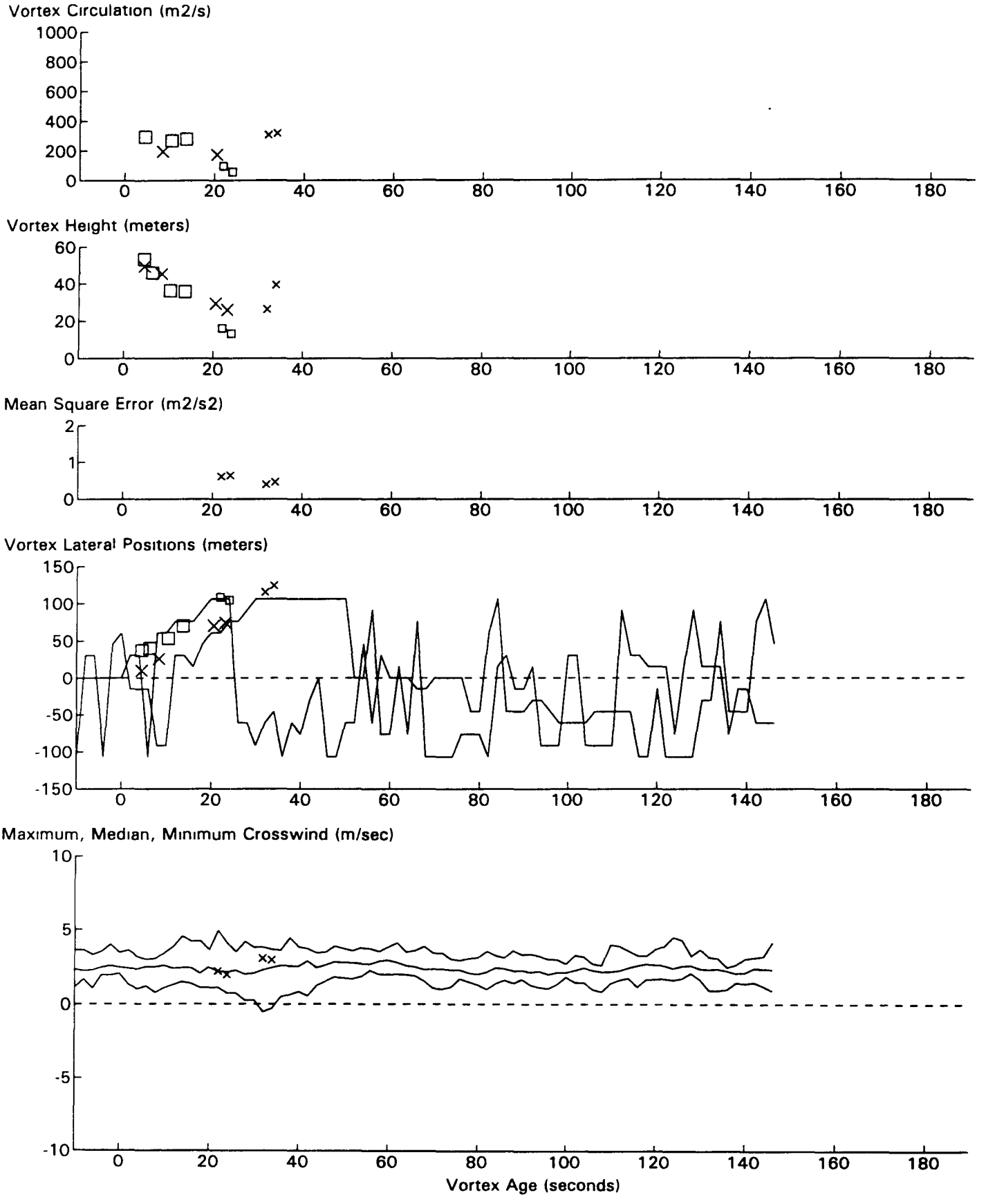

B727 JFK 31R GWVSS Data for File: I:RM11D13.140 11/13/96 21:26:39 dt= 39 CWturb=0.45

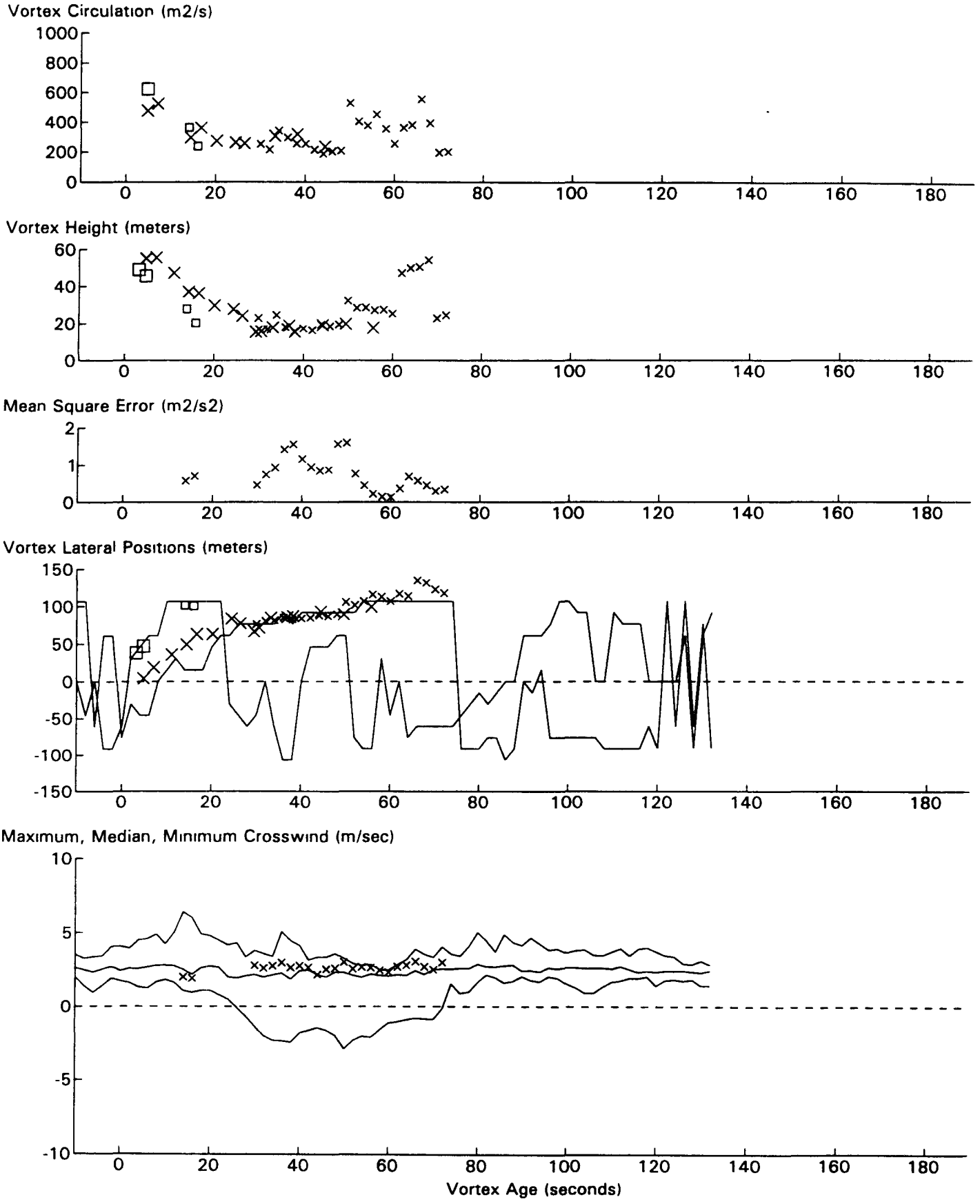

B747 JFK 31R GWVSS Data for File: I:RM11D13.144 11/13/96 21:37:45 dt= 40 CWturb=0.58

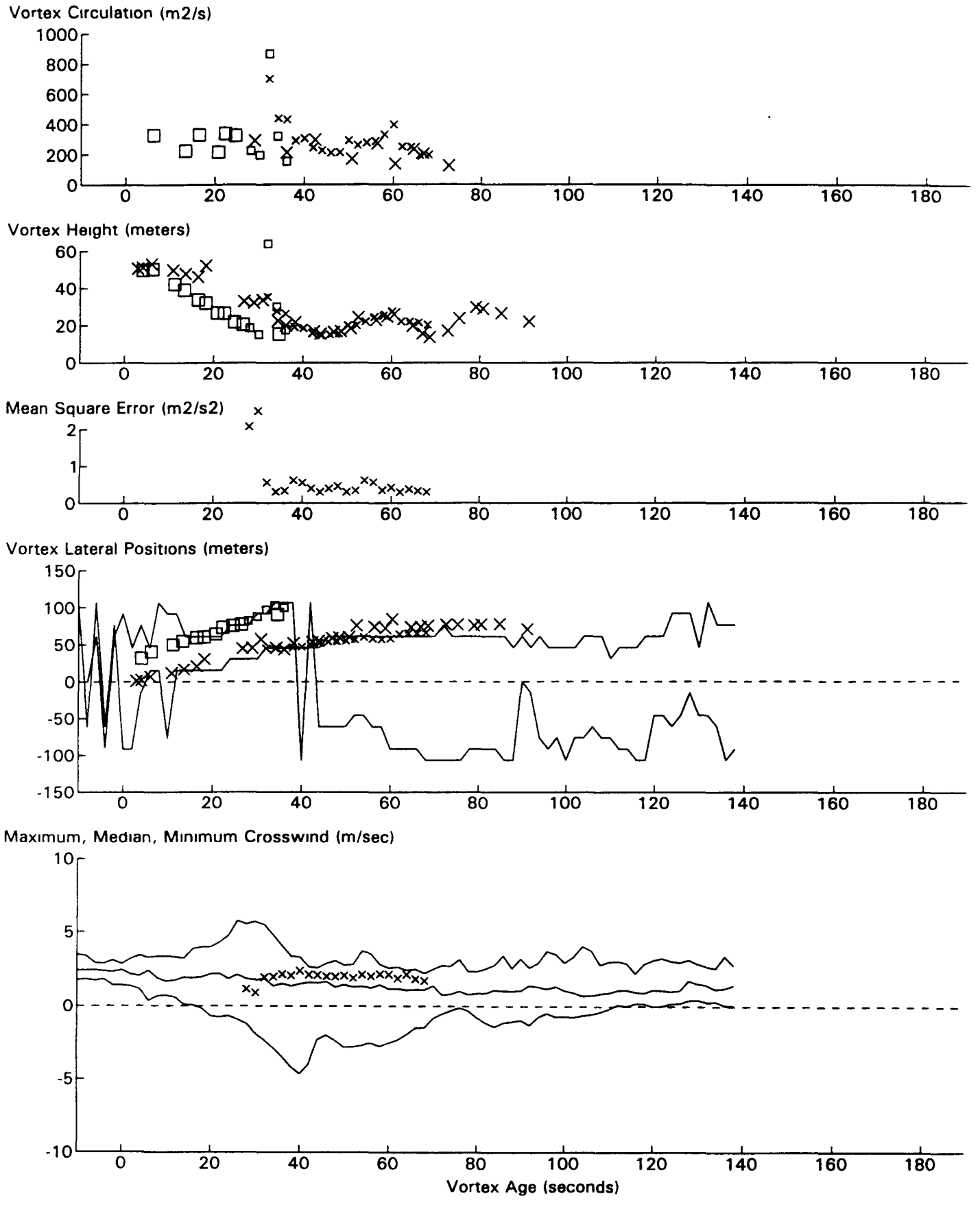

EA30 JFK 31R GWVSS Data for File: I:RM11D13.145 11/13/96 21:39:57 dt= 40 CWturb=0.61

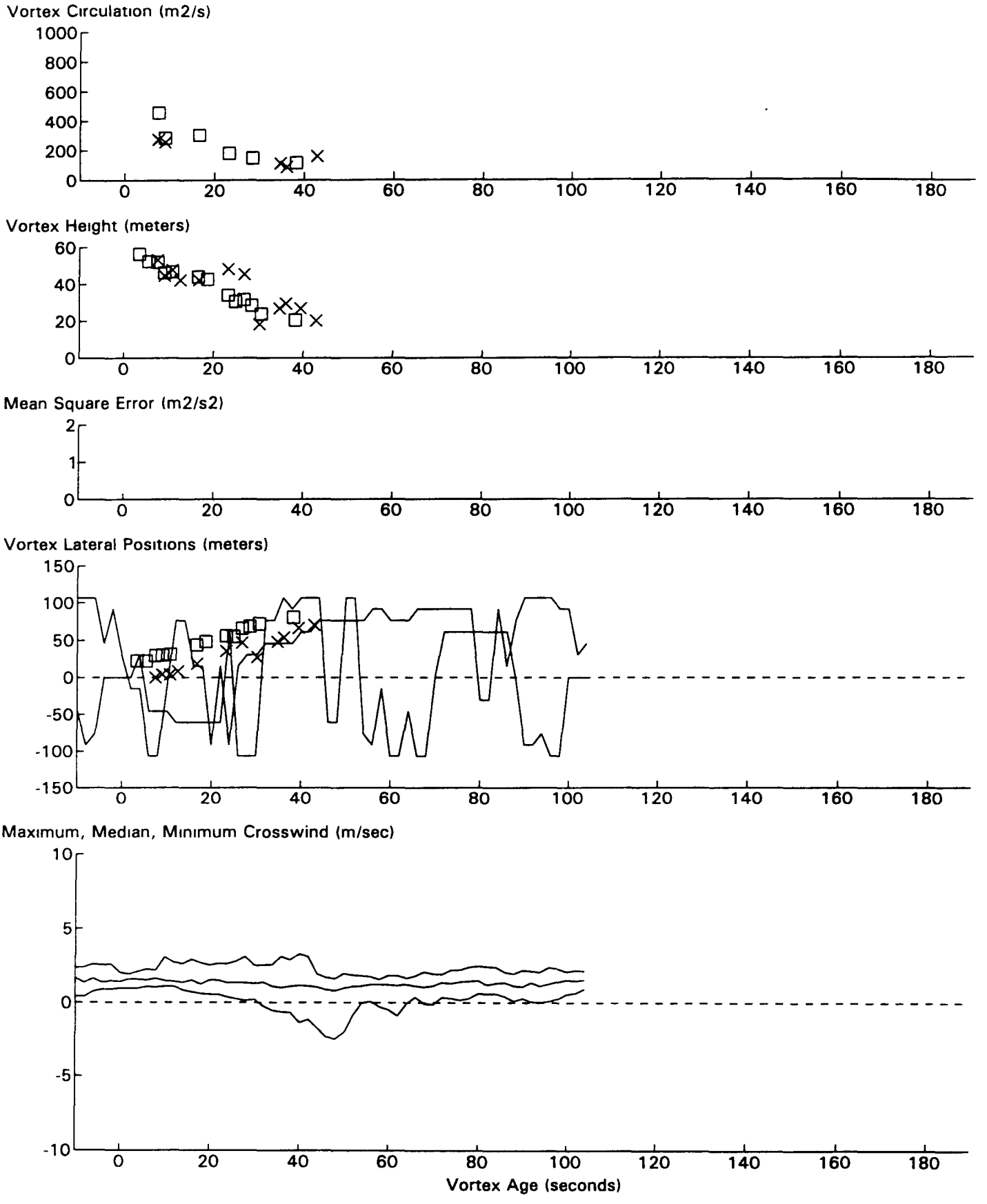

MD80 JFK 31R GWVSS Data for File: I:RM11D13.147 11/13/96 21:43:37 dt= 39 CWturb=0.57

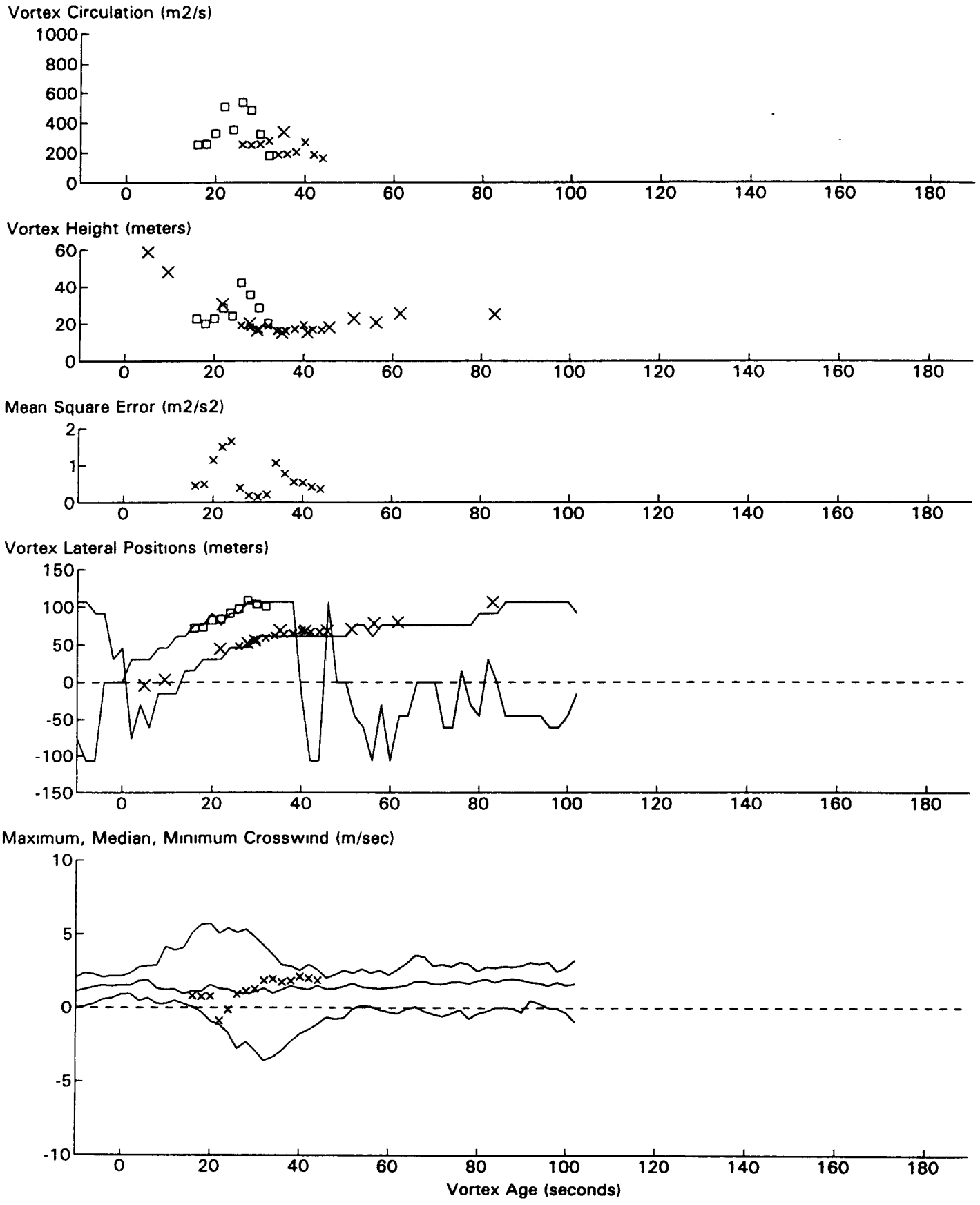

EA30 JFK 31R GWVSS Data for File: I:RM11D13.148 11/13/96 21:45:21 dt= 39 CWturb=0.52

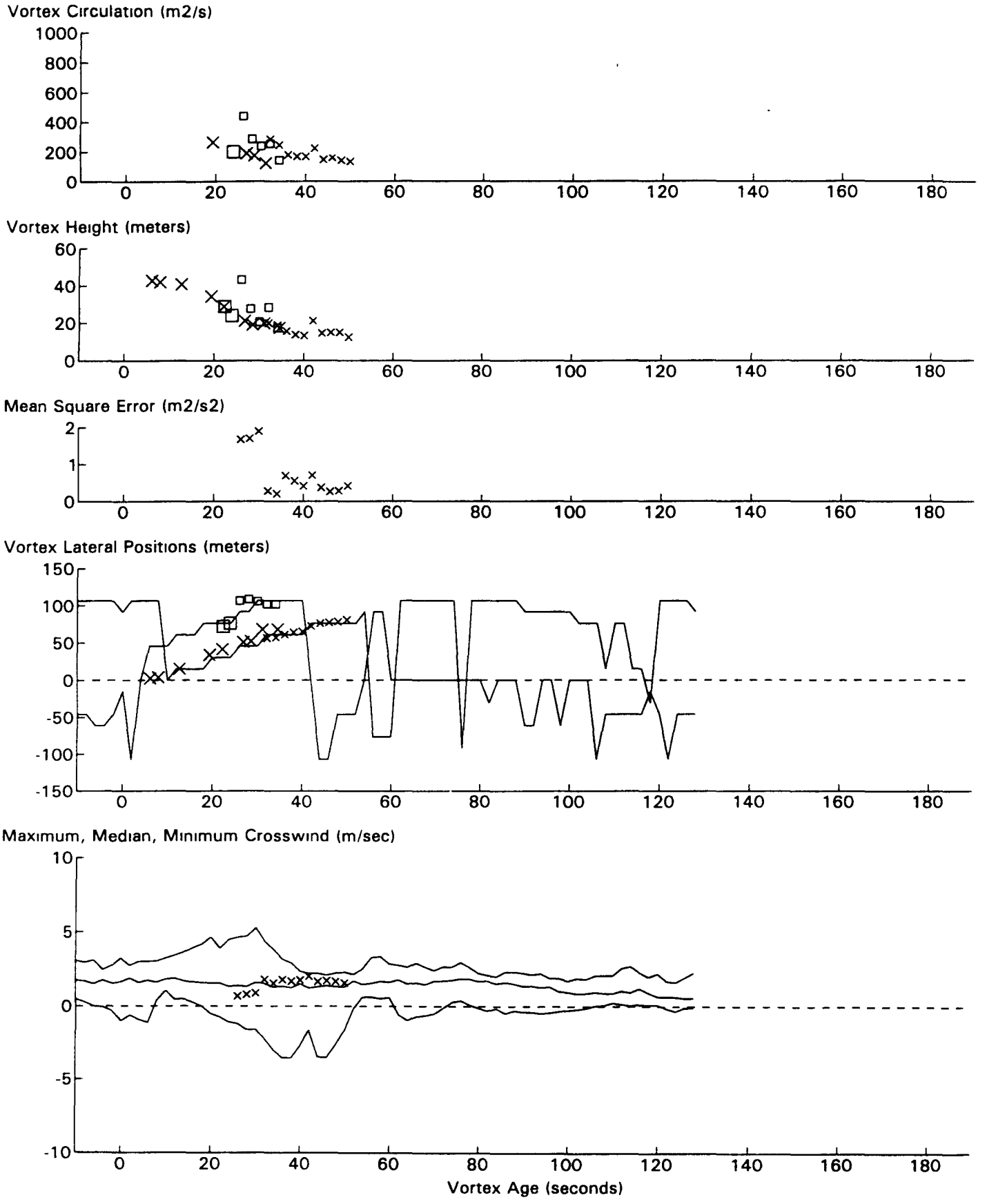

DC8 JFK 31R GWVSS Data for File: I:RM11D13.149 11/13/96 21:47:3 dt= 40 CWturb=0.53

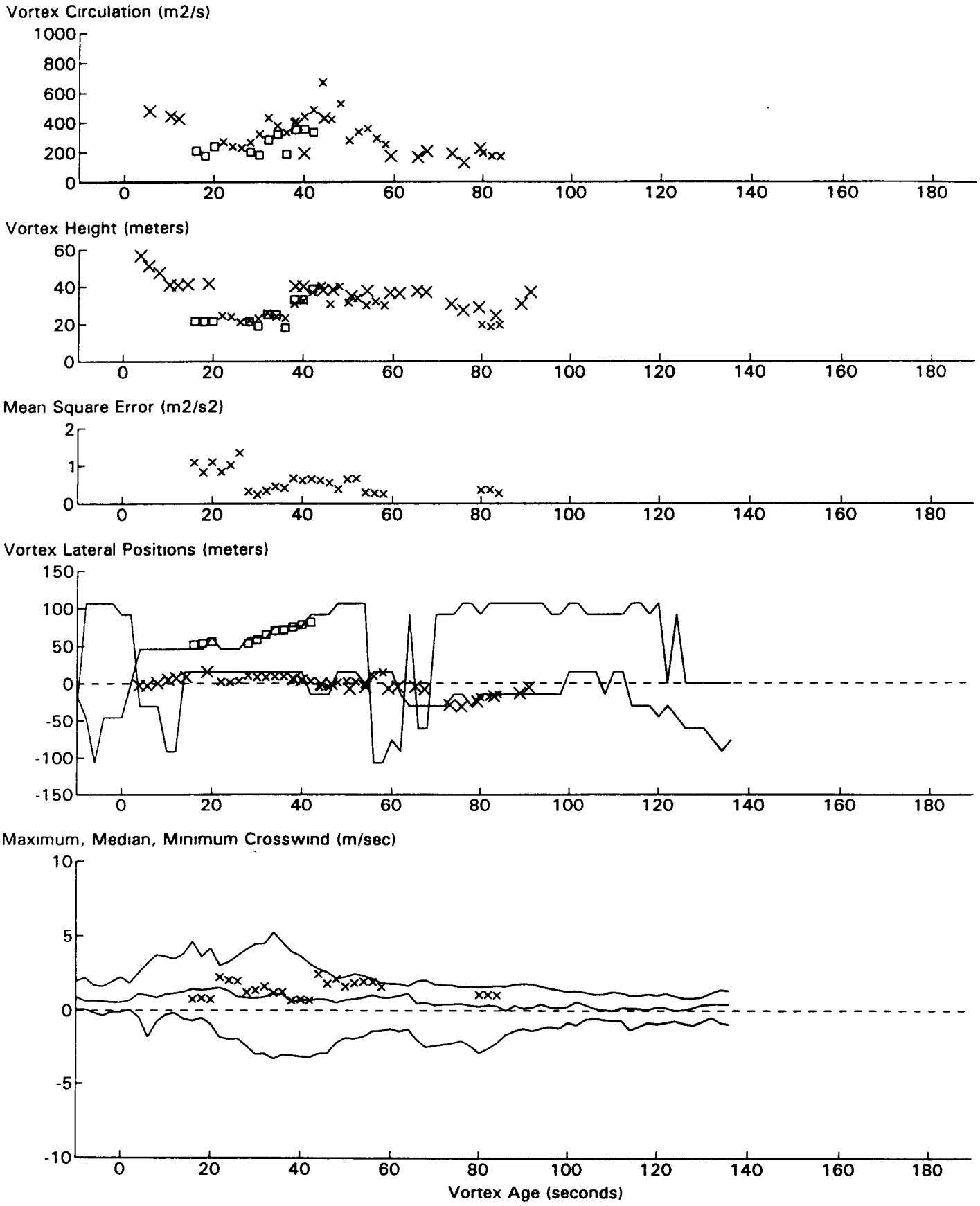

B747 JFK 31R GWVSS Data for File: I:RM11D13.150 11/13/96 21:49:11 dt= 40 CWturb=0.52

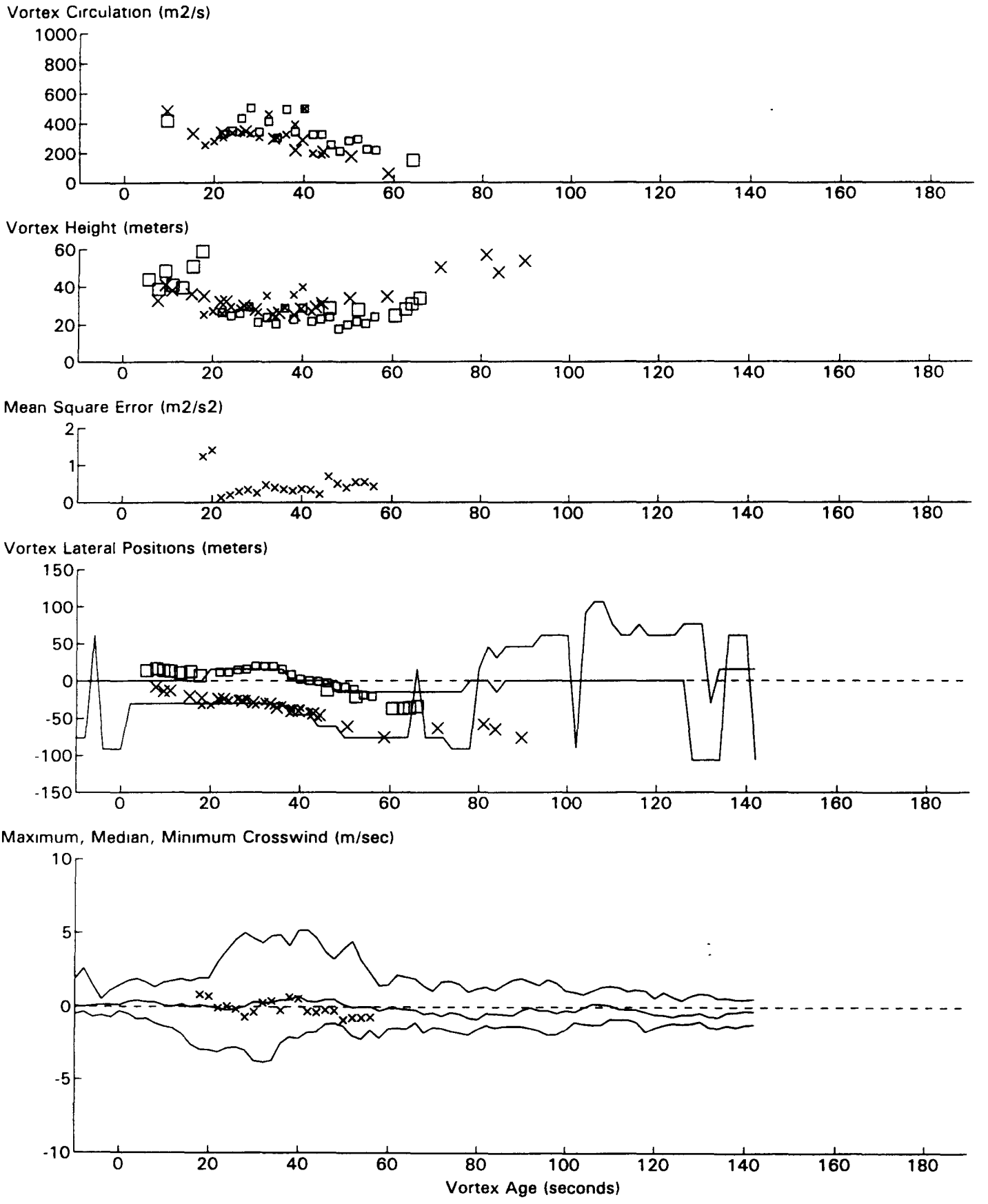

B767 JFK 31R GWVSS Data for File: I:RM11D13.152 11/13/96 21:52:41 dt= 40 CWturb=0.44

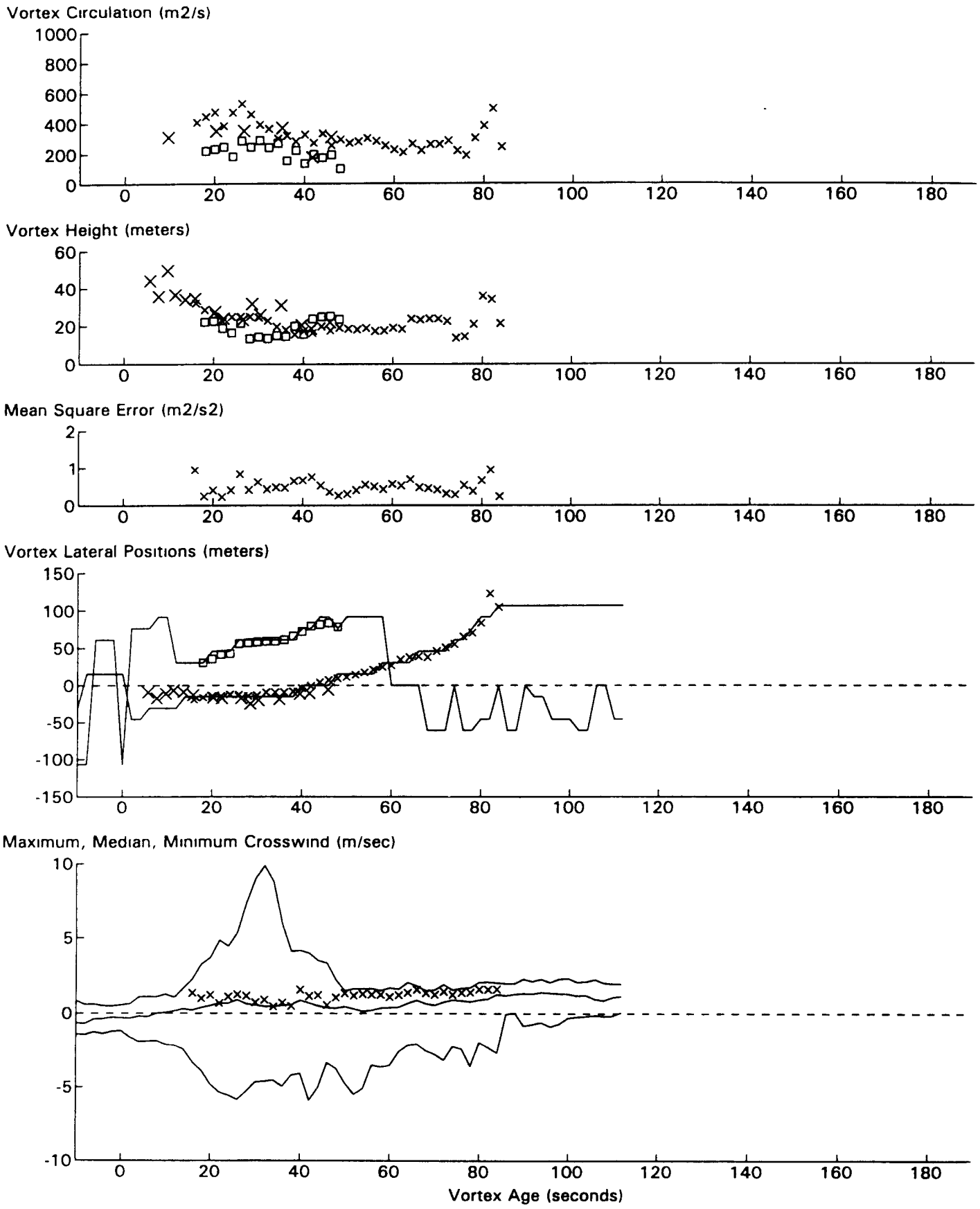

B767 JFK 31R GWVSS Data for File: I:RM11D13.153 11/13/96 21:55:3 dt= 40 CWturb=0.39

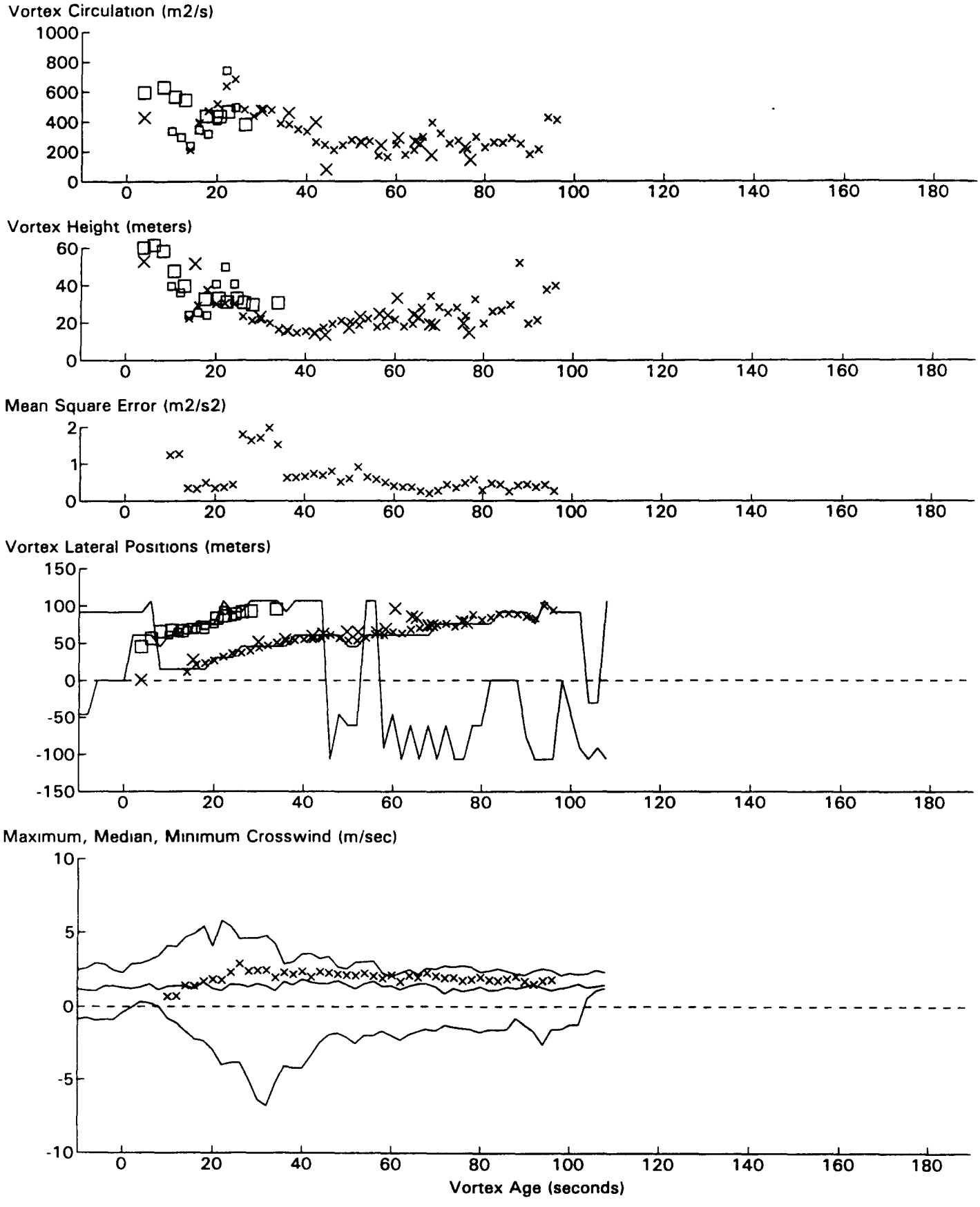

B747 JFK 31R GWVSS Data for File: I:RM11D13.156 11/13/96 21:59:55 dt= 39 CWturb=0.38

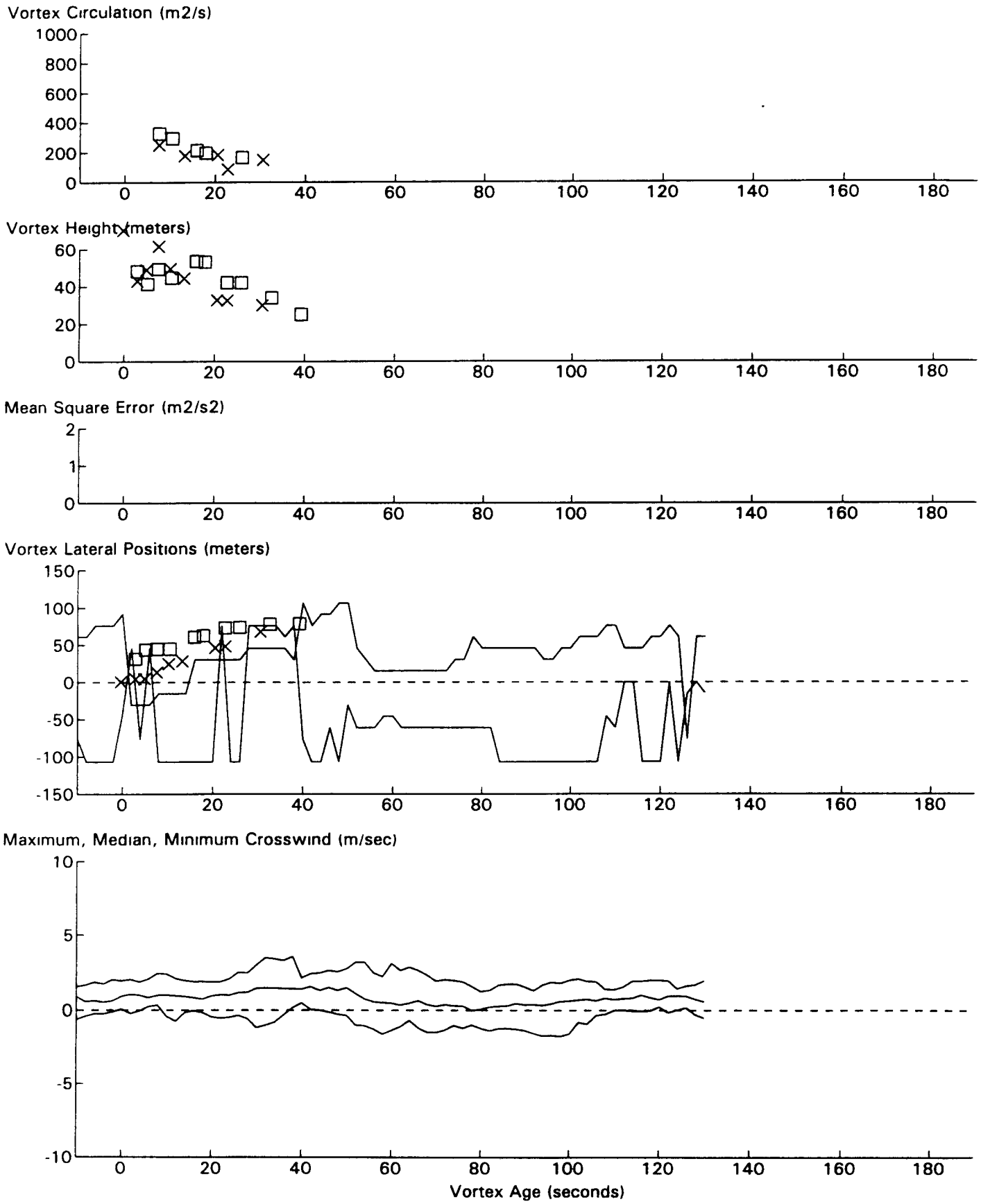

B767 JFK 31R GWVSS Data for File: I:RM11D13.158 11/13/96 22:4:4 dt= 38 CWturb=0.37

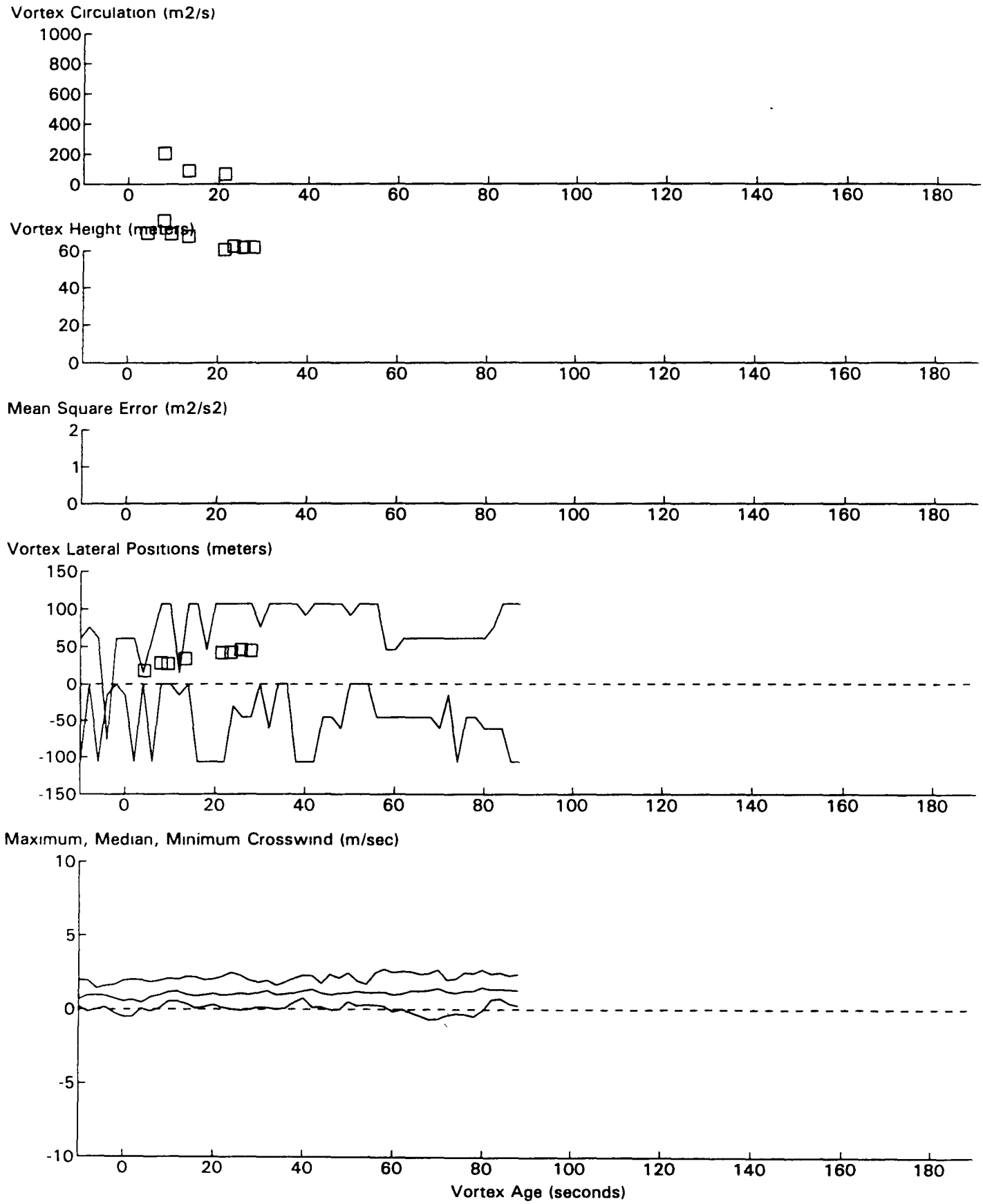

Prop JFK 31R GWVSS Data for File: I:RM11D13.159 11/13/96 22:6:14 dt= 39 CWturb=0.36

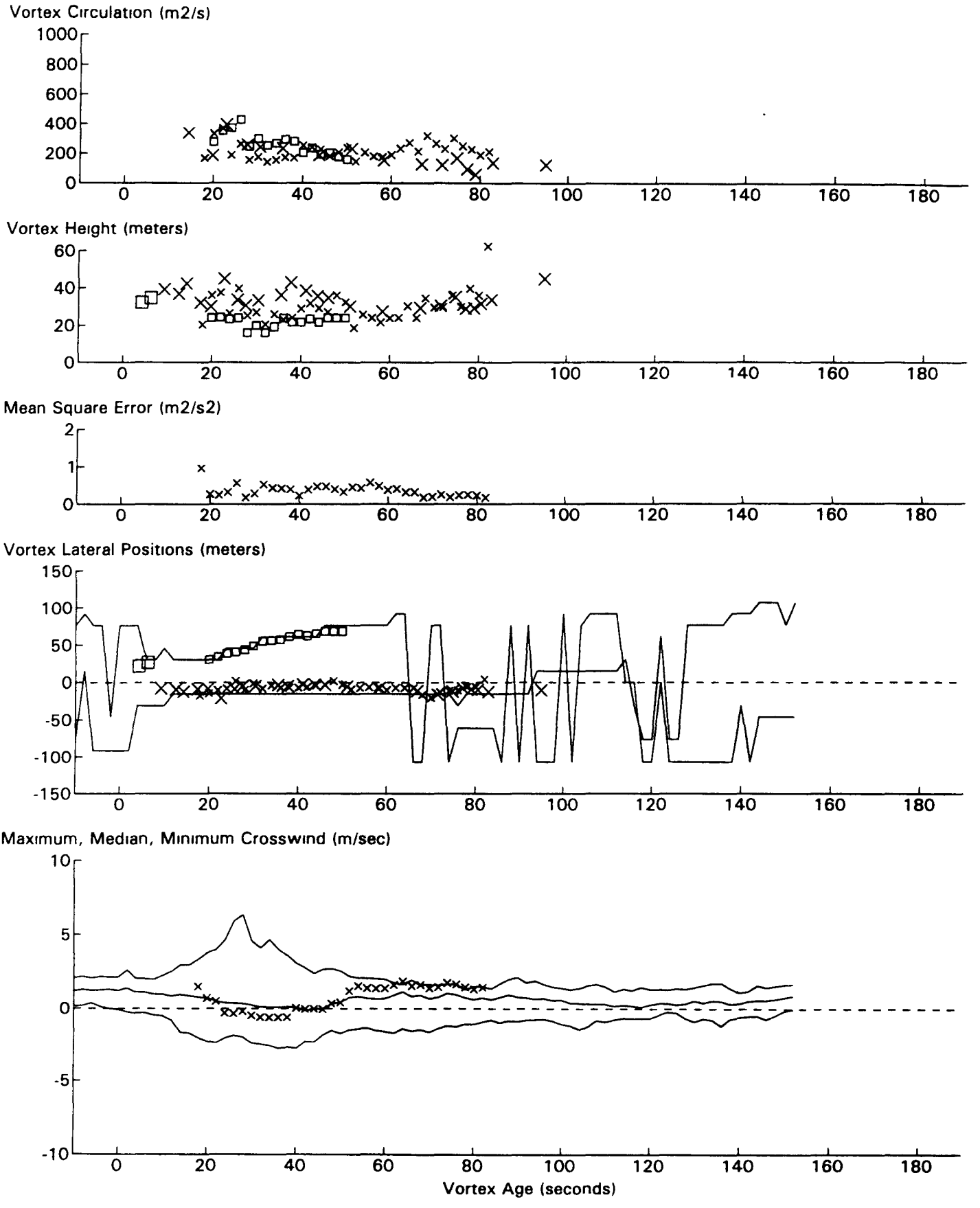

L101 JFK 31R GWVSS Data for File: I:RM11D13.162 11/13/96 22:11:46 dt= 38 CWturb=0.38

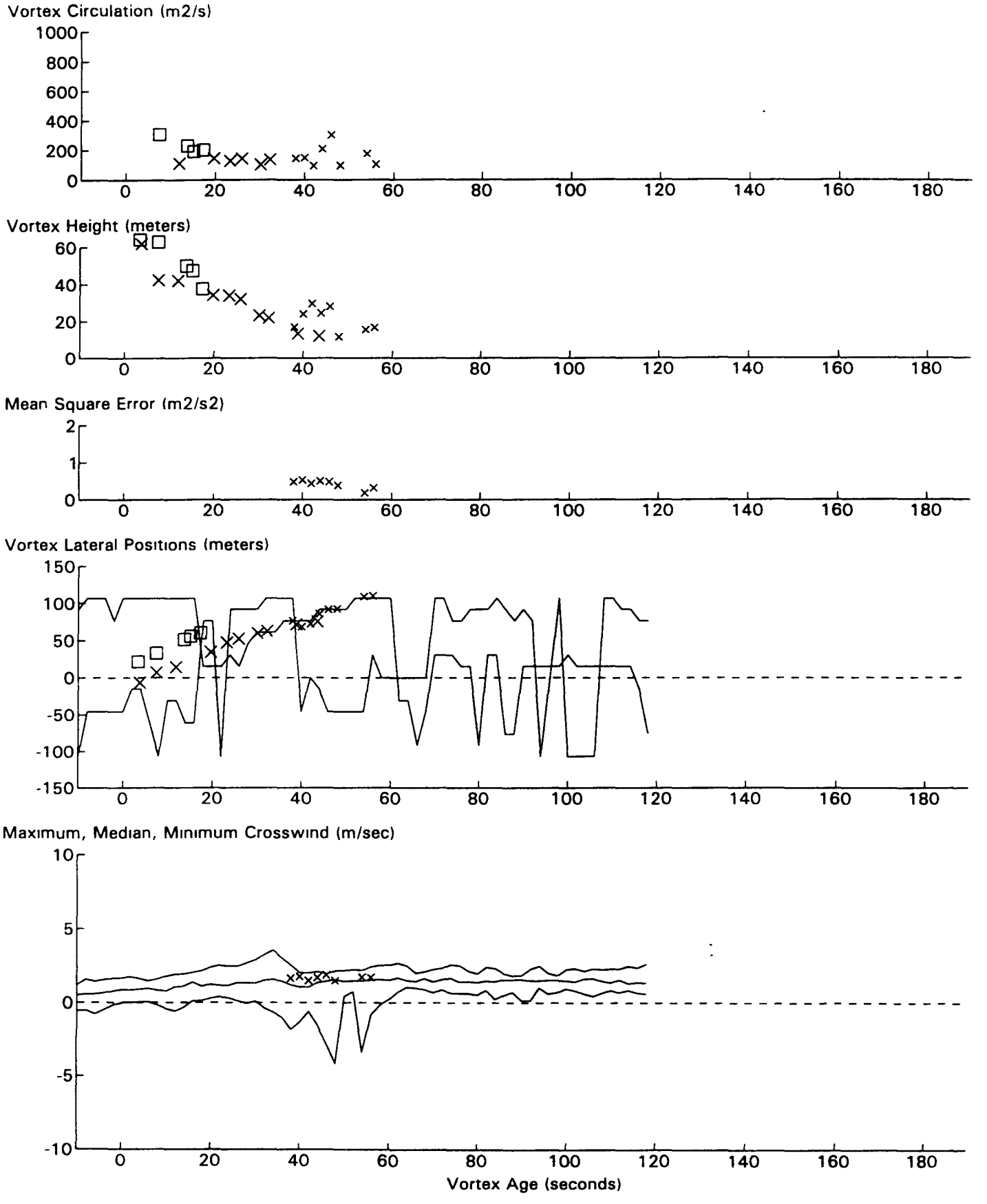

L101 JFK 31R GWVSS Data for File: I:RM11D13.163 11/13/96 22:14:18 dt= 39 CWturb=0.37

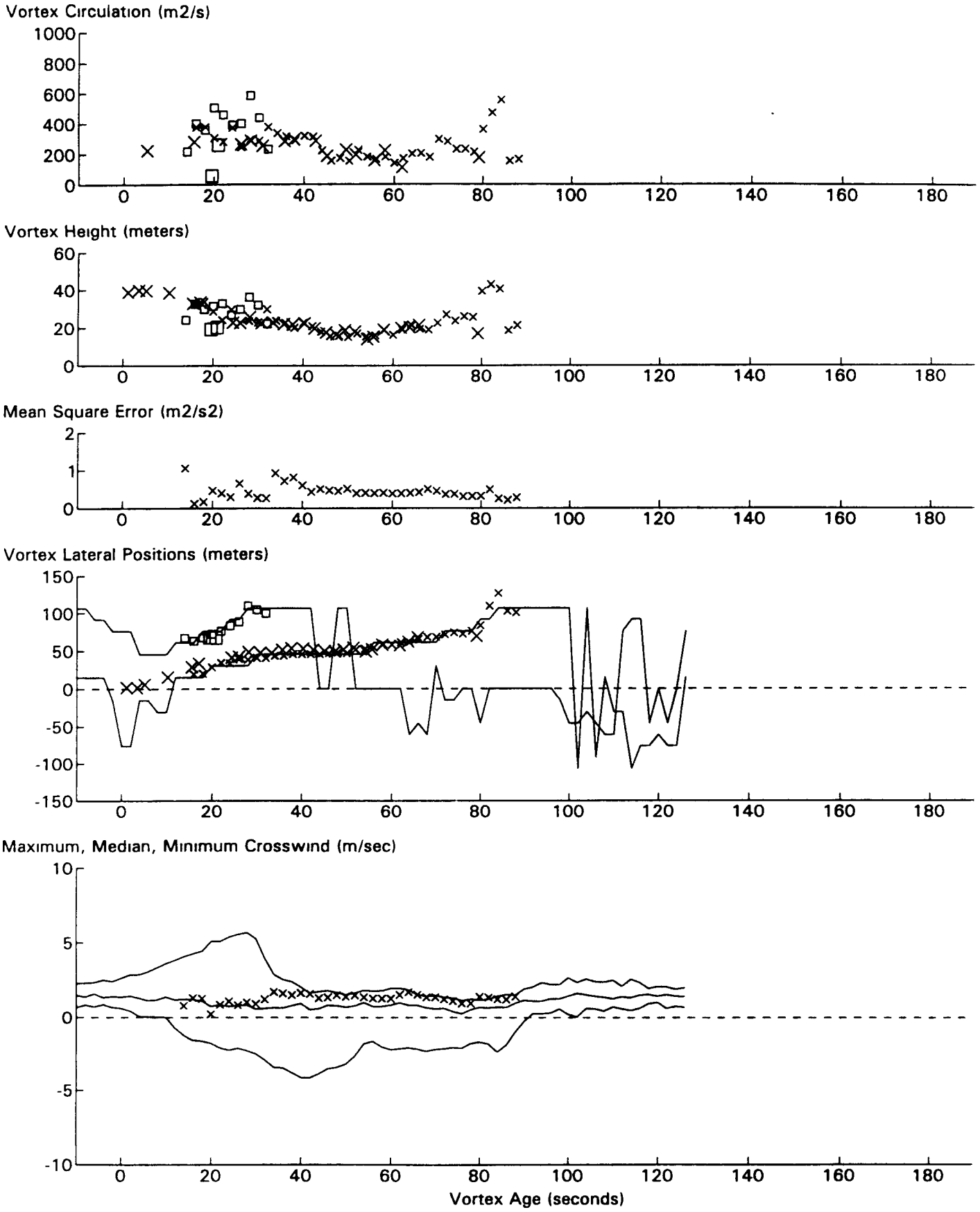

DC10 JFK 31R GWVSS Data for File: I:RM11D13.164 11/13/96 22:16:16 dt= 0 CWturb=0.35

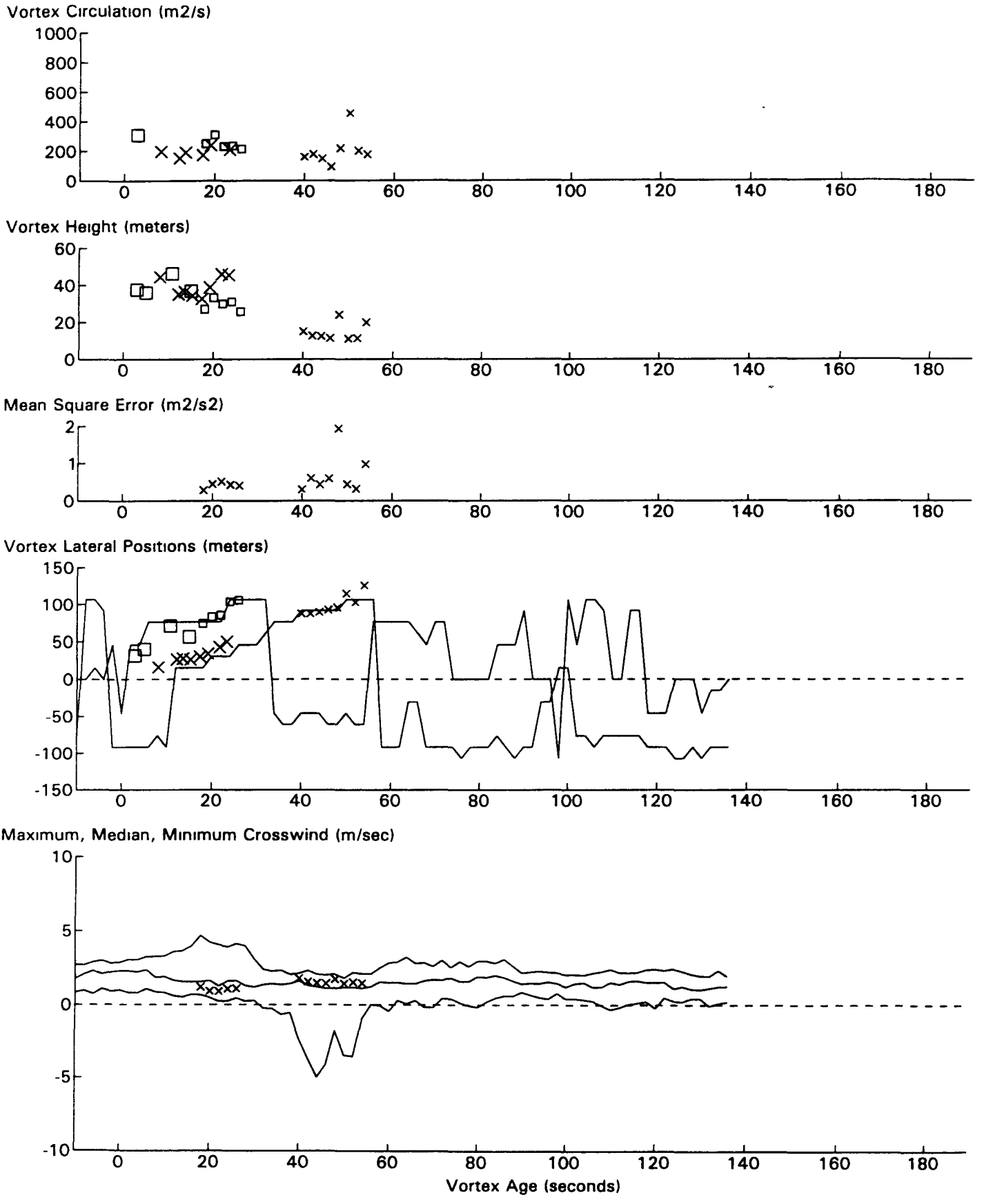

B767 JFK 31R GWVSS Data for File: I:RM11D13.166 11/13/96 22:20:16 dt= 40 CWturb=0.36

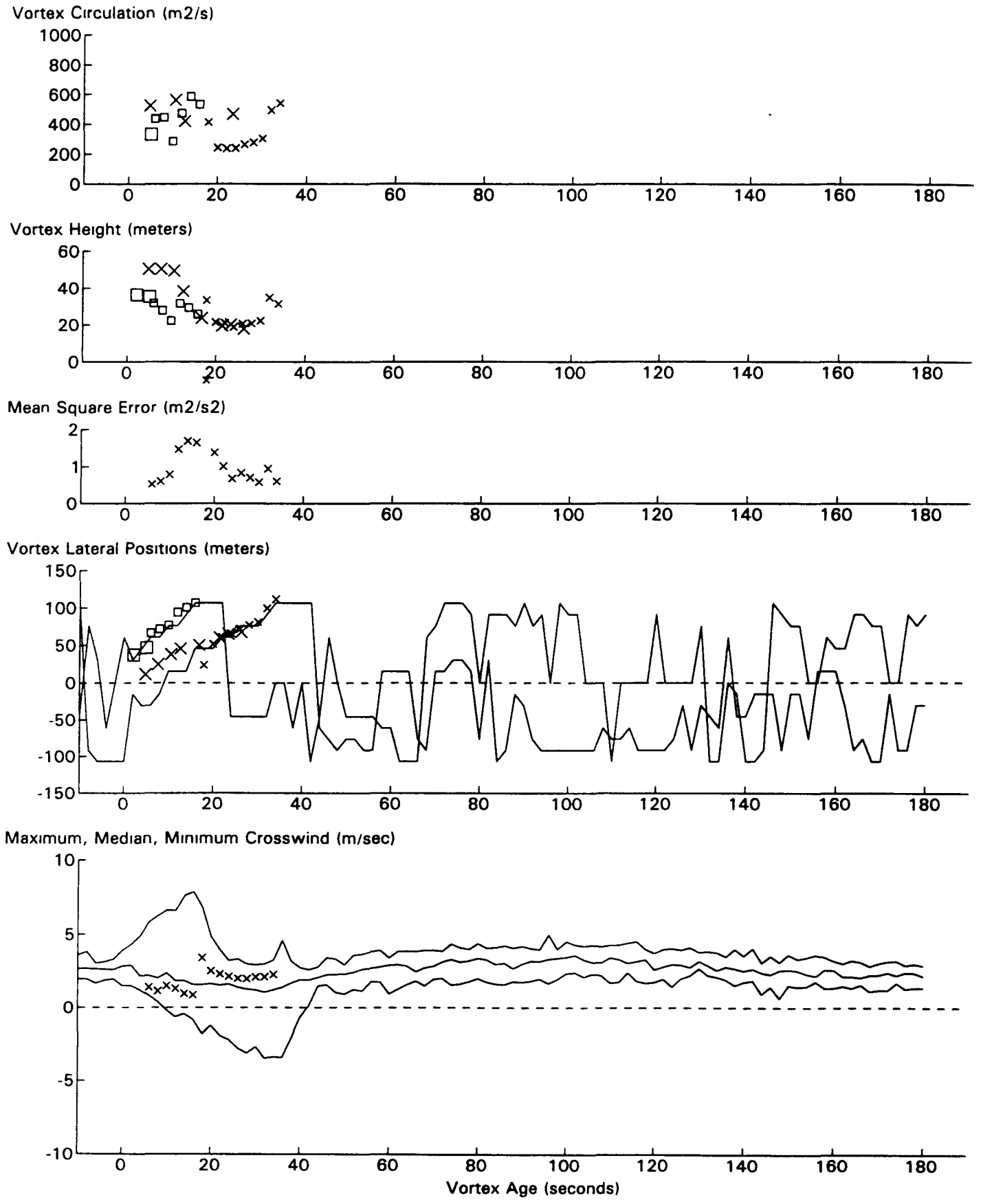

B747 JFK 31R GWVSS Data for File: I:RM11D13.170 11/13/96 22:27:48 dt= 0 CWturb=0.41

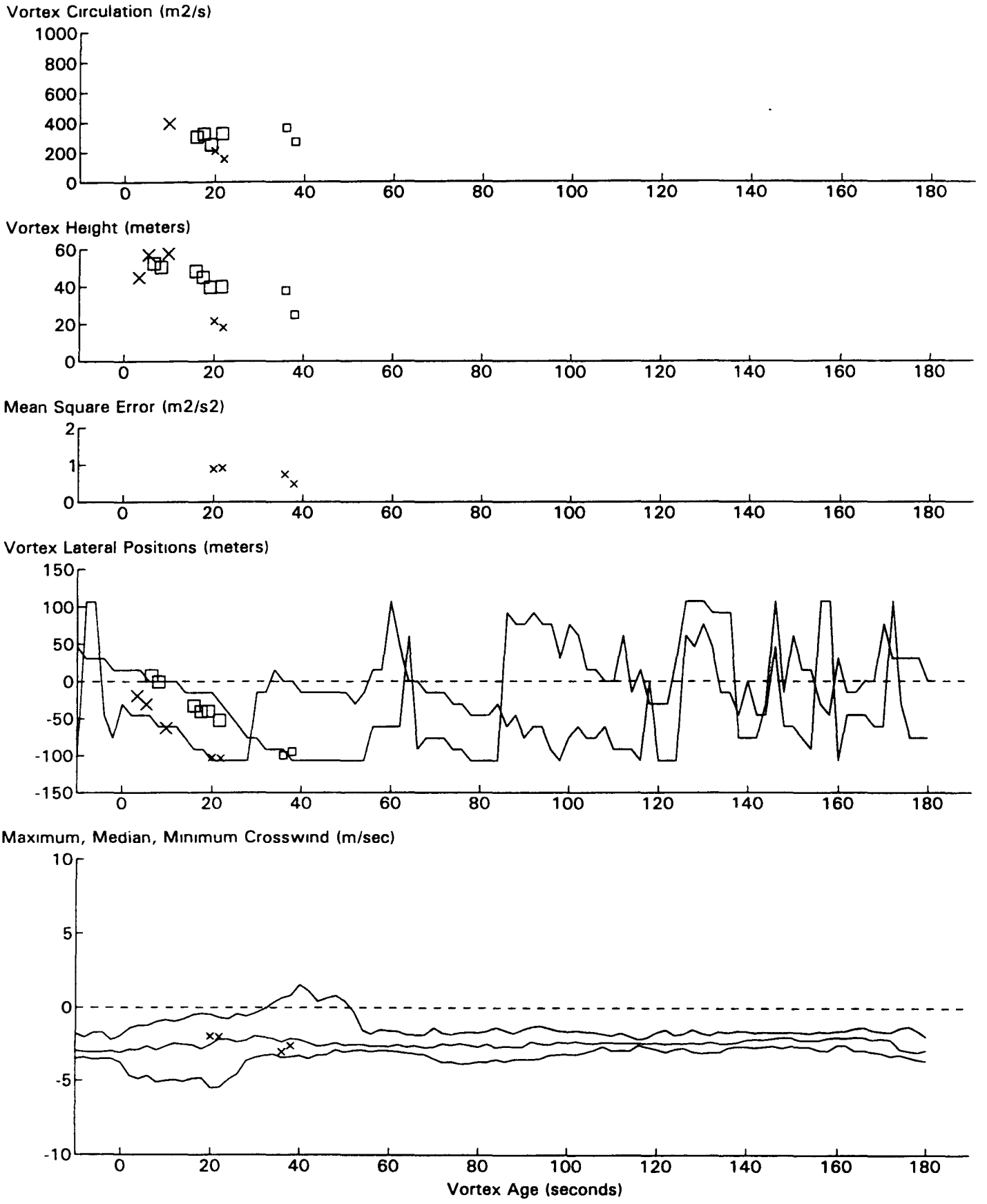

DC10 JFK 31R GWVSS Data for File: I:RM11D14.109 11/14/96 14:11:39 dt= 0 CWturb=0.38

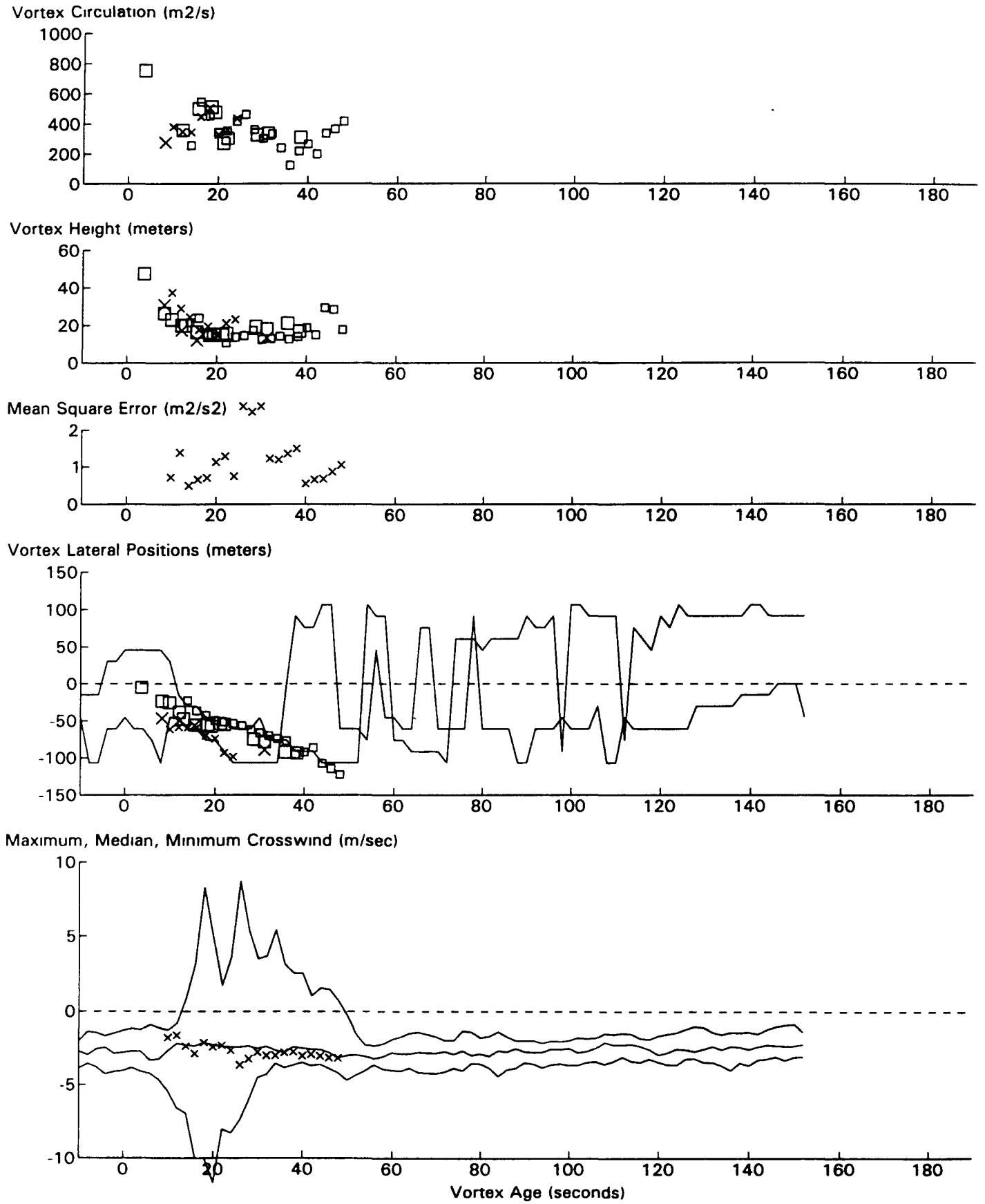

Conc JFK 31R GWVSS Data for File: I:RM11D14.114 11/14/96 14:25:23 dt= -4 CWturb=0.40

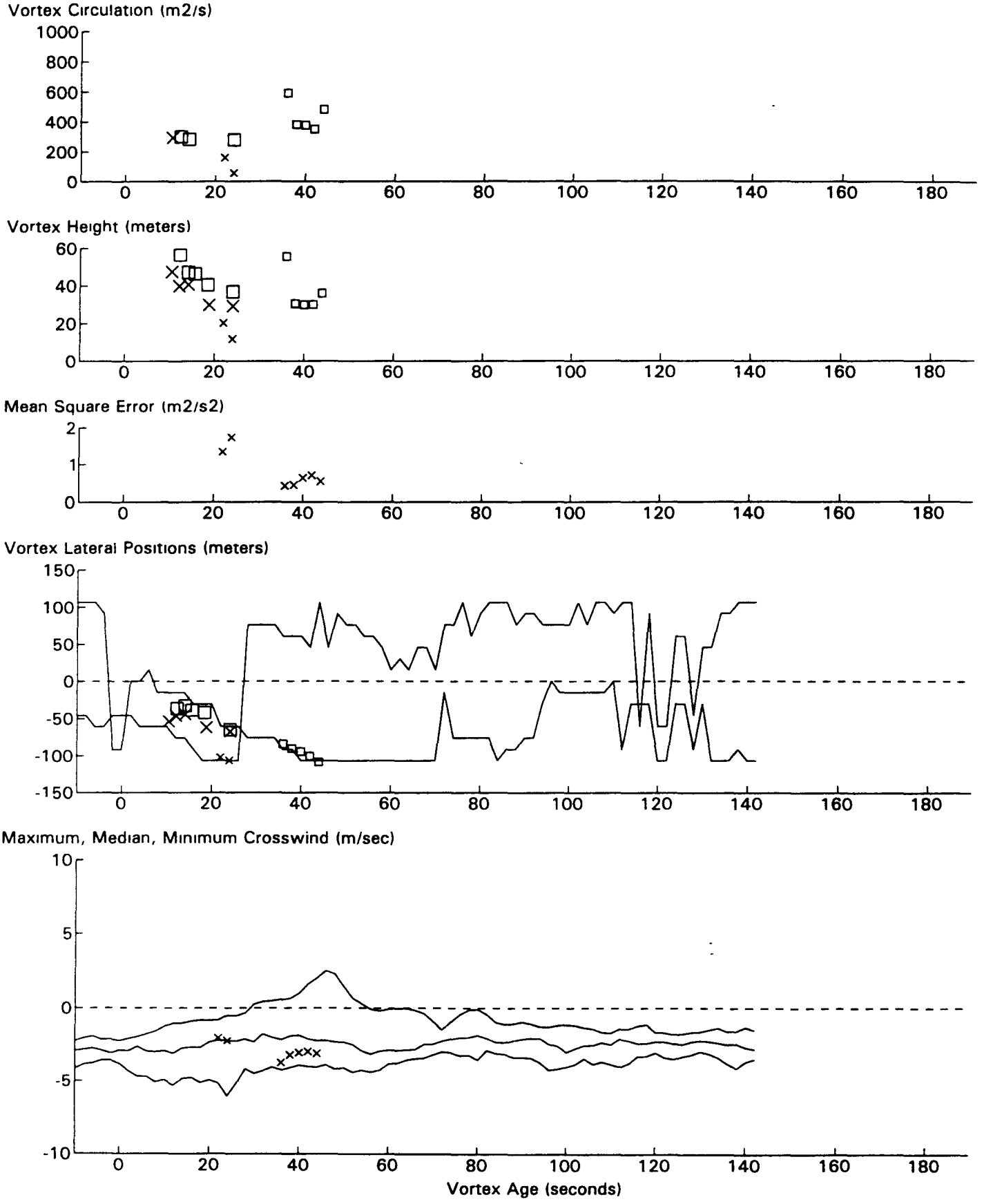

B767 JFK 31R GWVSS Data for File: I:RM11D14.117 11/14/96 14:31:20 dt= 9 CWturb=0.41

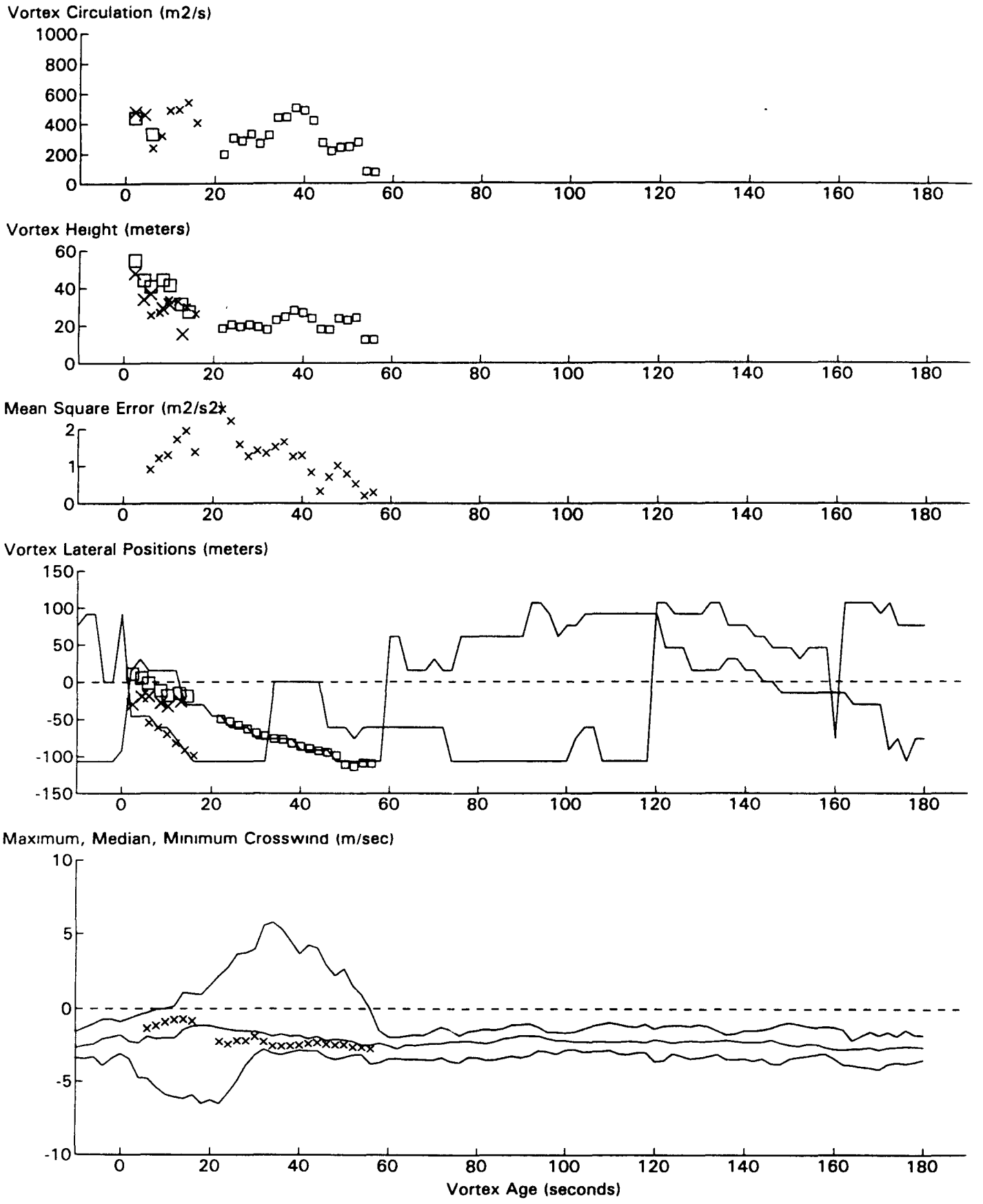

B747 JFK 31R GWVSS Data for File: I:RM11D14.126 11/14/96 15:15:49 dt= 0 CWturb=0.40

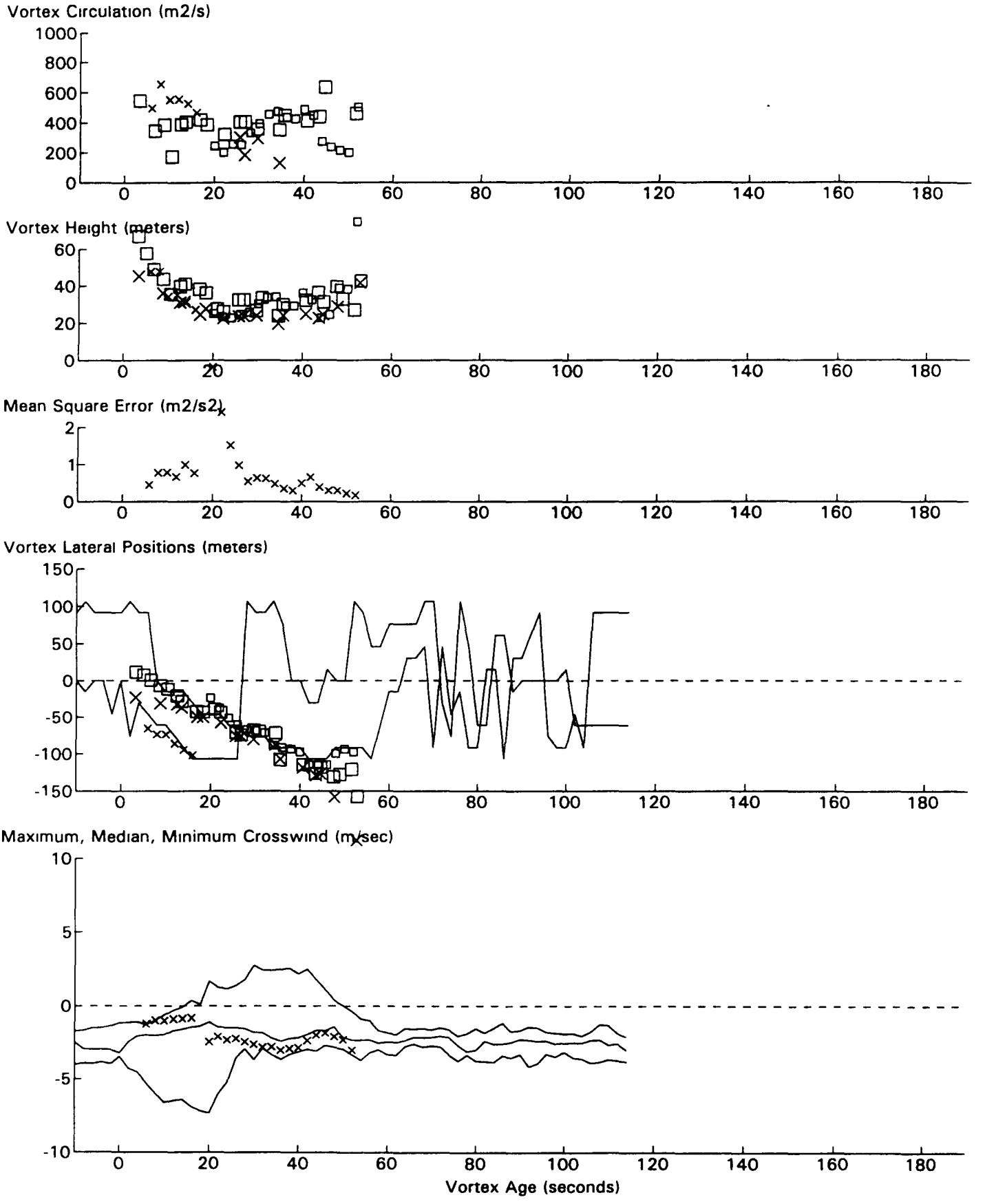

B747 JFK 31R GWVSS Data for File: I:RM11D14.132 11/14/96 15:35:57 dt= -9 CWturb=0.43

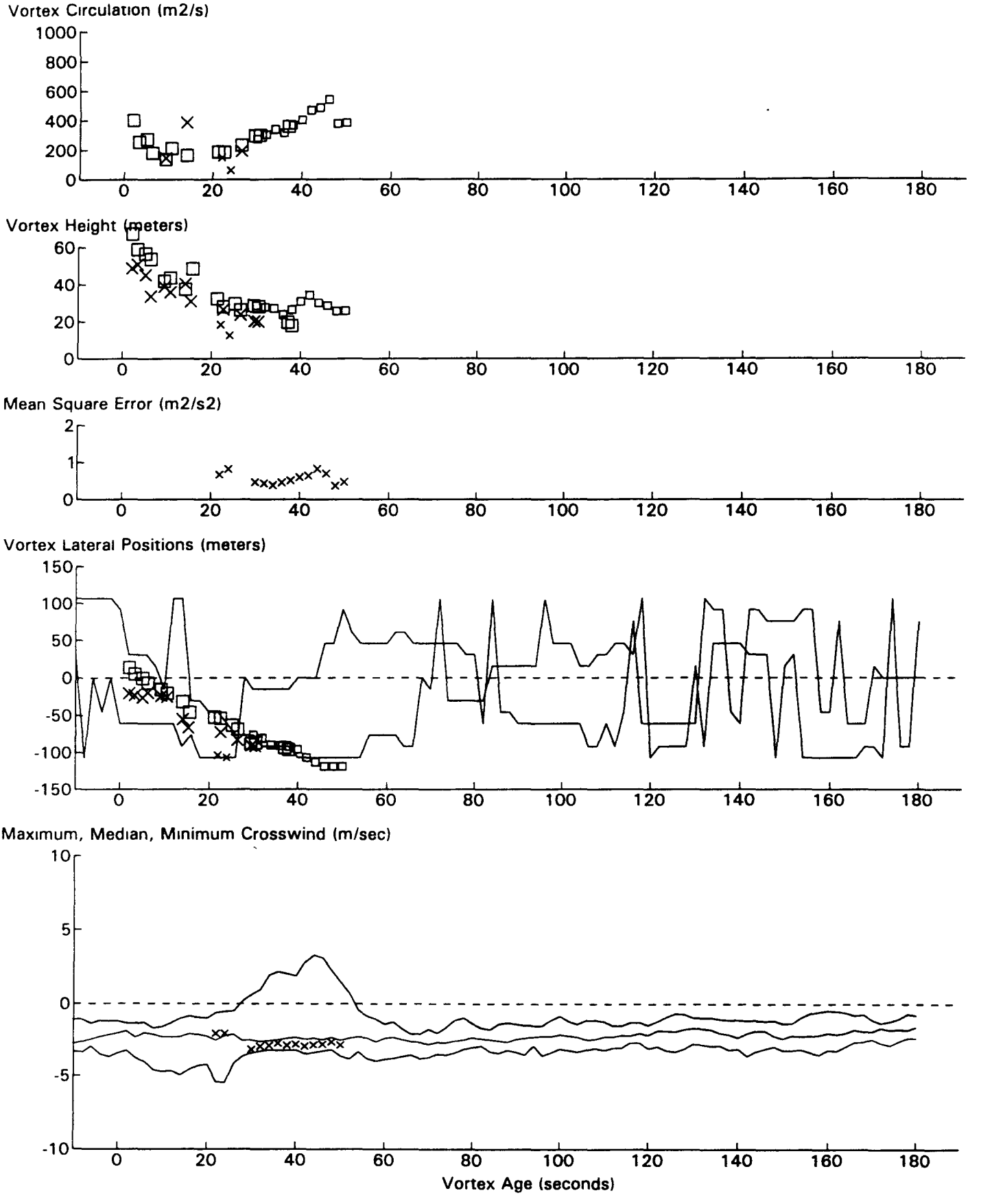

B767 JFK 31R GWVSS Data for File: I:RM11D14.134 11/14/96 15:39:11 dt= -9 CWturb=0.44

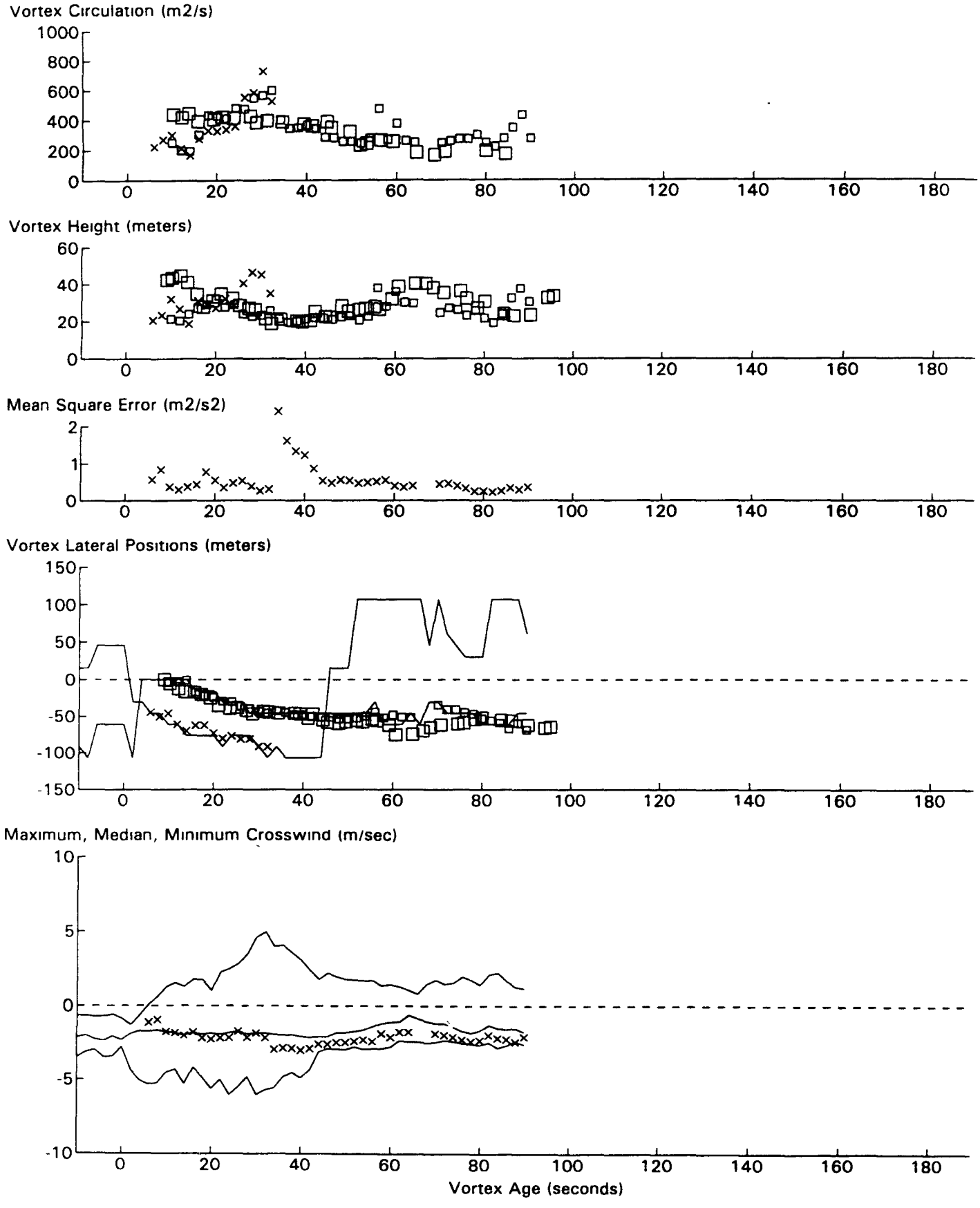

B747 JFK 31R GWVSS Data for File: I:RM11D14.203 11/14/96 20:18:14 dt= 0 CWturb=0.36

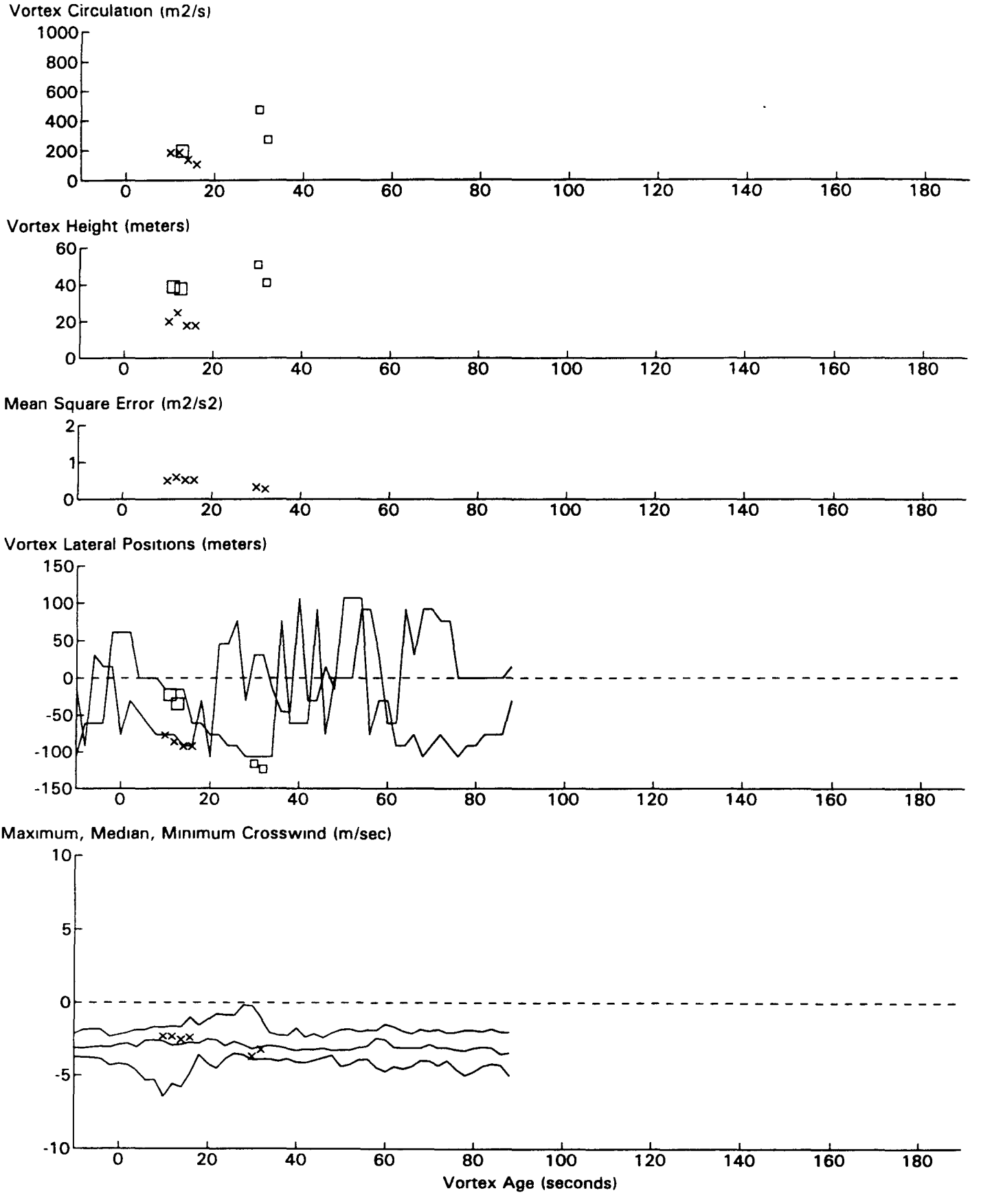

B767 JFK 31R GWVSS Data for File: I:RM11D14.212 11/14/96 20:33:46 dt= 0 CWturb=0.46

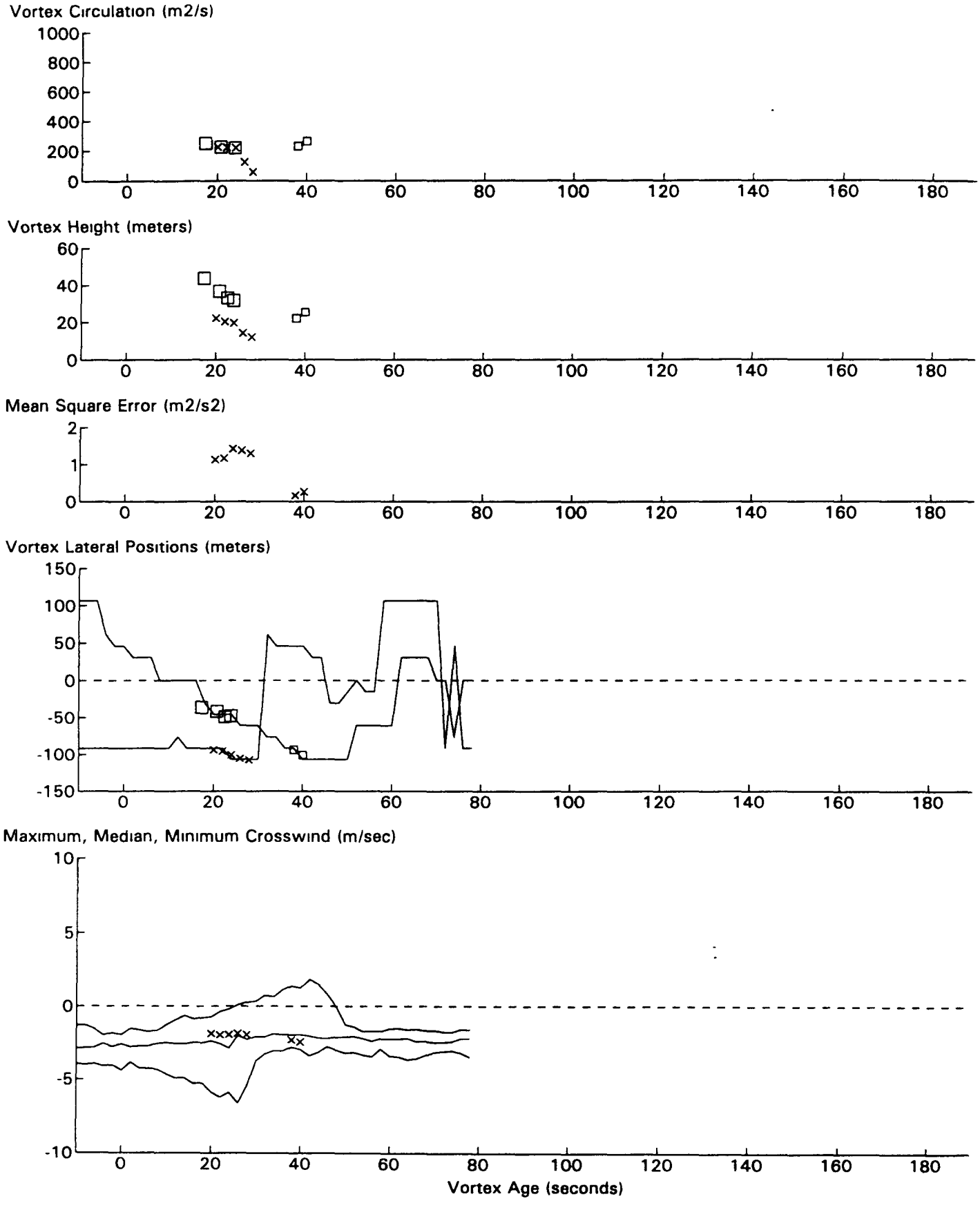

B767 JFK 31R GWVSS Data for File: I:RM11D14.215 11/14/96 20:38:25 dt= 0 CWturb=0.55

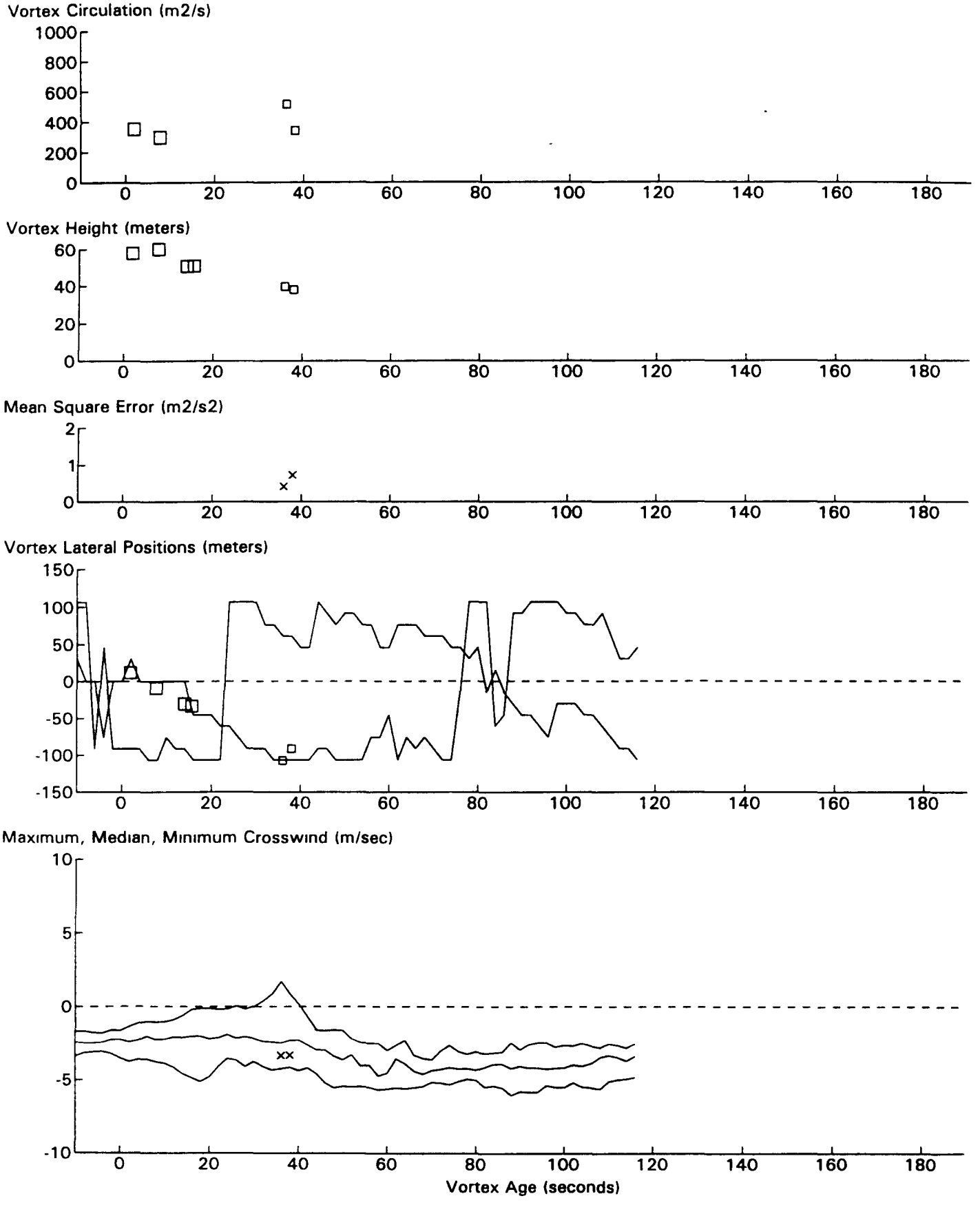

EA34 JFK 31R GWVSS Data for File: I:RM11D14.216 11/14/96 20:39:43 dt= -18 CWturb=0.56

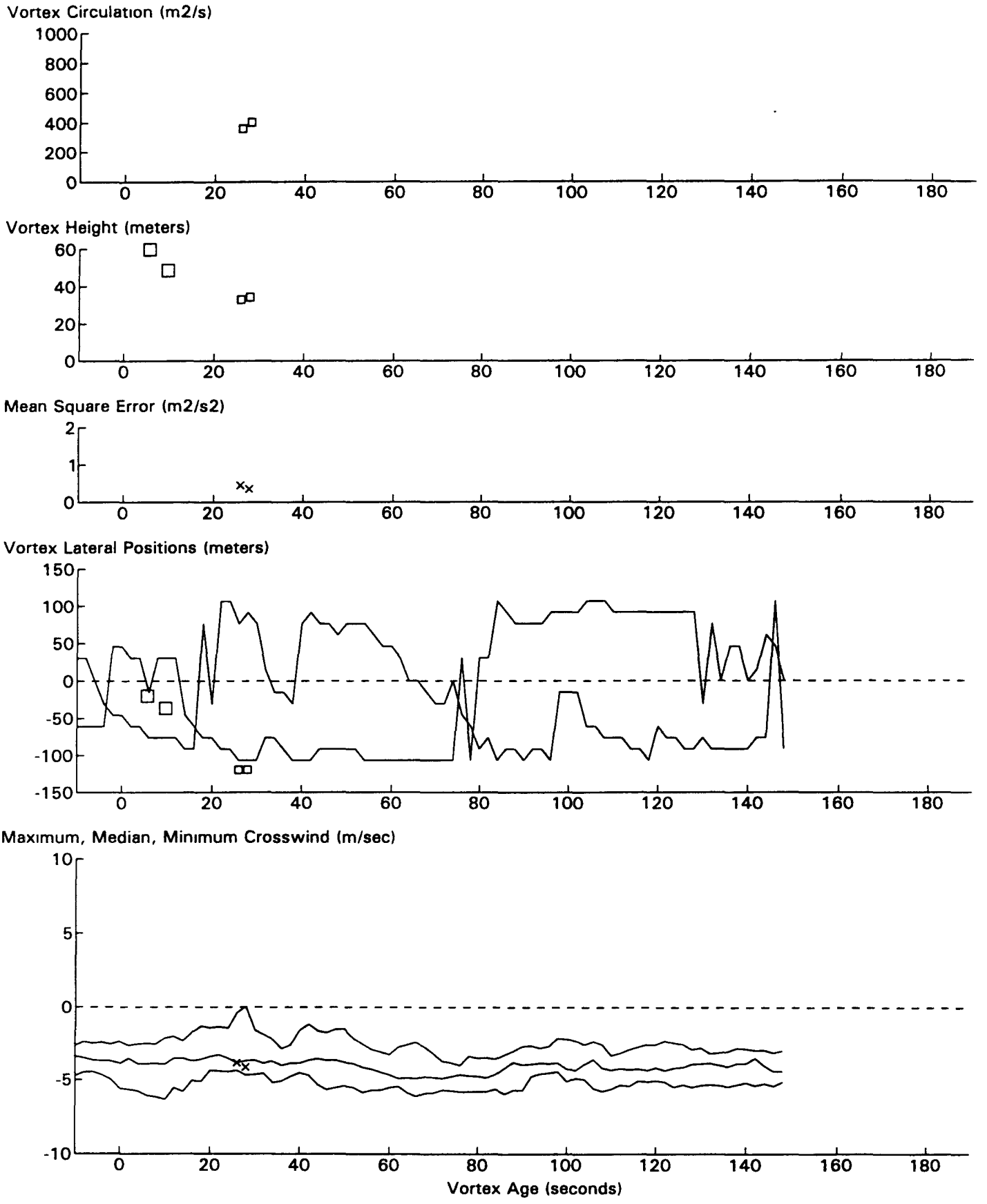

B767 JFK 31R GWVSS Data for File: I:RM11D14.218 11/14/96 20:43:13 dt= -19 CWturb=0.54

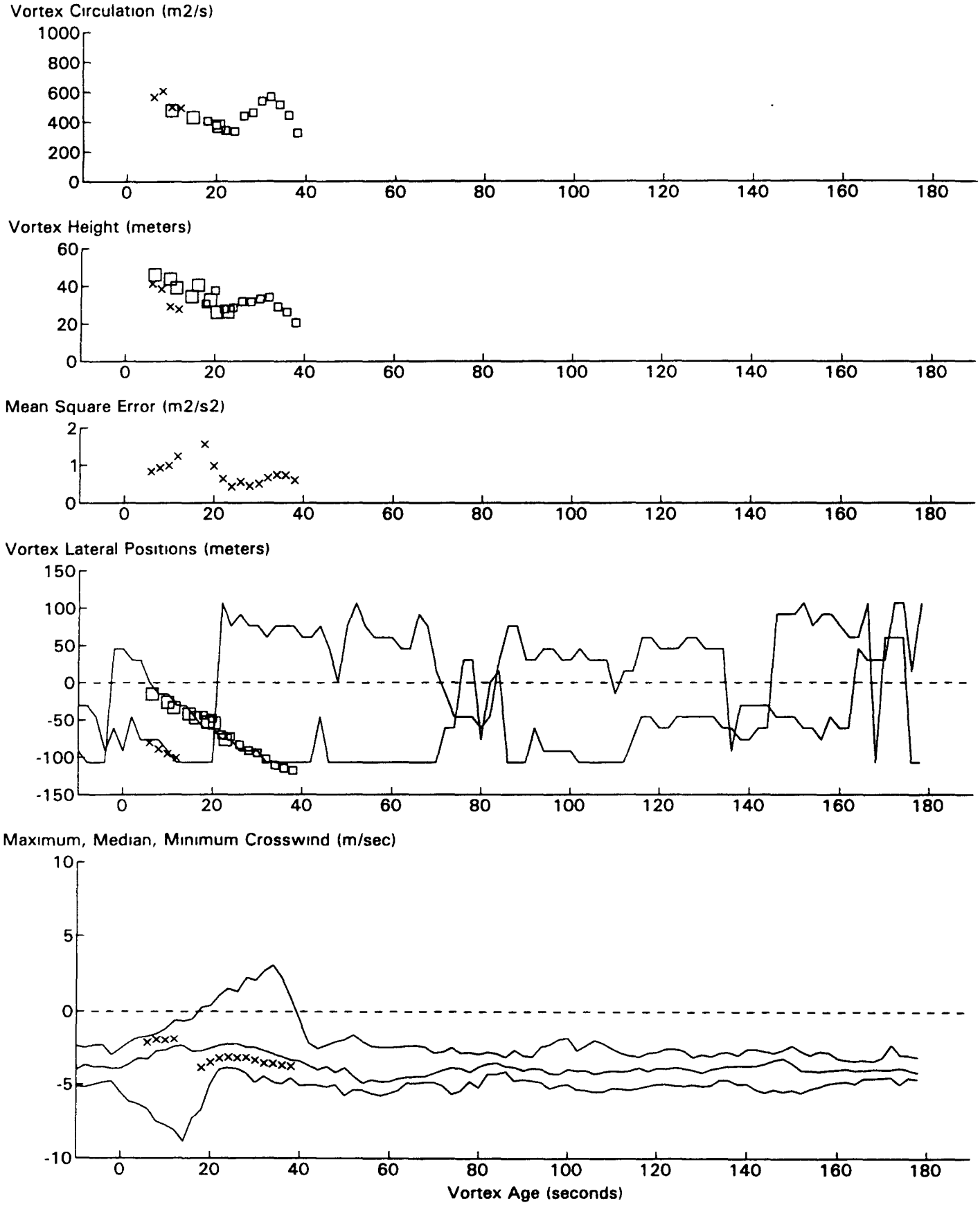

B747 JFK 31R GWVSS Data for File: I:RM11D14.222 11/14/96 20:53:25 dt = -18 CWturb = 0.47

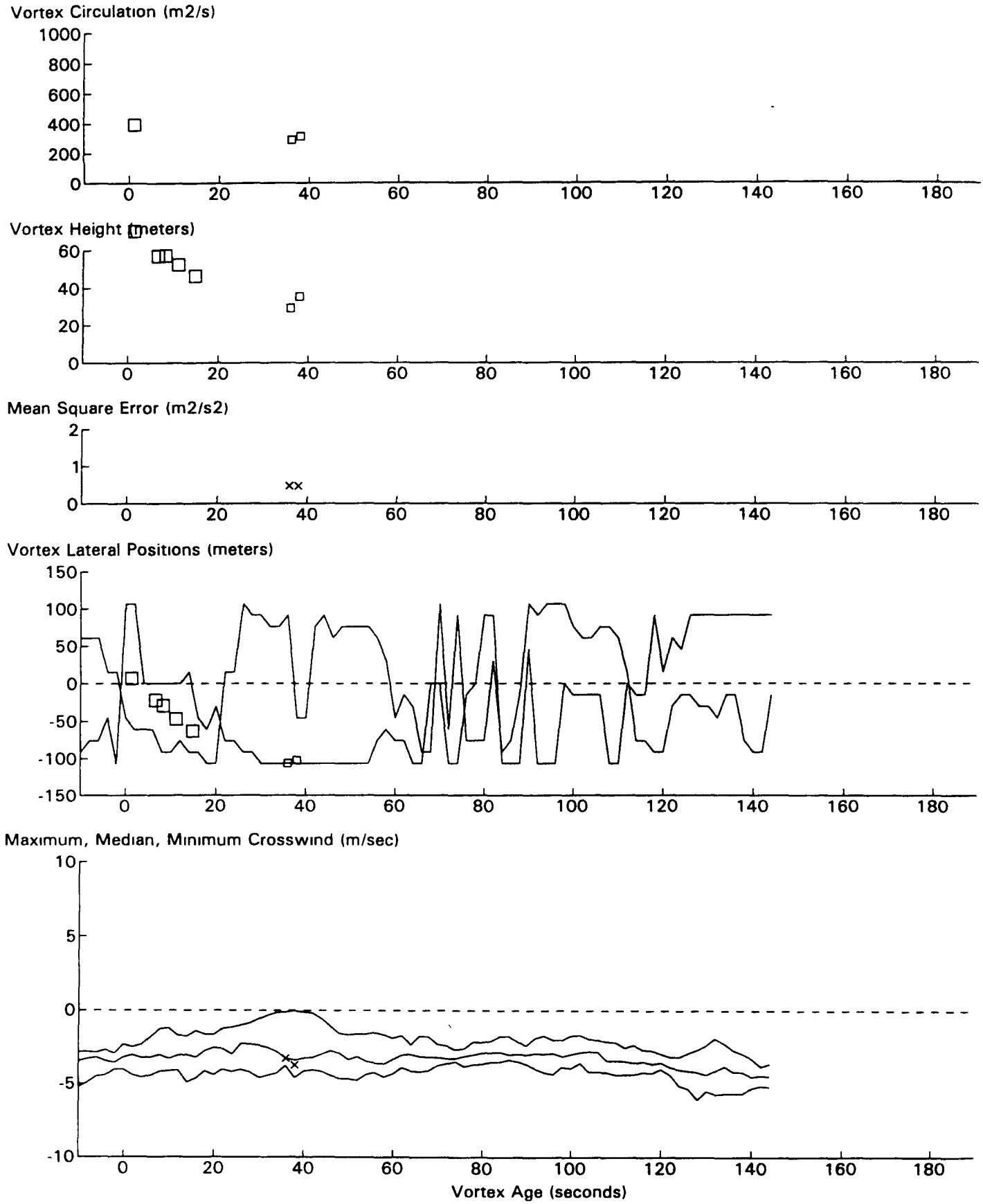

B767 JFK 31R GWVSS Data for File: I:RM11D14.224 11/14/96 20:58:25 dt= -19 CWturb=0.48

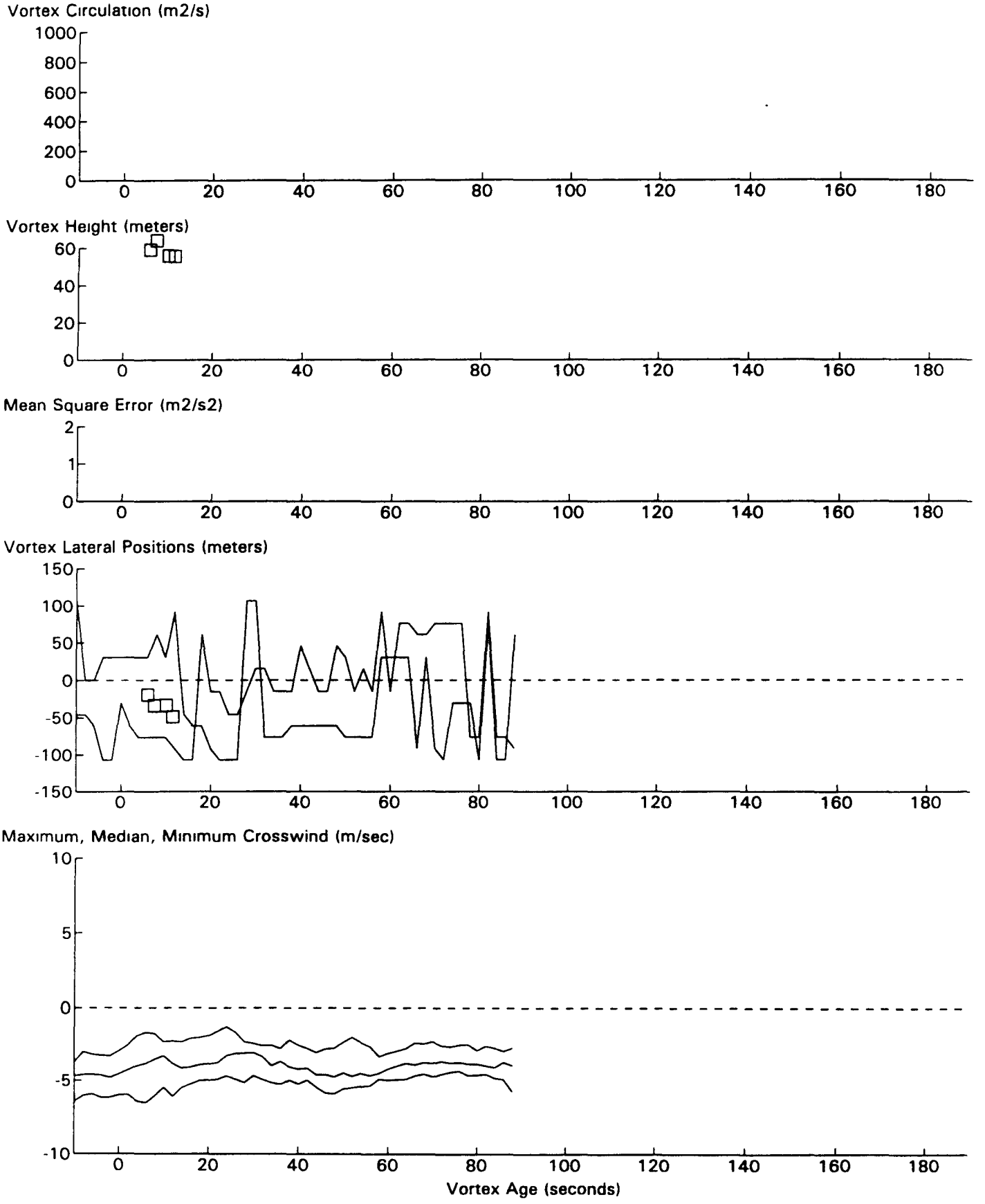

EA30 JFK 31R GWVSS Data for File: I:RM11D14.231 11/14/96 21:11:53 dt= -18 CWturb=0.51

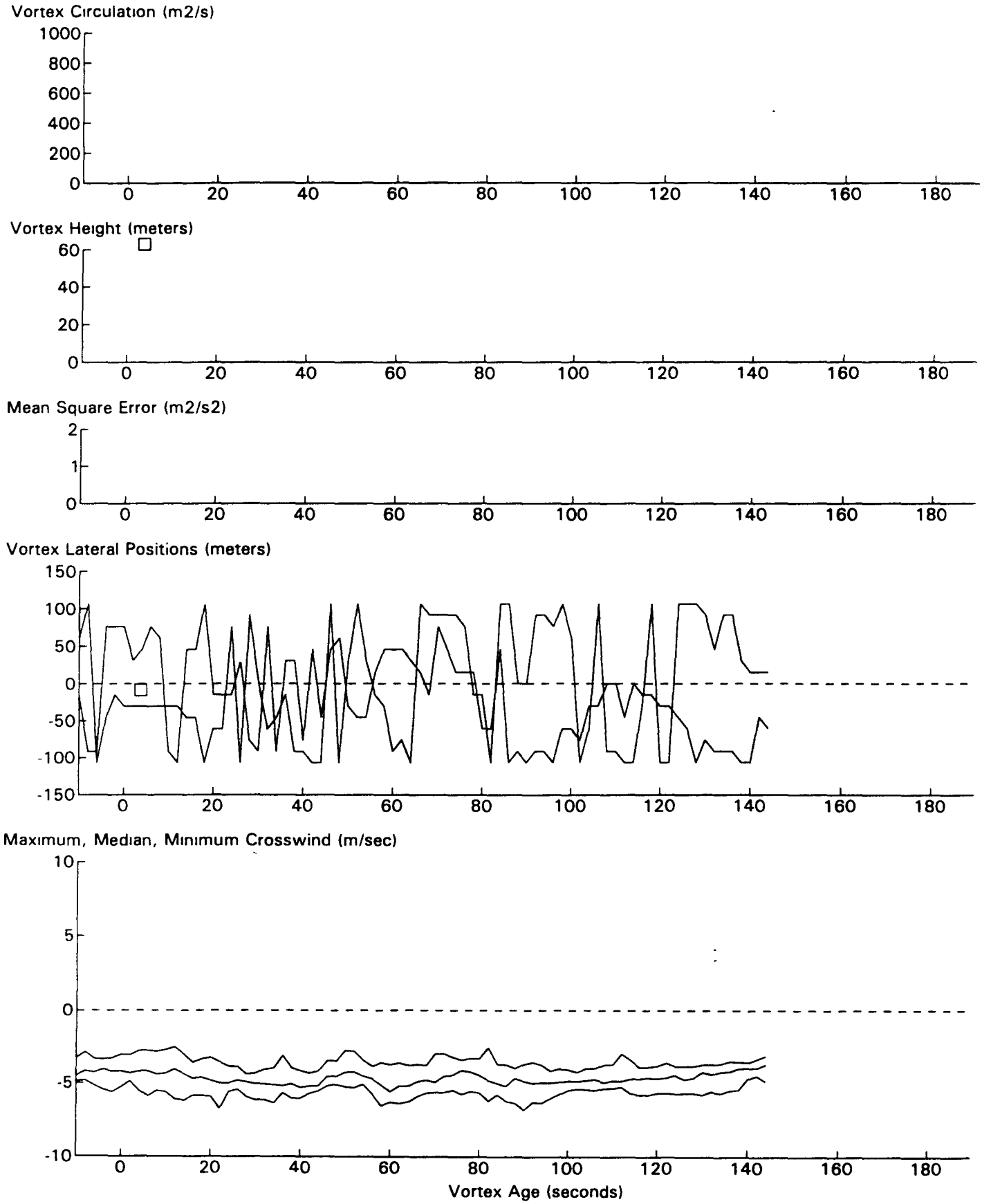

MD80 JFK 31R GWVSS Data for File: I:RM11D14.233 11/14/96 21:16:16 dt= -21 CWturb=0.55

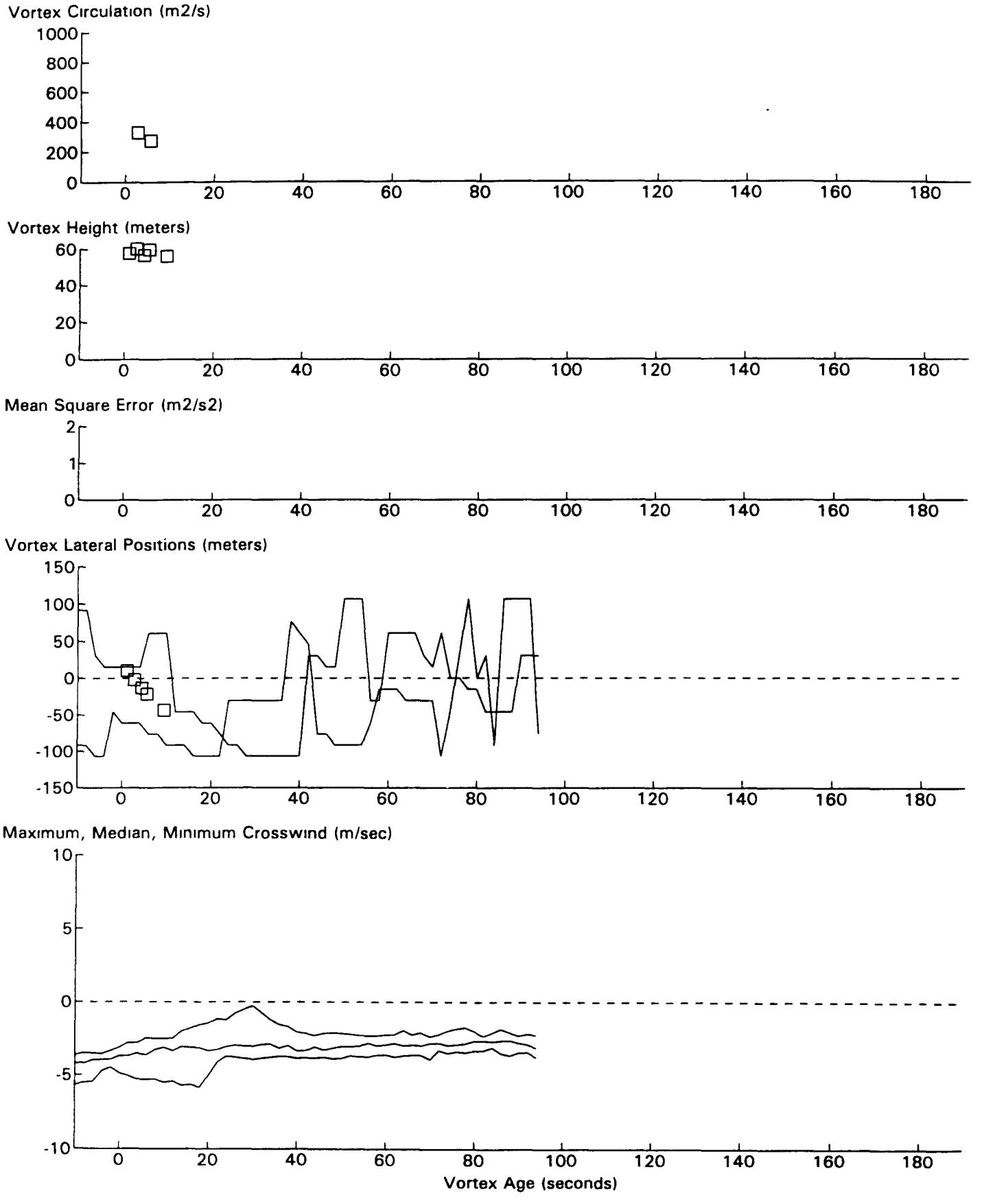

B767 JFK 31R GWVSS Data for File: I:RM11D14.234 11/14/96 21:18:40 dt= -19 CWturb=0.59

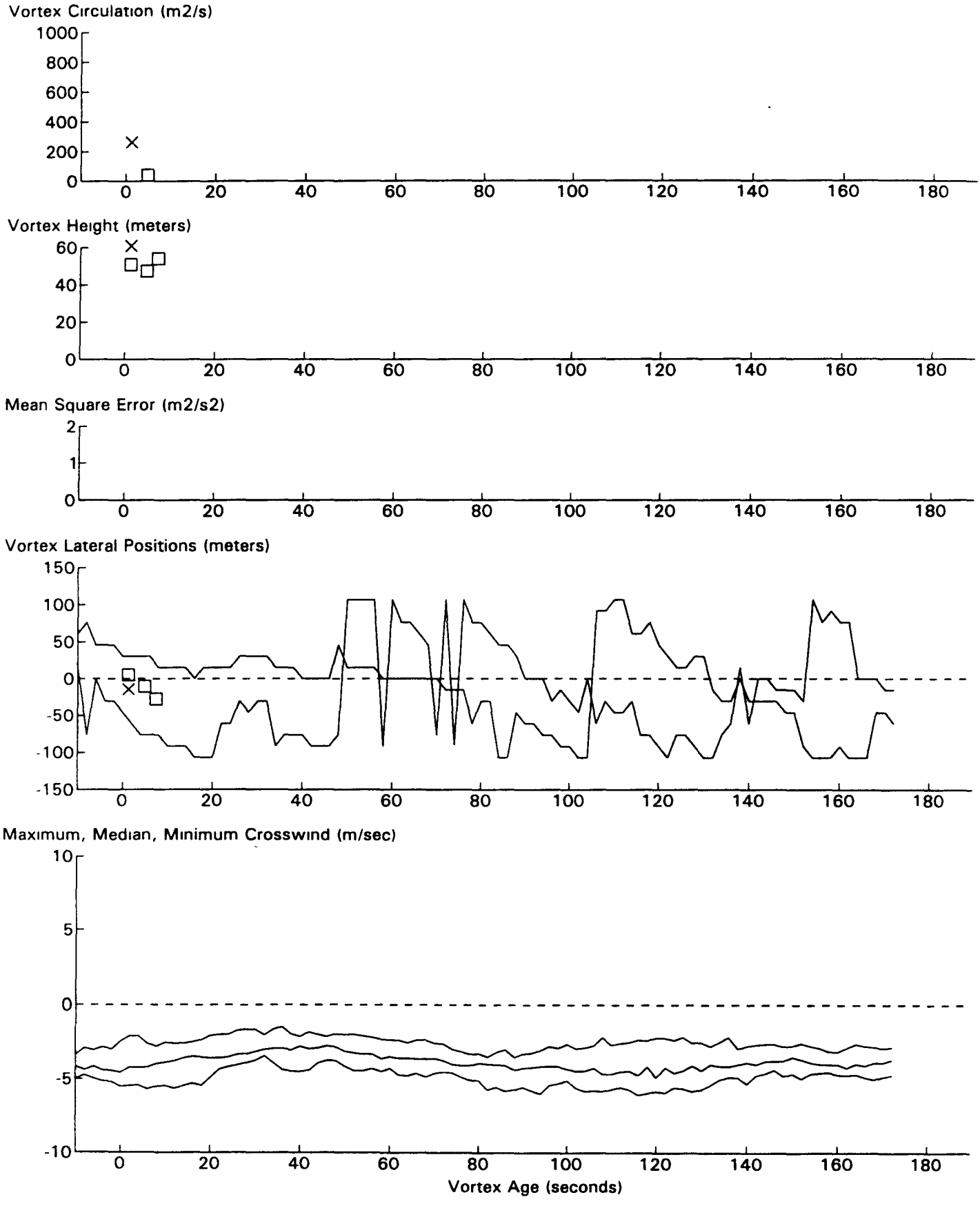

DC9 JFK 31R GWVSS Data for File: I:RM11D14.239 11/14/96 21:28:50 dt= -20 CWturb=0.56

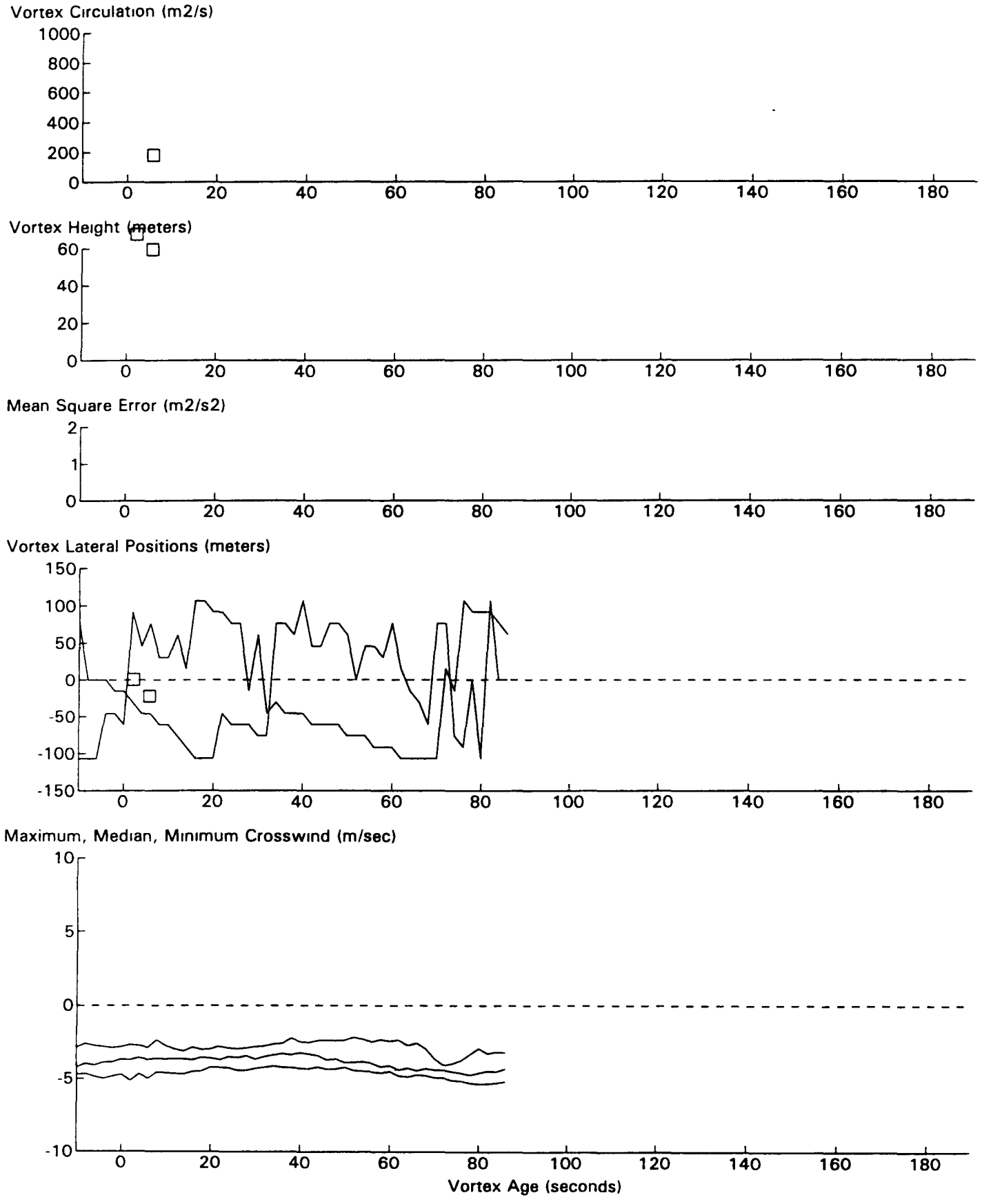

B727 JFK 31R GWVSS Data for File: I:RM11D14.240 11/14/96 21:31:42 dt= -19 CWturb=0.53

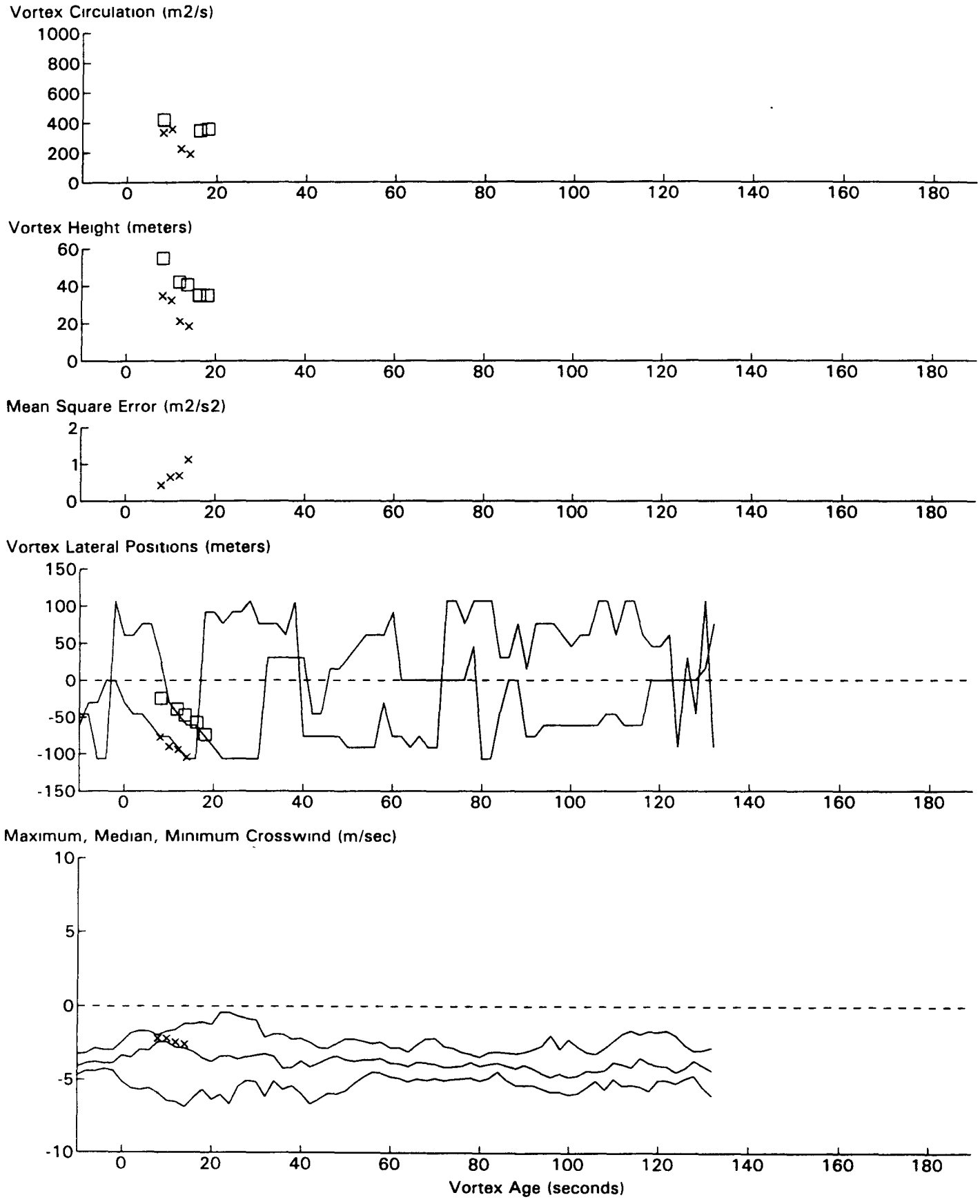

B747 JFK 31R GWVSS Data for File: I:RM11D14.242 11/14/96 21:34:40 dt= -20 CWturb=0.51

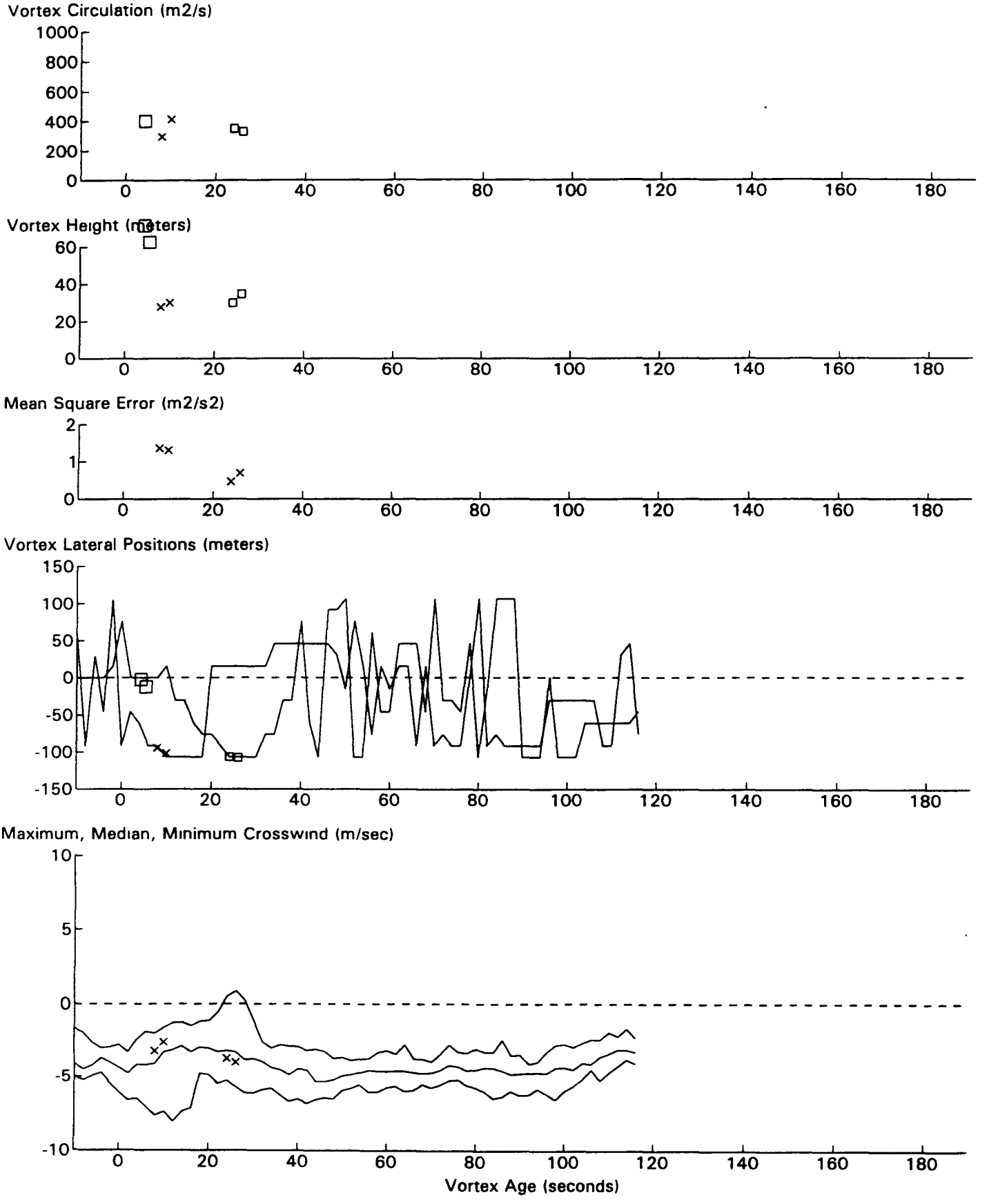

B747 JFK 31R GWVSS Data for File: I:RM11D14.243 11/14/96 21:36:52 dt= -19 CWturb=0.55

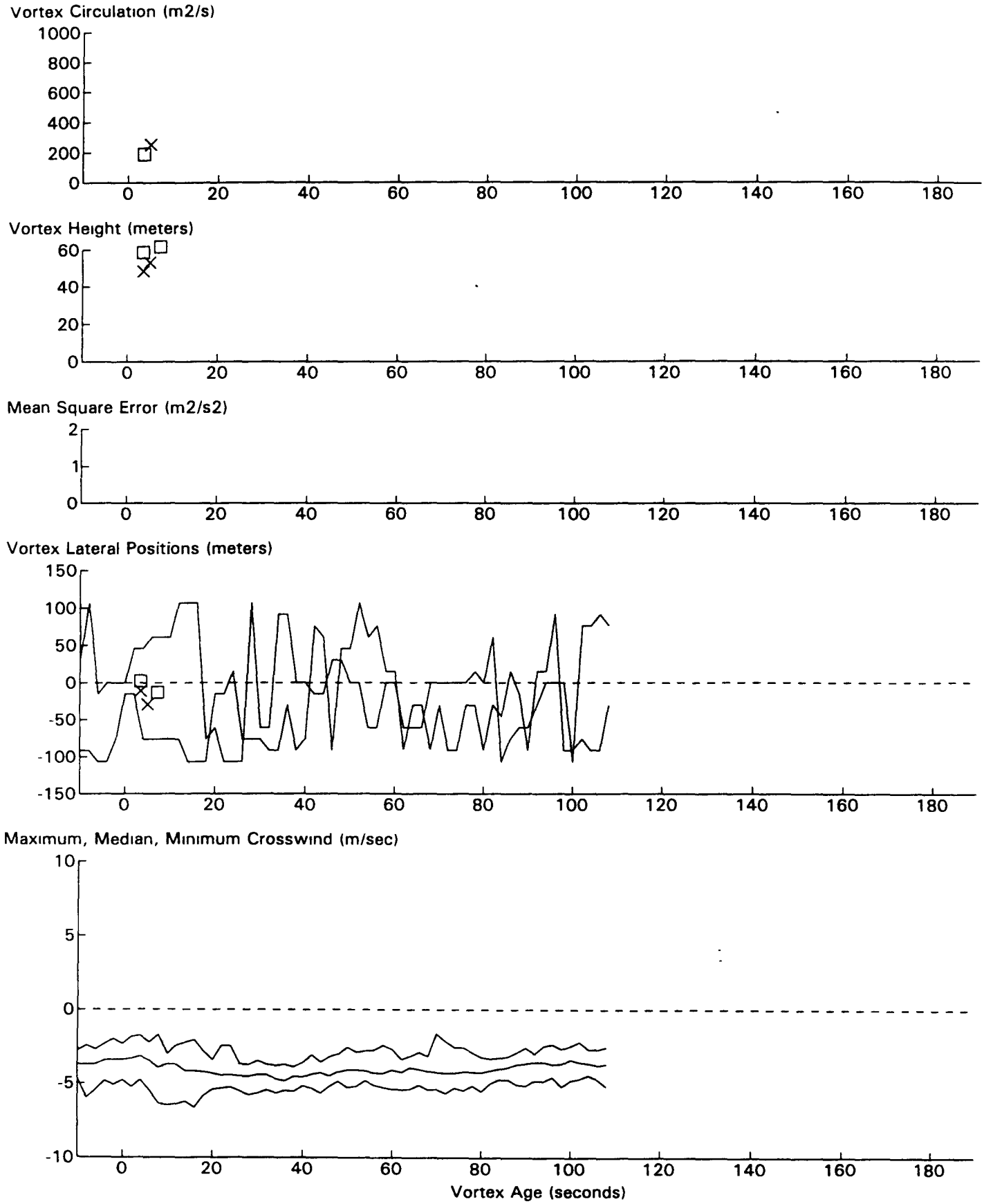

MD80 JFK 31R GWVSS Data for File: I:RM11D14.245 11/14/96 21:40:24 dt = -20 CWturb = 0.54

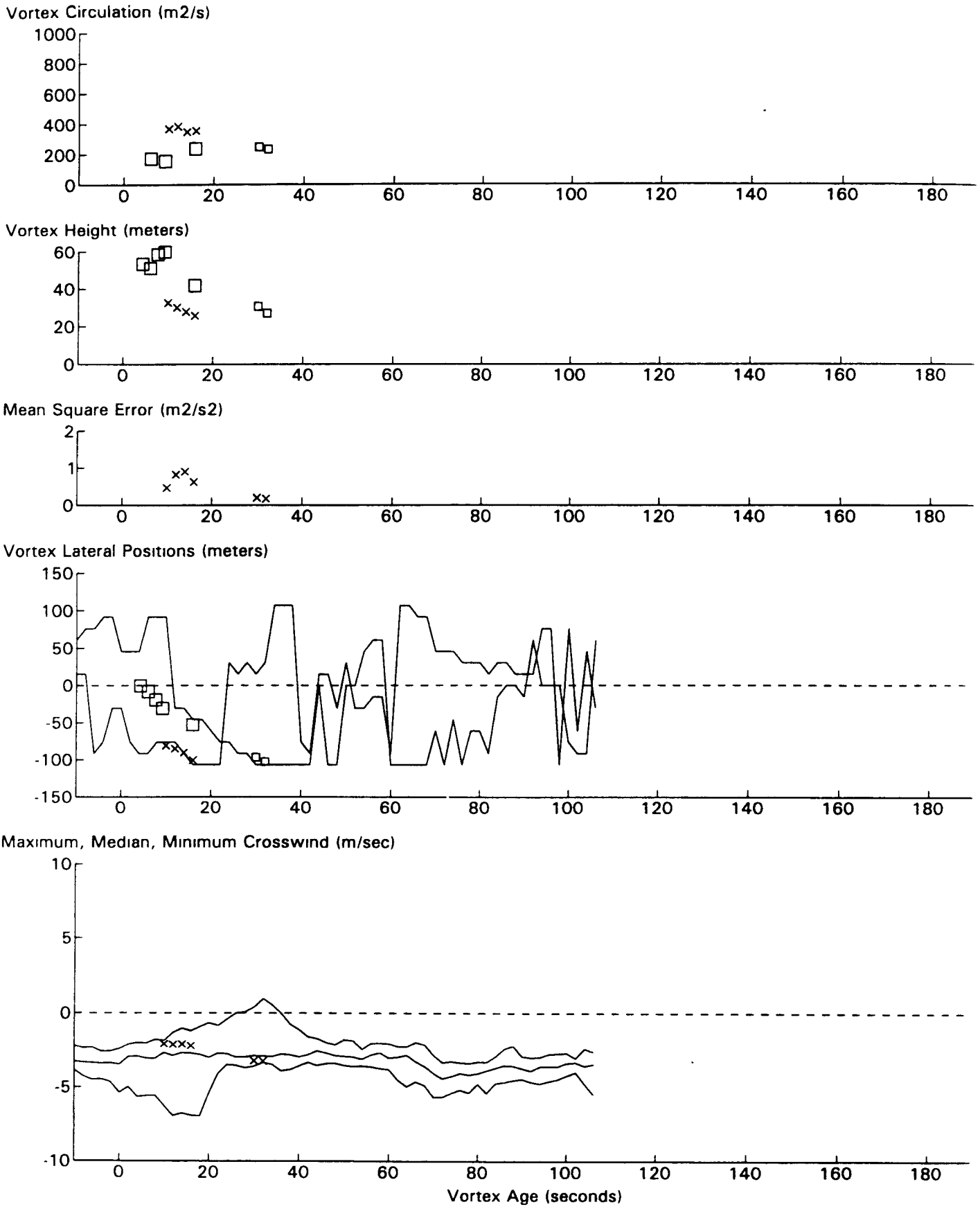

B767 JFK 31R GWVSS Data for File: I:RM11D14.250 11/14/96 21:49:13 dt= -20 CWturb=0.52

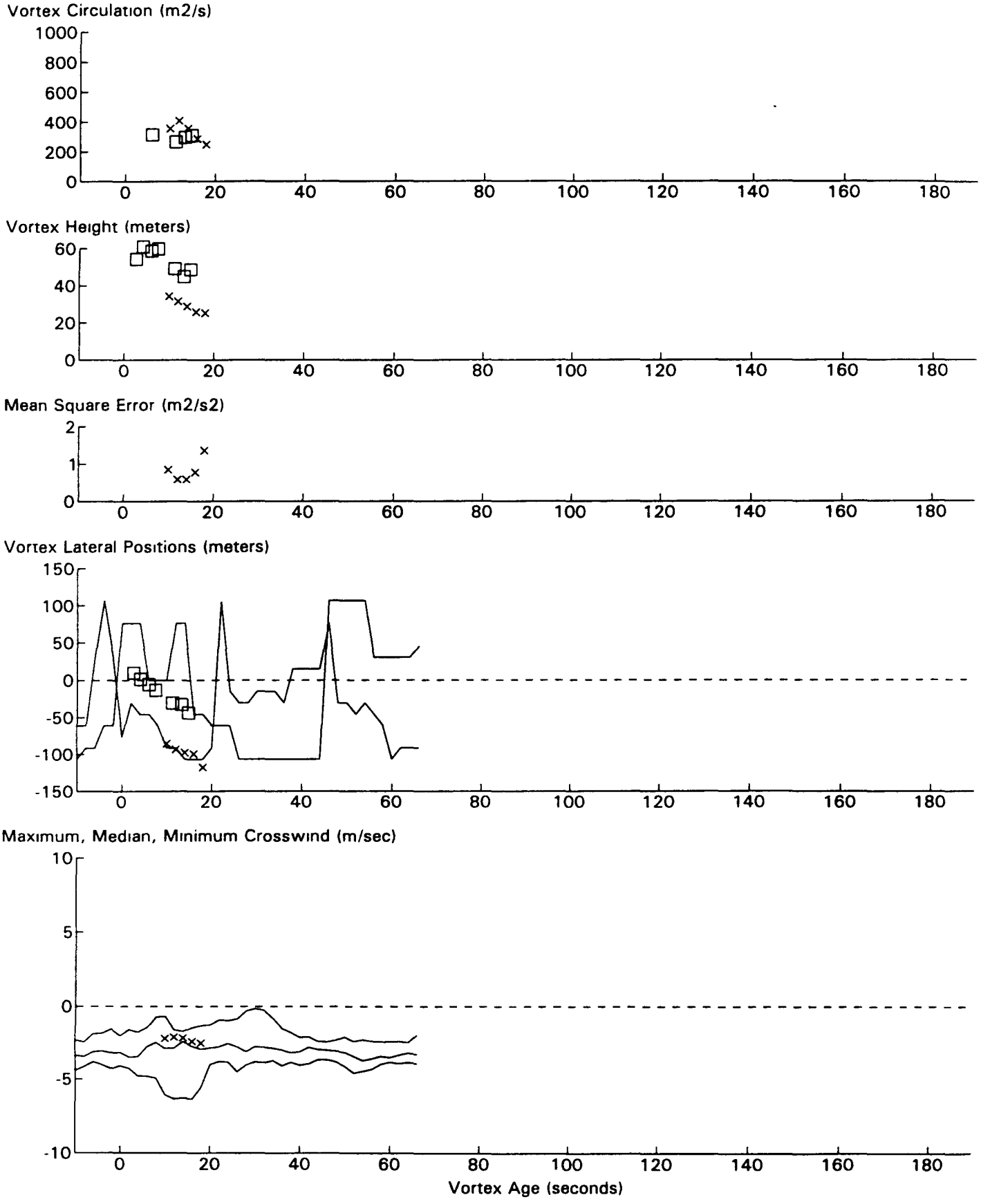

EA34 JFK 31R GWVSS Data for File: I:RM11D14.252 11/14/96 21:53:8 dt= -20 CWturb=0.49

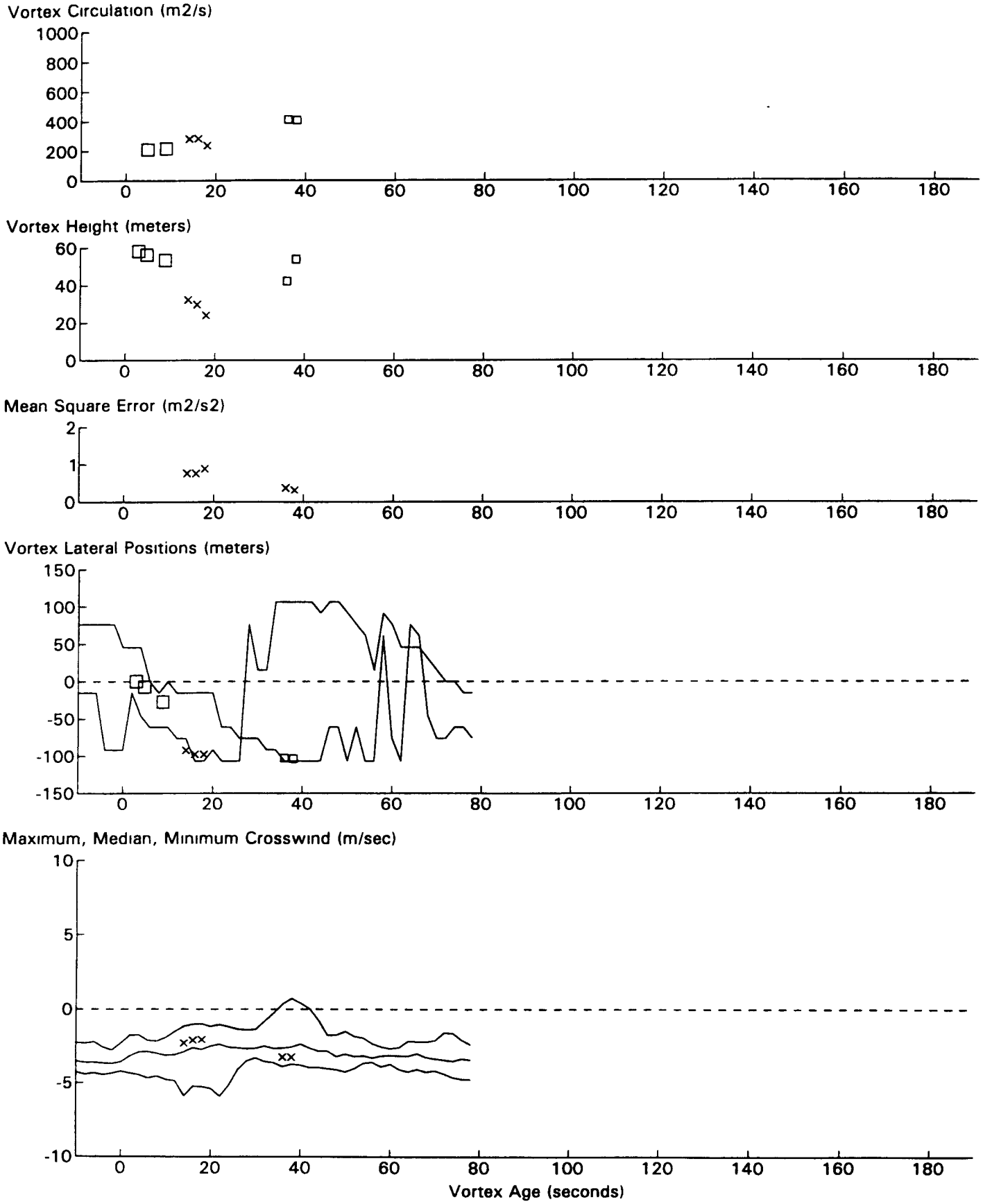

B767 JFK 31R GWVSS Data for File: I:RM11D14.254 11/14/96 21:55:43 dt= -20 CWturb=0.47

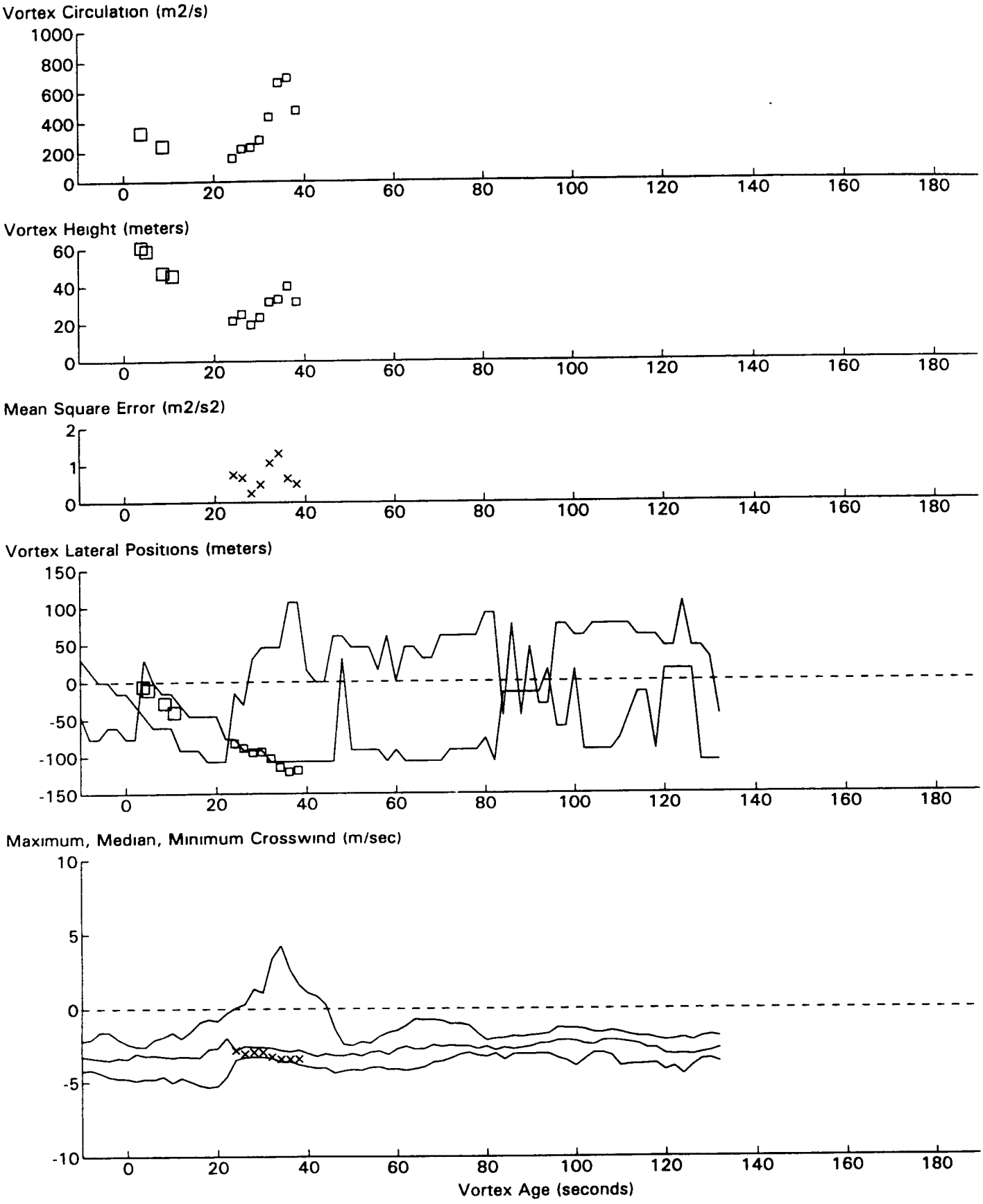

B767 JFK 31R GWVSS Data for File: I:RM11D14.255 11/14/96 21:57:1 dt= -21 CWturb=0.46

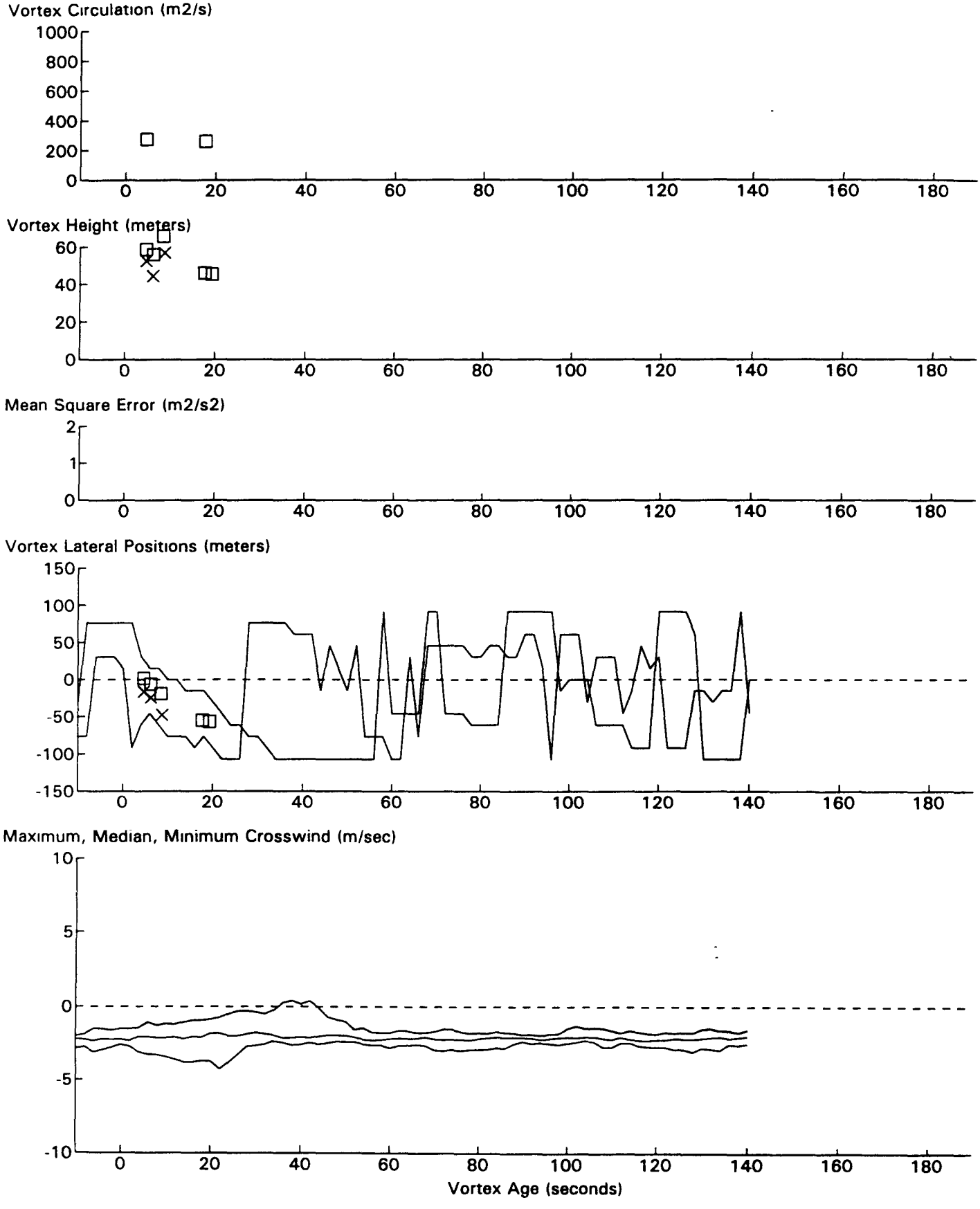

B767 JFK 31R GWVSS Data for File: I:RM11D15.025 11/15/96 12:4:44 dt= -24 CWturb=0.21

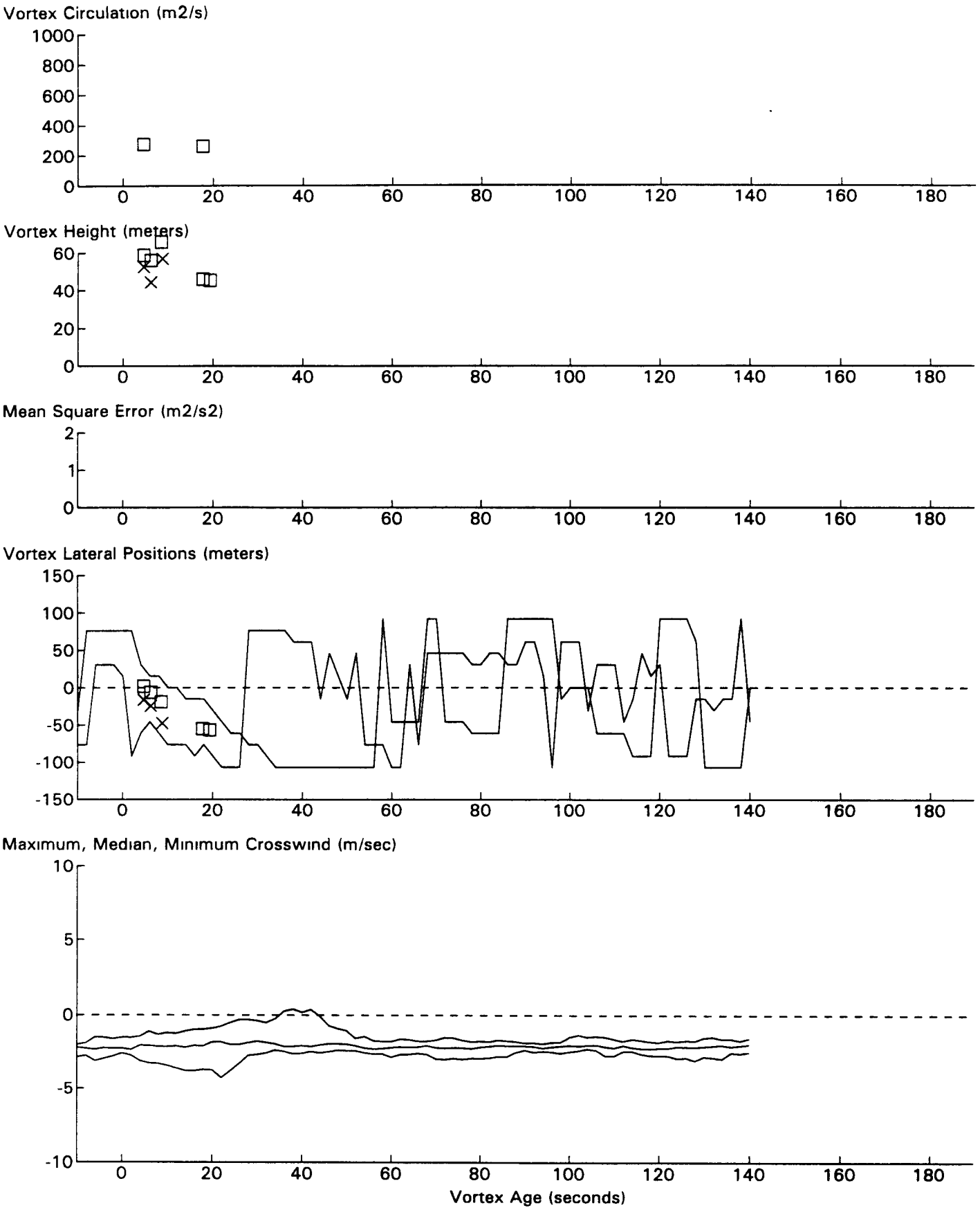

B767 JFK 31R GWVSS Data for File: I:RM11D15.025 11/15/96 12:4:44 dt= -24 CWturb=0.21

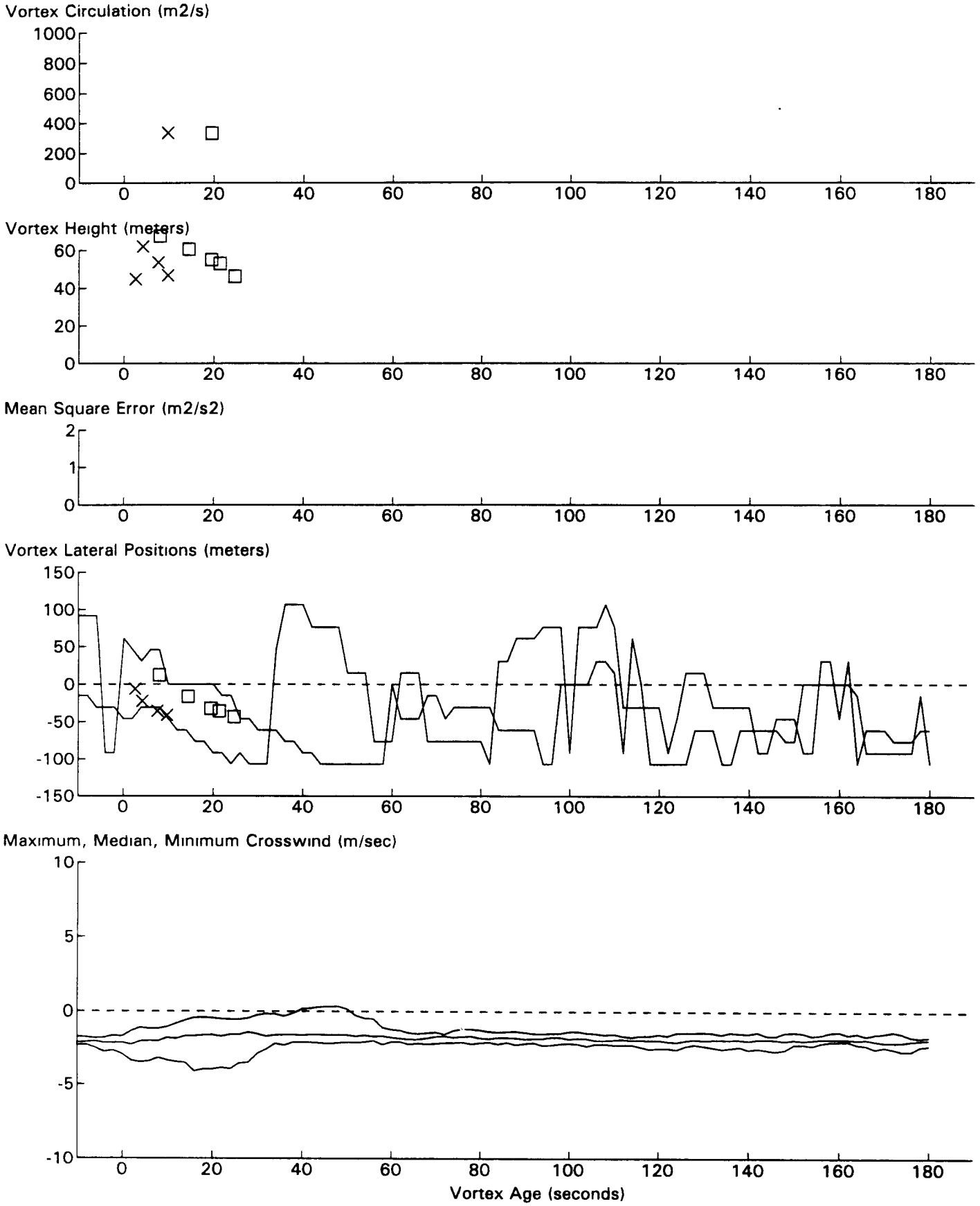

MD11 JFK 31R GWVSS Data for File: I:RM11D15.030 11/15/96 12:17:44 dt= -45 CWturb=0.20

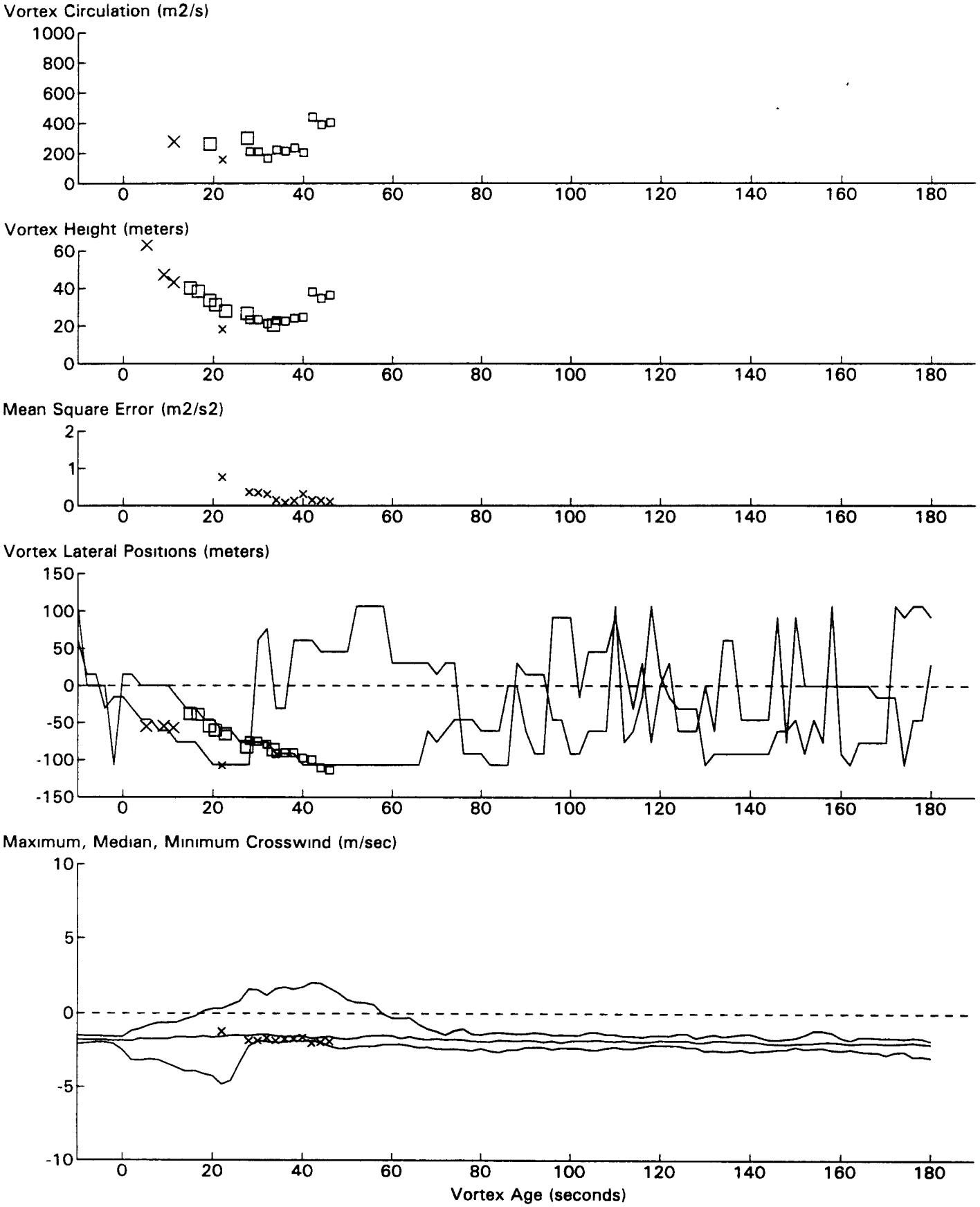

DC8 JFK 31R GWVSS Data for File: I:RM11D15.031 11/15/96 12:21:47 dt= -27 CWturb=0.19

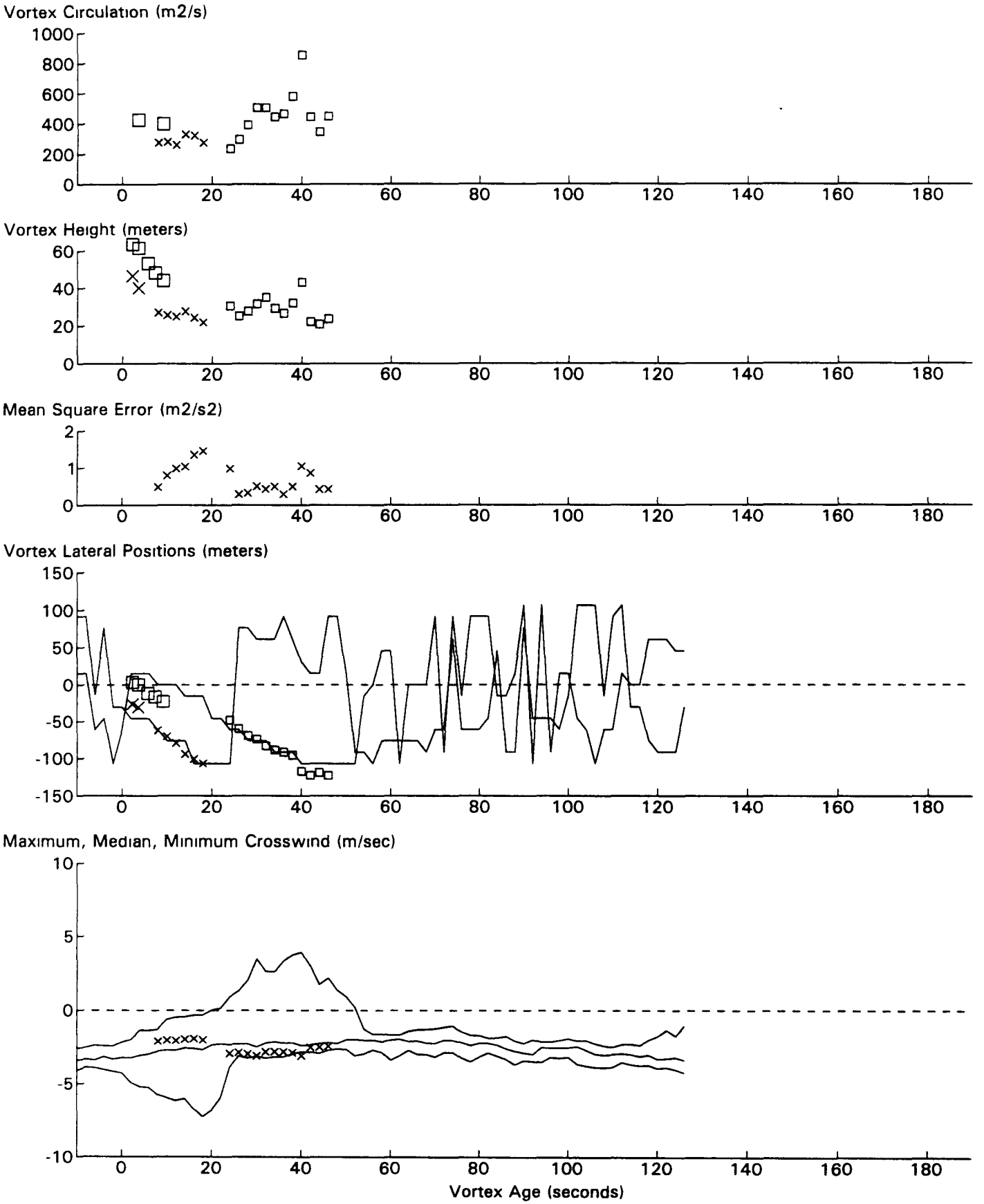

B747 JFK 31R GWVSS Data for File: I:RM11D15.036 11/15/96 12:50:10 dt= -27 CWturb=0.38

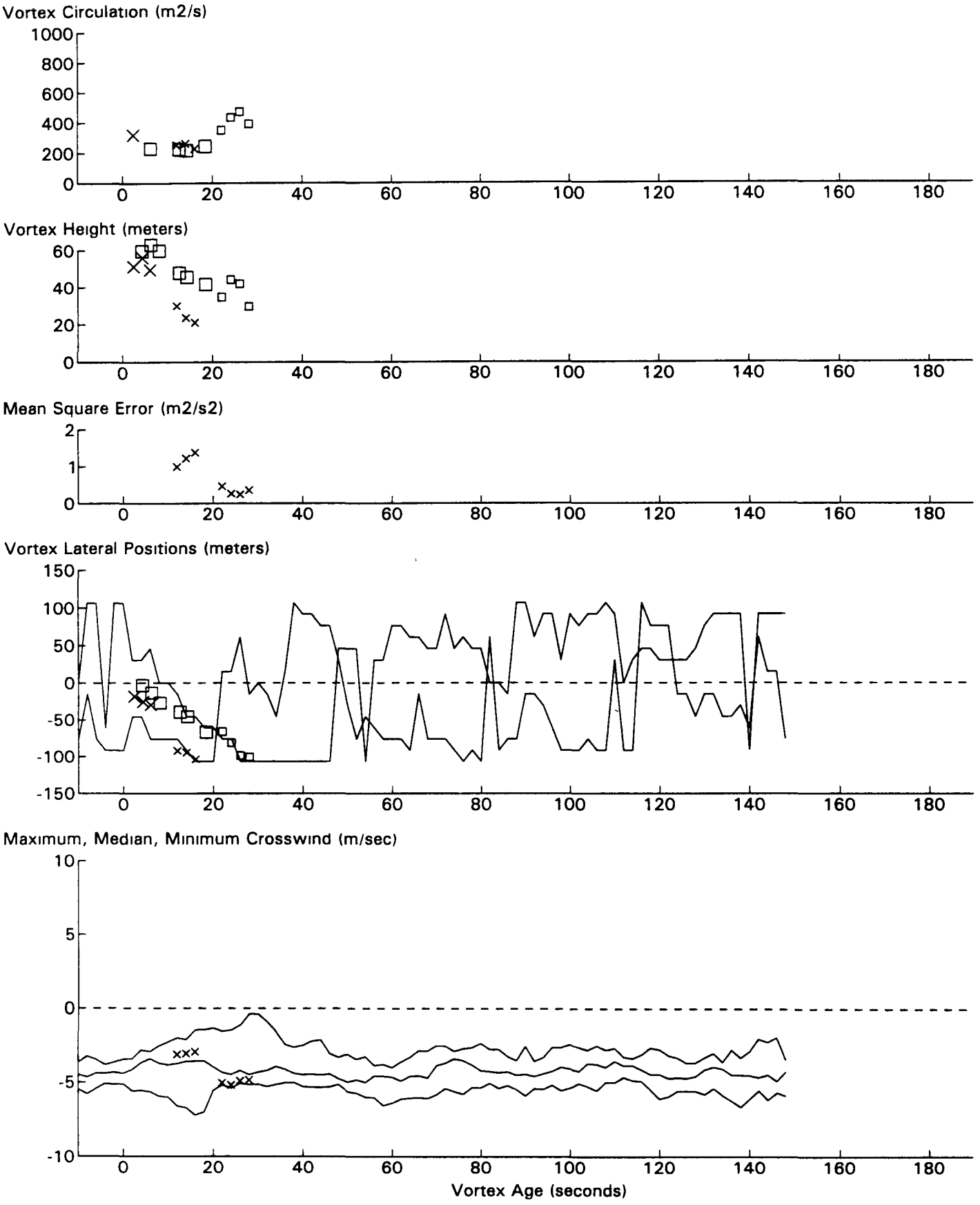

EA30 JFK 31R GWVSS Data for File: I:RM11D15.043 11/15/96 13:3:20 dt= -27 CWturb=0.44

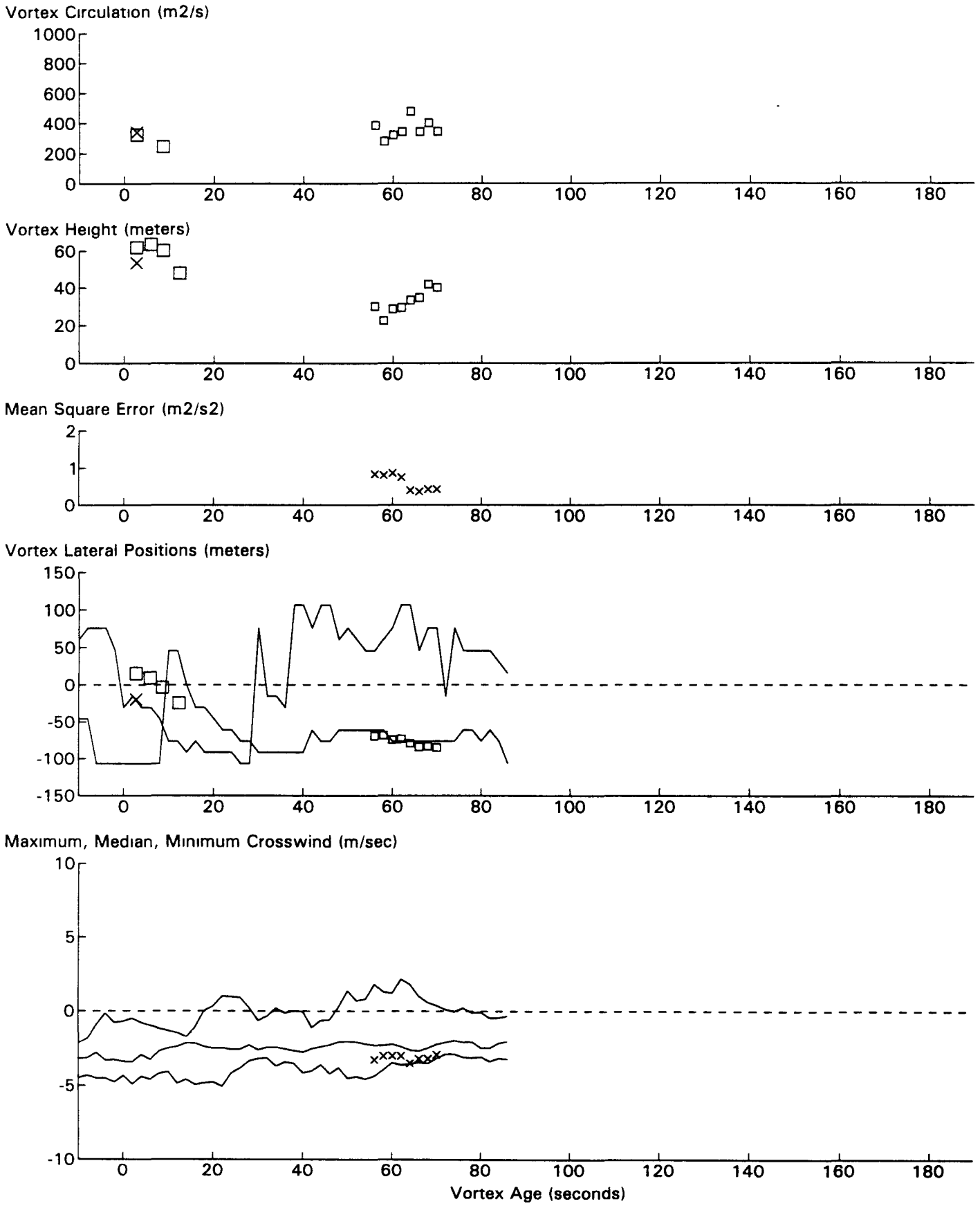

B767 JFK 31R GWVSS Data for File: I:RM11D15.141 11/15/96 20:5:4 dt= 49 CWturb=0.62

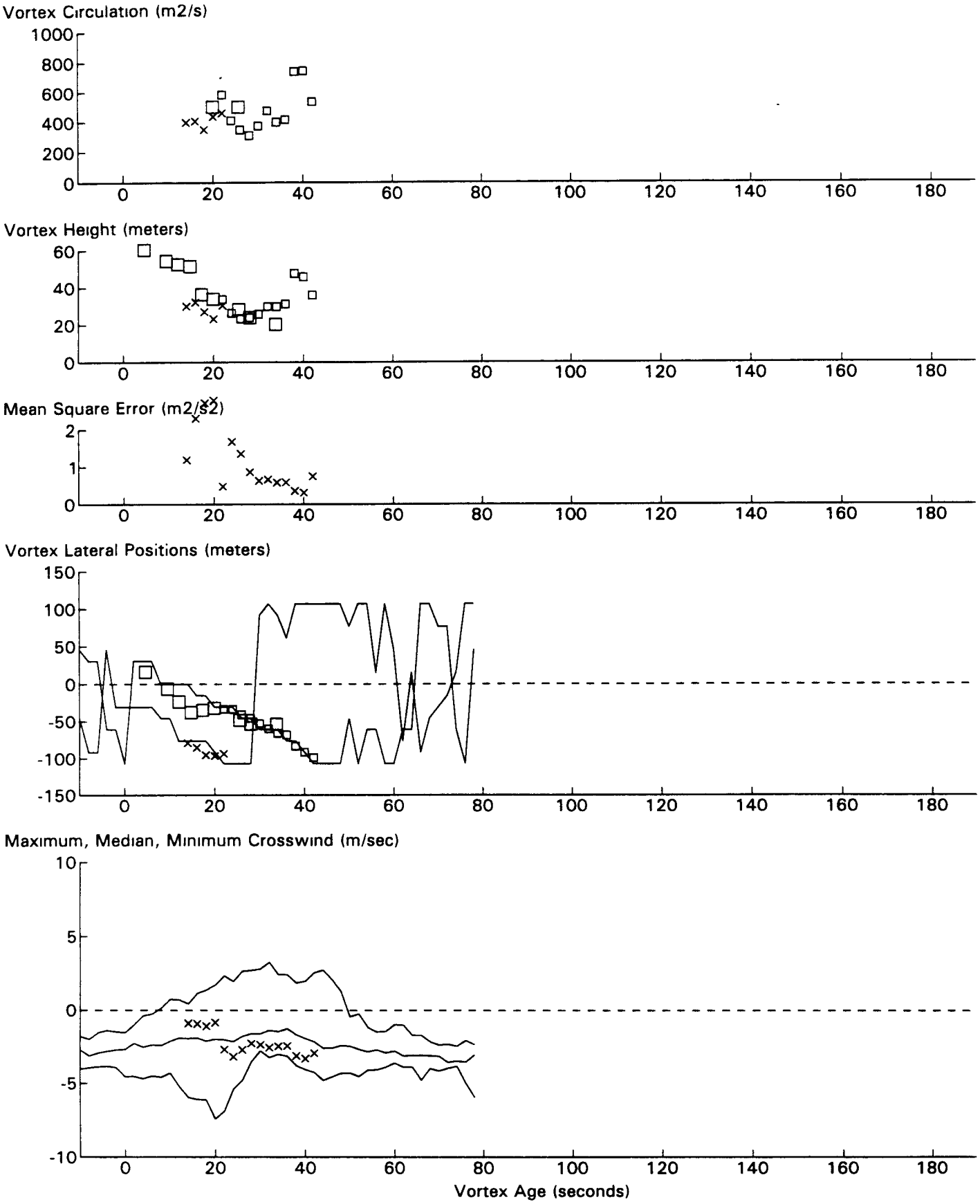

B747 JFK 31R GWVSS Data for File: I:RM11D15.147 11/15/96 20:14:16 dt= -39 CWturb=0.64

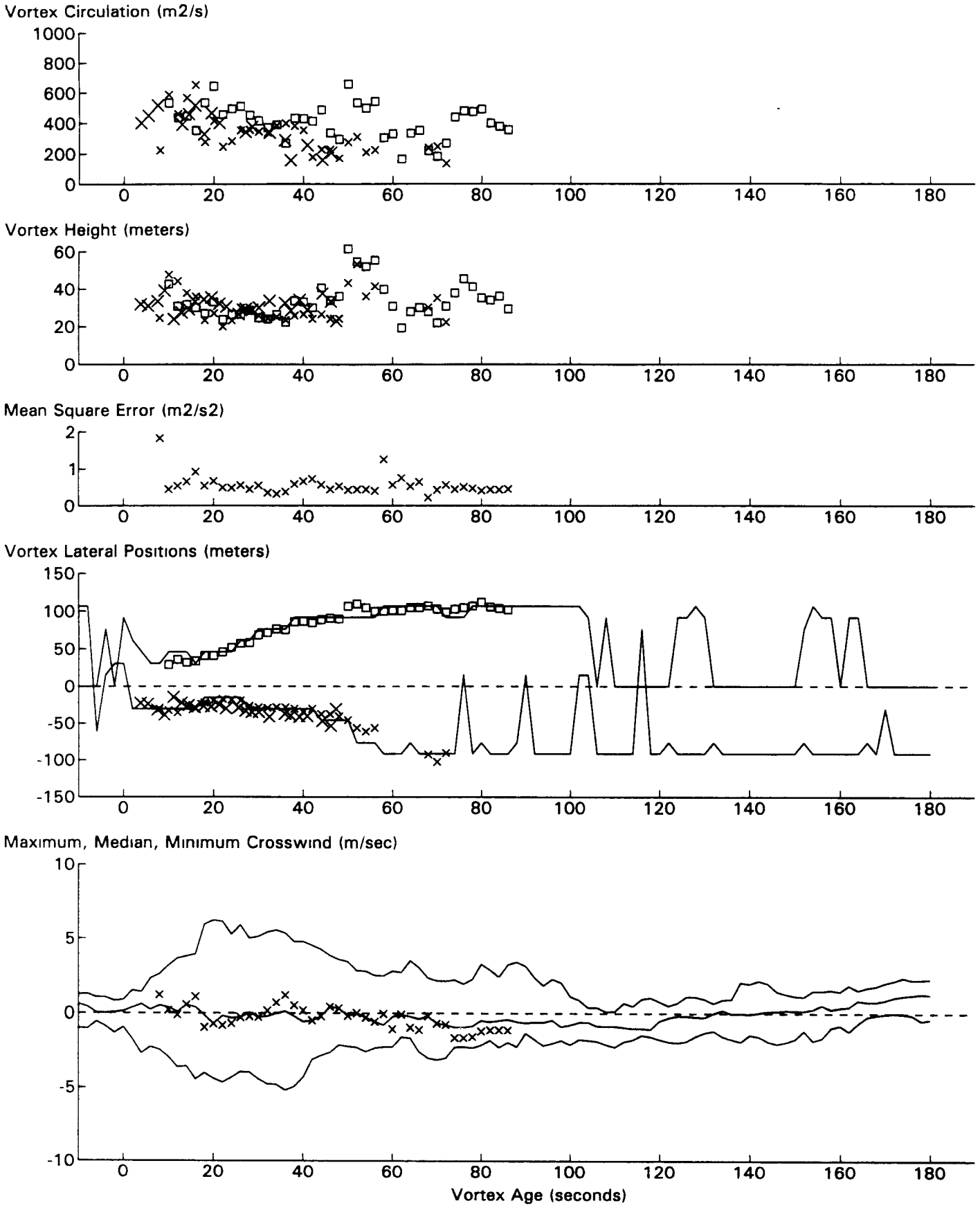

B747 JFK 31R GWVSS Data for File: I:RM11D20.228 11/20/96 18:47:50 dt= 0 CWturb=0.43

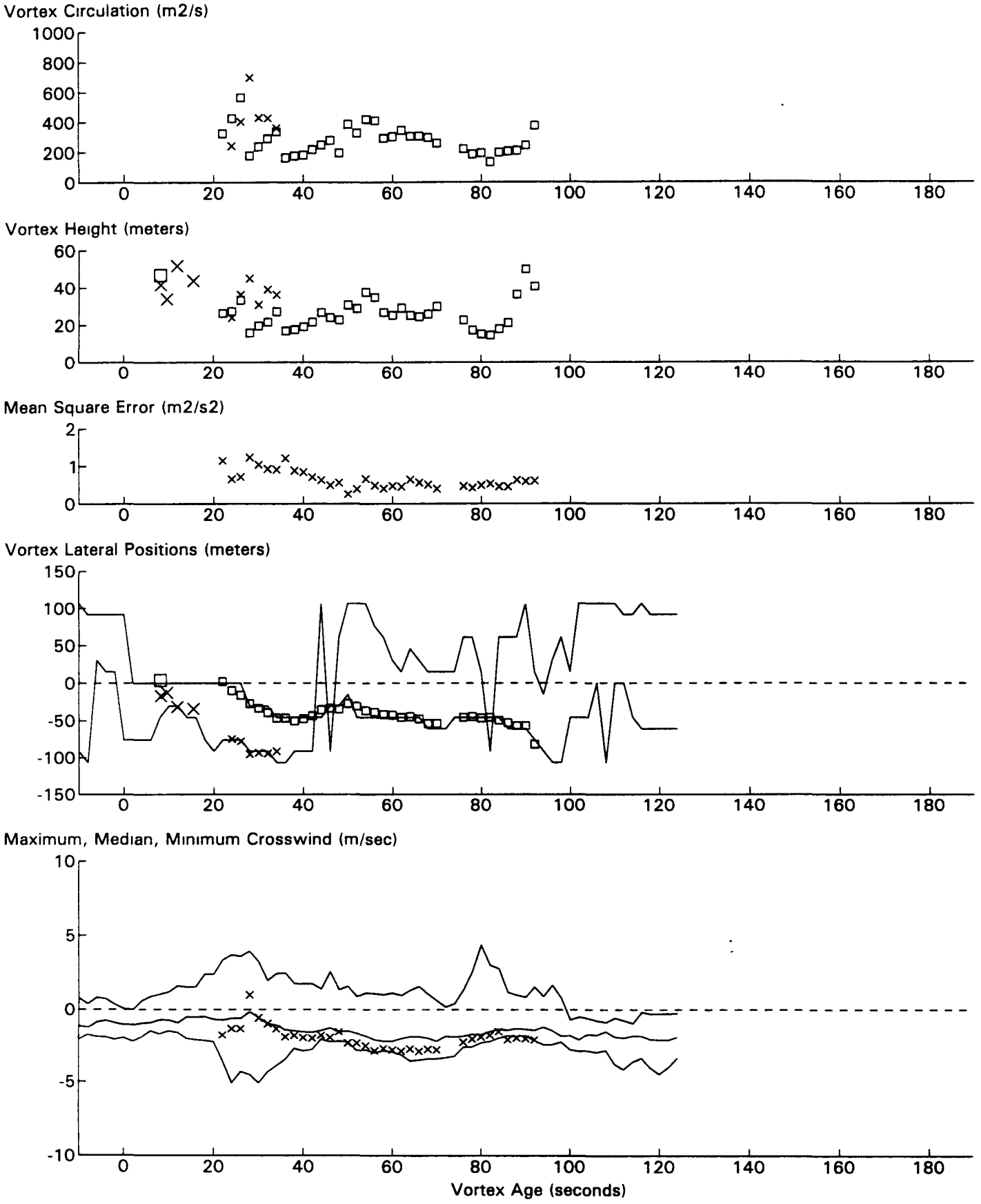

B767 JFK 31R GWVSS Data for File: I:RM11D20.235 11/20/96 19:4:56 dt= 0 CWturb=0.52

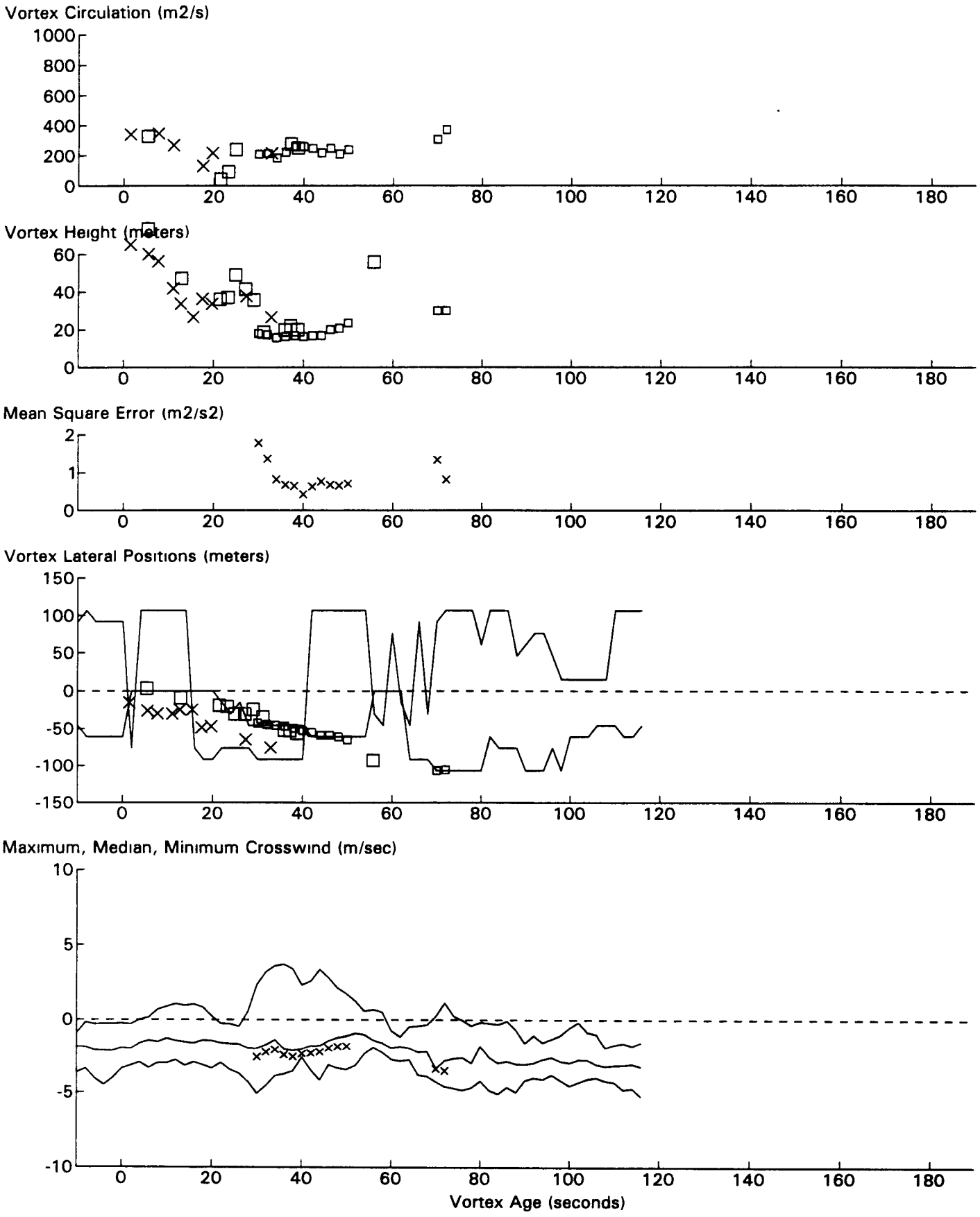

B757 JFK 31R GWVSS Data for File: I:RM11D20.236 11/20/96 19:7:0 dt= 0 CWturb=0.59

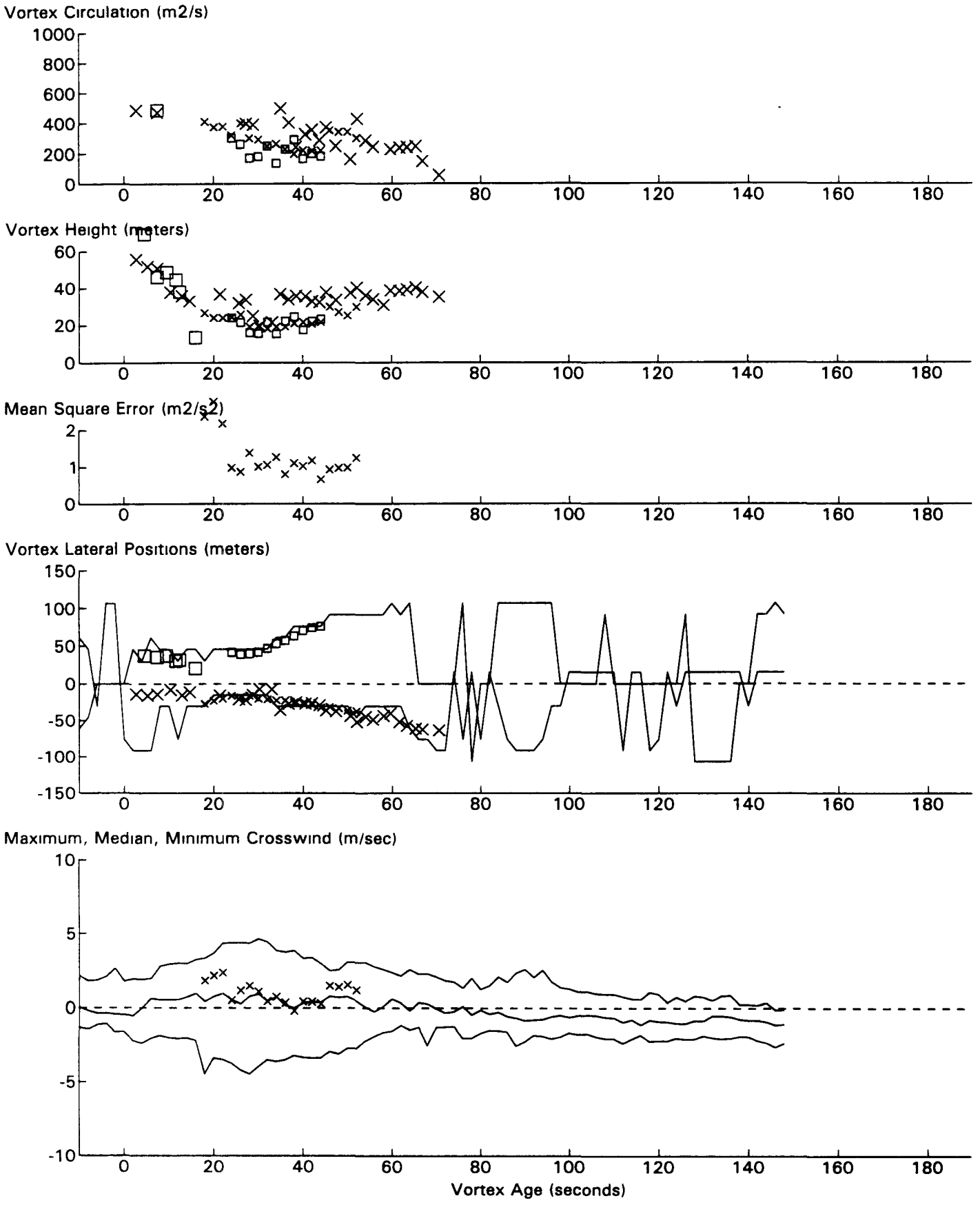

B747 JFK 31R GWVSS Data for File: I:RM11D20.238 11/20/96 19:11:26 dt= 0 CWturb=0.63

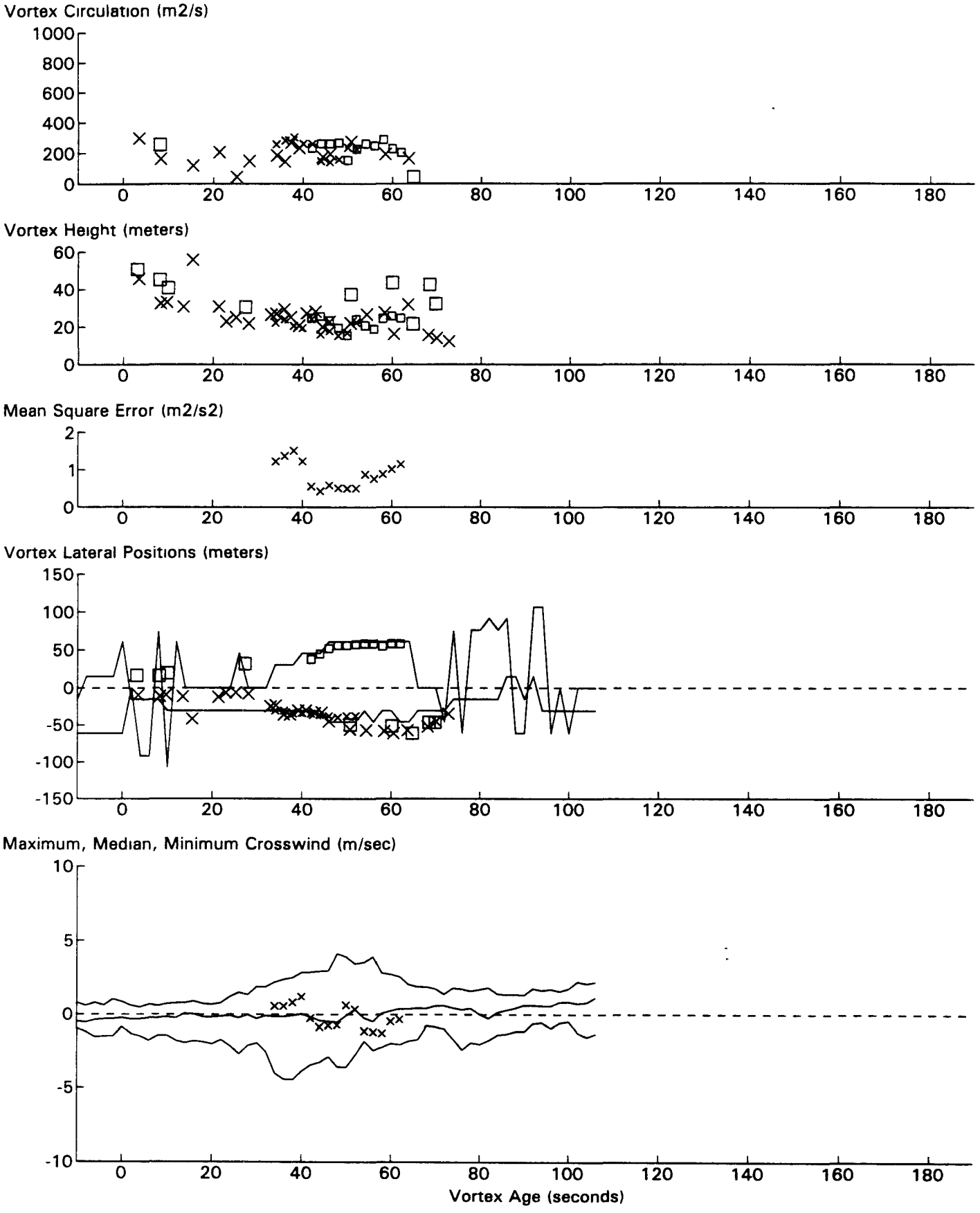

B757 JFK 31R GWVSS Data for File: I:RM11D20.242 11/20/96 19:25:43 dt= 0 CWturb=0.47

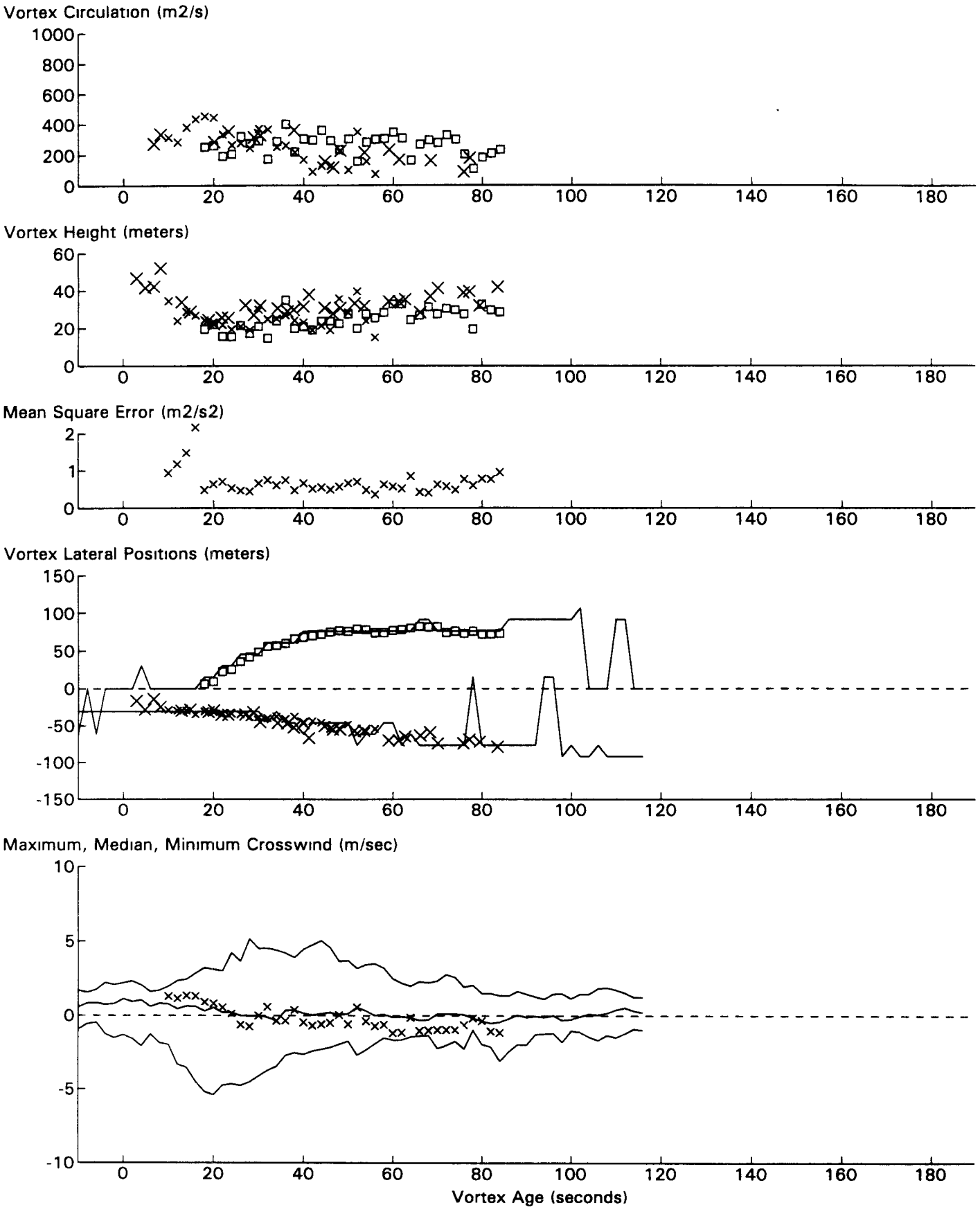

EA30 JFK 31R GWVSS Data for File: I:RM11D20.243 11/20/96 19:27:29 dt= 0 CWturb=0.42

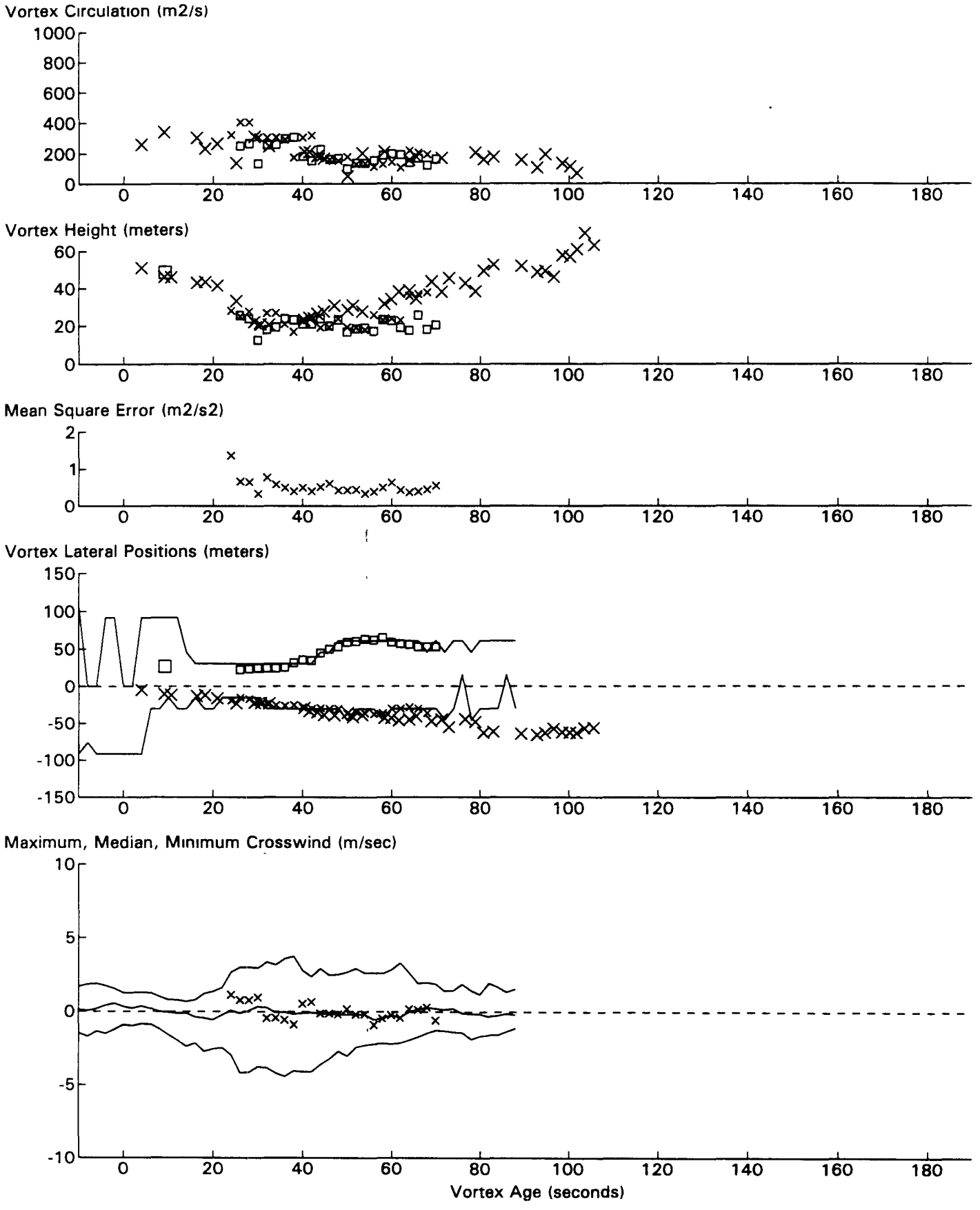

B757 JFK 31R GWVSS Data for File: I:RM11D20.244 11/20/96 19:29:25 dt= 0 CWturb=0.39

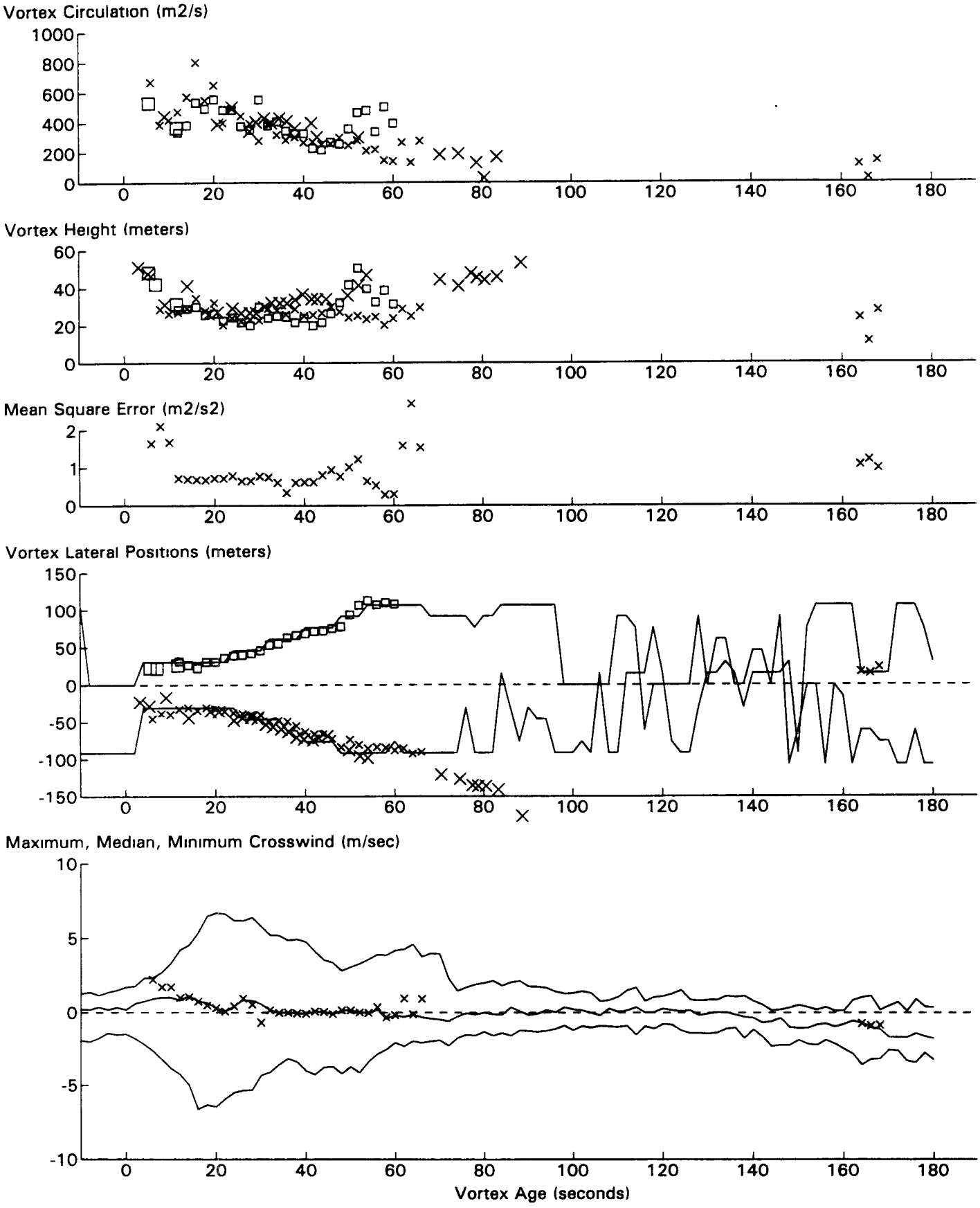

B747 JFK 31R GWVSS Data for File: I:RM11D20.246 11/20/96 19:32:55 dt= 0 CWturb=0.37

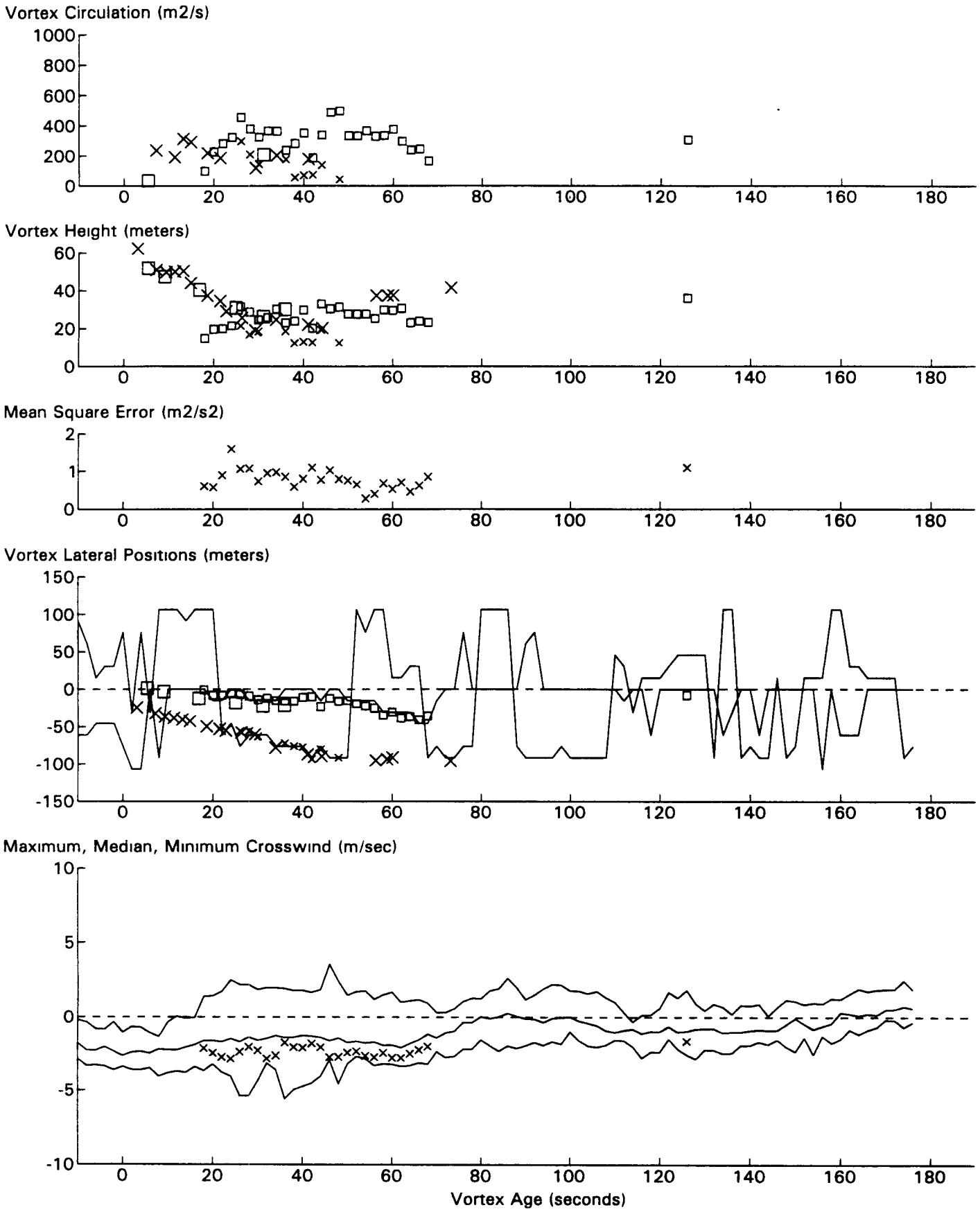

B757 JFK 31R GWVSS Data for File: I:RM11D20.247 11/20/96 19:36:9 dt= 0 CWturb=0.43

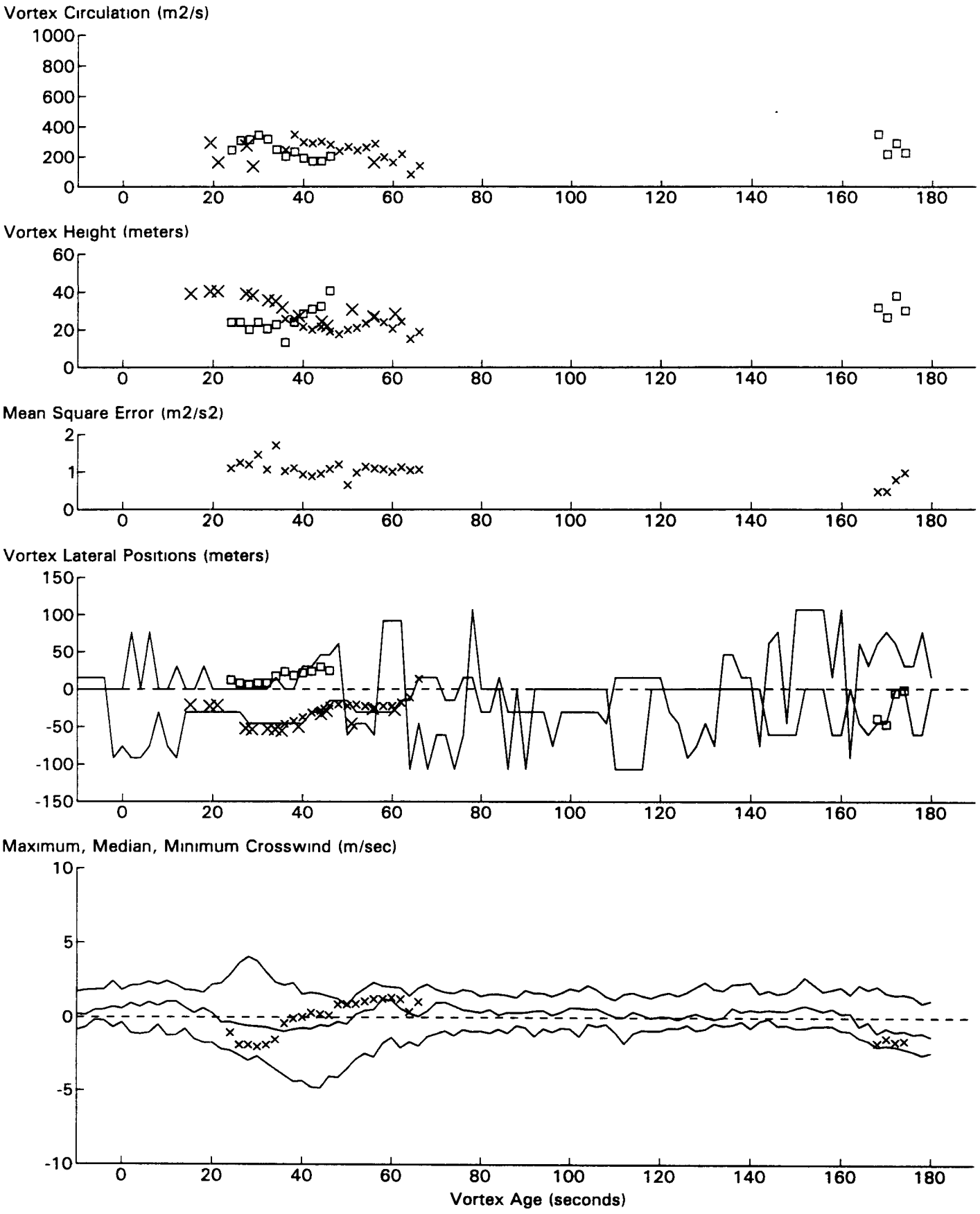

B767 JFK 31R GWVSS Data for File: I:RM11D20.248 11/20/96 19:39:5 dt= 0 CWturb=0.46

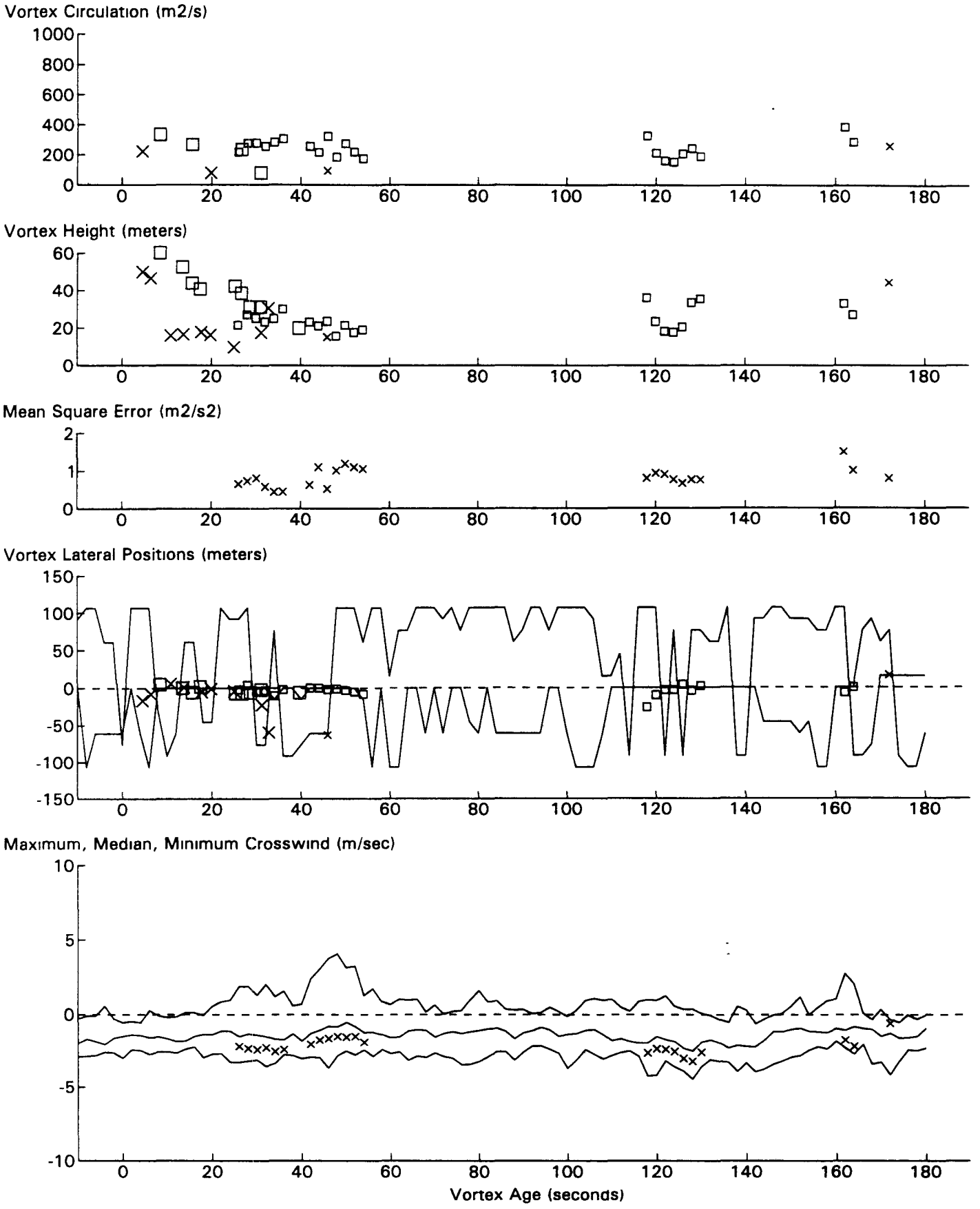

B767 JFK 31R GWVSS Data for File: I:RM11D20.249 11/20/96 19:43:39 dt= 0 CWturb=0.48

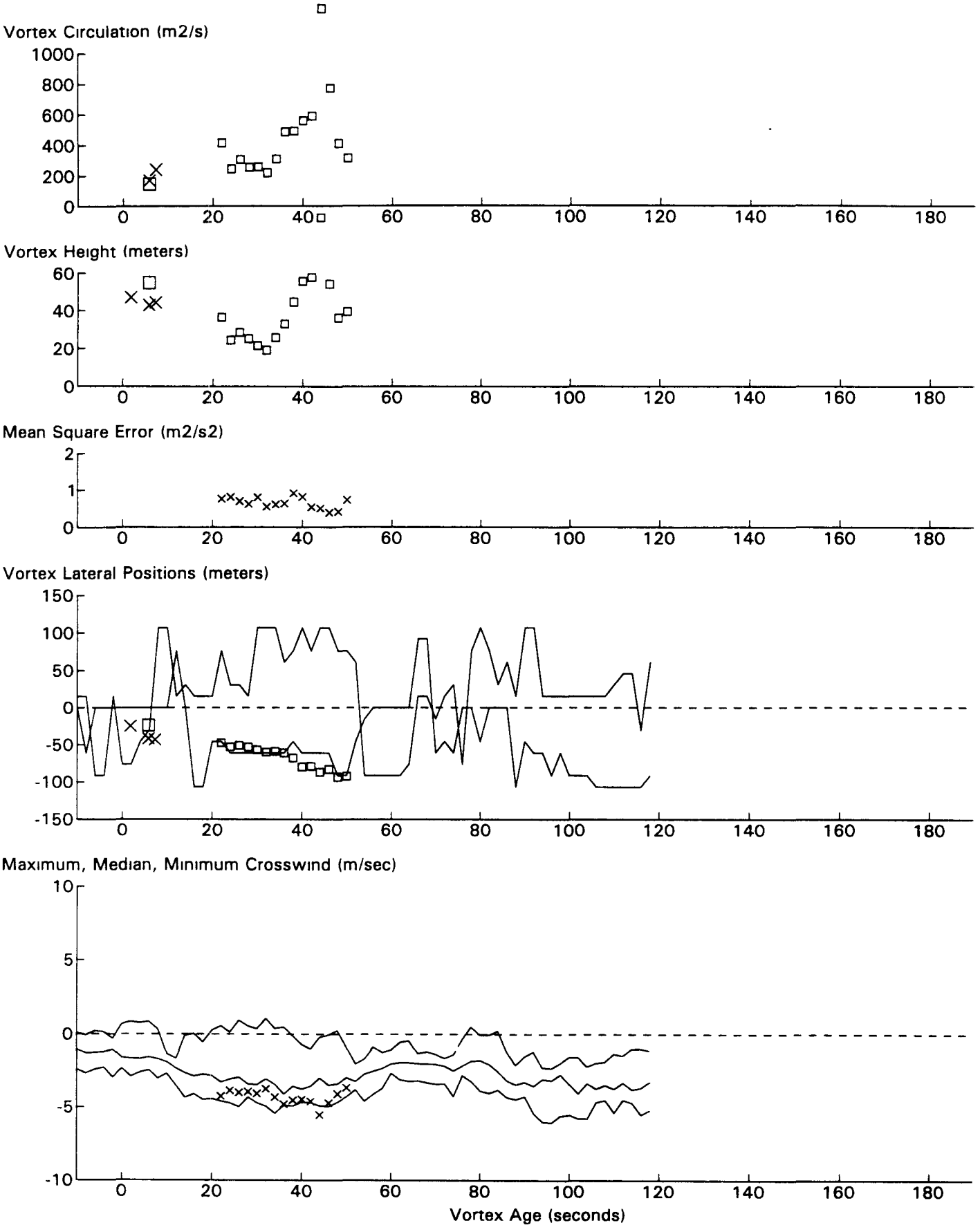

B727 JFK 31R GWVSS Data for File: I:RM11D20.250 11/20/96 19:47:33 dt = 0 CWturb = 0.52

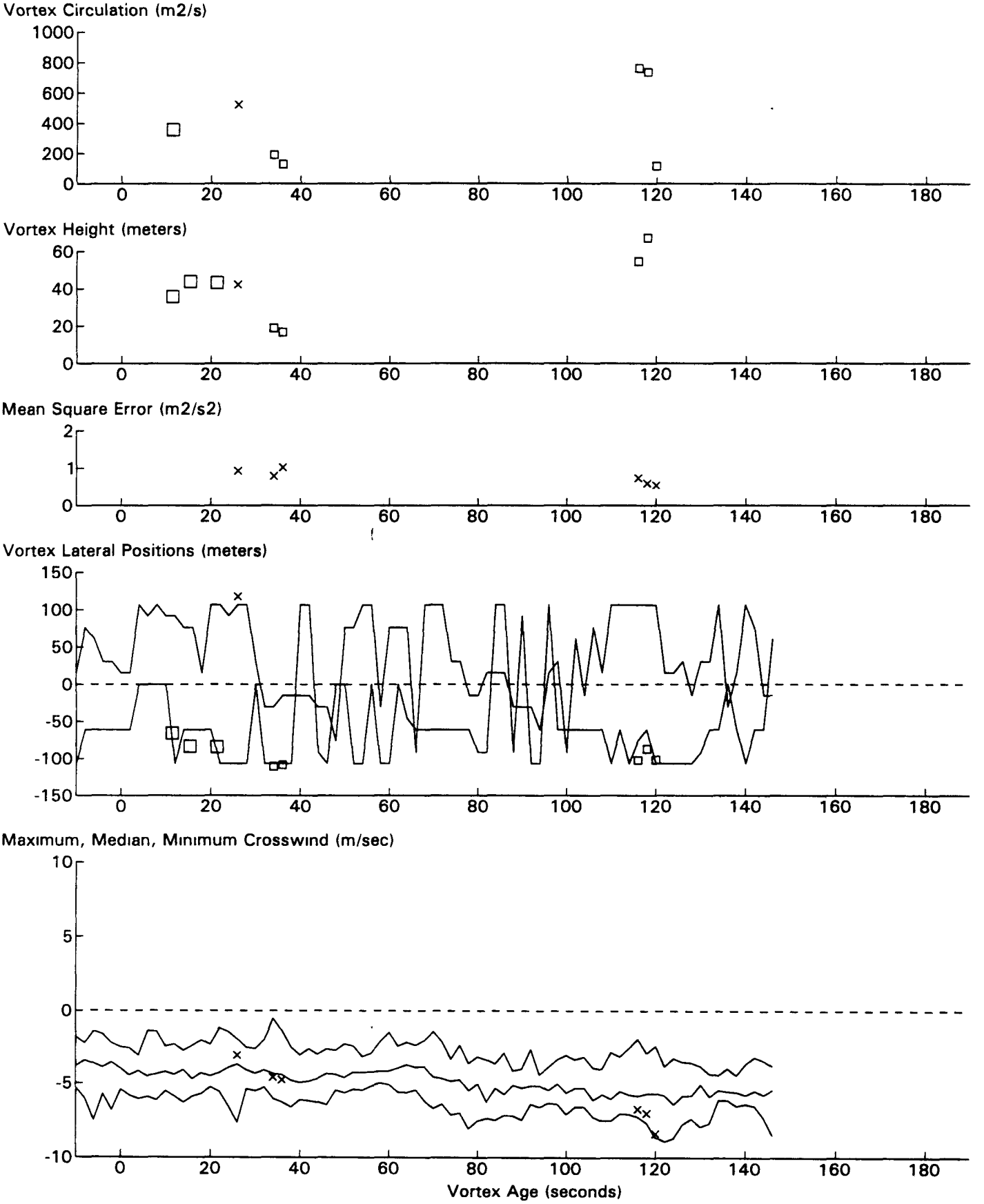

B767 JFK 31R GWVSS Data for File: I:RM11D20.253 11/20/96 19:54:13 dt= 0 CWturb=0.59

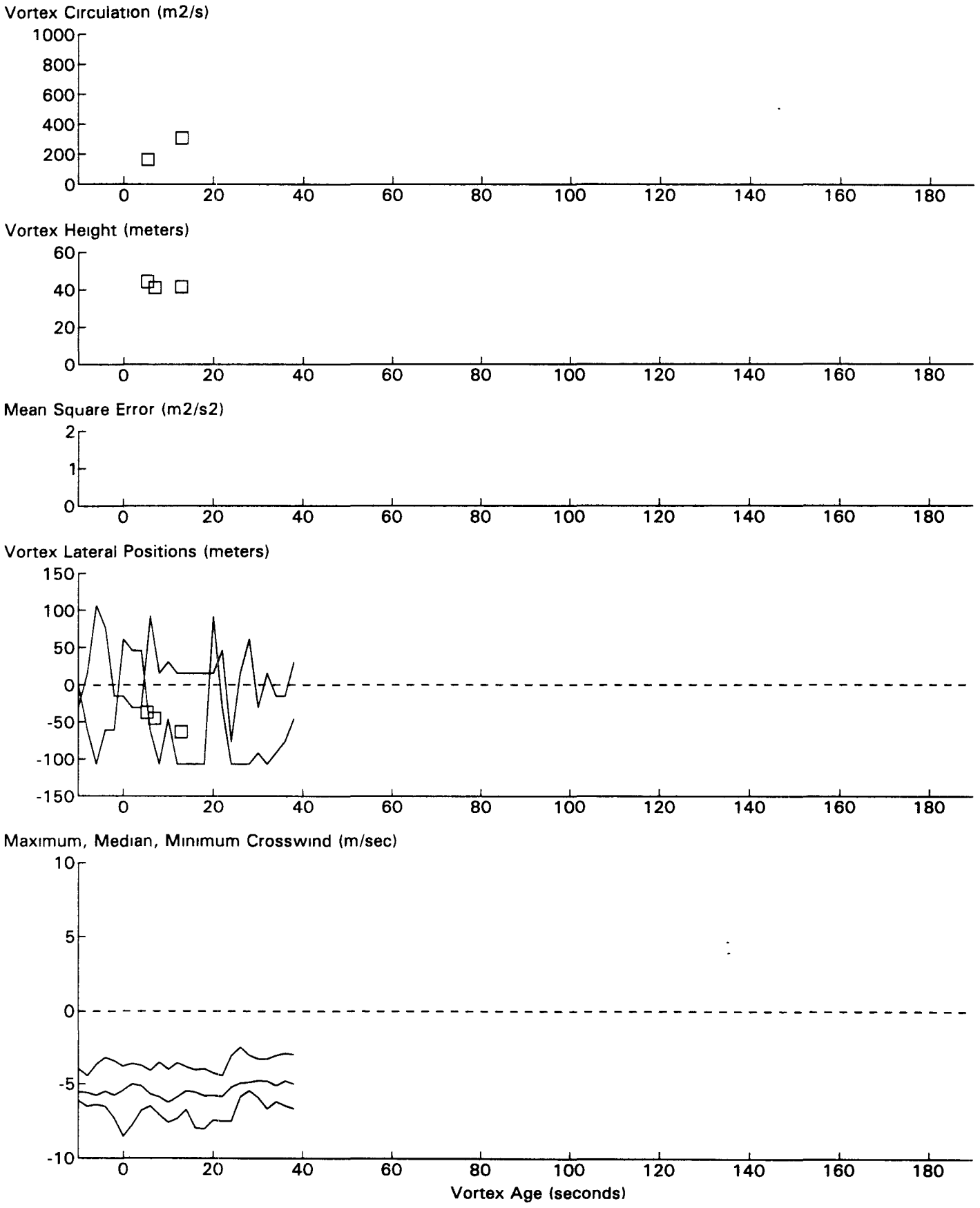

B727 JFK 31R GWVSS Data for File: I:RM11D20.254 11/20/96 19:56:39 dt= 0 CWturb=0.64

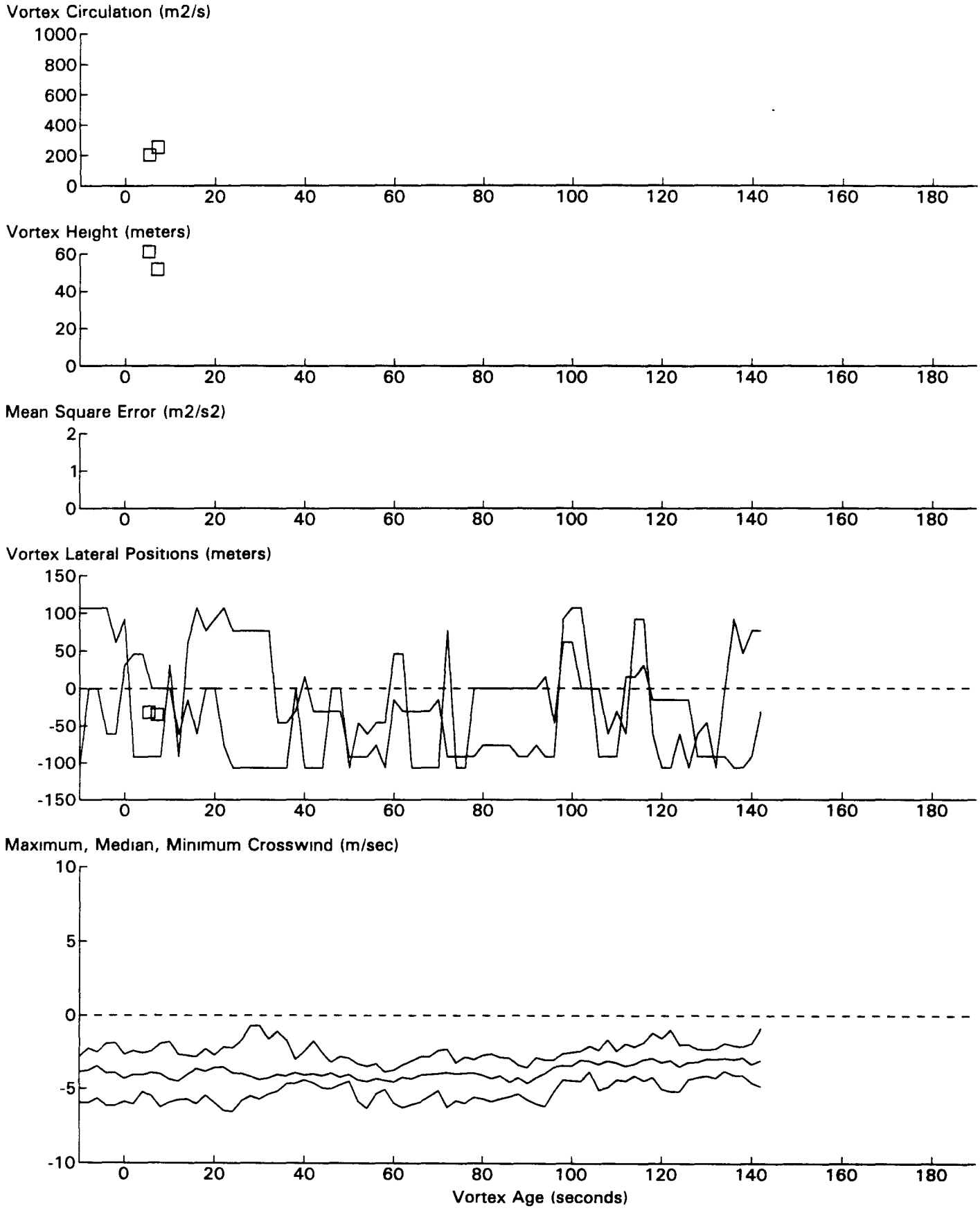

B767 JFK 31R GWVSS Data for File: I:RM11D20.257 11/20/96 19:59:12 dt= 0 CWturb=0.68

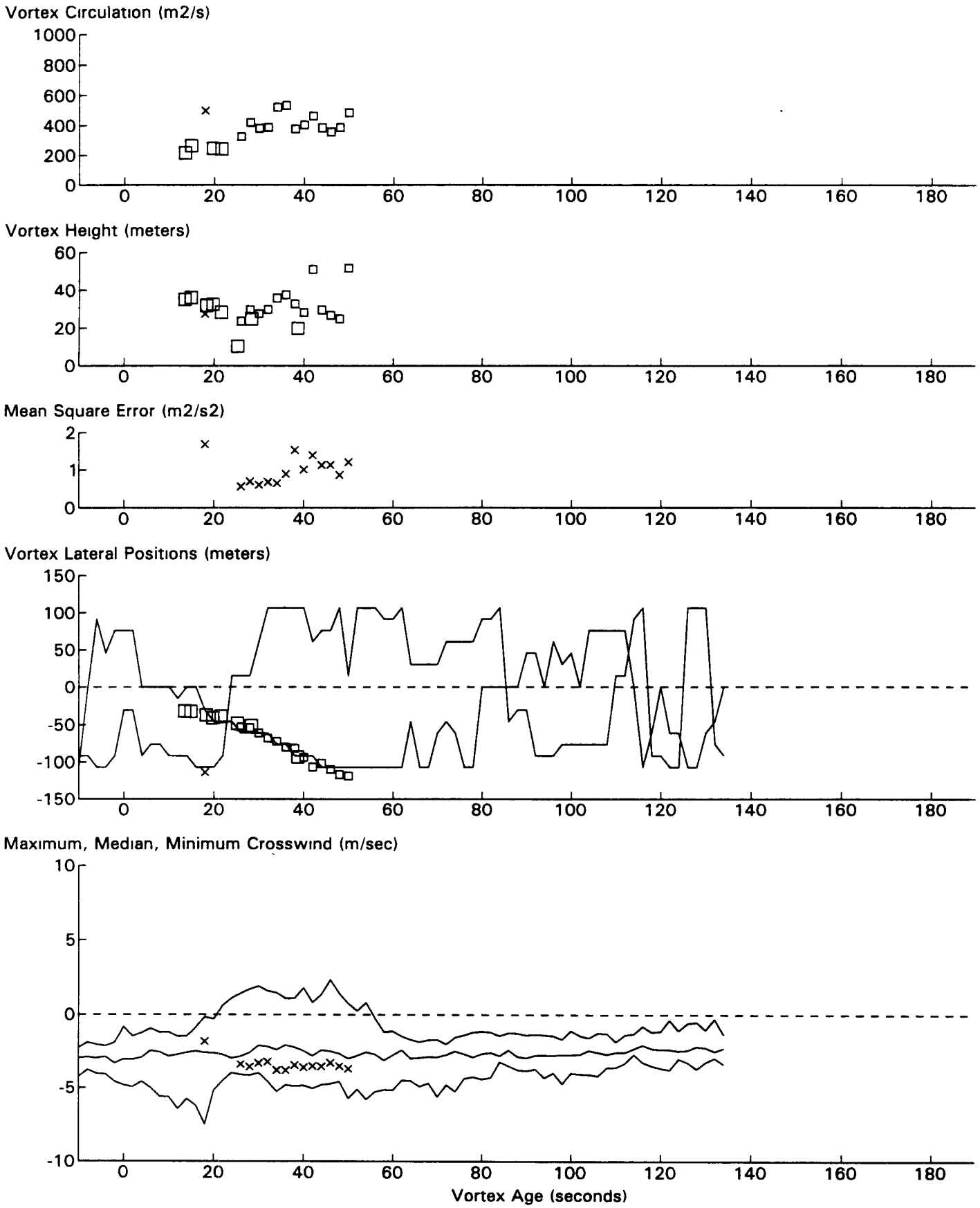

EA34 JFK 31R GWVSS Data for File: I:RM11D20.258 11/20/96 20:1:34 dt= 0 CWturb=0.69

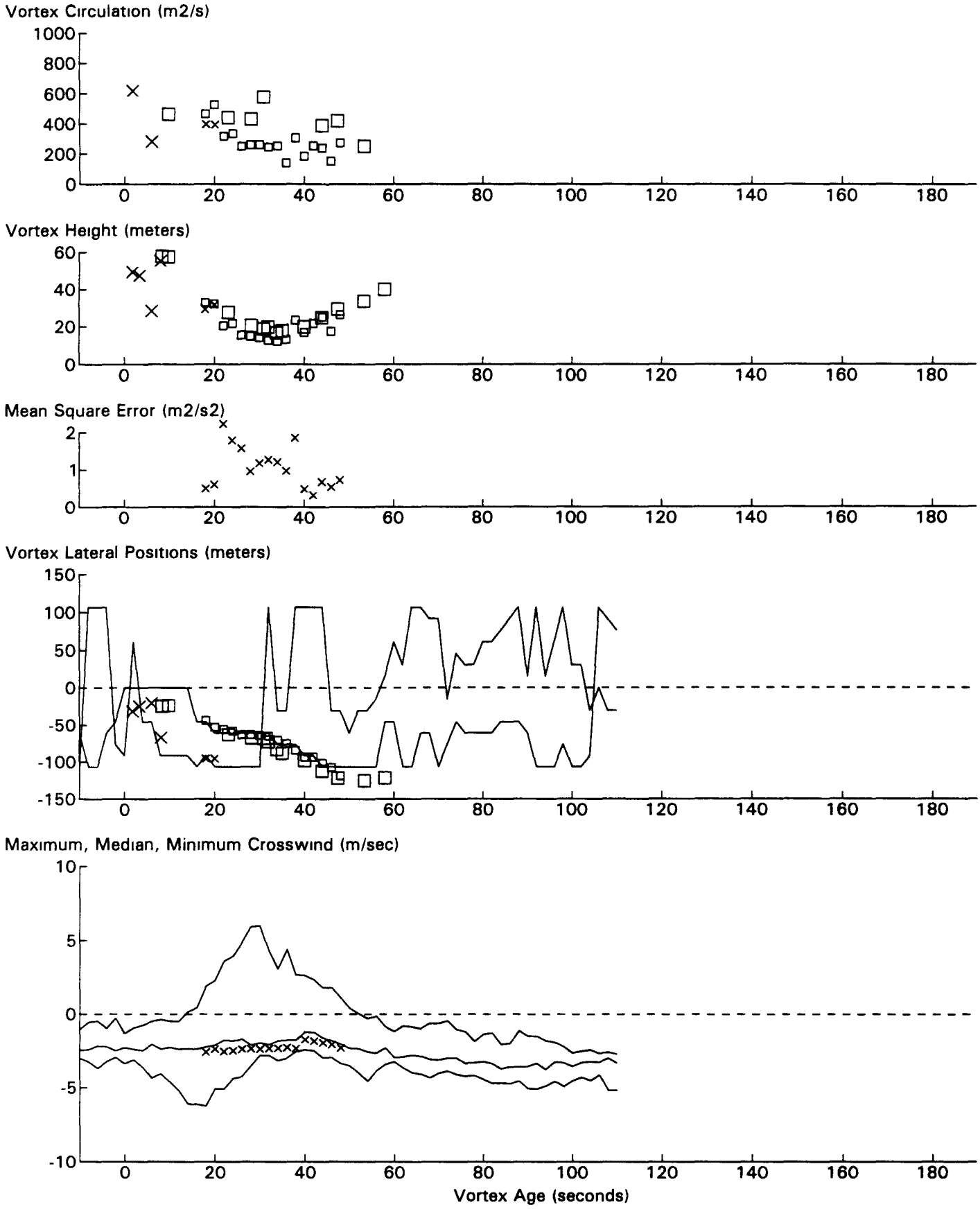

B747 JFK 31R GWVSS Data for File: I:RM11D20.259 11/20/96 20:3:48 dt= 0 CWturb=0.66

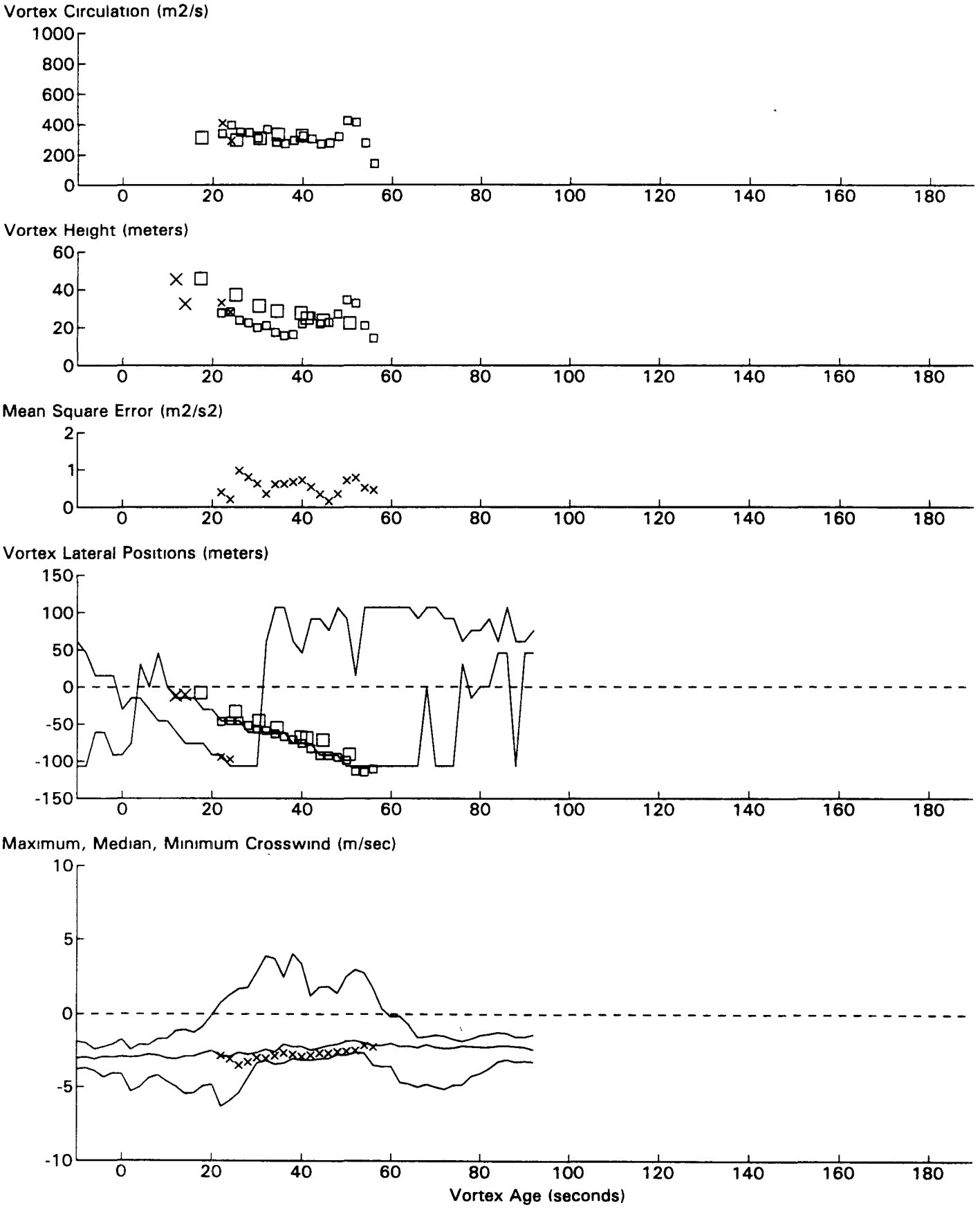

L101 JFK 31R GWVSS Data for File: I:RM11D20.265 11/20/96 20:12:15 dt= 0 CWturb=0.52

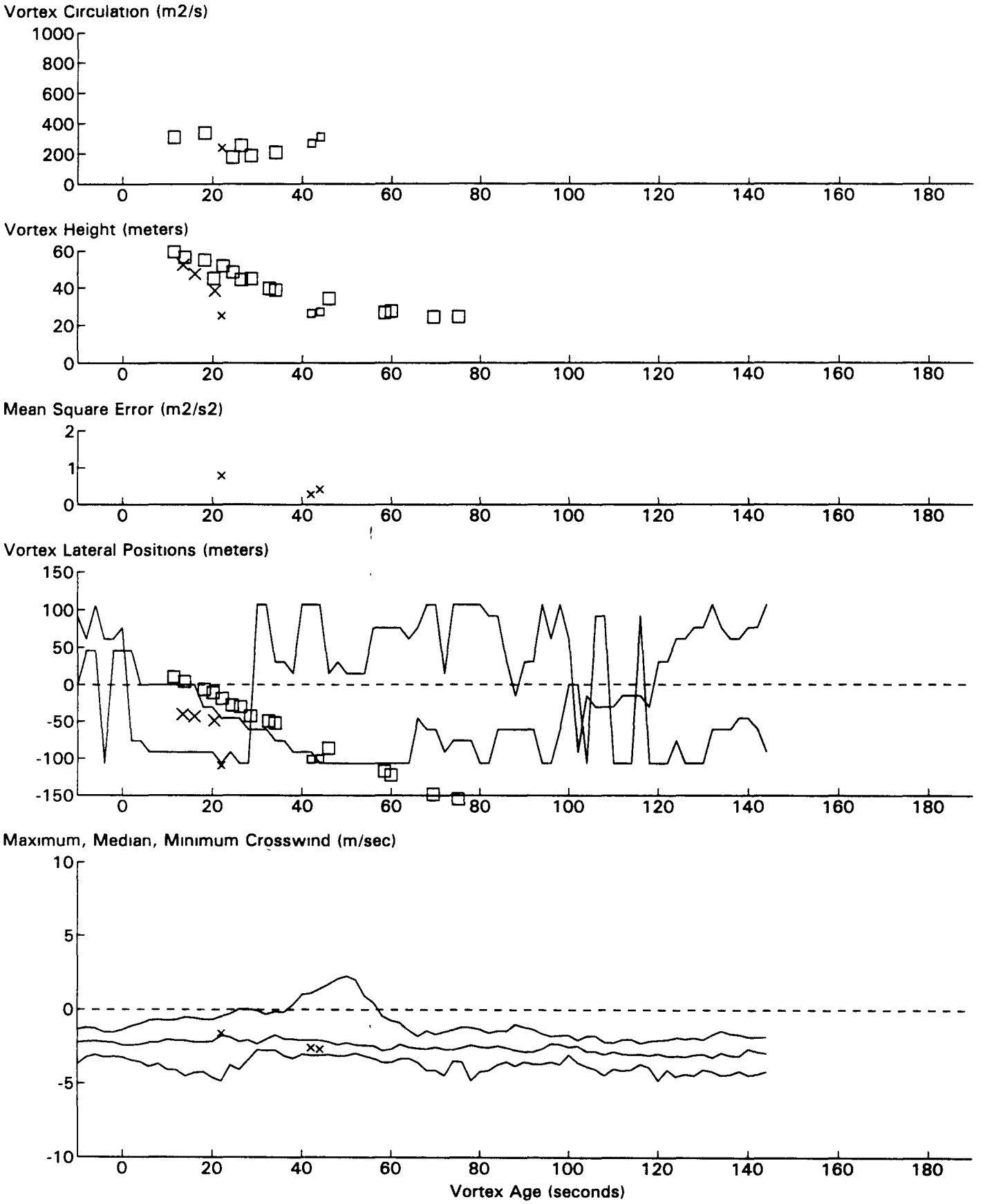

EA33 JFK 31R GWVSS Data for File: I:RM11D20.266 11/20/96 20:13:48 dt= 0 CWturb=0.51

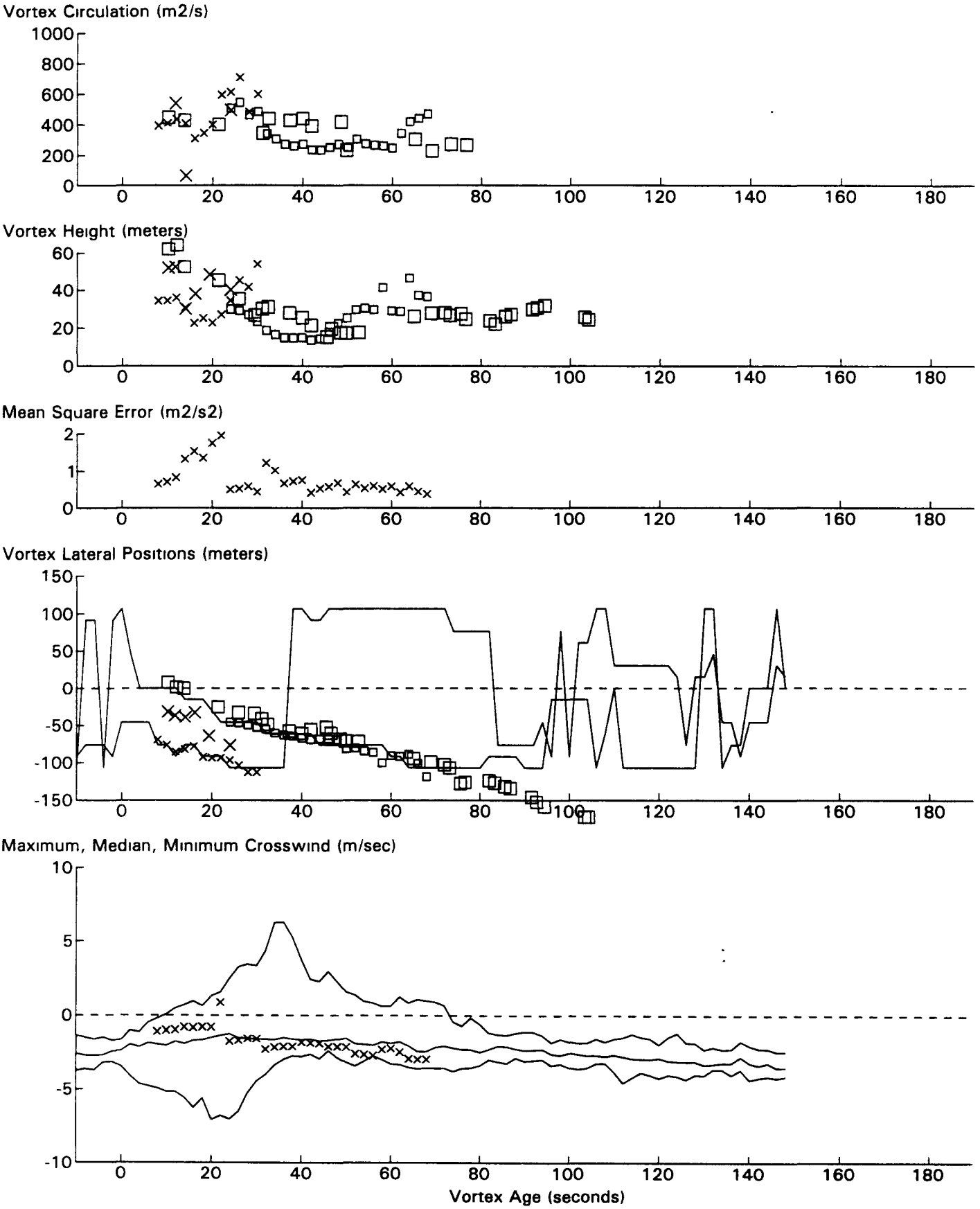

B747 JFK 31R GWVSS Data for File: I:RM11D20.268 11/20/96 20:18:8 dt= 0 CWturb=0.49

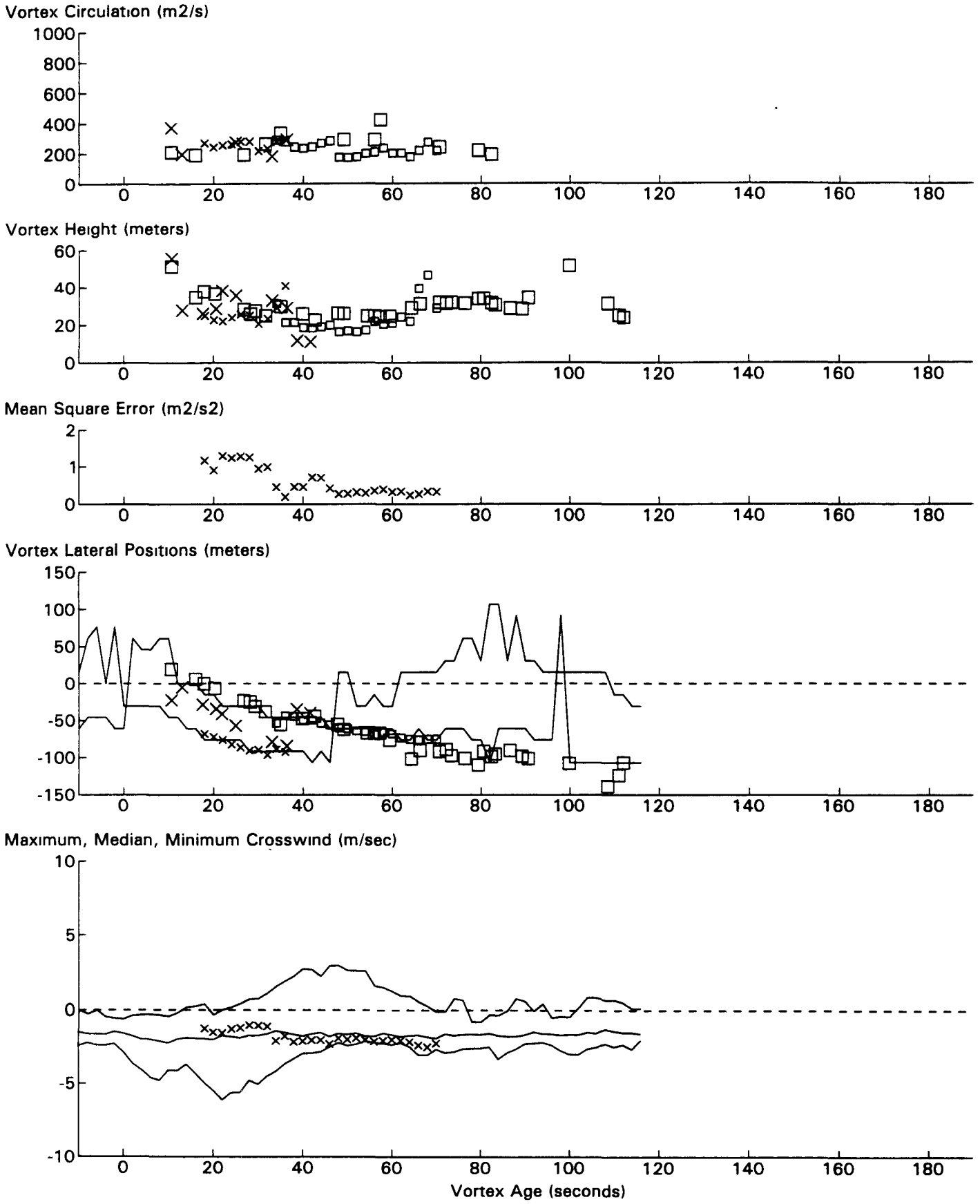

L101 JFK 31R GWVSS Data for File: I:RM11D20.271 11/20/96 20:25:24 dt= 0 CWturb=0.44

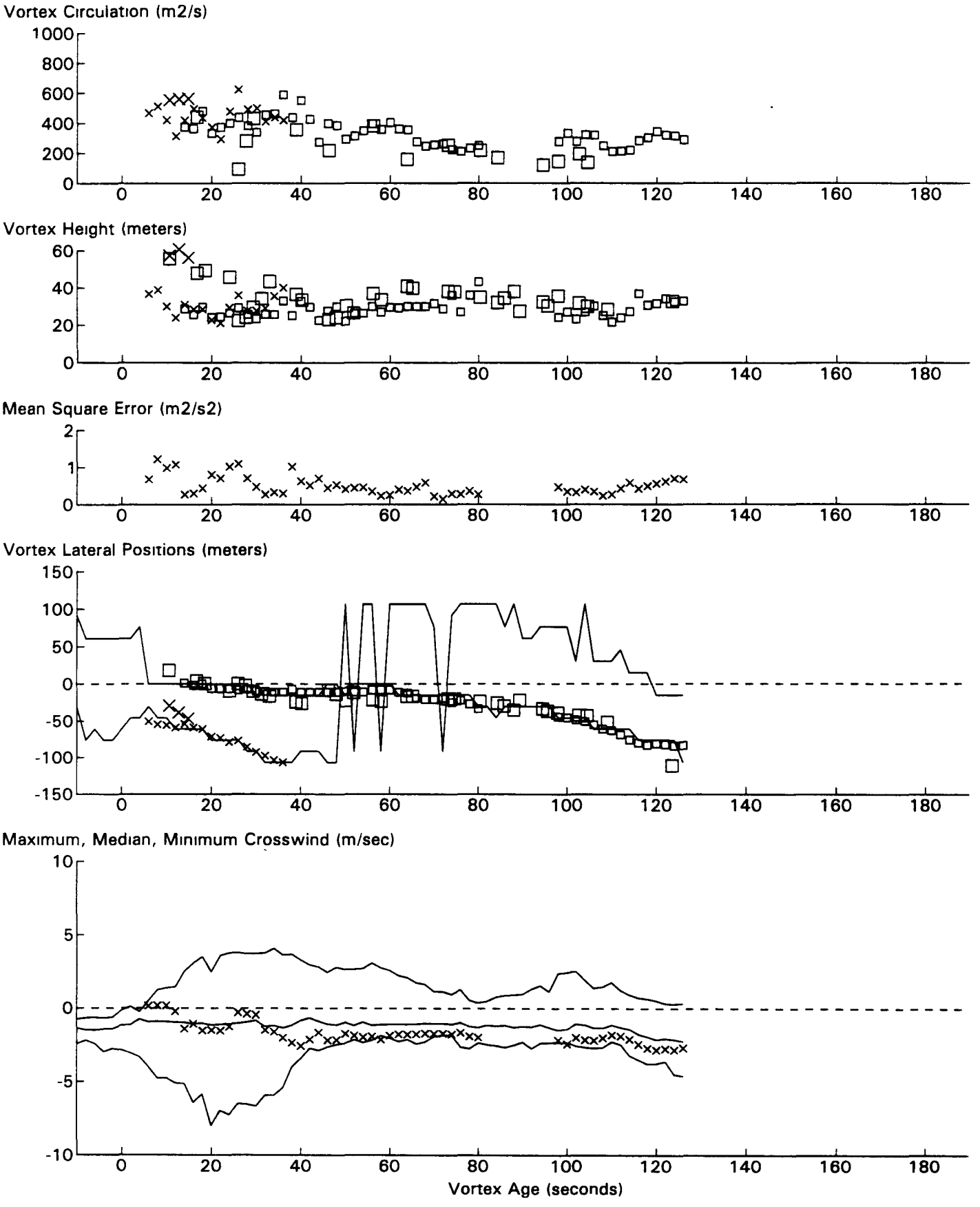

B747 JFK 31R GWVSS Data for File: I:RM11D20.274 11/20/96 20:30:44 dt= 0 CWturb=0.38

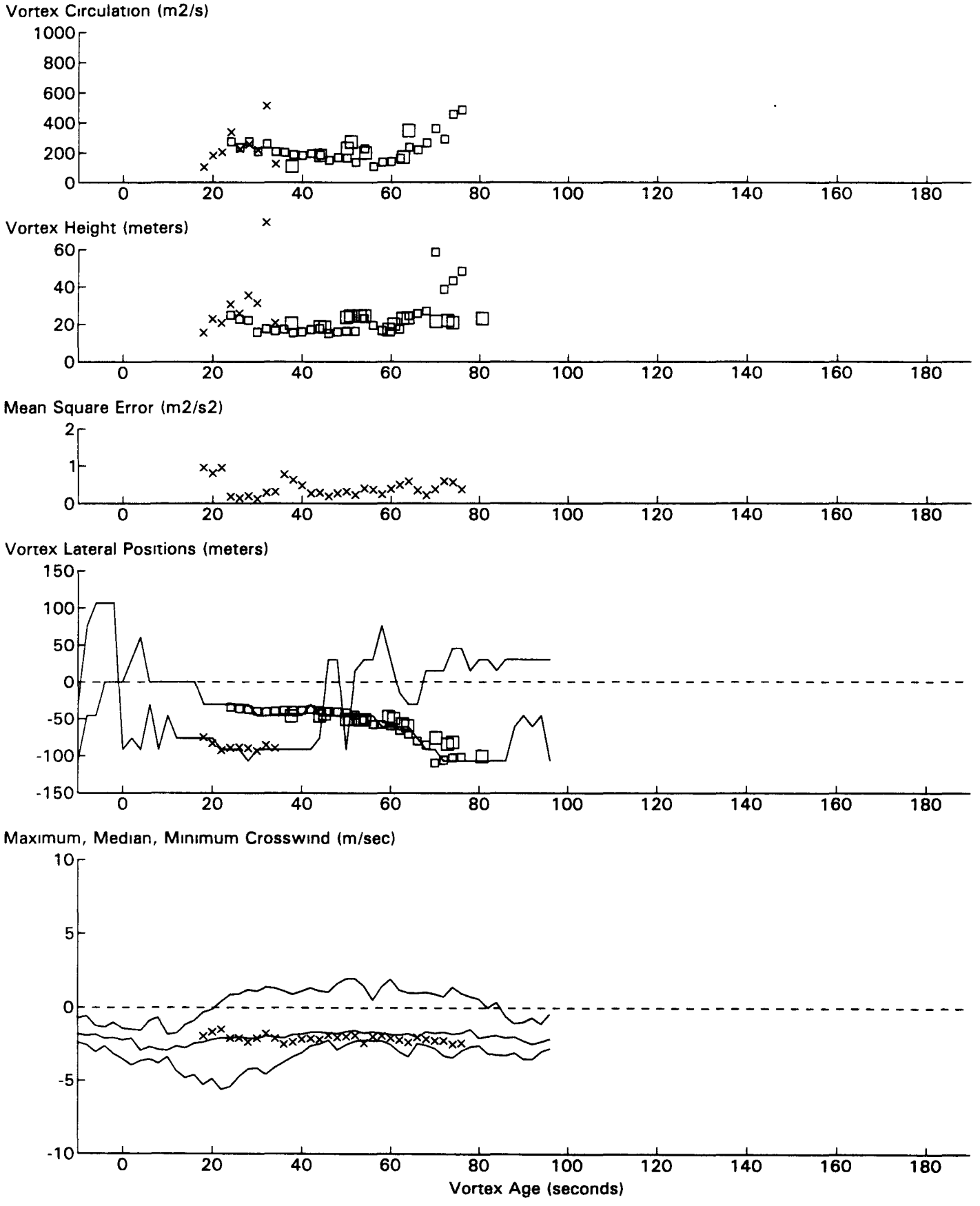

MD11 JFK 31R GWVSS Data for File: I:RM11D20.276 11/20/96 20:33:56 dt= 0 CWturb=0.38

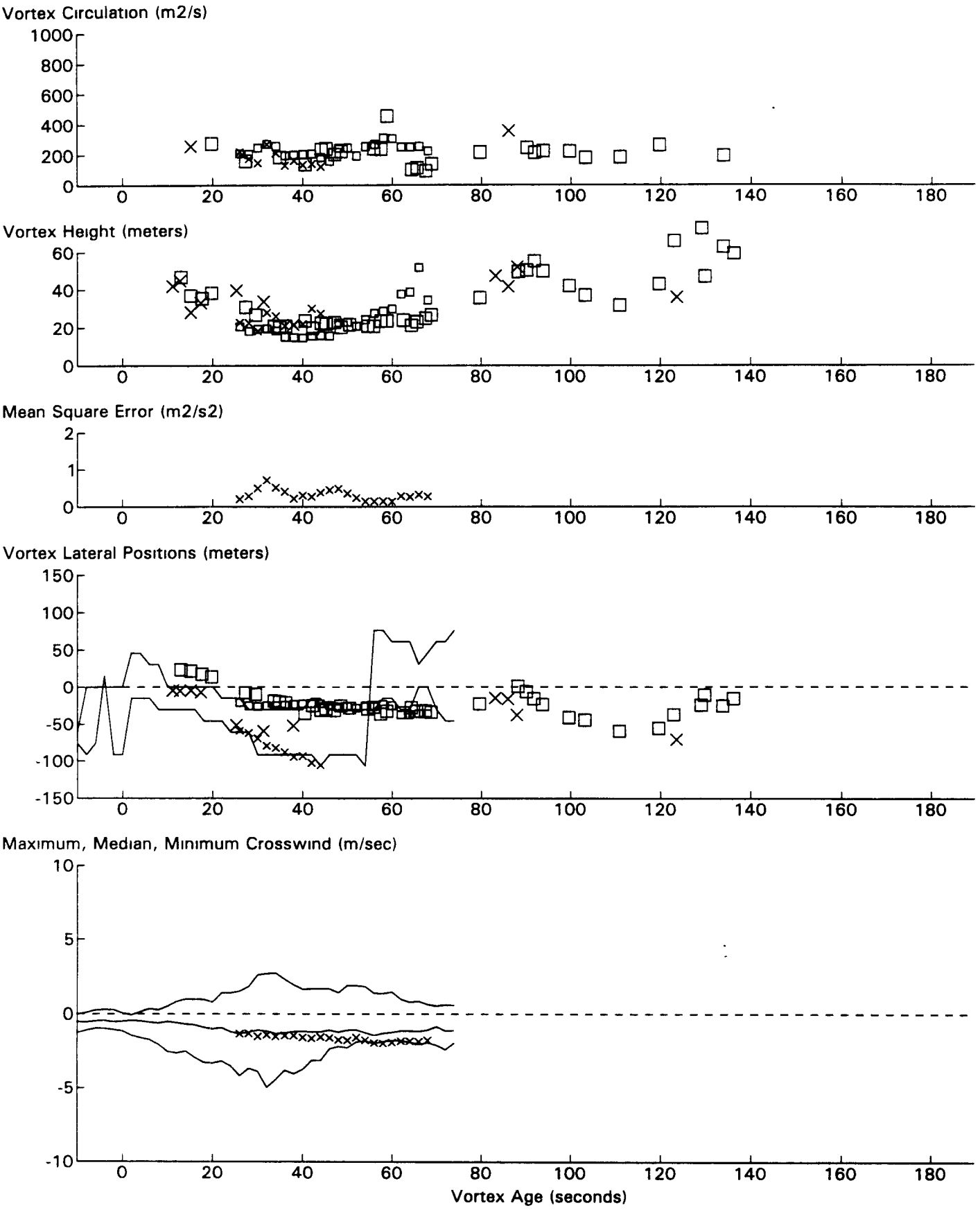

B757 JFK 31R GWVSS Data for File: I:RM11D20.278 11/20/96 20:37:46 dt= 0 CWturb=0.39

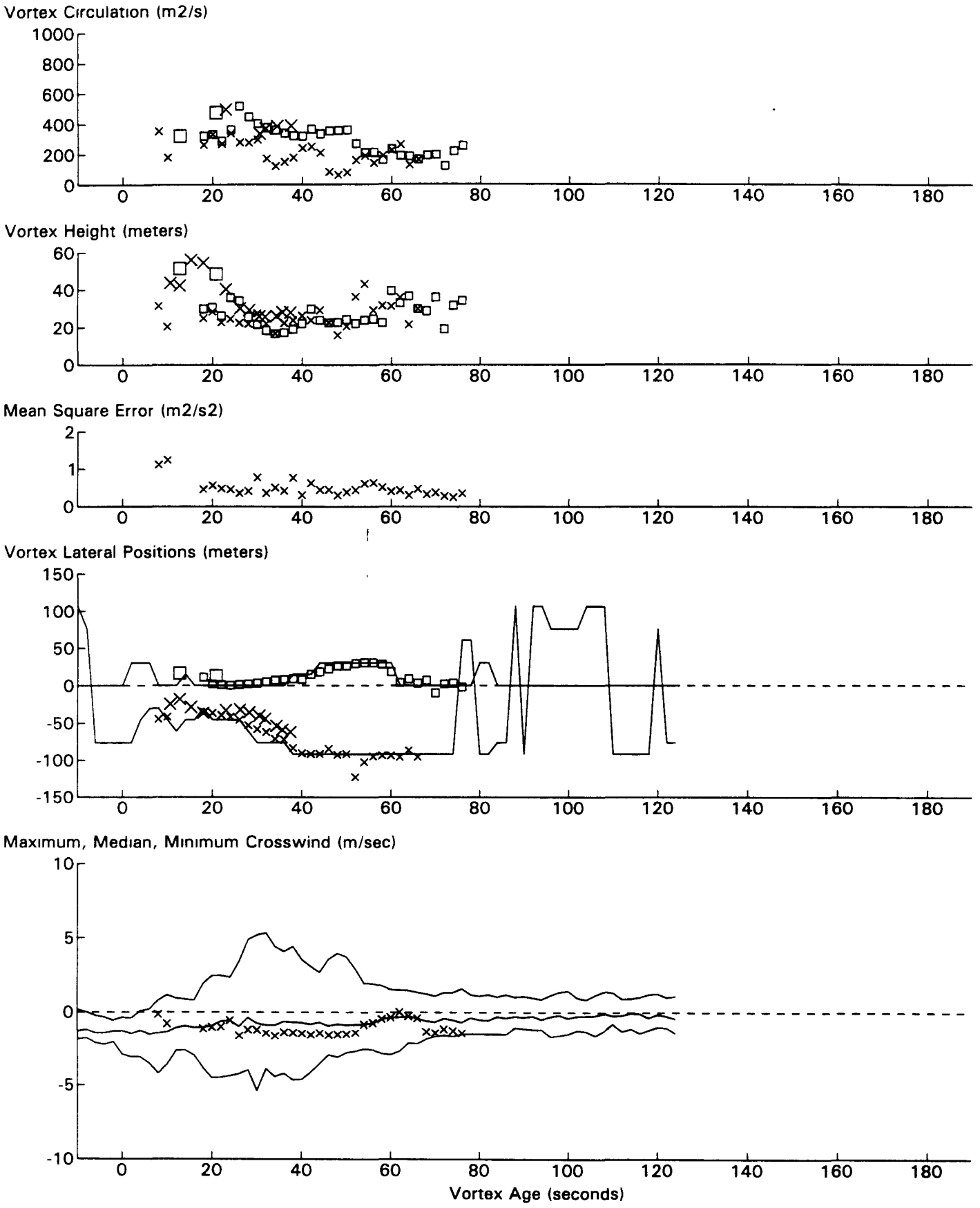

B747 JFK 31R GWVSS Data for File: I:RM11D20.280 11/20/96 20:41:16 dt= 0 CWturb=0.37

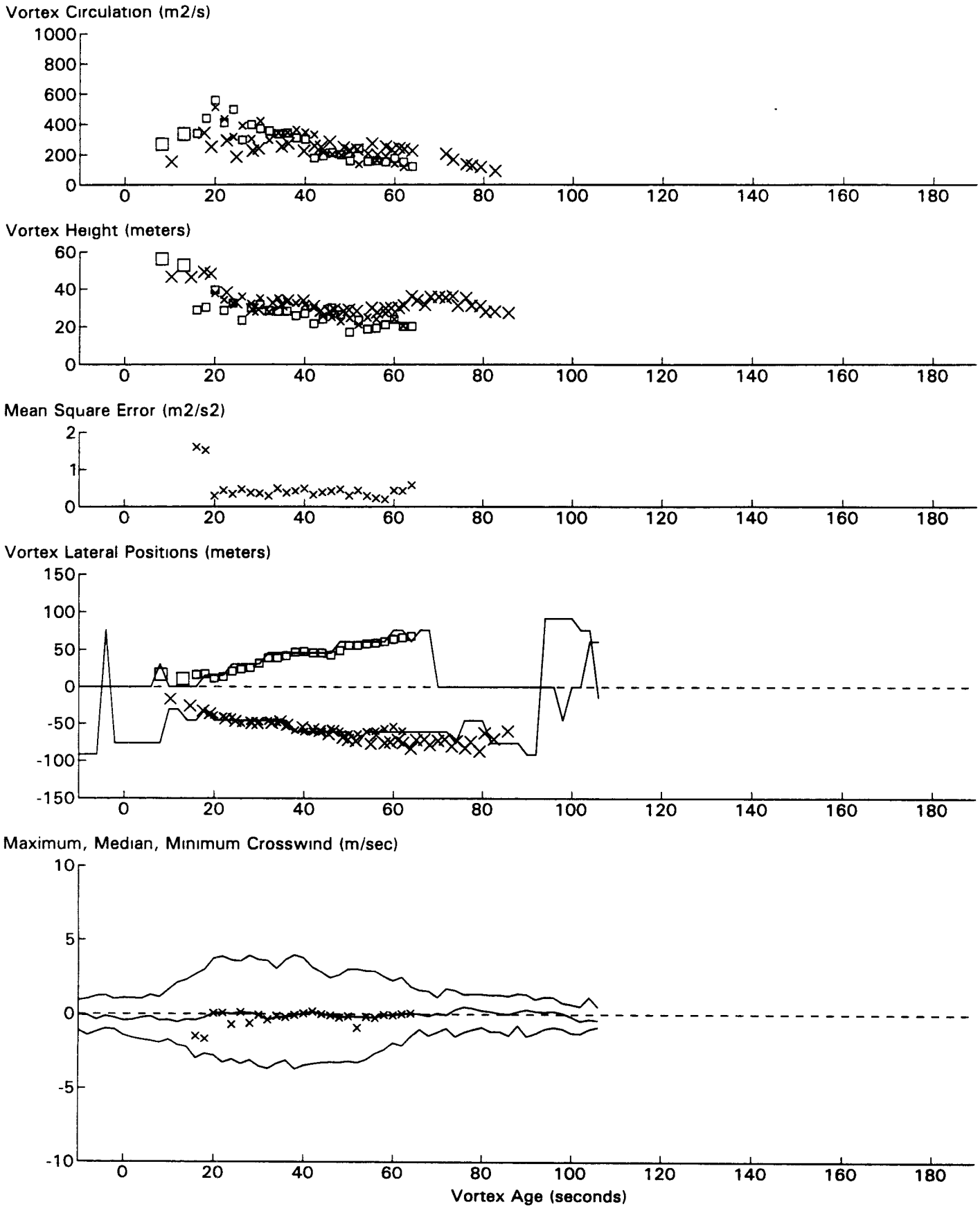

B767 JFK 31R GWVSS Data for File: I:RM11D20.281 11/20/96 20:43:20 dt= 0 CWturb=0.36

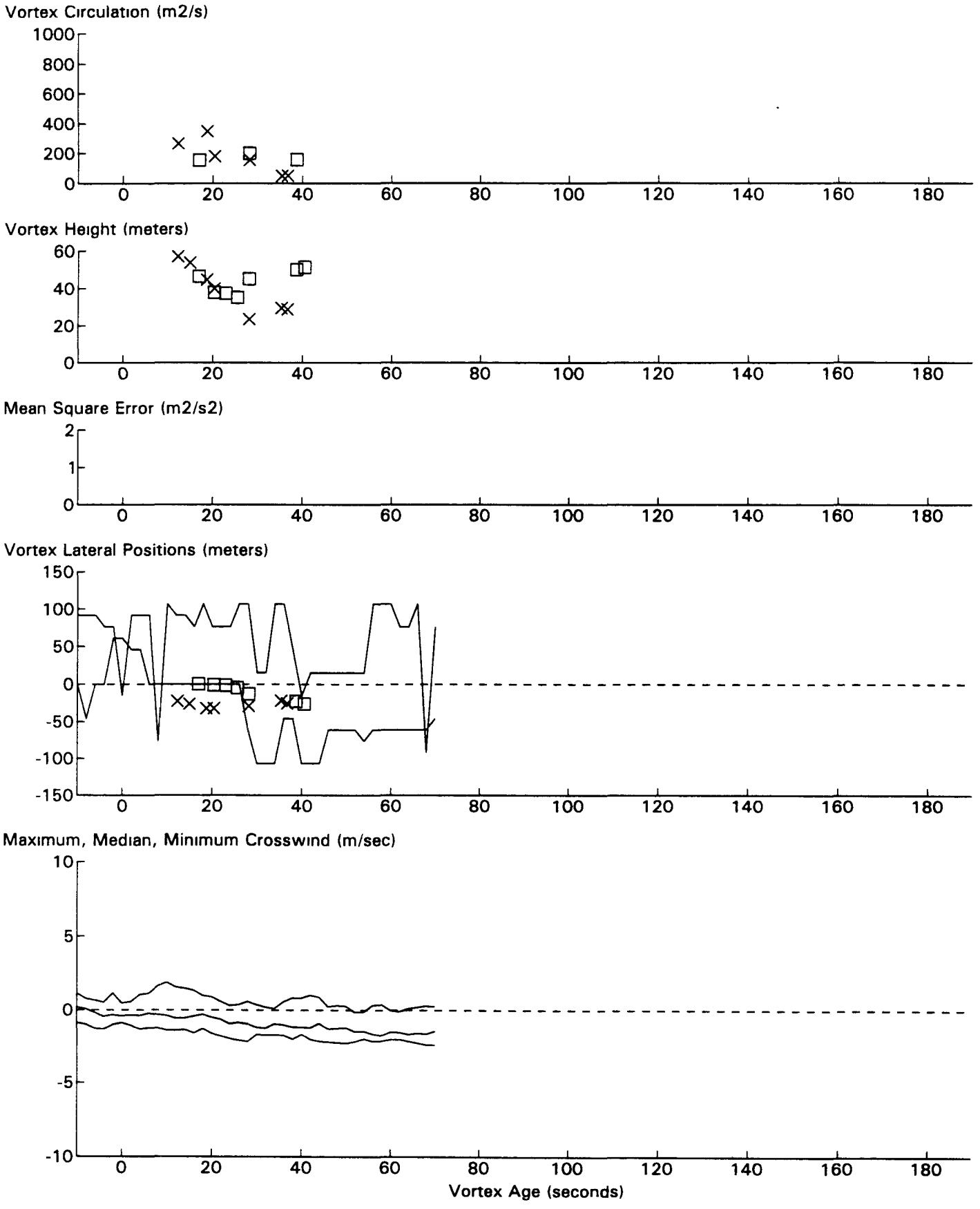

DC9 JFK 31R GWVSS Data for File: I:RM11D20.282 11/20/96 20:45:6 dt= 0 CWturb=0.35

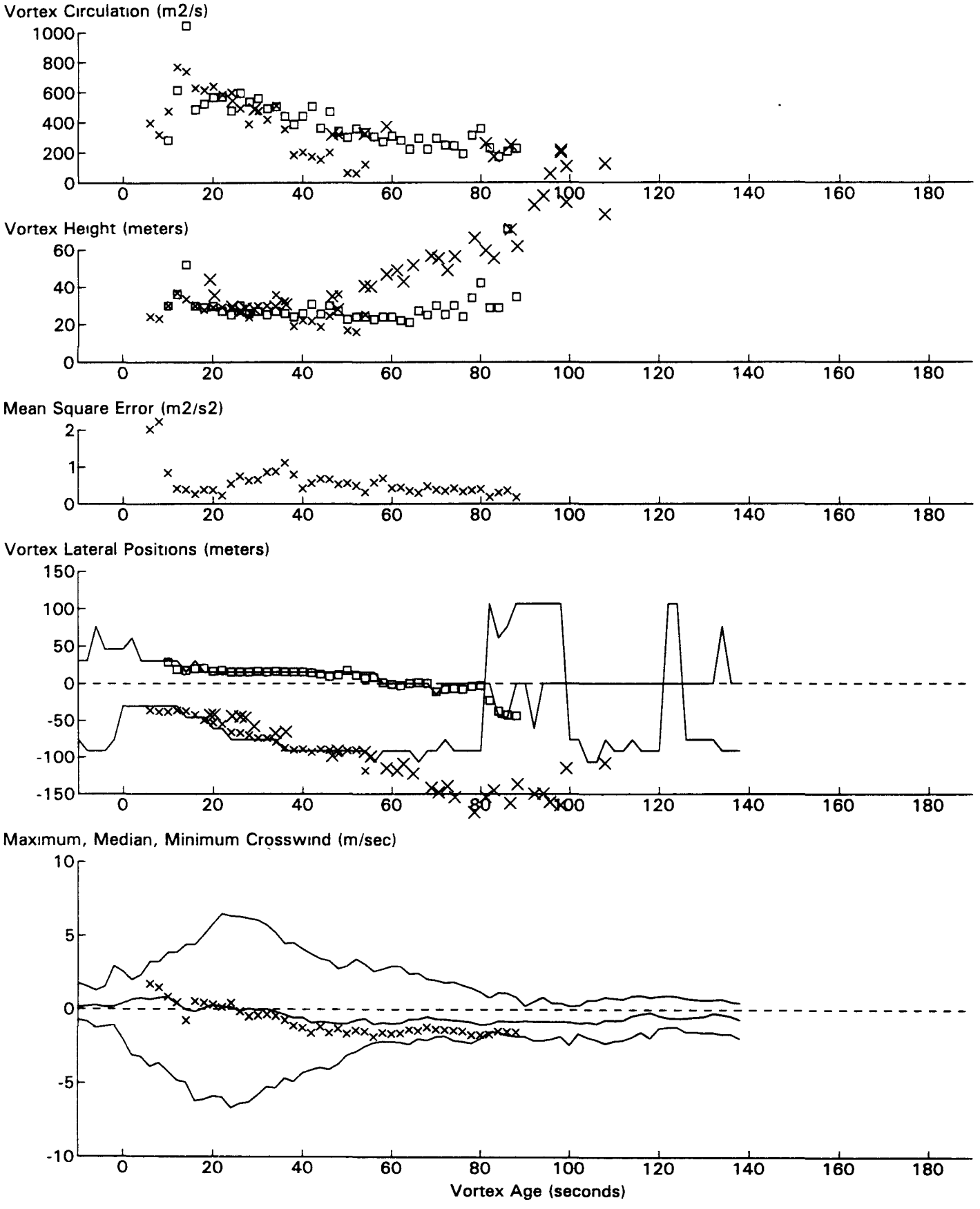

B747 JFK 31R GWVSS Data for File: I:RM11D20.284 11/20/96 20:47:15 dt= 0 CWturb=0.35

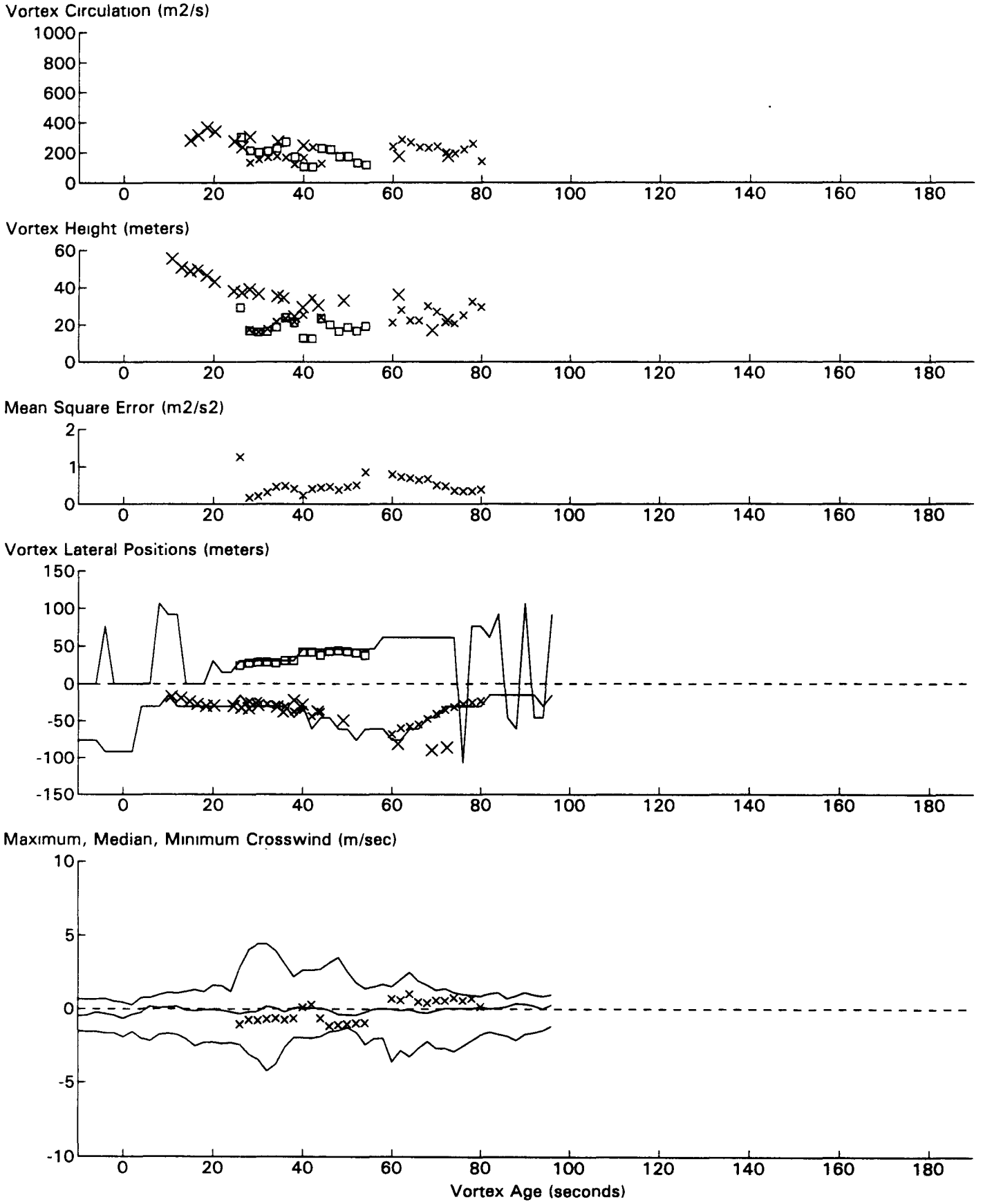

B757 JFK 31R GWVSS Data for File: I:RM11D20.285 11/20/96 20:49:32 dt= 0 CWturb=0.35

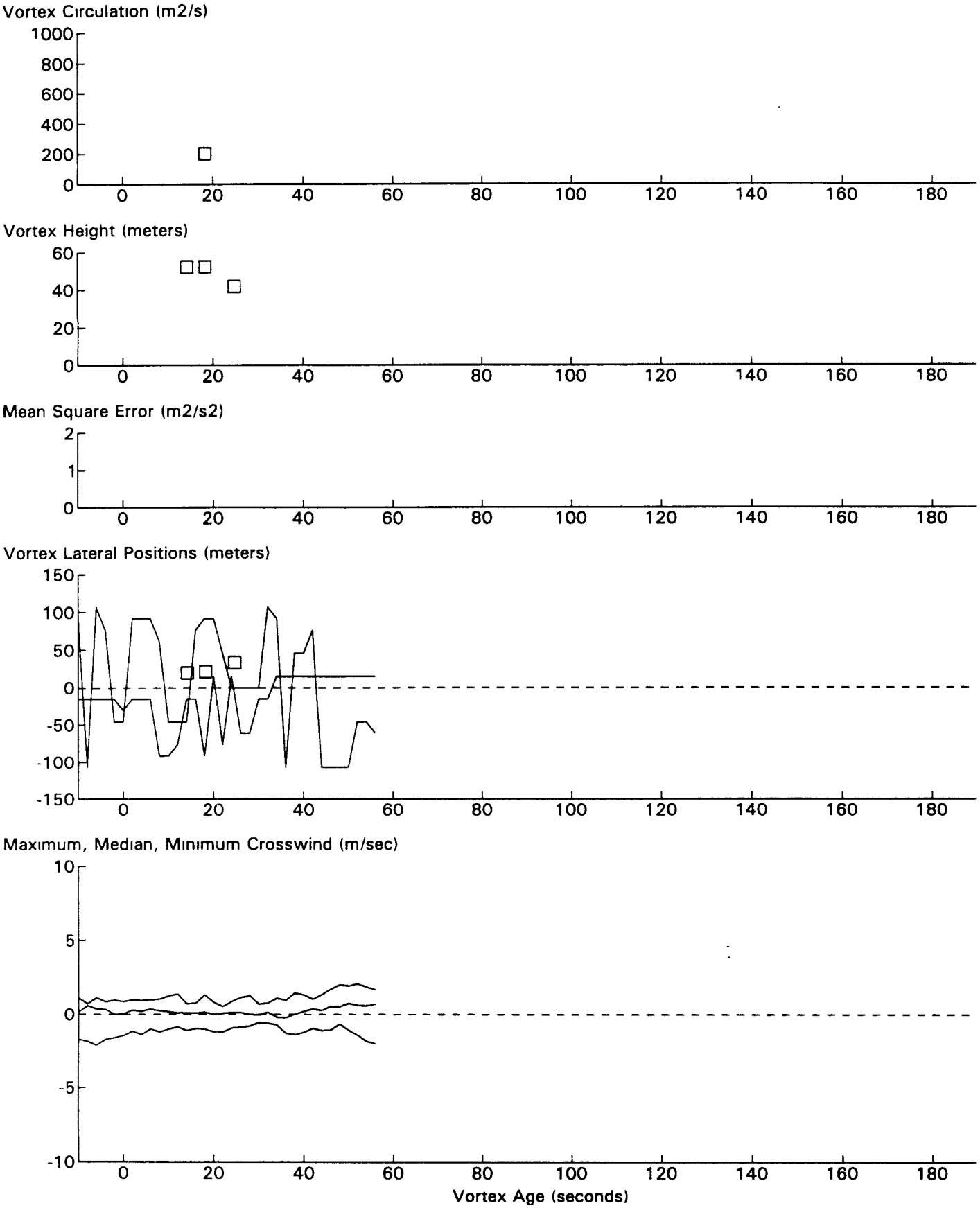

Braz JFK 31R GWVSS Data for File: I:RM11D20.286 11/20/96 20:51:8 dt= 0 CWturb=0.35

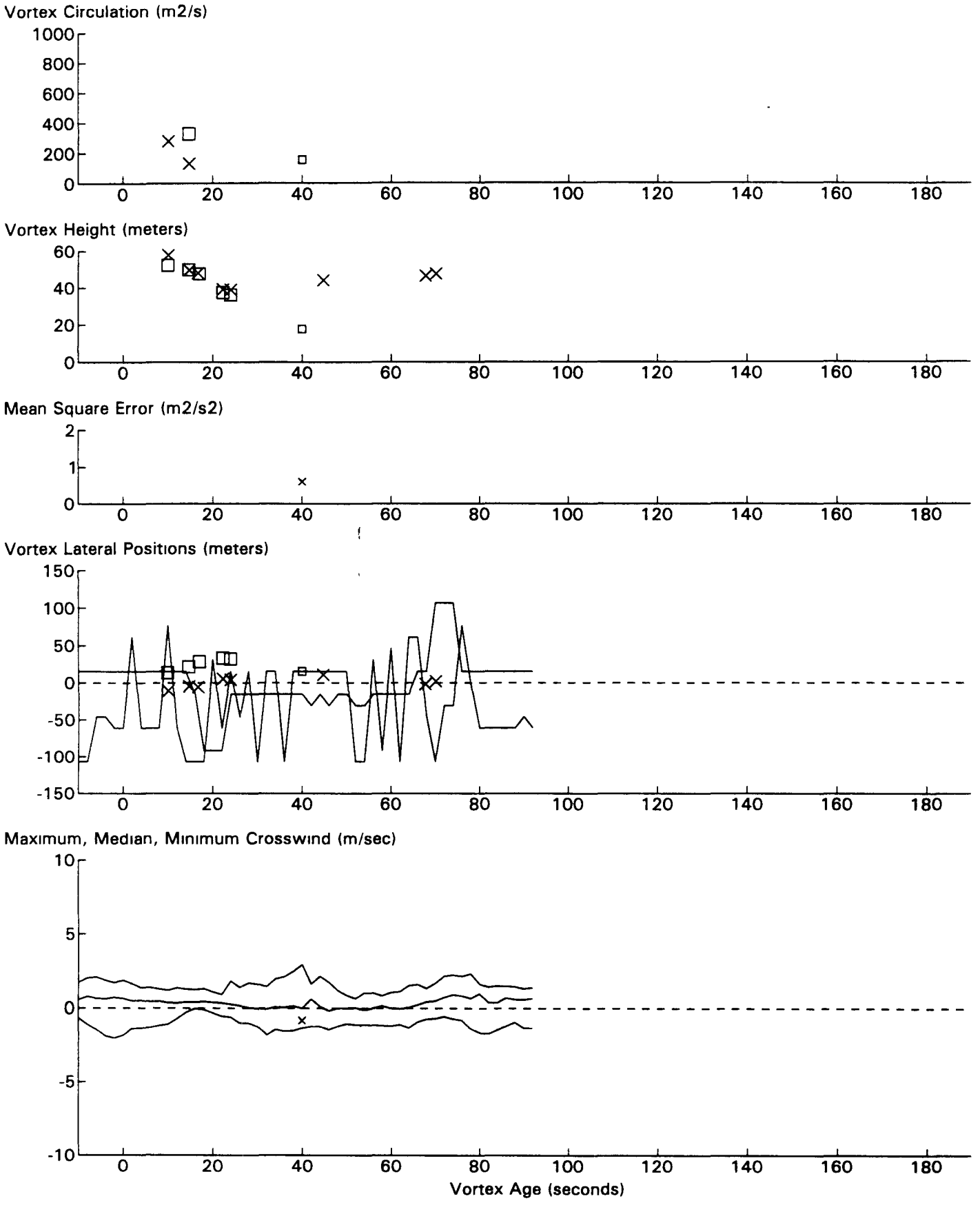

MD80 JFK 31R GWVSS Data for File: I:RM11D20.287 11/20/96 20:52:5 dt= 0 CWturb=0.35

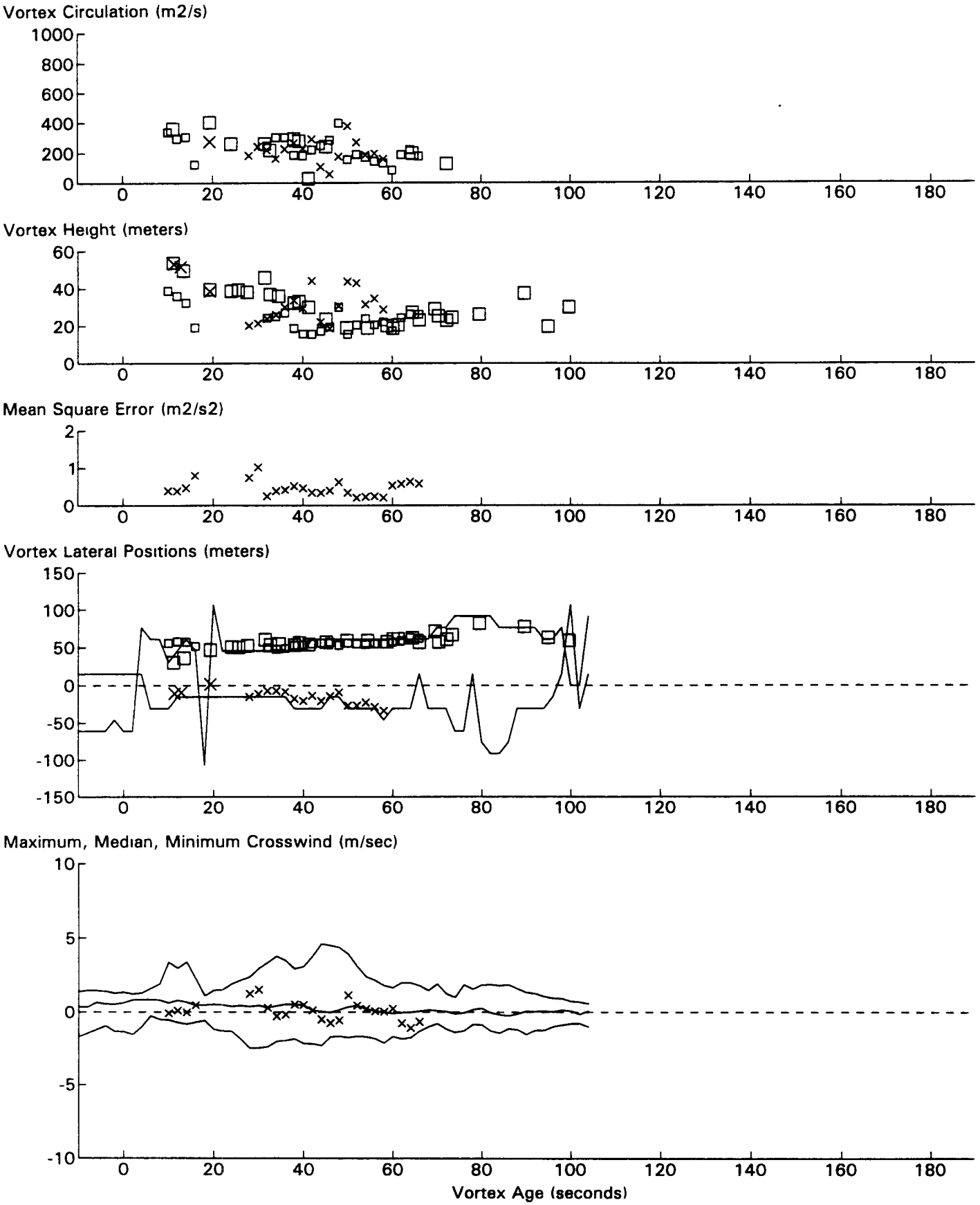

B767 JFK 31R GWVSS Data for File: I:RM11D20.288 11/20/96 20:53:37 dt= 0 CWturb=0.35

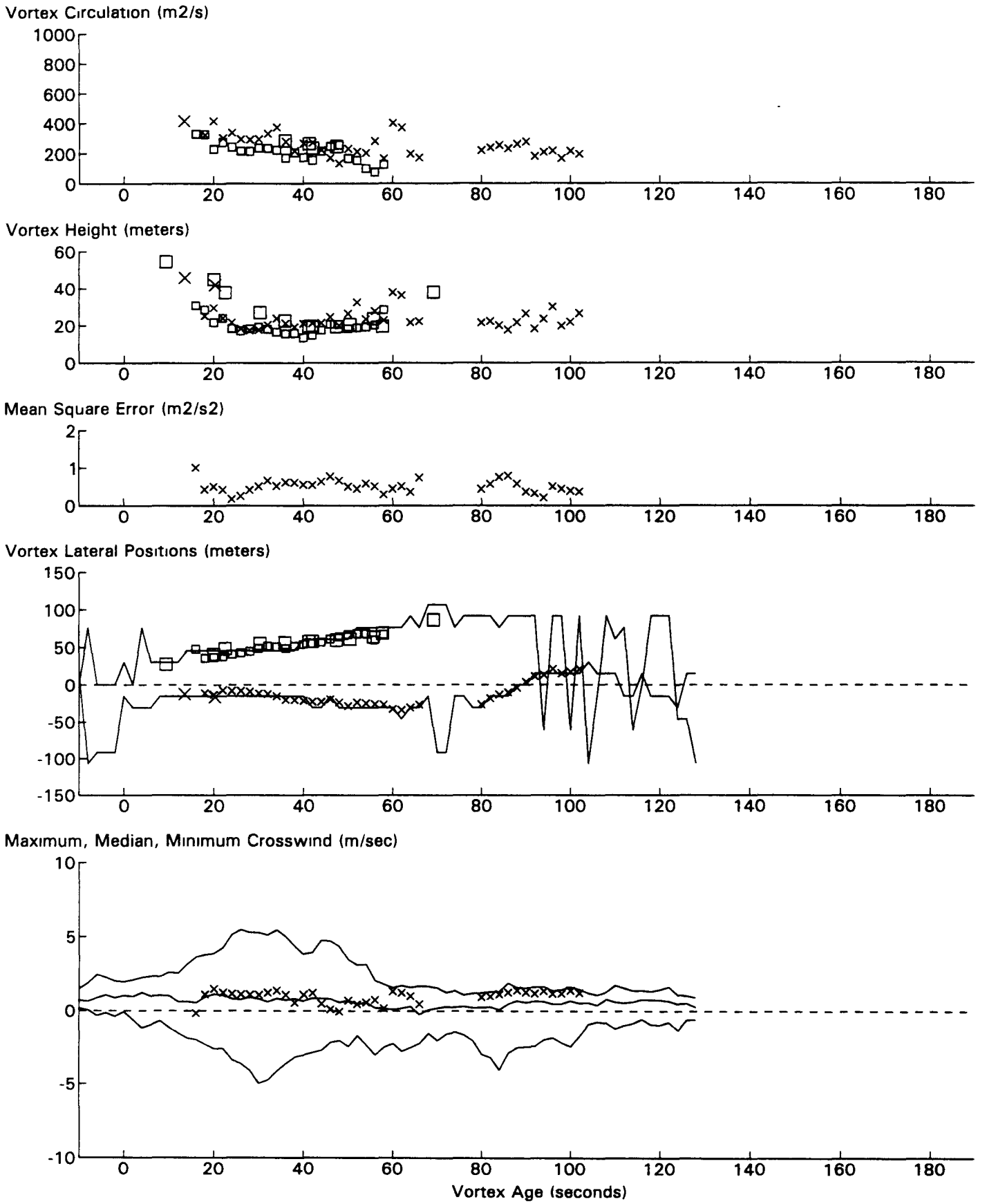

L101 JFK 31R GWVSS Data for File: I:RM11D20.290 11/20/96 20:56:57 dt= 0 CWturb=0.38

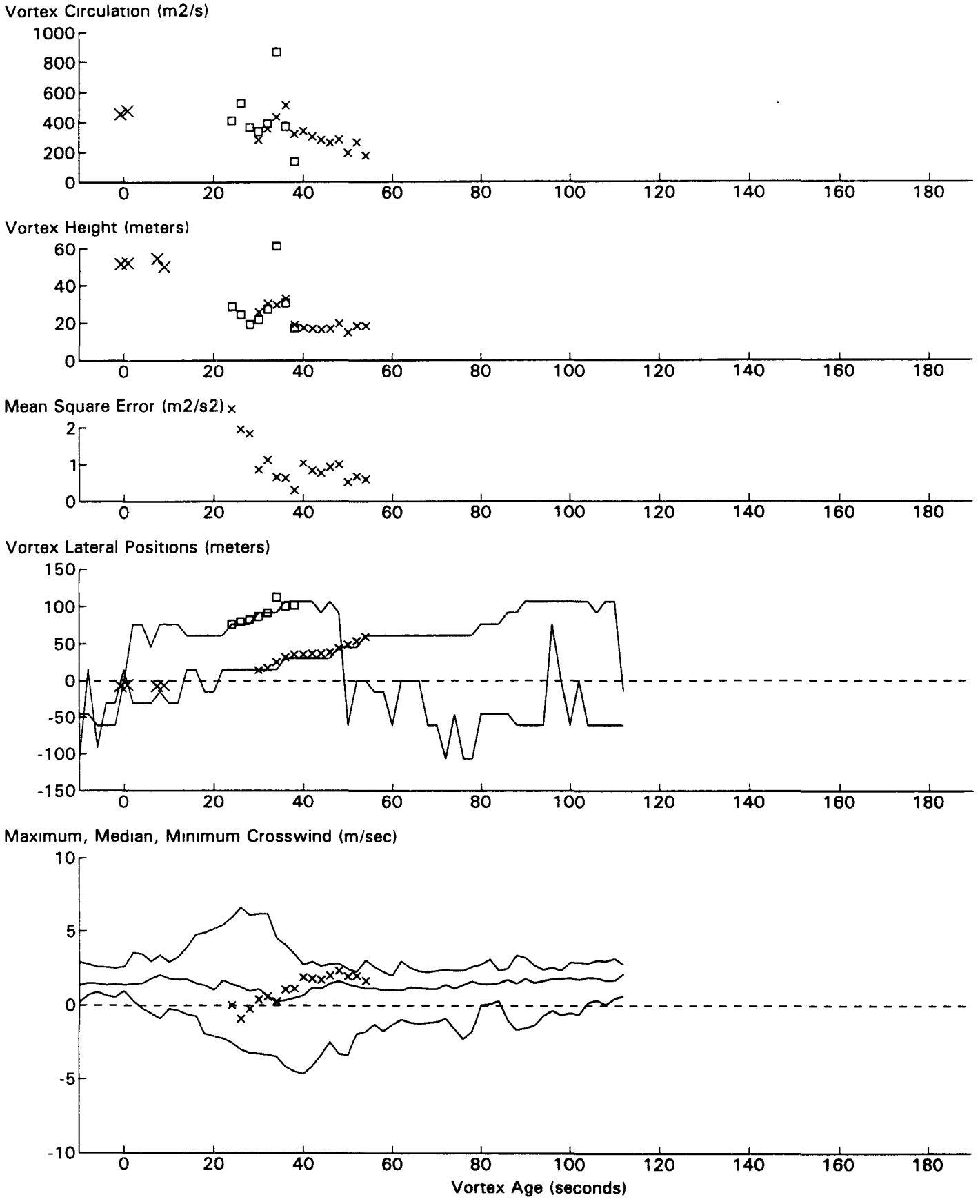

N/A JFK 31R GWVSS Data for File: I:RM11D20.292 11/20/96 21:0:23 dt= -3600 CWturb=0.71

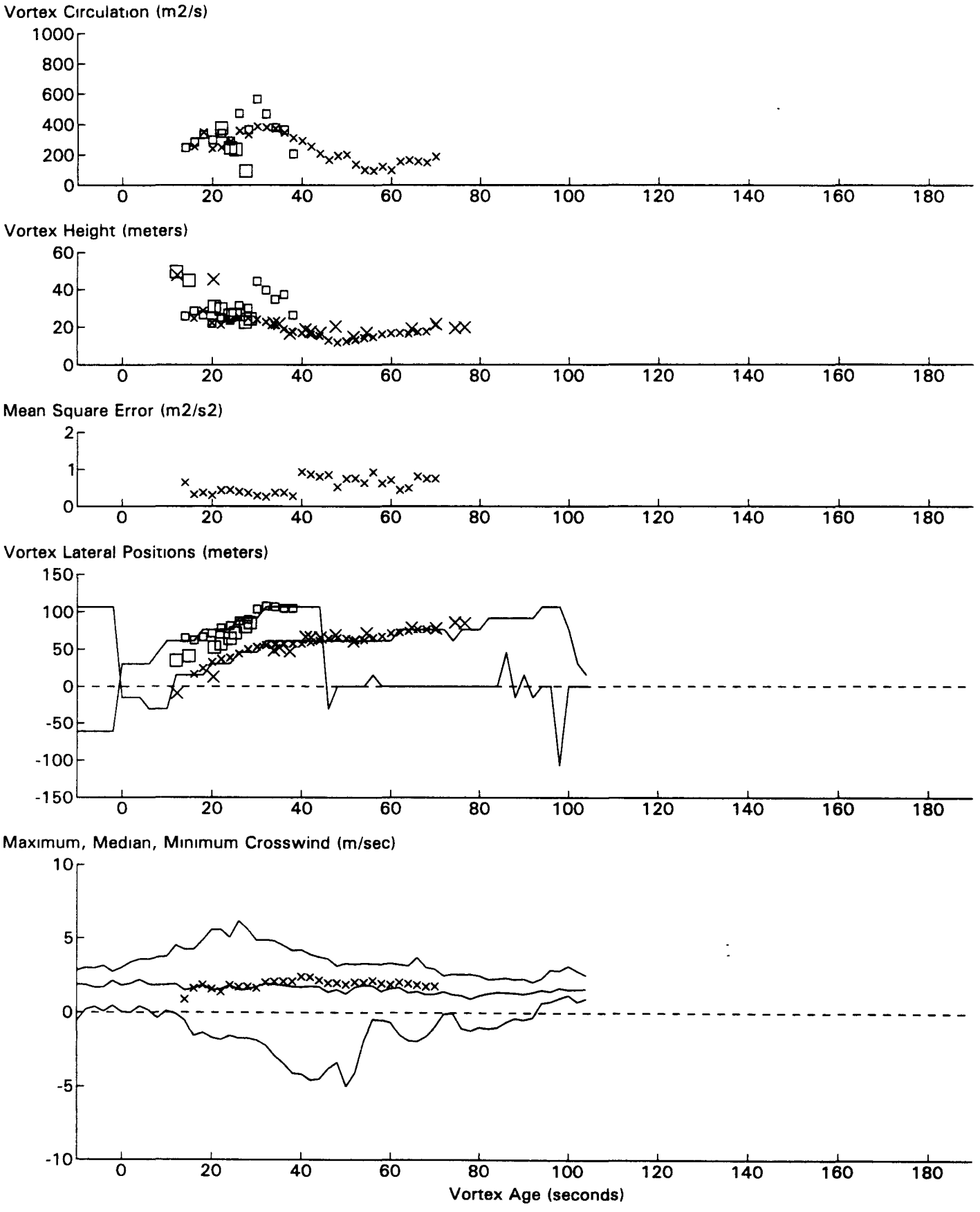

B767 JFK 31R GWVSS Data for File: I:RM11D20.293 11/20/96 21:2:15 dt= 0 CWturb=0.42

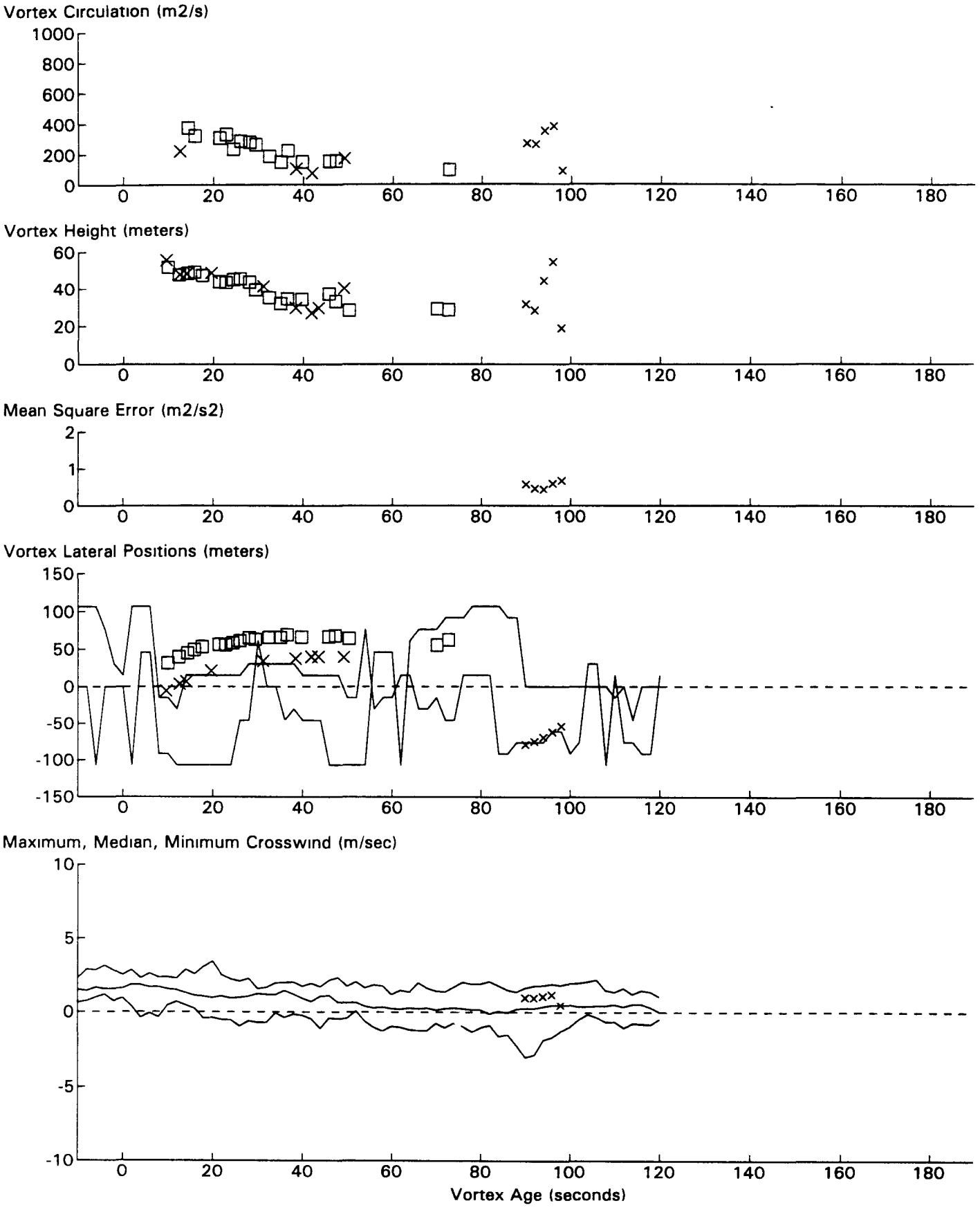

B767 JFK 31R GWVSS Data for File: I:RM11D20.294 11/20/96 21:3:59 dt= 0 CWturb=0.40

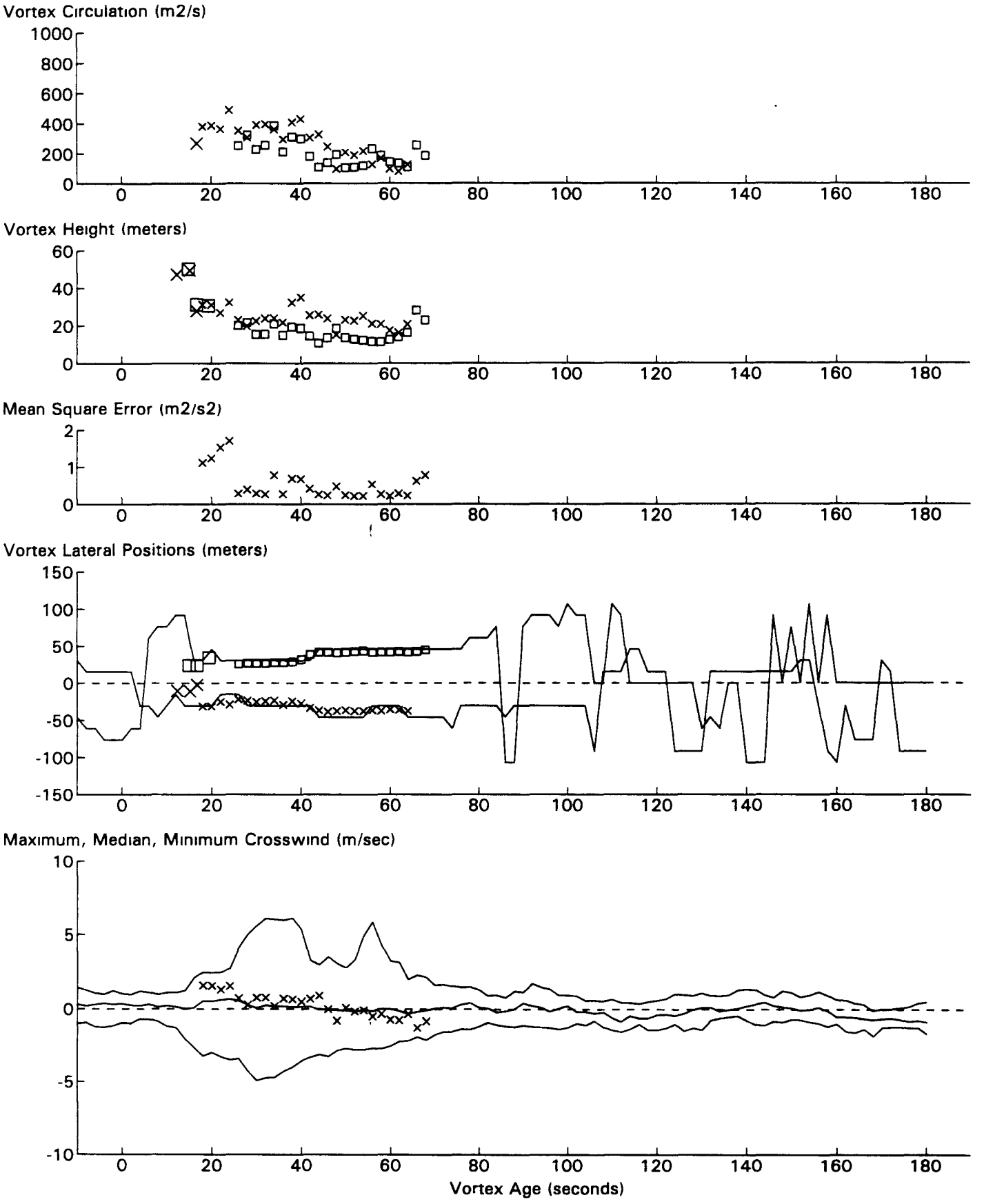

B767 JFK 31R GWVSS Data for File: I:RM11D20.296 11/20/96 21:7:53 dt= 0 CWturb=0.43

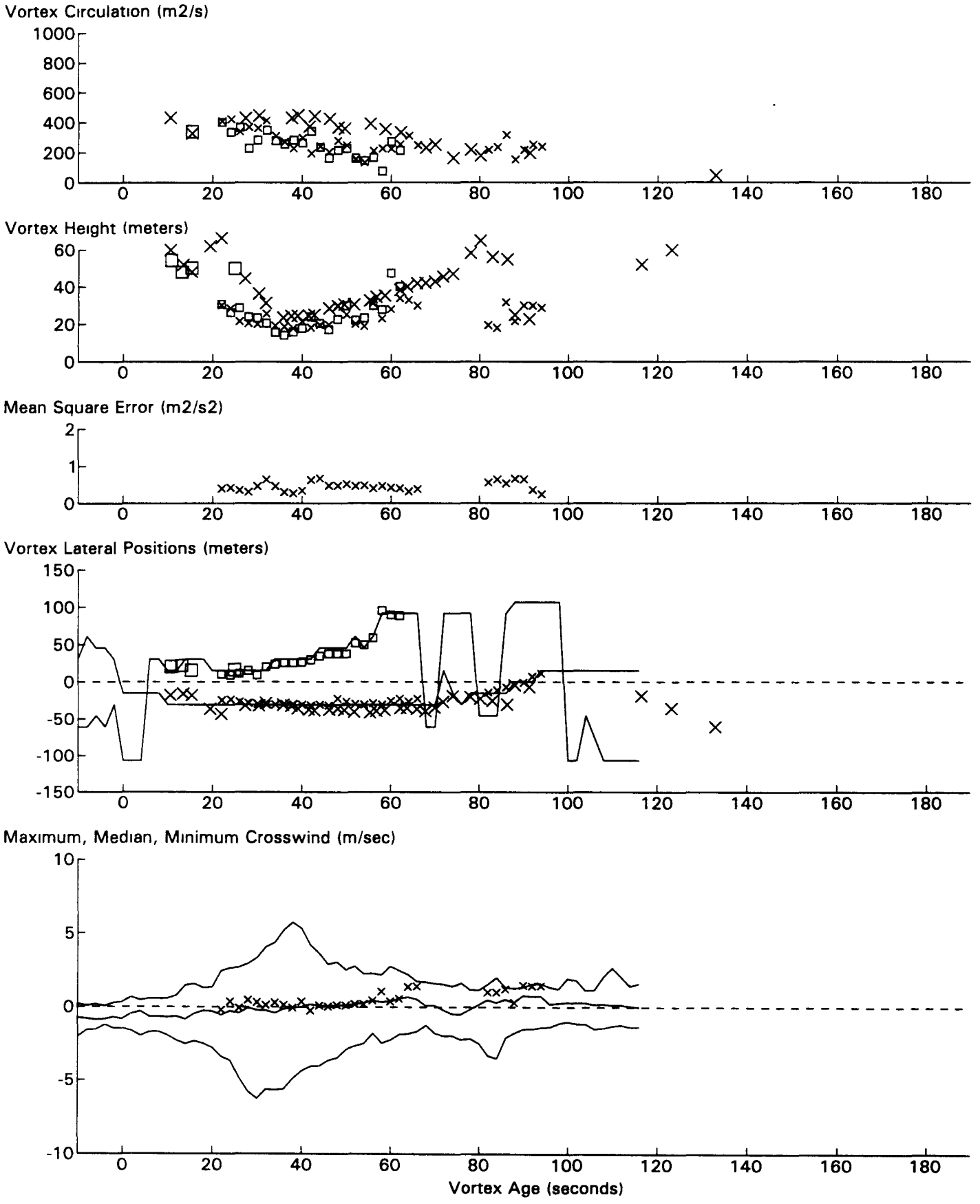

B747 JFK 31R GWVSS Data for File: I:RM11D20.297 11/20/96 21:11:57 dt= 0 CWturb=0.42

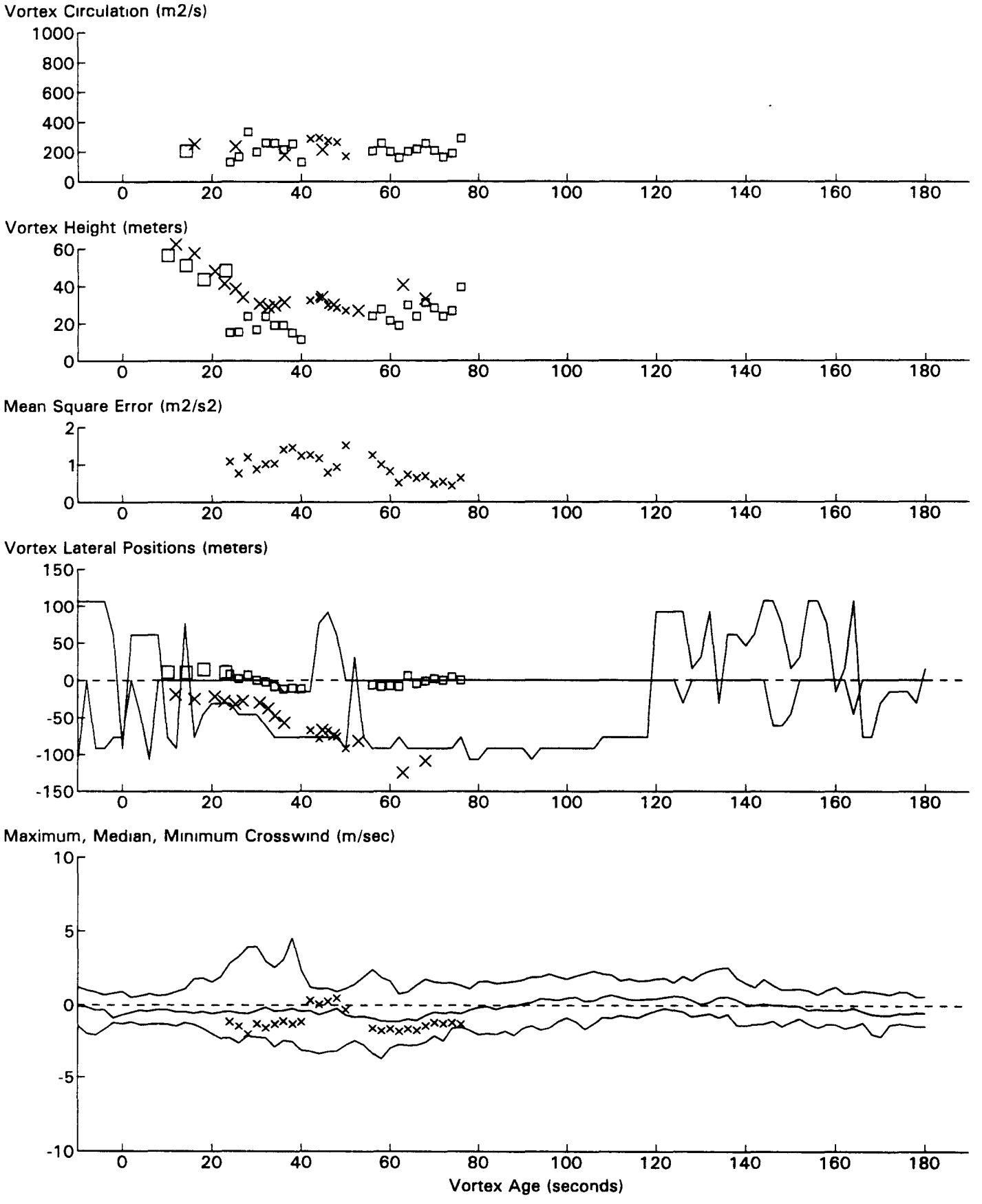

B727 JFK 31R GWVSS Data for File: I:RM11D20.299 11/20/96 21:15:45 dt= 0 CWturb=0.41

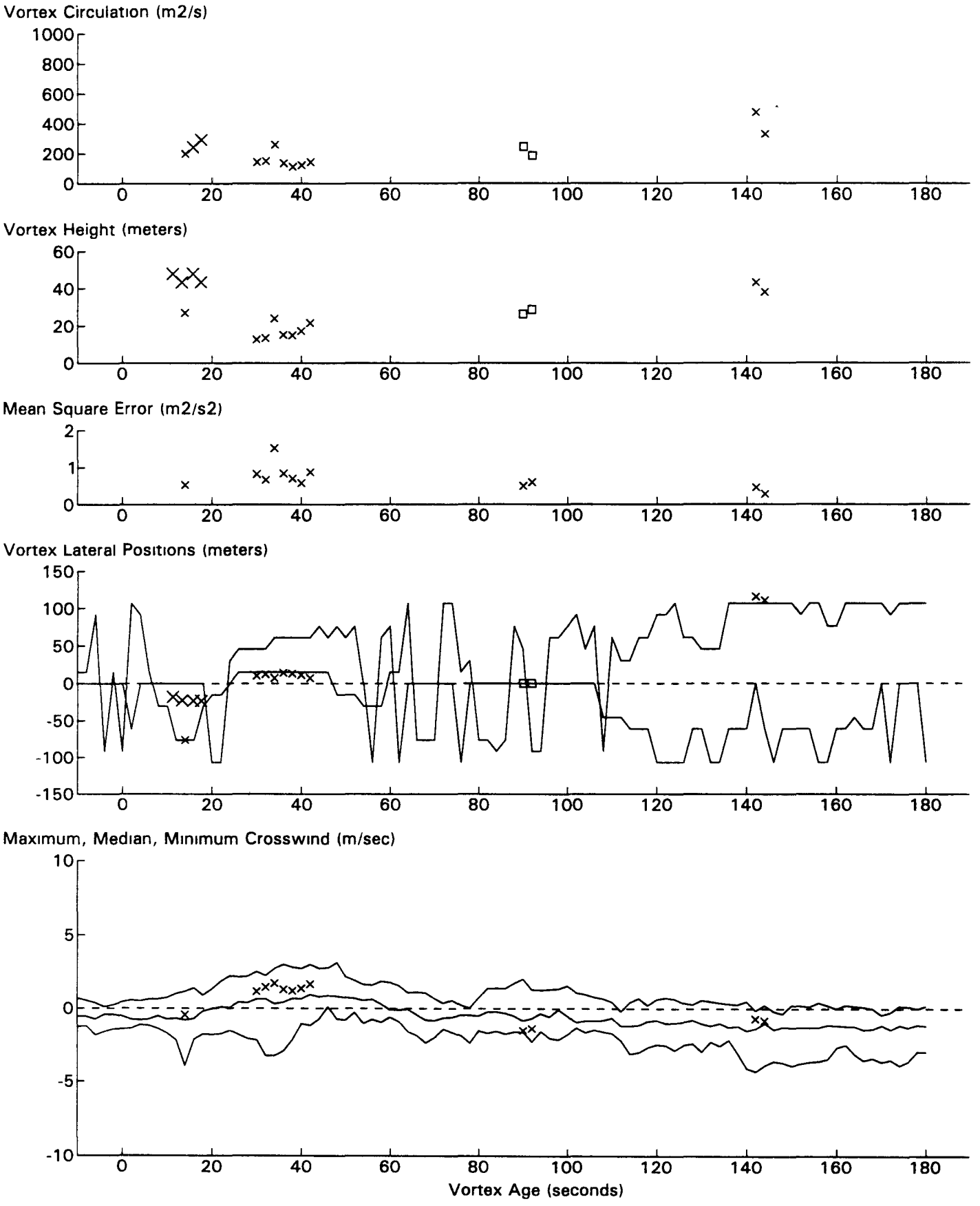

MD80 JFK 31R GWVSS Data for File: I:RM11D20.300 11/20/96 21:19:1 dt= 0 CWturb=0.39

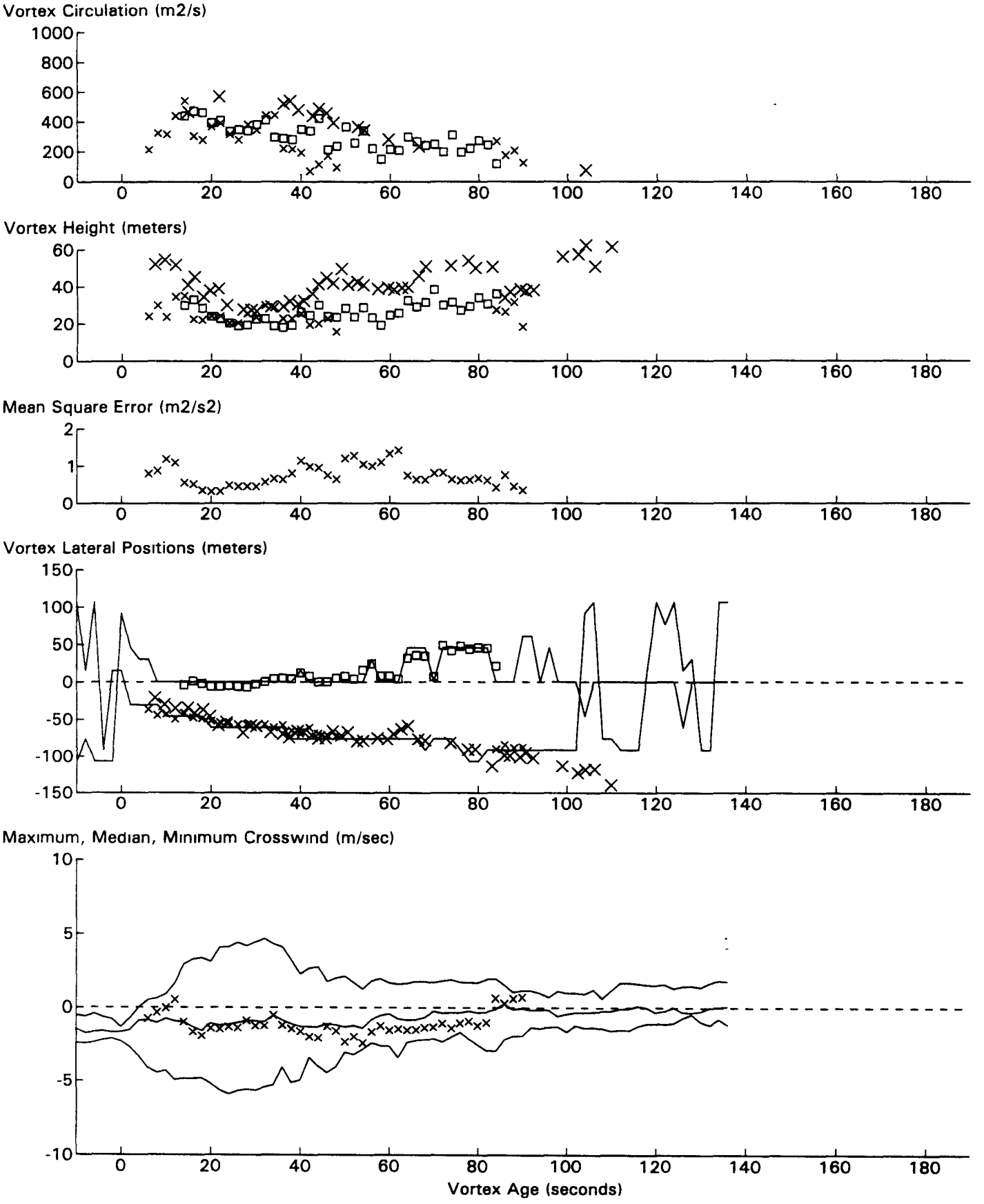

B747 JFK 31R GWVSS Data for File: I:RM11D20.303 11/20/96 21:25:53 dt= 0 CWturb=0.44

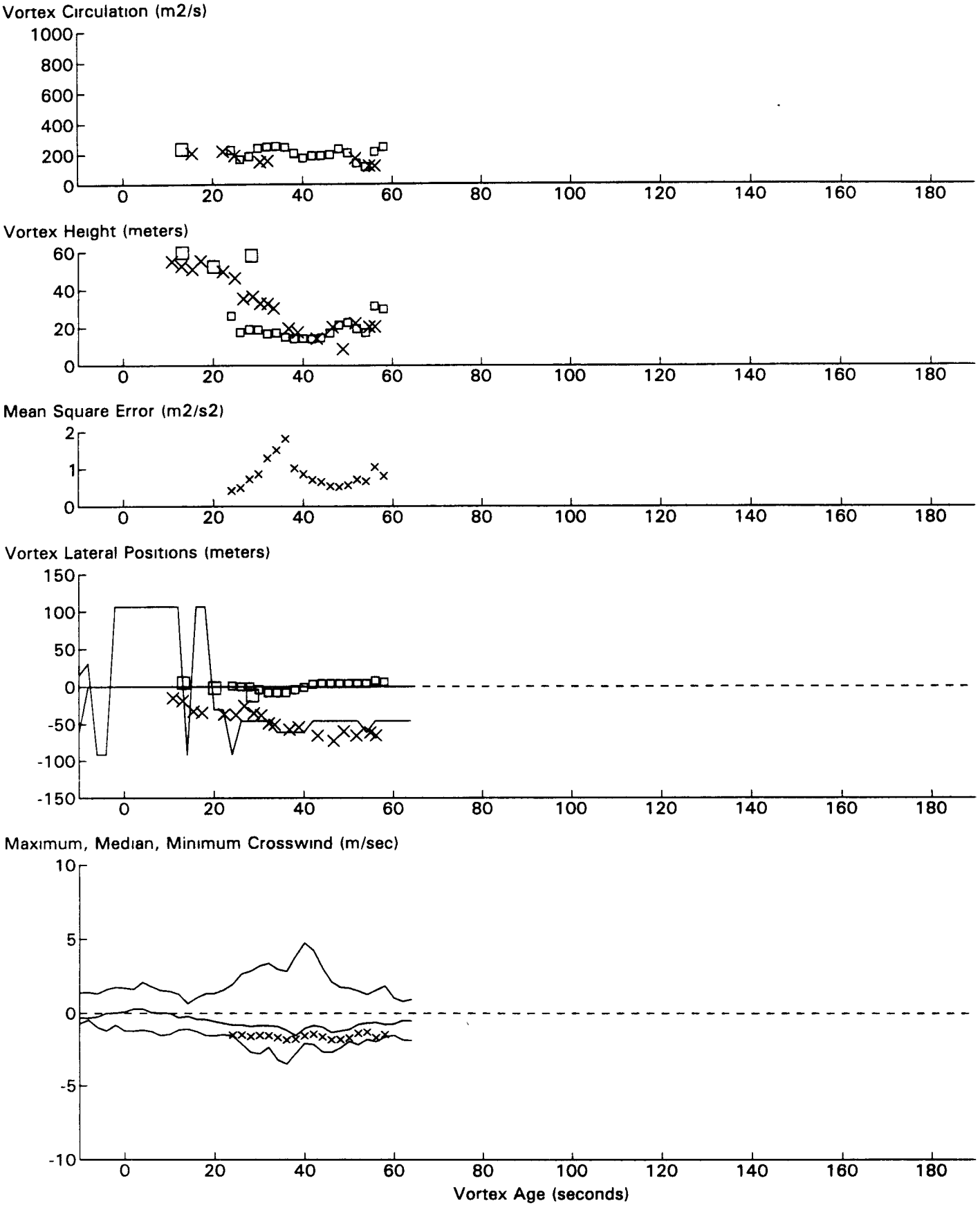

B727 JFK 31R GWVSS Data for File: I:RM11D20.304 11/20/96 21:28:9 dt= 0 CWturb=0.44

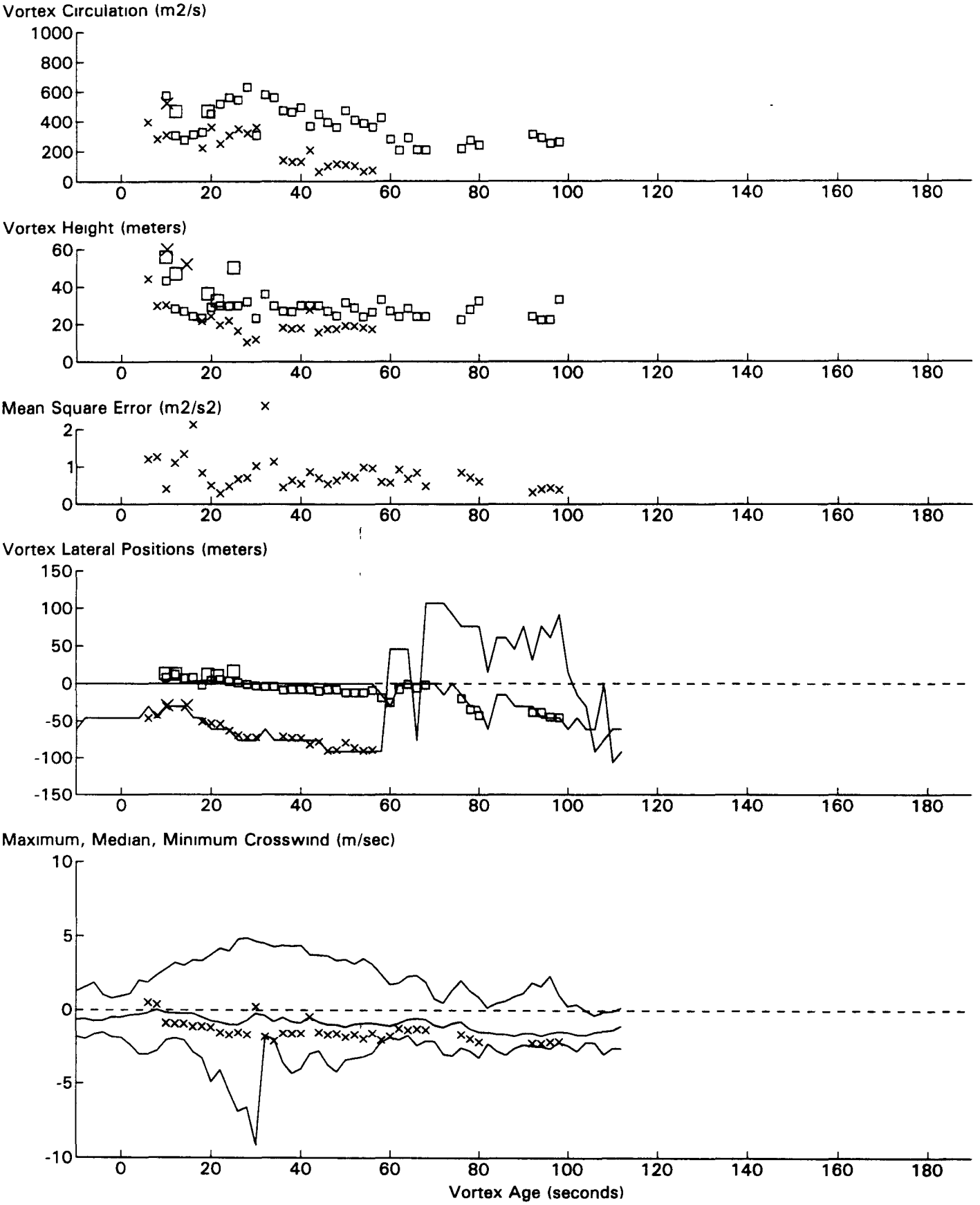

B747 JFK 31R GWVSS Data for File: I:RM11D20.305 11/20/96 21:29:13 dt= 0 CWturb=0.44

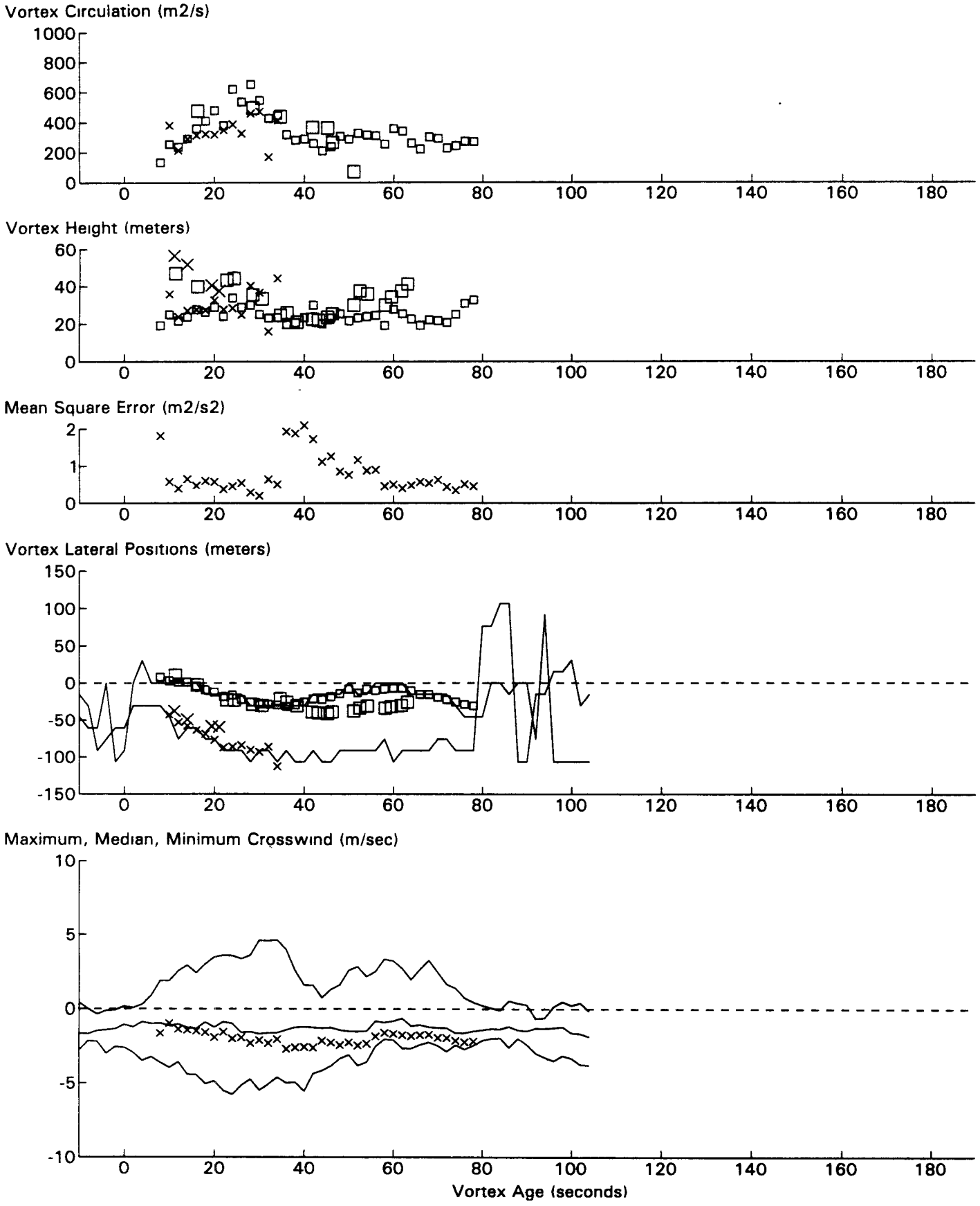

B747 JFK 31R GWVSS Data for File: I:RM11D20.306 11/20/96 21:31:5 dt= 0 CWturb=0.43

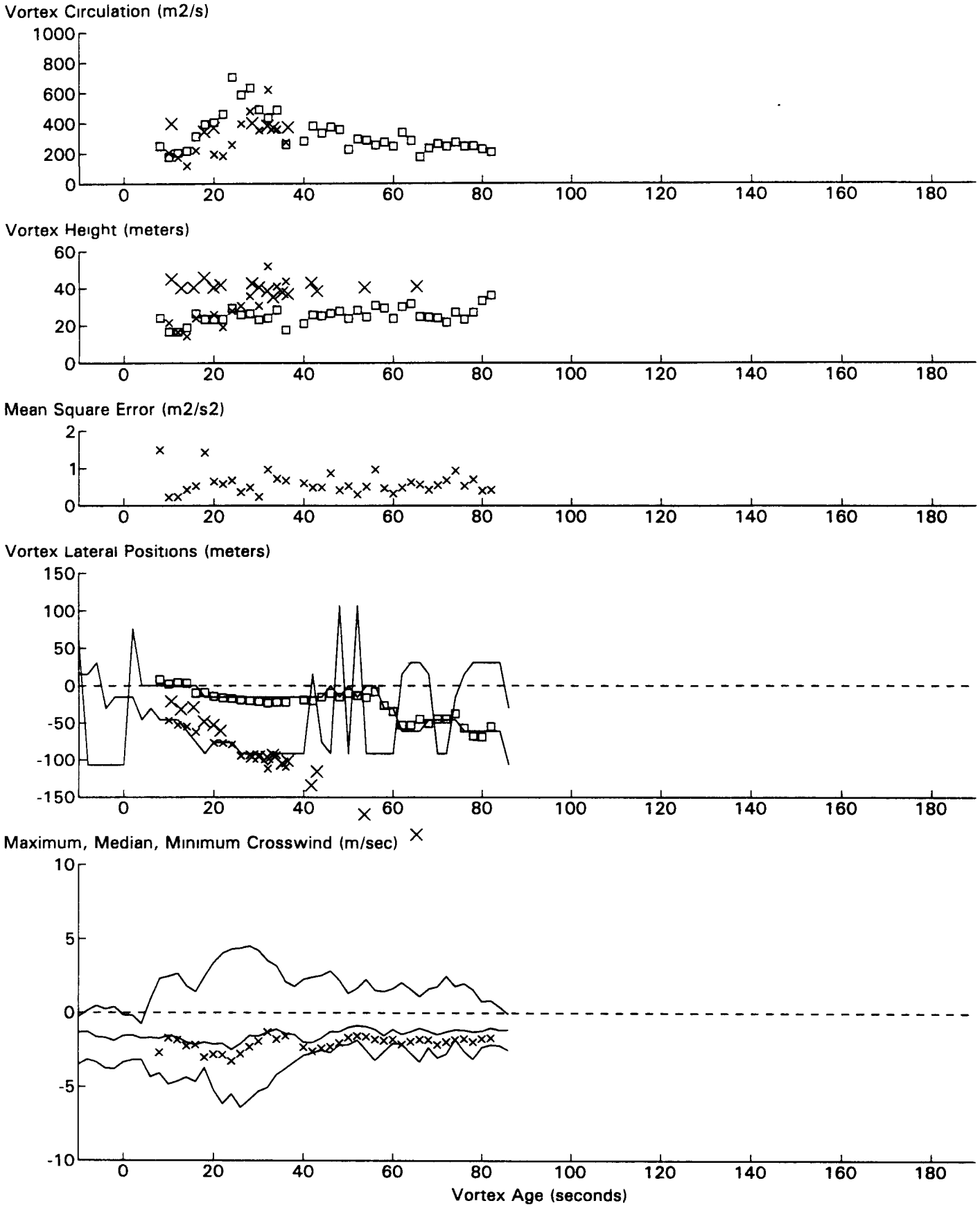

B747 JFK 31R GWVSS Data for File: I:RM11D20.307 11/20/96 21:32:49 dt= 0 CWturb=0.45

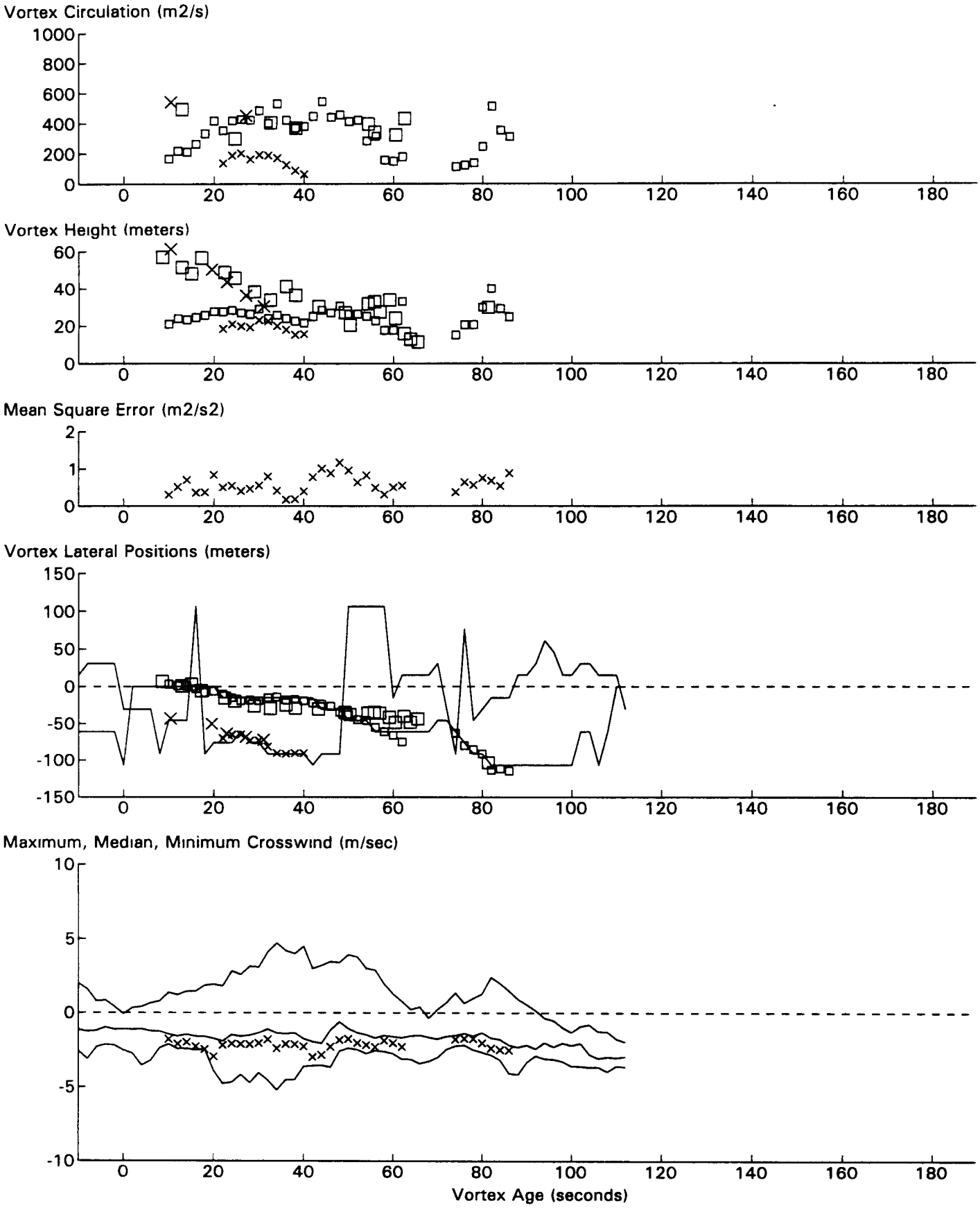

B747 JFK 31R GWVSS Data for File: I:RM11D20.308 11/20/96 21:34:16 dt= 0 CWturb=0.45

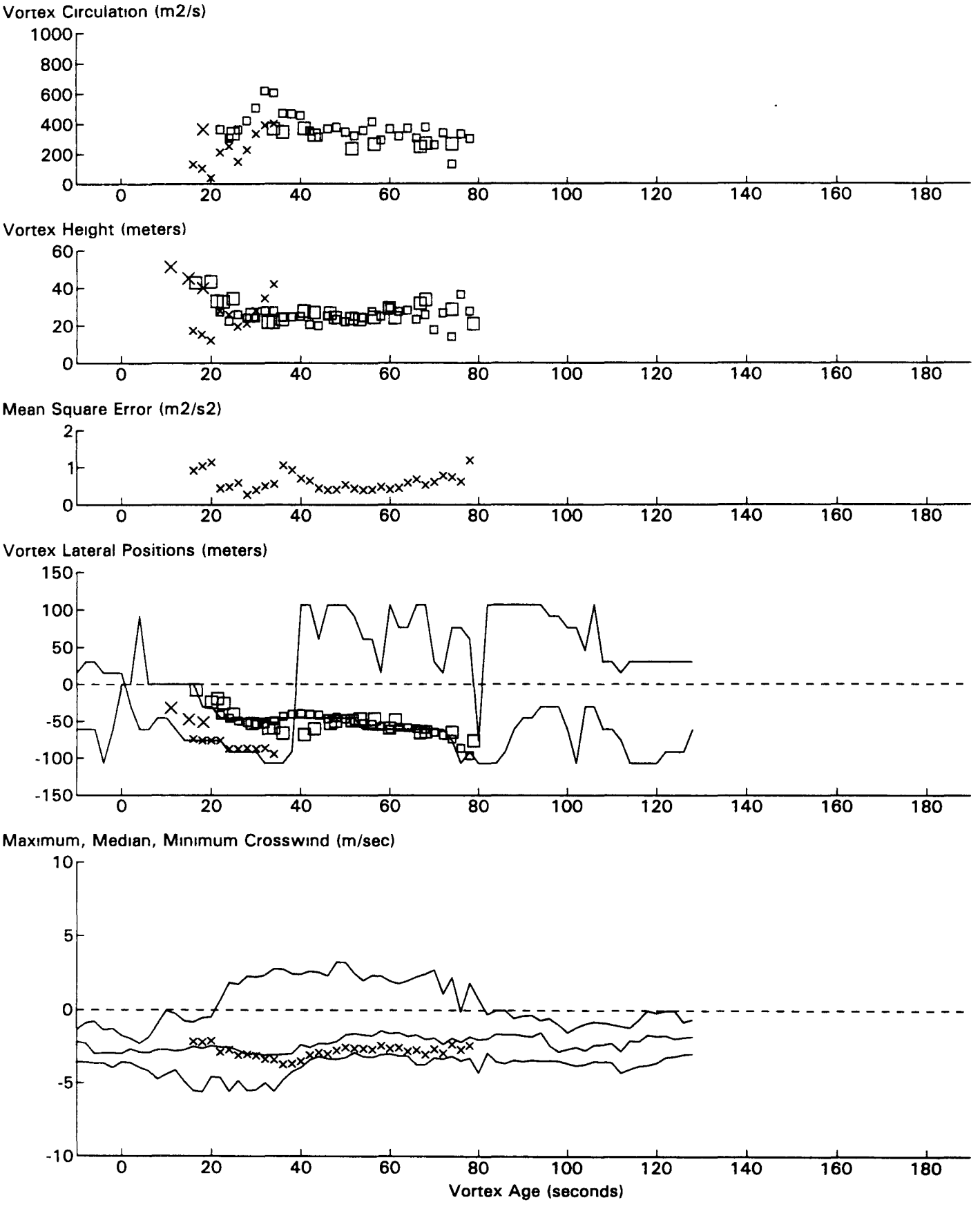

DC10 JFK 31R GWVSS Data for File: I:RM11D20.309 11/20/96 21:36:7 dt= 0 CWturb=0.44

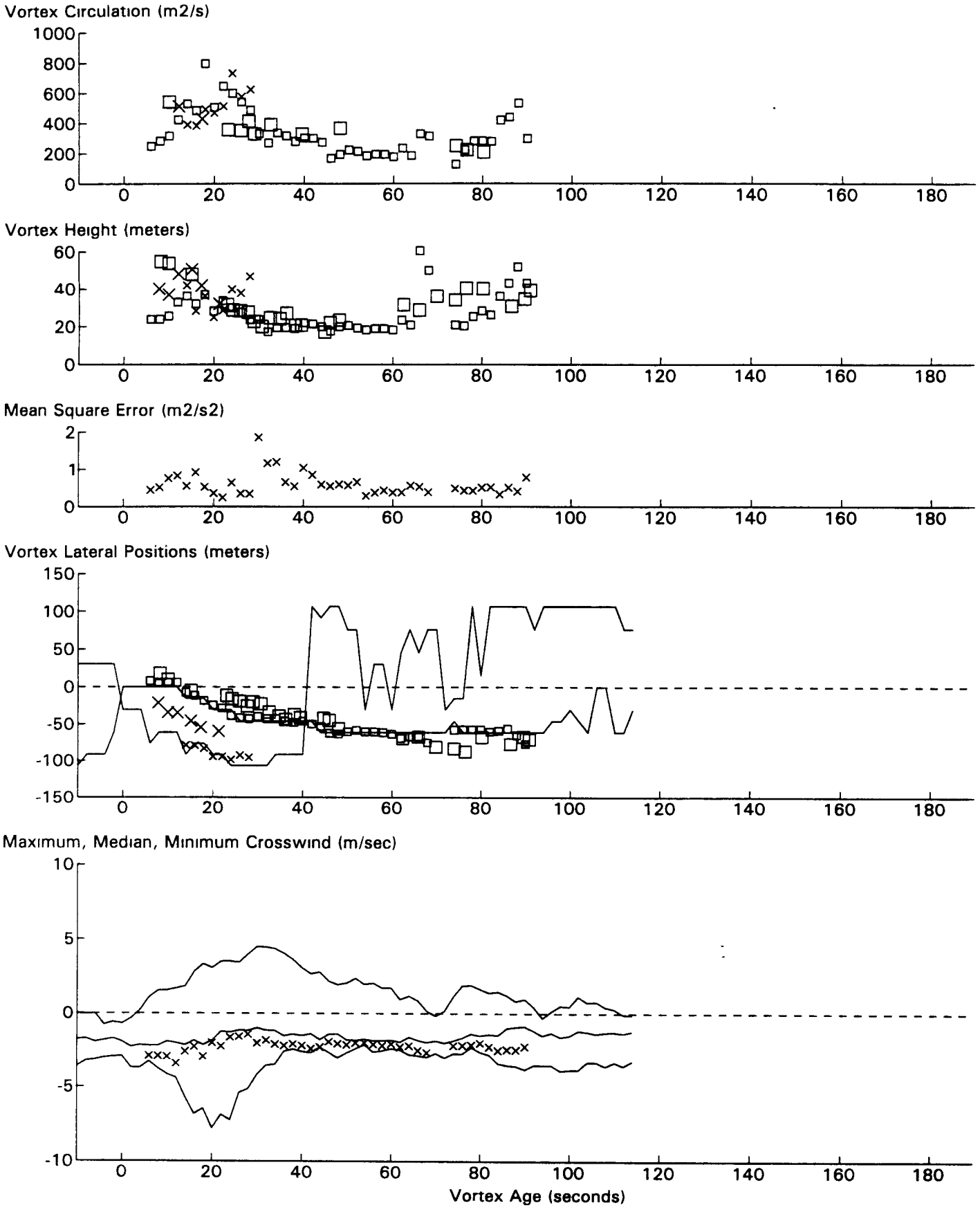

B747 JFK 31R GWVSS Data for File: I:RM11D20.310 11/20/96 21:38:16 dt= 0 CWturb=0.43

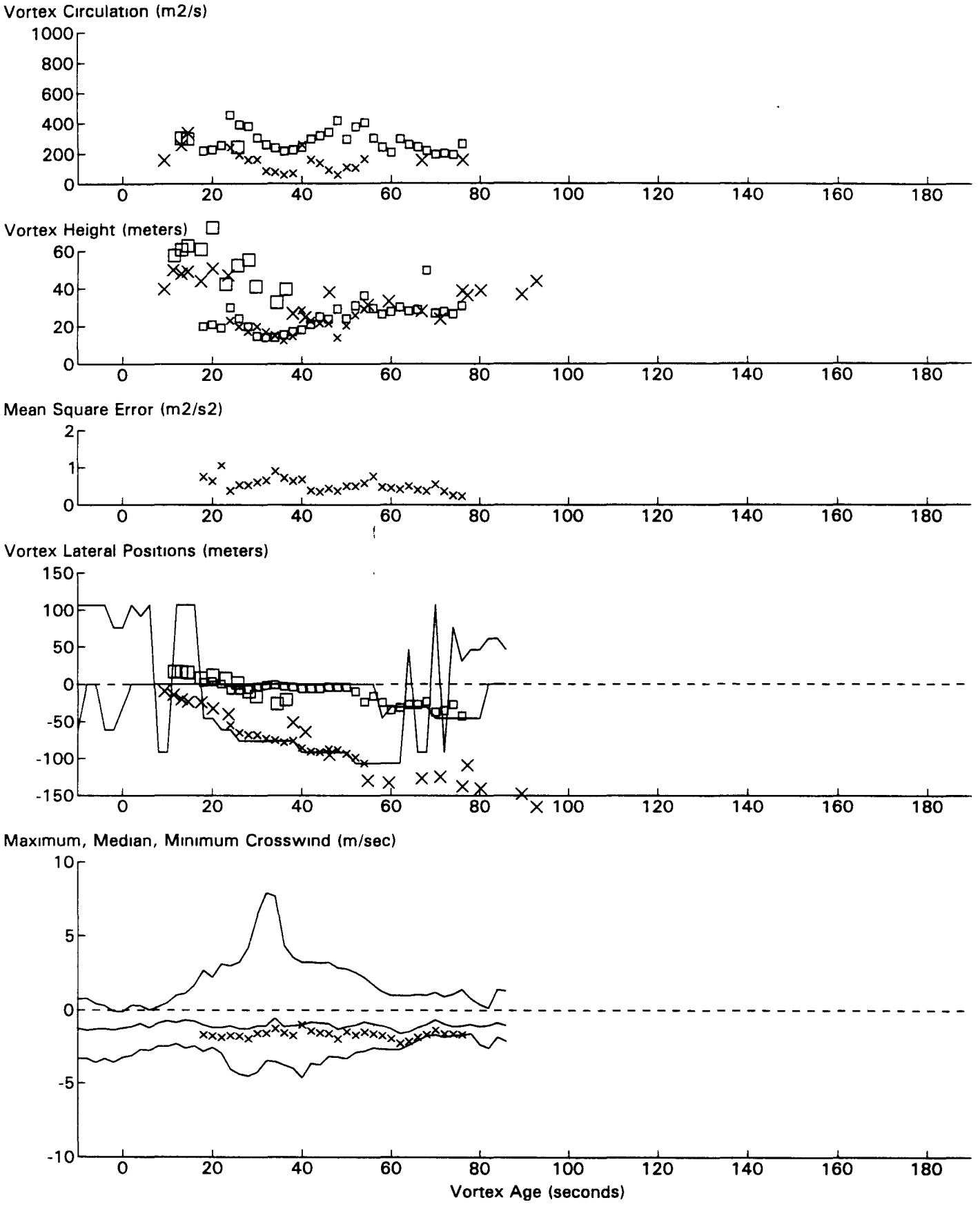

B767 JFK 31R GWVSS Data for File: I:RM11D20.311 11/20/96 21:40:10 dt= 0 CWturb=0.44

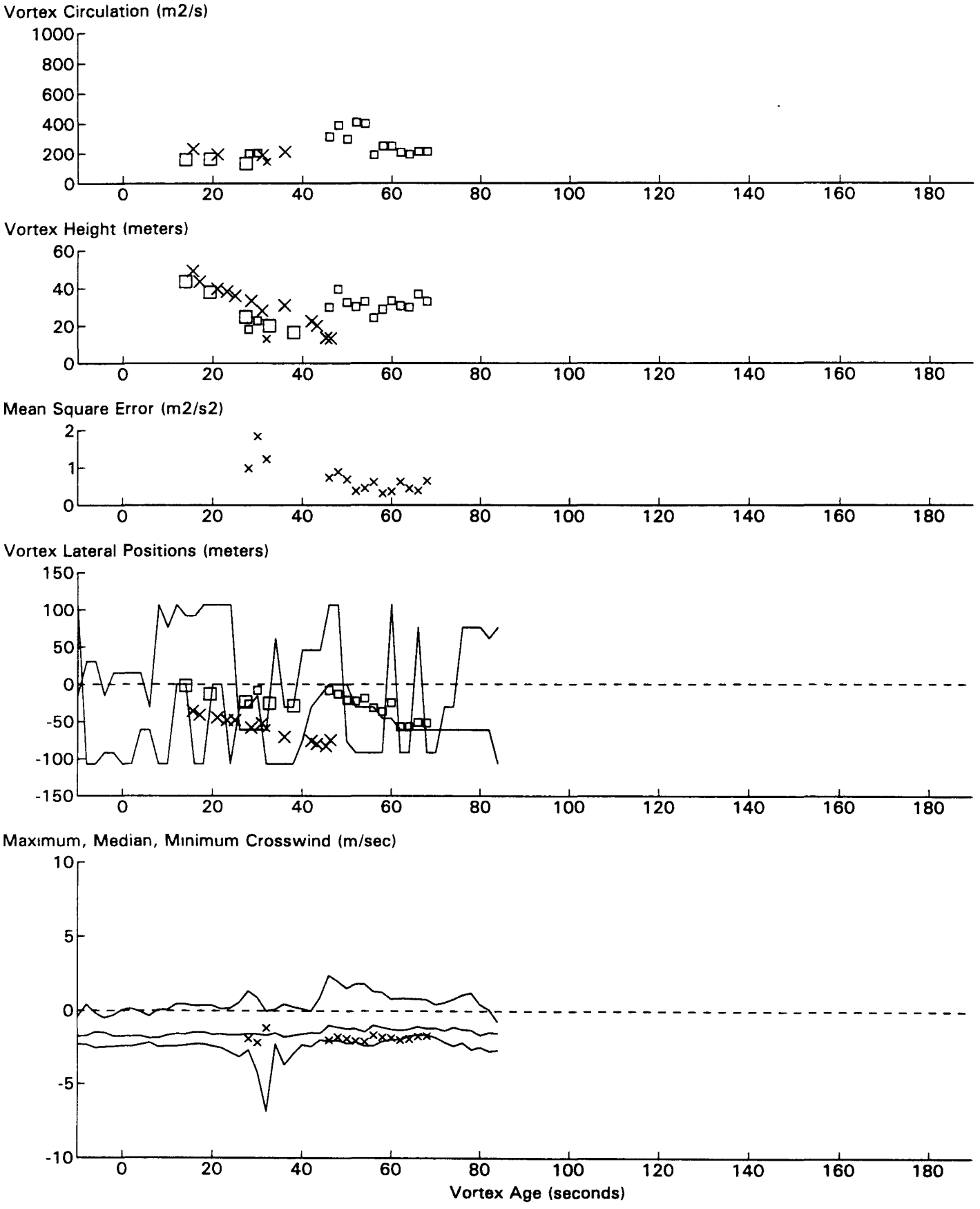

DC9 JFK 31R GWVSS Data for File: I:RM11D20.313 11/20/96 21:43:26 dt= 0 CWturb=0.45

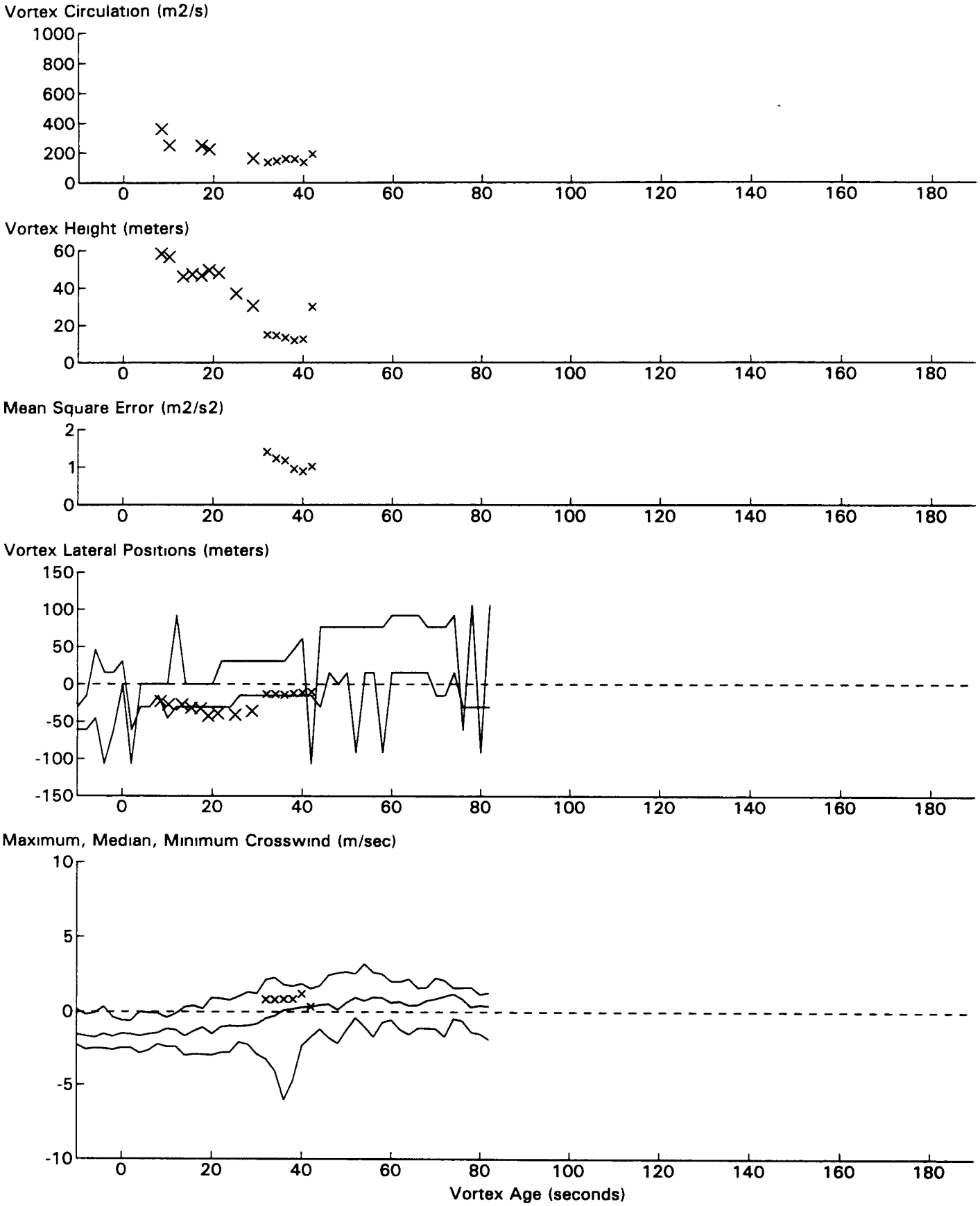

DC9 JFK 31R GWVSS Data for File: I:RM11D20.316 11/20/96 21:47:56 dt = 0 CWturb = 0.44

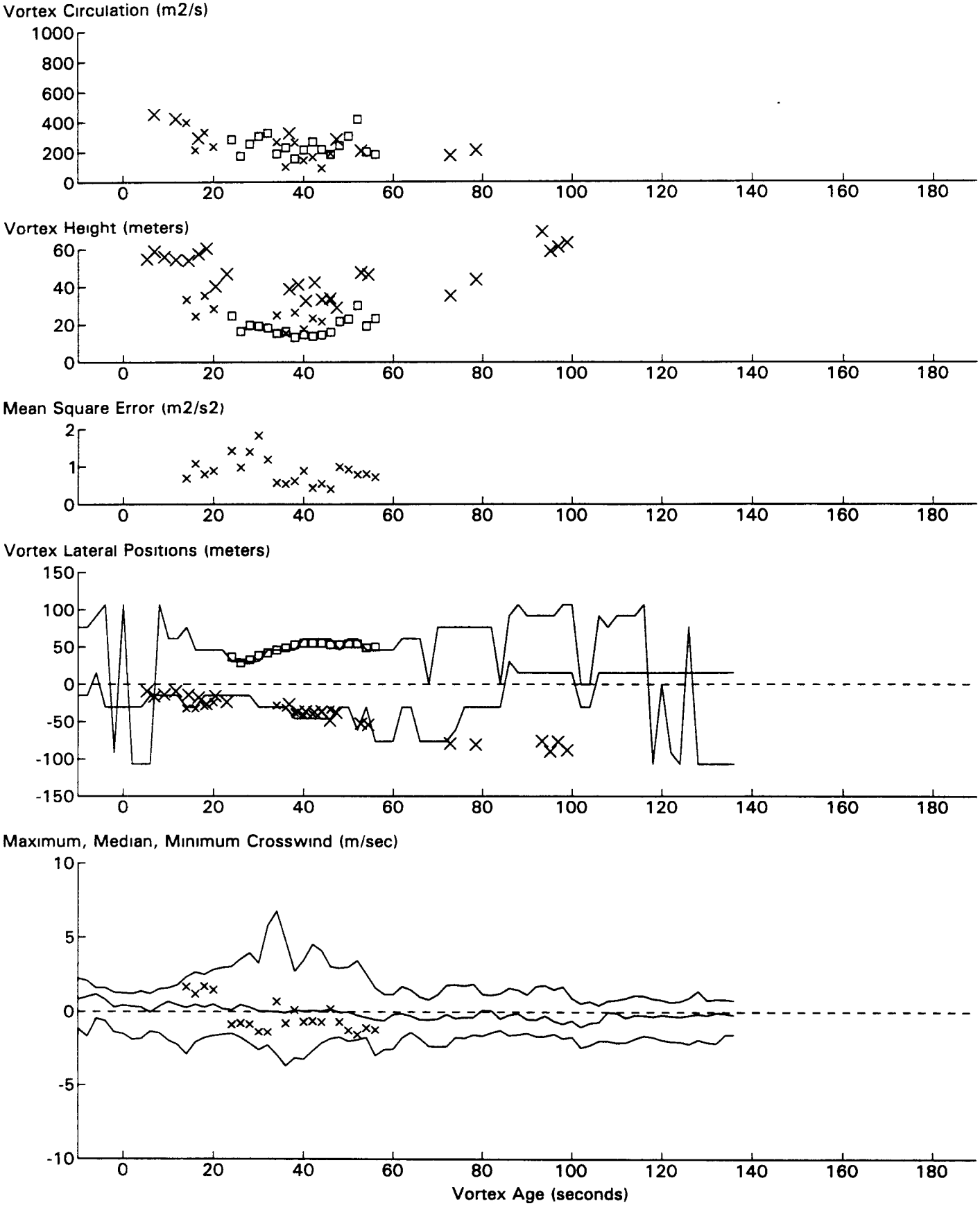

B767 JFK 31R GWVSS Data for File: I:RM11D20.317 11/20/96 21:49:18 dt= 0 CWturb=0.48

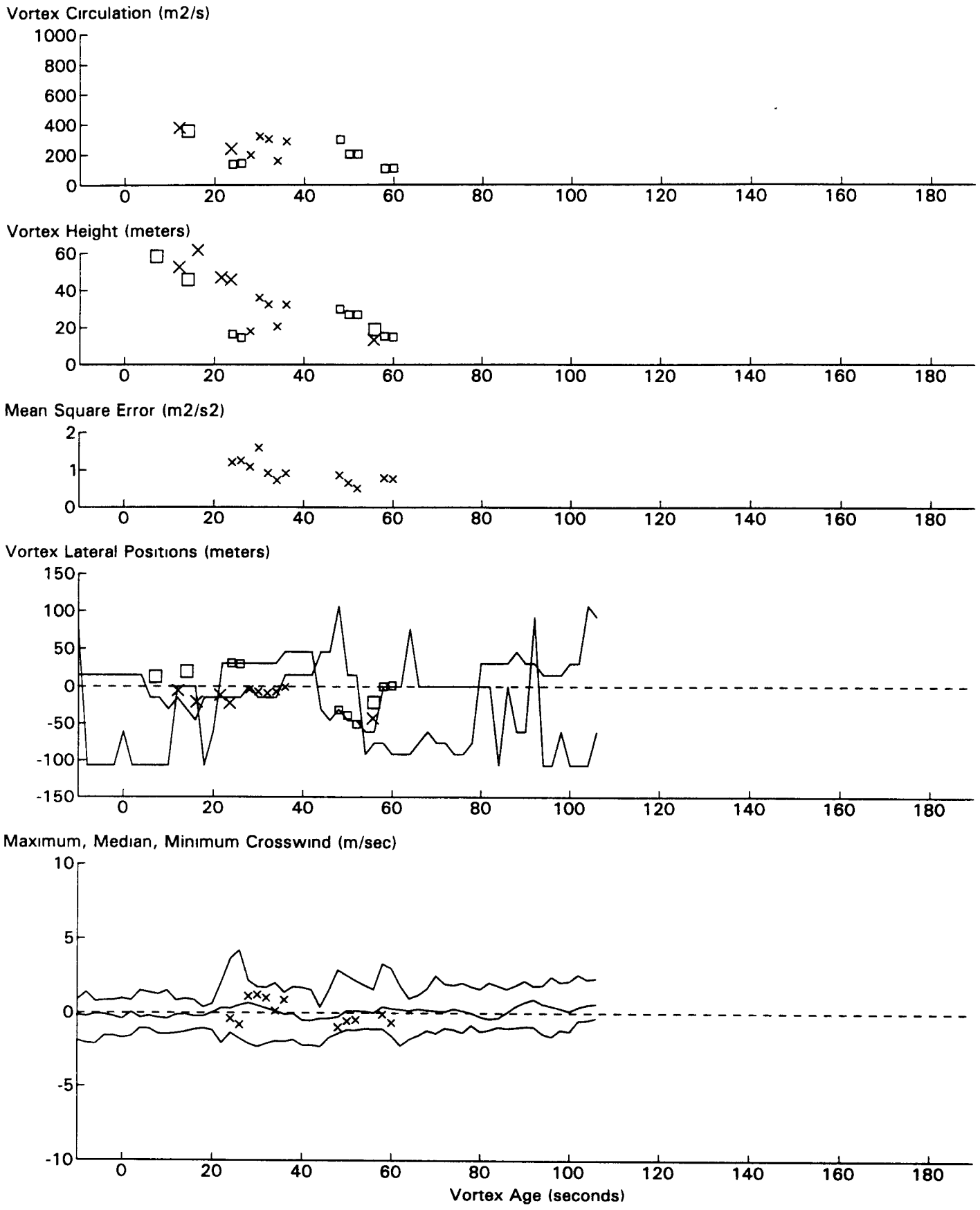

DC9 JFK 31R GWVSS Data for File: I:RM11D20.318 11/20/96 21:51:34 dt= 0 CWturb=0.46

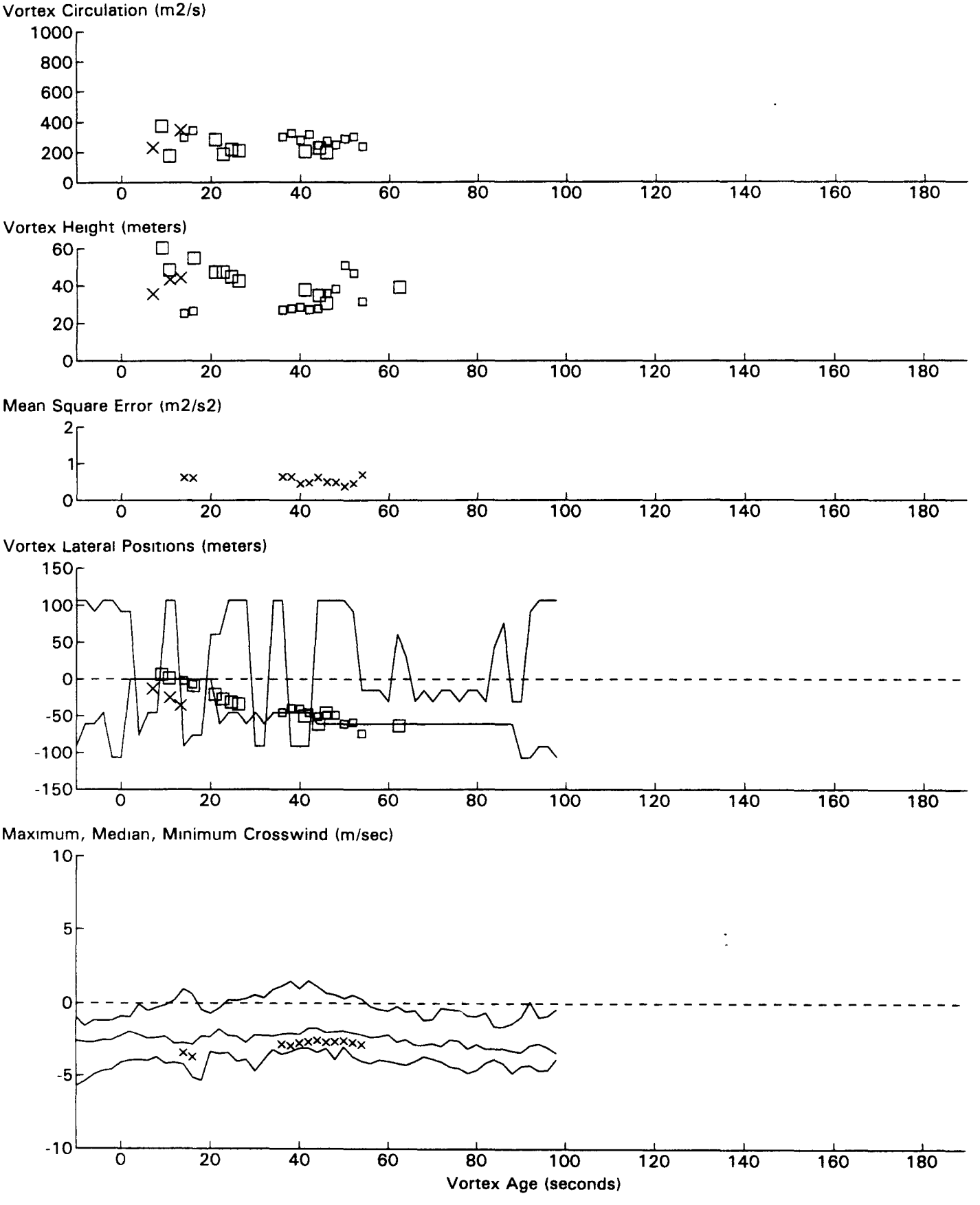

B767 JFK 31R GWVSS Data for File: I:RM11D20.322 11/20/96 21:57:4 dt= 0 CWturb=0.54

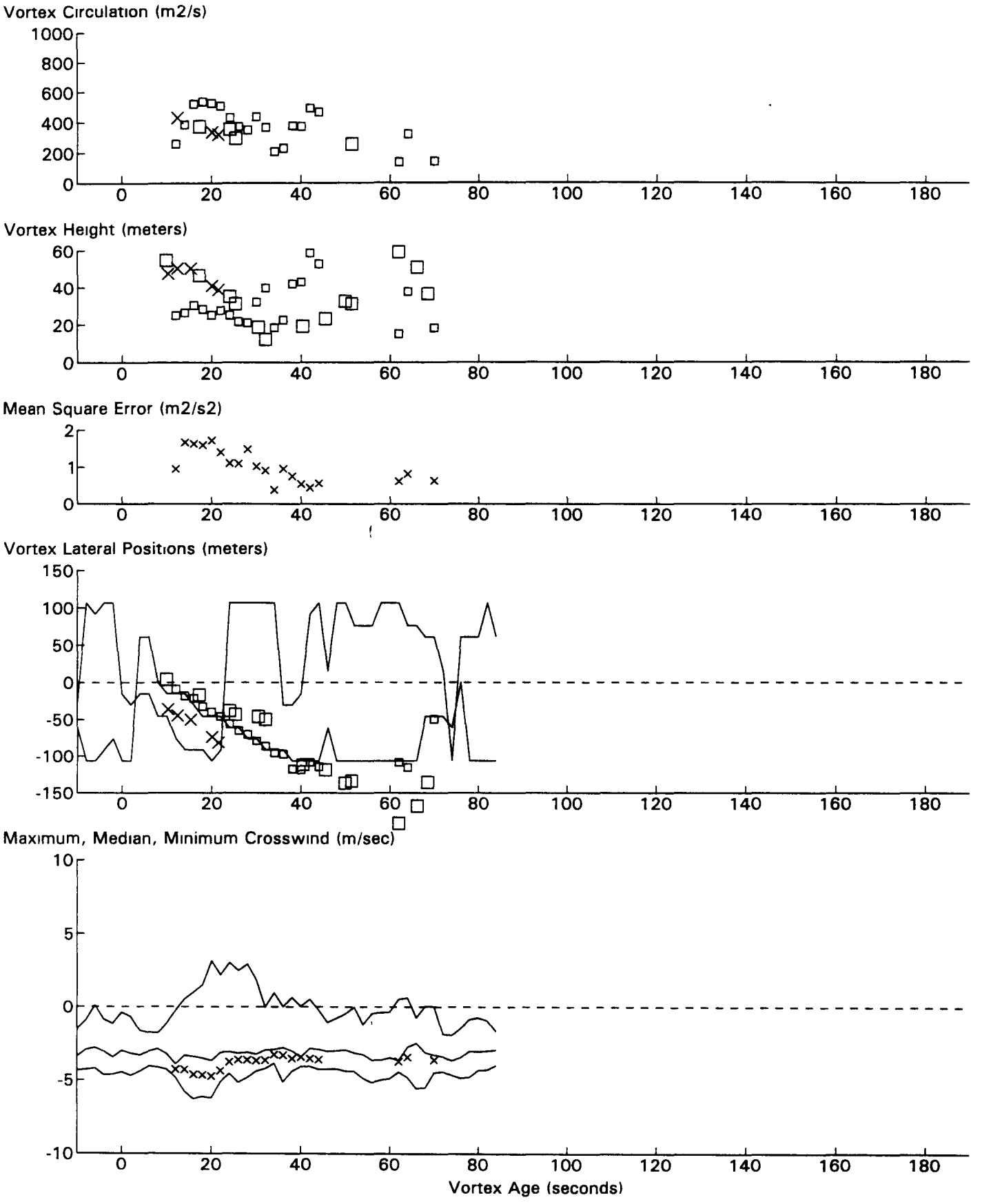

N/A JFK 31R GWVSS Data for File: I:RM11D20.323 11/20/96 21:58:42 dt= 0 CWturb=0.55

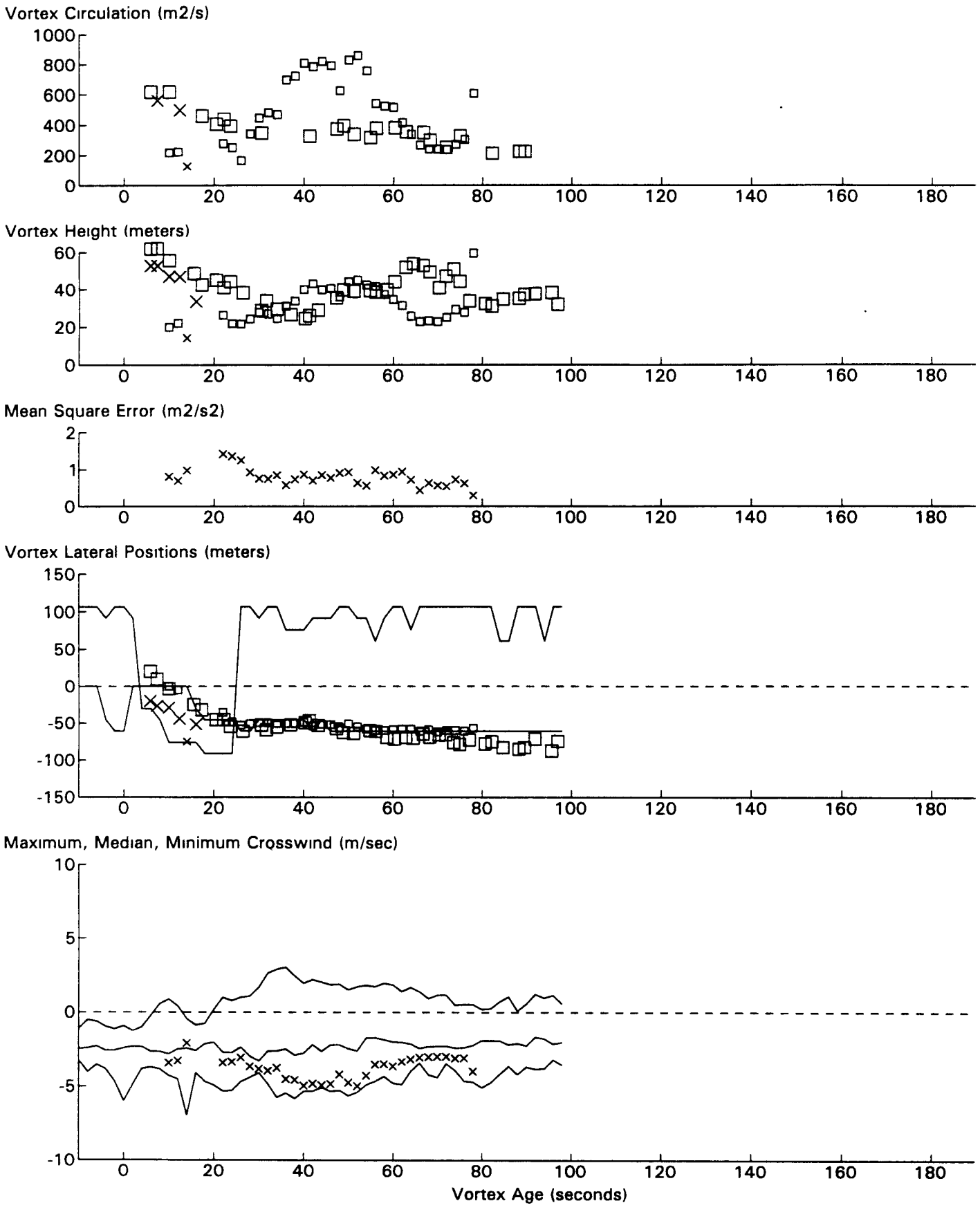

B747 JFK 31R GWVSS Data for File: I:RM11D20.325 11/20/96 22:1:30 dt= 0 CWturb=0.58

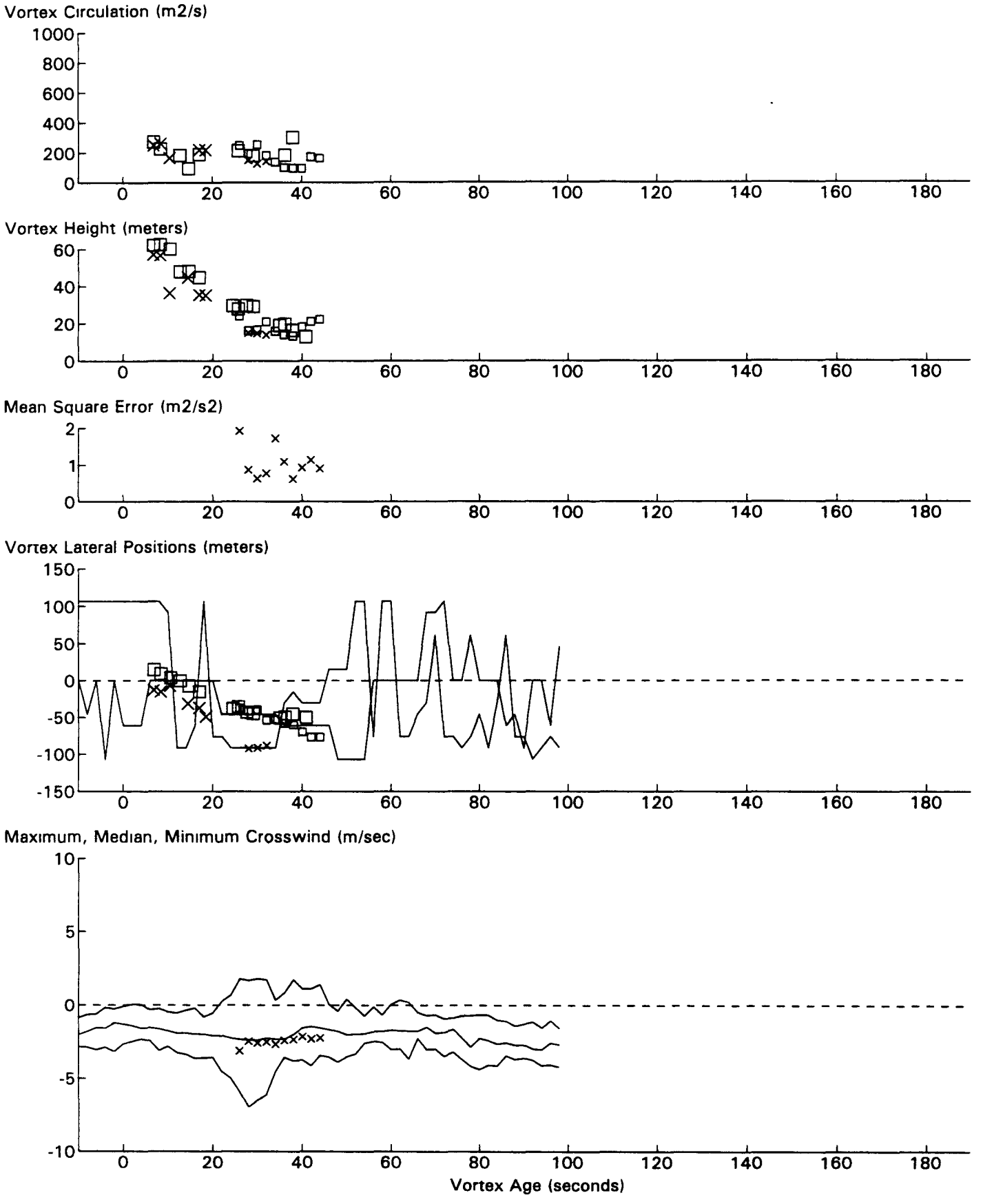

EA32 JFK 31R GWVSS Data for File: I:RM11D20.327 11/20/96 22:4:40 dt= 0 CWturb=0.60

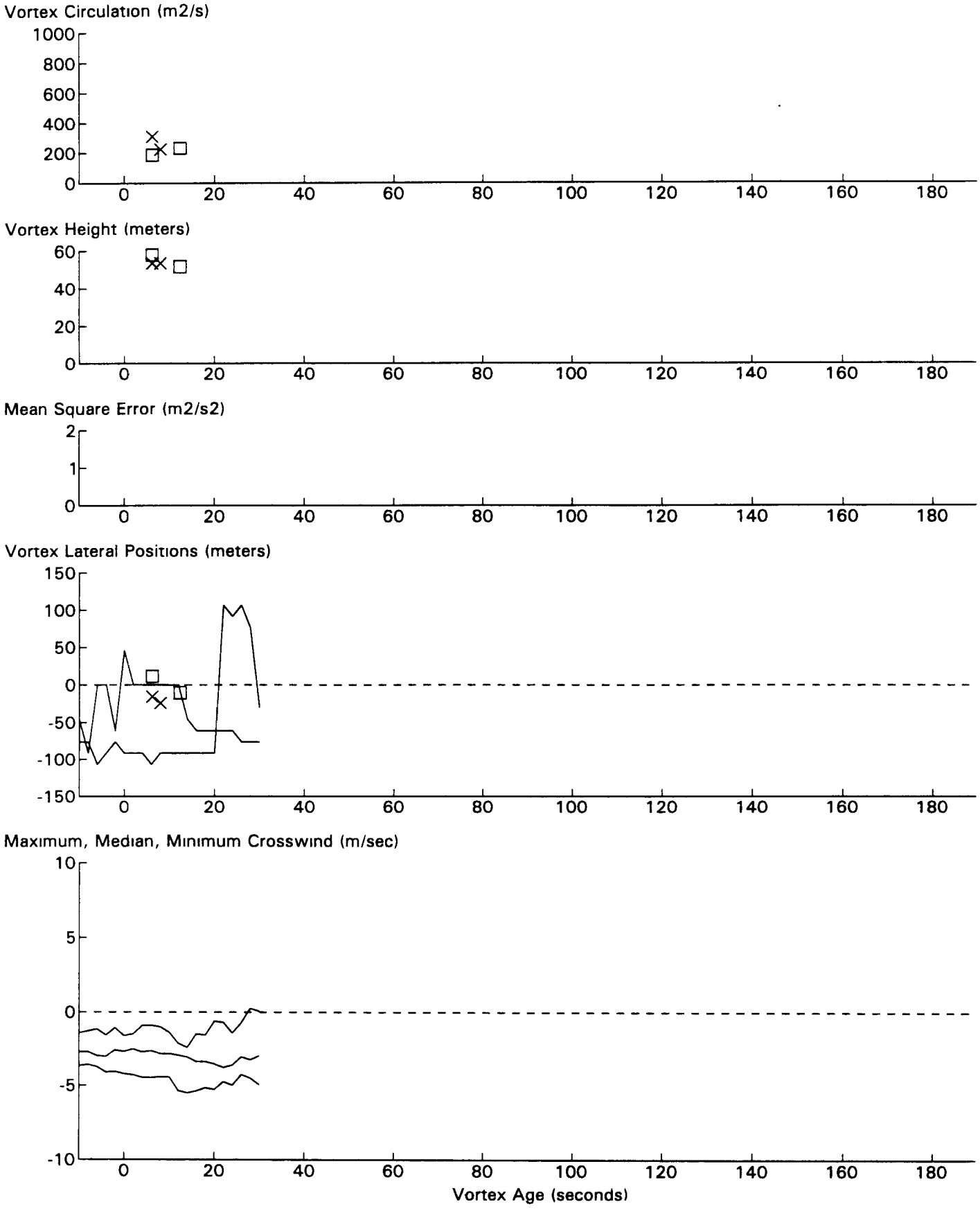

B727 JFK 31R GWVSS Data for File: I:RM11D20.328 11/20/96 22:6:19 dt= 0 CWturb=0.63

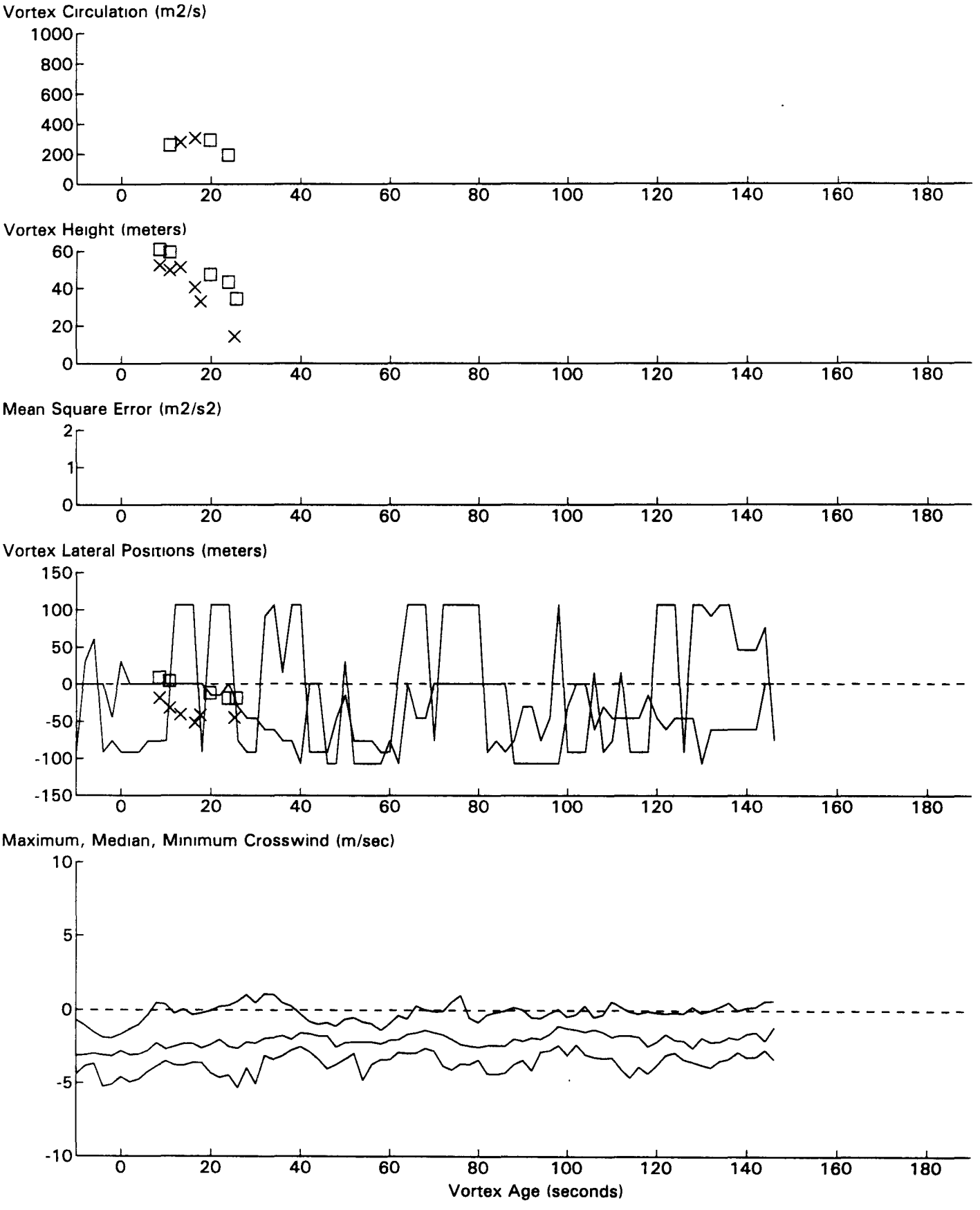

B767 JFK 31R GWVSS Data for File: I:RM11D20.330 11/20/96 22:8:0 dt= 0 CWturb=0.66

REFERENCES

1. Abramson, S. and Burnham, D.C., "Ground-Based Anemometer Measurements of Wake Vortices from Landing Aircraft at Airports," AGARD-CP-584 Conference Proceedings, The Characterization & Modification of Wakes from Lifting Vehicles in Fluids, 20-23 May 1996, Trondheim, Norway, November 1966, pp. 13-(1-7).

2. Sullivan, T.E. and Burnham, D.C., "Ground Wind Sensing System Calibration Tests," Report No. FAA-RD-80-13, February 1980, Transportation Systems Center, Cambridge, MA.

3. Burnham, D.C. and Abramson, S., "Data Base of Ground-Based Anemometer Measurements of Wake Vortices at Kennedy Airport," Report No. DOT/FAA/ND-97-6, June 1997, Volpe Center, Cambridge, MA.

4. Burnham. D.C. and Abramson, S., "Wind Data from Kennedy Airport," Report No. DOT/FAA/ND-97-3, May 1997, Volpe Center, Cambridge, MA.

5. Burnham, D.C., "Chicago Monostatic Acoustic Vortex Sensing System: Volume I: Data Collection and Reduction," Report No. FAA-RD-79-103, I, DOT Transportation Systems Center, Cambridge, MA.

6. Heinrichs, R.M., Freehart, R.E., Dasey, T.J., and Mandra, R.S., "Development and Performance of a CW Coherent Laser Radar for Detecting Wake Vortices," in *Coherent Laser Radar*, Vol. 19, 1995, OSA Technical Digest Series (Optical Society of America, Wash. D.C., 1995), pp. 186-189.

7. Heinrichs, R.M., Dasey, T.J., Matthews, M.P., Campbell, S.D., Freehart, R.E., Perras, G.H., and Salamitou, P., "Measurements of Aircraft Wake Vortices at Memphis International Airport with a CW CO2 Coherent Laser Radar," *Proc. SPIE: Air Traffic Control Technologies II*, SPIE Paper No. 2737-20, April 1996.

8. Huffaker, R.M., Jelalian, A.V., and Thomson, A.F., "Laser Doppler System for Detection of Aircraft Trailing Vortices," *Proceedings of IEEE*, Vol. 58, No. 3, March 1970.

9. Burnham, D.C., "B-747 Vortex Alleviation Flight Tests: Ground Based Sensor Measurements," Report No. DOT-FAA-RD-81-99, DOT Transportation Systems Center, Cambridge, MA, February 1982.

10. Koepp, F., "The Infrared Doppler Lidar: An Important Tool for Experimental Investigation of Aircraft Wake Vortices," in *Technical Digest on Coherent Laser Radar: Technology and Applications, 1991* (Optical Society of America, Wash. D.C., 1991), Vol. 12, pp. 306-308.

11. Constant, G., Foord, R., and Forrester, P.A., "Coherent Laser Radar and the Problem of Aircraft Wake Vortices," *J. Mod. Opt.* 41, 2153 (1994).

12. Heinrichs, R.M. and Dasey, T.J., "Analysis of Circulation Data from a Wake Vortex Lidar," AIAA 97-0059, 35th Aerospace Sciences Meeting & Exhibit, January 6 - 9, 1997, Reno, NV.

13. Salamitou, P., Dasey, T.J., Heinrichs, R.M., and Hansman, R.J., "Range Estimation for CW Lidar Aircraft Wake Vortex Detection," submitted to *Applied Optics*.

14. Burnham, D.C., Abramson, S.L., and Rudis, R., "Performance of RASS Vortex Detection/Measurement System," to be published.

15. Rudis, R.P., and Burnham, D.C., "Comparison of Sodar and Lidar Measurements of Aircraft Wake Vortices," Preprint for ISARS'96 Conference, Moscow, Russia, May 1996.

16. Hinton, D.A., "An Aircraft Spacing System (AVOSS) For Dynamical Wake Vortex Spacing Criteria," AGARD-CP-584 Conference Proceedings, The Characterization & Modification of Wakes from Lifting Vehicles in Fluids, 20-23 May 1996, Trondheim, Norway, November 1966, pp. 23-(1-12).